RPN99

DNA 2787F
PIFR-227/294

INTENSE ELECTRON BEAM GENERATION, TRANSPORT, AND DIAGNOSIS

Final Report

May 1973

Prepared for
Defense Nuclear Agency
Washington, D.C. 20305

This effort was supported by Defense Nuclear Agency under: NWER Subtask Code LA013 Work Unit Code 17

Approved for public release;
distribution limited.

Preparing Agency
Physics International Company
2700 Merced Street
San Leandro, California 94577

ABSTRACT

This report describes intense electron beam generation, transport, and diagnosis oriented toward the development of technology required for construction of an advanced X-ray source. Generation and transport of beams was performed both with and without externally applied magnetic fields; (azimuthal, B_θ, and longitudinal, B_z, magnetic fields were employed). Electron beam and X-ray diagnostics developed or modified for use in this work are described along with theoretical work on diode and beam transport phenomena.

FOREWORD

The work summarized in this report was performed over the time period from January 1970 through July 1971 under DASA contracts DASA01-70-C-0063 and DASA01-71-C-0052. The programs were monitored by Lt. Colonel R. P. Sullivan and Major Benjamin Pellegrini, DNA. Work in this report was performed primarily by members of the Intense Beams Group. The most recent program was managed by Drs. Sidney Putnam and Gerald Yonas, and supervised by Ian Smith (in conjunction with the Snark upgrade work described in Volume II). Beam work during the first program period was managed by Dr. Philip Spence and supervised by Dr. Gerald Yonas. Principal investigators were Dr. James Benford (linear pinch transport), Bruce Ecker (recent Snark diode work and linear pinch transport), Dr. John Guillory (beam transport theory), Gary Loda (diode work on the low voltage Mylar line), Donald Pellinen (electron beam diagnostics), Dr. Charles Stallings (B_z transport), and Don Wood (X-ray diagnostics). John Creedon's work on parapotential diode theory was a substantial contribution to the diode task.

CONTENTS

CONTENTS (cont.)

ILLUSTRATIONS

ILLUSTRATIONS (cont.)

ILLUSTRATIONS (cont.)

ILLUSTRATIONS (cont.)

ILLUSTRATIONS (cont.)

ILLUSTRATIONS (cont.)

ILLUSTRATIONS (cont.)

ILLUSTRATIONS (cont.)

SECTION 1
INTRODUCTION

by S. Putnam and P. Spence

This report presents the results of experimental and analytical work directed toward the development of technology required for the generation, propagation, and control of multi-megampere electron beams. A brief history of high ν/γ beam work at Physics International (PI) is given in this section; this is followed by a more detailed review of the results of present programs. The remaining sections (each written by the principal investigator) cover the following work areas: diode studies, beam transport in azimuthal (B_θ) magnetic fields, beam transport in longitudinal (B_z) magnetic fields--experiment and theory, beam transport in neutral gas, diagnostics development, and conclusions.

1.1 PROGRAM HISTORY

This report summarizes DNA-funded electron beam transport, diode, and X-ray diagnostics work performed from January 1970 through July 1971 (concurrent with development and testing of the Snark generator). Prior to this period, the primary emphasis of beam work at PI was on generating and propagating high ν/γ beams and on developing an empirical understanding of neutral gas transport. DNA-funded work prior to 1970 (with appropriate report numbers) is summarized below.

1.1.1 February 1968 through August 1968: 738 Pulserad (DASA 2175).

a. High ν/γ beam behavior in neutral-gas-filled drift chamber; net current measurements; beam characteristics interpreted in terms of various degrees of charge and current neutralization.

b. Beam transport in metallic guide pipes (straight and curved) and in cones; transport efficiency measurements (~ 3 meter e-folding length); production of uniform fluence beams using guide cones.

c. Initial look at beam transport in longitudinal magnetic fields.

d. Diagnostics development; self-integrating B probes, anode Faraday cups, cathode voltage monitor.

1.1.2 November 1968 through August 1969: 738 Pulserad (DASA 2296, 2426).

a. Observation of time-dependent impedance collapse in high ν/γ diodes.

b. Primary current and net current measurements for transported beams.

c. Development of semi-empirical model including gas breakdown and conductivity to explain beam behavior and time dependence of net current.

d. Documentation of beam transverse energy determined from time-of-flight, electron transmission versus depth, and energy deposition versus depth measurements. Indication that transport efficiency was affected by loss of high transverse energy electrons.

e. Diagnostics development; Faraday cup, self-integrating Rogowski coils, low-inductance wall current shunt for measurement of primary and net currents in propagated beams.

f. Observations consistent with Graybill's experiments of accelerated ions produced by injection of electron beams into low-pressure gases.

g. Suggestion that use of a preionized plasma (to short out induced emfs) with external magnetic fields (to contain high transverse energy components) would enhance beam transport efficiency.

During this same period, generator technology was being developed at both Naval Research Laboratory (Gamble I, low-impedance water dielectric line) and Physics International (two Mylar dielectric striplines, 0.1 Ω, 100 kV, and 1.5 Ω, 500 kV, (Reference 1.1)). As a result of this development, construction of higher voltage and current modules was shown to be feasible.

The work summarized in this report covers two project periods: from January to October 1970 (during the initial construction and testing of Snark) and from November 1970 through July 1971 (during the upgrading and facilitization of Snark). The generator development and upgrading is reported separately in PIFR-226 and PIFR-296. Accomplishments of the beam transport and diode work during the two recent program periods are summarized below.

1.1.3 January 1970 to October 1970 (Project 21-227).

a. Low impedance diode studies on 0.3 Ω, 100 kV Mylar line; empirical modeling of impedance collapse due to anode explosion; development and use on Snark of rugged, hollow-geometry cathodes to minimize impedance collapse.

b. Efficient electron beam transport (500 to 600 kV, 160 kA), in Z-pinch discharge (preionization plus external B_θ); development of 10^6 ampere pinch for use on Snark.

c. Efficient beam transport (100 kV, 100 kA) in a quasi-theta pinch discharge (preionization plus external B_z).

d. Diagnostics development; capacitive diode voltage monitor, current monitor surrounding the cathode (Rogowski coil) for Snark, X-ray fluence and deposition versus depth calorimeters.

1.1.4 November 1970 to July 1971 (Project 21-294).

a. Diode impedance studies (Snark)--correlation with parapotential model. Measurement of current density variation with radius and time at anode plane.

b. Extension of beam transport in Z-pinch (Snark) to 700 kV, 300 kA showing efficient transport.

c. Development of two magnetically isolated cathodes and demonstration of beam mixing by injecting into a Z-pinch (Snark).

d. Demonstration of current density control using straight and tapered Z-pinch transport (Snark and PIML).

e. Efficient beam transport in B_z (Snark). Extensive parameter scan of field strength, gas pressure, preionization, transport distance, and current density.

f. Successful feasibility test of beam convergence in B_z using a ring cathode and a conical B_z field configuration.

g. Extension of diode impedance lifetimes with B_z applied to the diode.

1.2 PROGRAM REVIEW

The overall goal of the DNA-funded beam and diode programs (PI Projects 21-227 and 21-294) has been to obtain the necessary technical background to design a system from the viewpoints of cost, ease of operation, and reliability. When the 21-294 program was presented to DNA last October, our experience pointed to several possible generator-diode-transport systems, all of which required further experimental investigations. Examples of systems considered at that time are:

B_θ-System: Several 1 to 2 MA tubes or a single tube with a large-diameter ring-cathode array (cathode magnetically isolated), using linear pinch transport tubes to a common focal region with or without a separate combination stage.

Neutral Gas: Many small conducting pipes carrying ≈ 100 kA each, emanating from an array of diodes focused to a common point with or without a separate combination stage. The combination stage was envisioned to be either a neutral gas chamber at a pressure which gives rapid electrical neutralization but incomplete current neutralization, or a short linear pinch stage.

B_z Solenoid System: Several linear solenoids from separate tubes converging to a common focal region with or without a compression stage. Mixing or superposition of the individual beams was deemed unfeasible.

Conical B_z System: Current from a large ring cathode following along field lines to a smaller diameter region without change in the current density. This system was designed to give a relatively cold beam at formation, to minimize total magnetic field energy, and to avoid the necessity of beam compression. Moreover, it was felt that such a system would allow a greater degree of beam compression, if desired, than linear solenoid systems because of the lower beam temperature.

With these systems in mind, let us briefly review the state of the art at the start of the beam program last fall.

a. Diodes--virtually no investigation of impedance with currents substantially beyond the critical current ($I_c \cong 8500\ \beta\gamma\ r/d$); impedance collapse was postulated by PI to be due to anode plasma hydrodynamic motion.

b. Neutral Gas--transport efficiency dropped to about 30 percent over a meter when ν/γ was increased to the range of 4 to 5.

c. B_θ (linear pinch)--transport efficiency $\gtrsim$ 90 percent over 2-foot distances.

d. B_z--solenoid transport showed large scatter (40 to 85 percent) in transport efficiency over distances of ~ 1 meter at ν/γ in the range of 2.5 to 15. Preionization was shown to increase transport efficiency at higher current densities. The only modeling of transport efficiency was a diamagnetic pressure balance equation (Naval Research Laboratory, Cornell, Reference 1.2) which appeared to be inconsistent with adiabatic mirror compression results (Cornell, Reference 1.3). Mirror field geometries near the diode were shown to result in large beam energy losses.

Our program was therefore designed to fill in the many technical gaps of the various systems and to extend the existing B_θ, B_z work to the higher ν/γ and current densities. Our emphasis was both to demonstrate as many features of each system as possible with Snark and to elucidate the physics involved in these features, inasmuch as none of the systems appeared to be strictly additive or modular. More specifically, we list below the technical investigations deemed necessary for definition of the systems previously described and indicate the present status of the experimental work for each task.

1.2.1 Diode (B_z = 0) Tasks (Work Required for B_θ and Neutral Gas Systems).

a. Model impedance versus geometry and voltage, and design 0.8 to 1 ohm diode

b. Design high current, magnetically isolated cathodes

c. Achieve impedance lifetimes of ~ 120 nsec

d. Define beam injection conditions ($j_z(r,t)$) using apertured Faraday cups

Status of Work: All major program goals have been accomplished for the diode work. Parapotential modeling of impedance has been verified, thereby allowing design of cathodes for currents above I_C. Reproducible operation of diodes at $Z \lesssim 1$ has been achieved with impedance collapse only after ~ 110 to 120 nsec. Magnetic isolation designs have been tested. The apertured-Faraday-cup work has given the time dependence of the current density, $j(r,t)$, for several cathode configurations and has shown the existence of current density out to radii equal to the cathode radius even when a portion of the beam pinches strongly.

1.2.2 B_θ System Tasks.

a. Extend transport studies using Snark beams, develop scaling laws for field requirements

b. Investigate limits of fluence control using both linear and tapered pinches

c. Investigate beam combination feasibility in linear pinch geometry

Status of Work. The linear pinch transport program has successfully demonstrated and modeled transport of 13 kJ beams over distances of 2 feet with efficiencies $\gtrsim$ 90 percent. The feasibility of beam combination as a linear pinch has also been demonstrated. Fluence control (50 to 250 cm^2) has been shown by varying beam injection time in straight pinch and in tapered pinch configurations. Summary details of this work are given below.

Pinch Transport.

a. Efficient transport has been observed for beam currents between 120 and 310 kA, with average current densities over the cathode surface between 10^4 and 4×10^4 A/cm^2. Peak current densities have been in the range of 10^5 A/cm^2 (this last number is based on apertured Faraday cup data from a 120 kA beam on the 738 machine). Transported total energies have been 4 kJ to 13 kJ, at voltages of 500 kV and 750 kV respectively.

b. Fluence control has been demonstrated by varying the transported beam area from 240 cm^2 to 50 cm^2 at the 13 kJ level on Snark. (Also fluence control on 738 machine experiments.)

c. Single-particle motion in the external field of pinch explains all data to date. Scaling of these results requires:

- i Transport in a background medium with high conductivity to provide good current neutralization.
- ii B_θ large enough at a given radius to turn energetic electrons back to the beam channel before they reach the wall.
- iii Injection of beam particles into pinch field regions of positive drift velocity.

Beam Combination (450 kA Total, 650 keV, 17 kJ). Combination has been achieved with transport efficiency at approximately 90 to 100 percent, when two beams were injected inside a collapsing Z-pinch current sheet. Witness plate damage at the end of the 45-centimeter-long transport region clearly shows mixing of the two beams in an azimuthally symmetric pattern. As in the single beam experiment, the beam area can be varied by variation of injection time into the collapsing Z-pinch current sheet.

Beam Compression with Tapered Pinch; PIML Beam 350 keV, 2 kJ. Beam area has been reduced by a factor of two in the tapered pinch; however, transport efficiency was observed to be ~ 50 percent. The data indicate (1) compression of the beam up to 1.3 μsec after firing the Z-pinch, (2) failure to compress at times beyond the 1.3 μsec injection time.

1.2.3 B_z Systems Tasks.

a. Characterization of diode impedance versus tube geometry, voltage, and applied field.

b. Modeling of impedance collapse with B_z.

c. Investigation of transport efficiency versus B_z, gas pressure, and degree of preionization.

d. Determination of length scaling of transport efficiency.

e. Investigation of conical B_z system feasibility.

Status of Work. Linear solenoidal transport work has accomplished the generating and transporting of beams with peak current densities of 10^4 to 10^5 A/cm^2 (nonuniform current densities) over distances up to a meter with transport efficiencies $\geqslant$ 80 percent. Diode current density has been shown to exhibit a radial dependence which has been qualitatively modeled. The impedance has been maintained over the acceptably long times of $\sim$ 120 nsec, even at current densities $\gtrsim$ 30 kA/cm^2. Preliminary experiments with the conical B_z system on Snark have shown that a sheet beam from a large annular cathode can be reduced in diameter without compression. More specific data on solenoid transport are given below.

a. DNA Mylar Line (DML) (120 keV, 135 kA) transport data showed 90 percent transport efficiency at 10^5 A/cm^2 ($\nu/\gamma \sim 35$) over 20 centimeters upon injection into a preionized plasma.

b. Physics International Mylar Line (PIML) transport data at 200 keV and area averaged peak current density of 3.5 kA/cm^2 showed better than 90 percent transport efficiency for 1 meter.

c. Snark transport data at 600 keV mean energy and area-averaged peak current density of 9 kA/cm^2 over 60 cm^2 achieved 90 percent efficiency over 1 meter.

d. Snark experiments with 20 to 30 kA/cm^2 area-averaged current density peaks show a transport efficiency of about 80 percent at 1/2 meter. The peak current density on the beam axis is of the order of three times the area-averaged current density, or, in other words, 40 percent of the total current flows within about 10 percent of the beam area.

e. Neutral gas study tasks: this portion of the program has addressed only one specific aspect of such systems; i.e., can relatively cold beam injection conditions be achieved in the diode at 1 MeV with uniform current densities in the 25 kA/cm^2 range? Such an accomplishment would eliminate the necessity of substantial beam compression. Our relatively small effort has not been promising. It would seem that any neutral gas system will require considerably more work to demonstrate feasibility. In particular, a more attractive approach would be to extract much lower current densities, followed by compression before the converter is reached. This status must be compared, of course, to the already demonstrated ability to efficiently transport high current density and high ν/γ with B_θ and B_z systems.

REFERENCES

1.1 S. Shope, G. Yonas, I. Smith, R. Ward, P. Spence, and B. Ecker, "Development and Application of Mylar Strip-lines," DASA 2482, PIFR-137, Physics International Company, San Leandro, California, January 1970.

1.2 L. Levine, et al; Bulletin of American Physical Society; Vol. 15, #11; p. 1401, 1970.

1.3 H. Davitian; Bulletin of American Physical Society; Vol. 15, #11; p. 1452, 1970.

SECTION 2

DIODE STUDIES, $B_z = 0$

by B. Ecker

2.1 INTRODUCTION

In the context of the continuing development of intense high ν/γ electron beam generators, the following studies of high ν/γ diode physics have been performed under the projects titled "Development of an Advanced X-ray Source" and "Advanced Photon Source Technology Program."

2.1.1 Diode Impedance.

a. Impedance lifetimes must be long enough for the generator energy to be converted into relativistic electron current in the diode. Impedance collapse, the drop in diode impedance apparent from diode current and voltage diagnostics when solid cathodes or small anode-cathode gaps are used, must therefore not occur earlier than ~ 130 nsec.

b. A verified physical theory of the pinched beam diode that predicts diode current as a function of cathode dimensions, anode-cathode spacing, and applied voltage is required so that diodes can be routinely designed to accommodate future generator output specifications. For example, diode impedance in the range 0.8 to 1.0 Ω was necessary in the program just completed in order to sufficiently match the Snark generator.

2.1.2 Beam Radial Structure at the Anode Window. In addition to being directly relevant to the attainment of desired current densities, the radial structure of the current density at the anode window is an important initial condition for beam transport systems. With $B_z = 0$, the B_θ (linear pinch) and neutral gas configurations are the relevant systems. It was well known at the outset of the program that high ν/γ beams pinch in the diode, with much of the beam energy concentrated around the axis over a cross-sectional area considerably smaller than the cathode area. However, it was not clear if indeed all of the electrons are swept in toward the axis or if some current reaches the anode at radii comparable to the cathode radius. Since there is much more cross-sectional area at the larger radii than near the axis, relatively low-current densities flowing in the "wings" could possibly result in a substantial portion of the total energy being left out of the tightly pinched, high-current density core. In view of the relevance of this possibility to attainment of the desired beam specifications and to the entrance design of beam transport systems, the radial structure of the current density was investigated at the anode plane using Faraday cups specially developed for this purpose.

2.1.3 Multiple Diode Decoupling. One alternative design plan for higher current generators involves combination of parallel beams generated from a number of diodes in a single tube. In this configuration, however, the individual high-current diodes are perturbed by asymmetries in the diode return current path and by the net magnetic field due to the other diodes in the tube. Studies have therefore been necessary to determine if these effects, described below, can be suppressed in the anode-cathode gaps where the beams are generated.

Results regarding diode impedance, beam radial structure, and decoupling of diodes, with $B_z = 0$, constitute the next four subsections.

2.2 DIODE IMPEDANCE CHARACTERISTICS

2.2.1 Impedance Collapse. The use of anode-cathode spacings of less than 4 mm in low impedance diodes brought with it the phenomenon of impedance collapse. The term impedance collapse connotes an appreciable drop in diode impedance during the pulse. Diode impedance is, in general, a function of voltage and geometry (dimensions). The time-dependence of the applied voltage is therefore one cause of time dependence in the impedance, but we were unable to find a causal relationship between the measured variations in diode impedance and those in voltage alone. For example, the voltage rises, peaks, and declines, while in most cases the impedance declines monotonically throughout the pulse. It became clear that we needed to hypothesize that impedance is affected by time variations in the geometry as well as in the voltage. The explanation suggested by this program involves the physical closing of the anode-cathode gap, d_o, due to expansion of the anode plasma at a rate of typically 1.5 cm/μsec. In studies using the DML generator, a model was developed in which the anode is assumed to consist of a highly conductive plasma, exploding from its midplane at a velocity of 1.5 cm/μsec, beginning at t = 10 nsec. This explosion is the thermomechanical response of the anode to the high energy density loading of the electron beam. This anode velocity is consistent with framing camera data taken on other e-beam machines at similar dose levels. Figure 2.1 shows the good fit to the data that this model gives. The solid lines are empirical impedance values calculated using the Child's Law* with time-dependent gap spacing,

$$Z = \frac{4.27 \times 10^5}{V_o^{\frac{1}{2}}} \frac{d^2}{A} \quad \text{(mks)} \qquad (2\text{-}1)$$

---

*Measurements of the radial structure of the current density J (r,t), described below, showed that the beam had not yet pinched during most of the interval shown in Figure 2.1, so that the use of Child's Law in this analysis is justified.

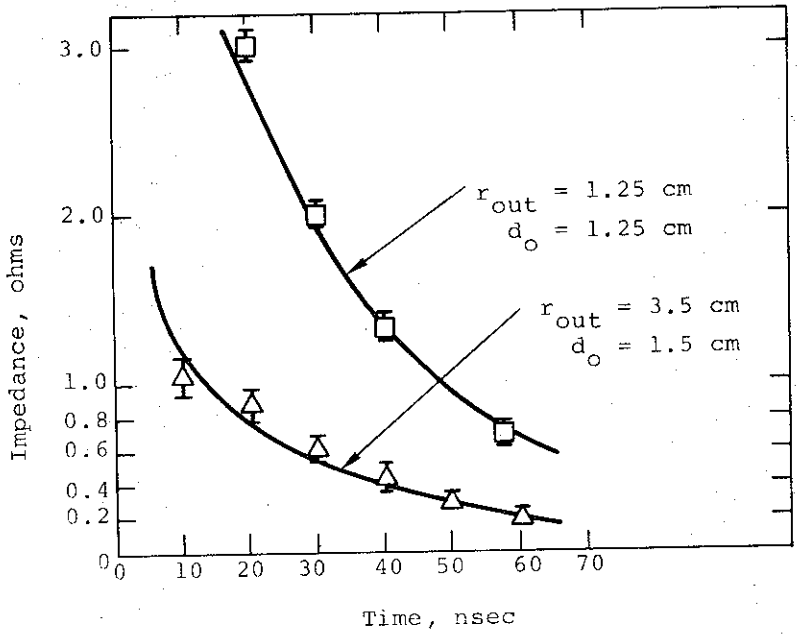

Figure 2.1 Diode impedance with solid cathode, DML generator. Solid lines indicate theoretical, points indicate experimental.

where A is the cathode emission area, $d = d_o - v(t-10^{-8})$, $v = 1.5 \times 10^{-8}$ m/sec is the assumed anode velocity, t is the time (t > 10 nsec) and V_o is the diode potential difference in megavolts. The individual points in Figure 2.1 are the experimental data, with the error bars indicating a spread of three shots.

These results were obtained using "solid" cathodes, that is, cathodes with needle electron emitters distributed over $0 \leqslant r \leqslant r_{out}$, where r is radial distance measured from the longitudinal (cylinder) axis and r_{out} is the cathode outer radius (Figure 2.2). To delay the effects of impedance collapse, "hollow" cathodes were used on which the electron-emitting surface extends over $r_{in} \leqslant r \leqslant r_{out}$, an annulus. This configuration was tested on the basis of the following qualitative arguments. The high-current beams pinch and deposit energy in the anode most heavily near the axis (near $r = 0$). At early times, though, energy deposition does occur in the anode directly opposite the annular cathode surface. But before pinch, the current is relatively low and is distributed over a large area, while after pinch the current is higher and is distributed over a much smaller area. The total deposited energy dose per unit area in the anode is not great enough to cause immediate anode explosion opposite the cathode; rather, the high-velocity anode expansion primarily responsible for impedance collapse occurs in the vicinity of the axis, and impedance collapse is suppressed if r_{in} is sufficiently large (Figure 2.2). This effect is clearly visible in Figure 2.3, which shows a typical impedance time-history using the large annular cathode shown in Figure 2.8a. The impedance waveform reaches a relatively constant plateau, and not until very late in the pulse does it exhibit apparent collapse.

Although a quantitative theoretical prediction of the entire waveform has not been attained, a steady-state approximation has been derived which predicts the impedance during the plateau phase (Appendix A).

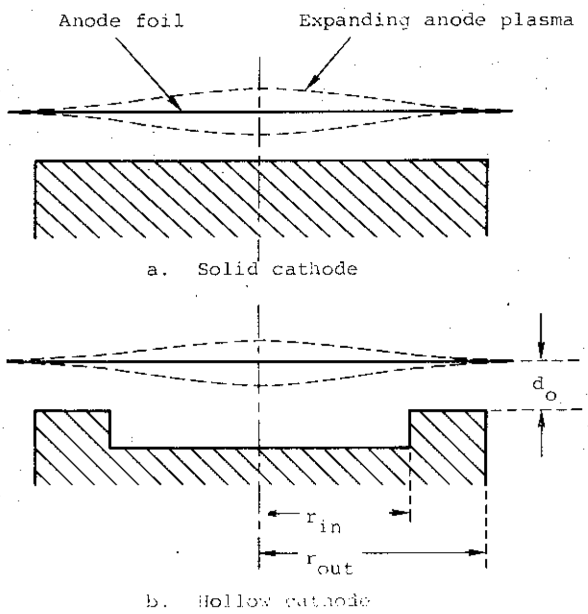

Figure 2.2 Anode expansion in relation to (a) solid cathode and (b) hollow cathode. Expansion is hypothesized to be greatest near axis; hollow cathode is least affected.

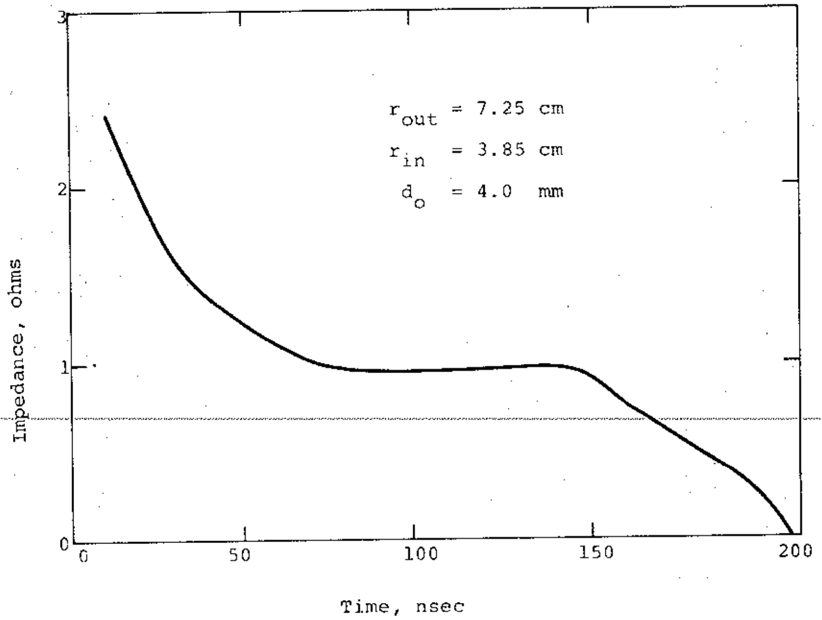

Figure 2.3 Impedance waveform, Shot 687. Peak current was 498 kA at t = 90 nsec.

2.2.2 High ν/γ Impedance. Child's Law, expressed as an impedance formula in Equation (2-1), successfully predicts the voltage-current characteristics of planar diodes only when the electron velocities are paraxial, since this condition is assumed in its derivation. When the beam pinches in the diode, this condition is no longer satisfied and Child's Law is inaccurate. The cause of pinch is the strong azimuthal magnetic field whose source is the beam current itself.

An approximate criterion for the current level at which diode pinch occurs has been given by Friedlander and Jory (Reference 2.1). Their model assumes that pinching of the beam will begin when the diode current is equal to I_c, which is the largest possible current at which an electron emitted paraxially from the edge of the cathode can reach the anode, due to influence of the self magnetic field. This critical current is

$$I_c(\text{amps}) = 8500\beta\gamma(r_{out}/d_o) \tag{2-2}$$

where

r_{out} = cathode outer radius
d_o = anode-cathode spacing
$\gamma = (1 - \beta^2)^{-\frac{1}{2}} = 1 + eV_o/m_e c^2$

This model assumes that there is no space-charge neutralization in the diode (i.e., positive ions are not present) and no radial electric fields. It gives no information as to the velocity of the pinch collapse or the current distribution at the anode during the pinch. This expression for I_c can be derived by setting the anode-cathode spacing d_o equal to the Larmor radius of an electron with kinetic energy eV_o (V_o = diode potential) moving in the magnetic field at the cathode edge. (This is an approximate calculation, but the same formula for I_c results from spatially revolved EM trajectory calculations for an electron emitted paraxially at the cathode edge, if it is assumed that the applied axial electric field is uniform, the magnetic field varies negligibly over the trajectory, and the radial electric field is zero.)

As an example, consider the parameters typical of some of our diode experiments on the Snark generator: $r_{out} = 72.8$ mm, $d_o = 3.5$ mm, $\beta\gamma \approx 2$ ($V_o \approx 500$ kV). This gives $I_c \approx 350$ kA. Currents of about 500 kA were attained at 500 kV, which suggests that diode pinch is to be expected. Witness plate damage and J(r,t) measurements, described below, verified this.

The only analytical framework (to our knowledge) developed for the description of diodes with pinched flow (strong self-magnetic fields) is that of parapotential flow theory, which has been applied to the case of the high-current, high ν/γ diode by de Packh (Reference 2.2), Friedlander, et al. (Reference 2.1), and Creedon (Reference 2.3). This picture rests on the possibility that there is a class of electron trajectories in the diode that are force-free. To see this, consider the following arguments: in beam pinch, electrons emitted near the cathode outer edge, $r = r_{out}$, move to a much smaller radius as they traverse the anode-cathode gap. Such an accumulation of charge near the axis must depress the axial electric field at the cathode at interior radii, so that electron emission is predominantly from the cathode periphery. The instantaneous equipotentials of the applied field are pictured as in Figure 2.4a.

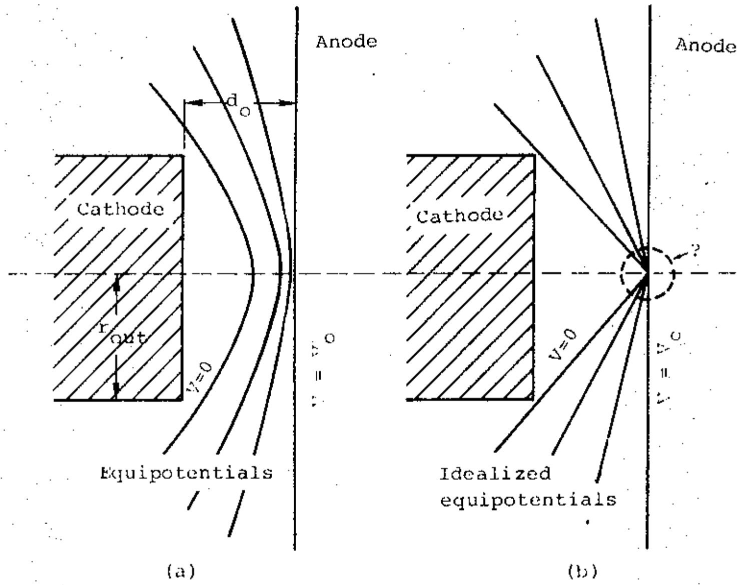

Figure 2.4 (a) Physical schematic of equipotentials during pinched flow;

(b) Idealized equipotentials along which electrons are assumed to flow toward axis. Circled area with question mark indicates region of orthopotential flow untreated by parapotential model.

The electric force is of course perpendicular to the equipotentials. An electron moving radially inward along a single equipotential also experiences a magnetic force (due to the azimuthal magnetic field B_θ) that is also perpendicular to the equipotential and is opposite the electric force. These two forces will be of equal magnitude and cancel if the electron velocity divided by the speed of light is $\beta = E/B_\theta$ (cgs units); in such a case no net force acts on the electron, and its motion is force-free as well as parapotential. (This is akin to the situation in a magnetron, with the magnetic field acting as an insulator in the interelectrode space.) The assumption of steady-state ($\partial I_o/\partial t = 0$), parapotential, force-free flow provides partial information on the spatial dependence of the current density, charge density, and fields. The added requirements of Ampere's law and Poisson's equation result in a fundamental equation of the flow [de Packh (Reference 2.2)] :

$$\nabla^2 V = 2r^{-2} dI^2/d^2 V \text{ (cgs)} \tag{2-3}$$

where r is the radius in cylindrical geometry, $V = V(r,z)$ is the potential, and $I = I(r,z)$ is the total current flowing within radius r through the plane z = constant. Solutions to Equation (2-3) indicate that a "bias current" must flow in the axial direction inside the parapotential flow in order for the conditions for the flow to be satisfied. The bias current, arbitrary except for a lower limit, is included in the current I in Equation (2-3); analytically it is a parameter whose physical origin is outside the theory as it now stands. de Packh has shown that the minimum allowable bias current corresponds to electron parapotential flow along all equipotentials, including those grazing along the anode. Higher bias currents constrain the flow to lower-lying equipotentials, raising the impedance of the diode.

A simple picture due to Creedon (Reference 2.3) that facilitates application of the parapotential analysis to high-aspect-ratio planar diodes is shown in Figure 2.4b. The equipotentials of Figure 2.4a are idealized into conical surfaces over most of the interelectrode region. The electrons are assumed to be already flowing along the equipotentials just outside the cathode edge; the model does not attempt to describe why or how this occurs, although emission from the cathode shank is the probable source. Near the axis, Figure 2.4b is unphysical. Presumably the flow near r = 0 is orthopotential and is not included in this model. It is assumed that the flow near r = 0 does not effect the parapotential flow elsewhere in the diode. The model does not treat the distribution of current at the anode plane.

As developed fully in Appendix A, Creedon treats the "grazing" case mentioned above and finds the voltage-current characteristics shown by the smooth curve in Figure 2.5 for which

$$I_o = 8500\ (r_{out}/d_o)\ \gamma\ \ln[\gamma + (\gamma^2 - 1)^{\frac{1}{2}}]\ (\text{mks}) \qquad (2\text{-}4)$$

The total current I_o was measured using a calibrated Rogowski coil embedded around the diode, and the voltage V_o was measured using capacitive dividers in each of the two Snark modules and an annular capacitive divider around the diode. The latter voltage monitor and the Rogowski coil, illustrated in Figure 2.6, were specially designed for the stringent spatial requirements in the Snark tube and diode. Output waveforms for two shots are shown in Figure 2.7. The results of many such measurements are plotted in Figure 2.5 for comparison with Creedon's predicted curve. They agree well with the steady-state parapotential calculations over the ranges of $7.26 \leqslant r_{out}/d_o \leqslant 20.8$, $170\text{ kV} \leqslant V_o \leqslant 970\text{ kV}$. The type of cathode surface used, roll-pin or concentric circular ridge (Figures 2.8, a and b and 2.9) does not appear to be discernible from the data. This gives added support to the view that in the pinched beam case, beam electrons originate primarily near the cathode periphery, rather than from the planar cathode surface. We interpret these results to be strong evidence that parapotential flow occurs in our diodes around the time of peak current. Equation (2-4) has therefore assumed the status of a verified formula which indicates the diode geometry r_{out}/d_o to be used to obtain desired current I_o with diode voltage V_o.

2.3 DECOUPLING OF DIODES

To study the current feed and magnetic interaction perturbation effects of adjacent diodes, a double diode configuration,

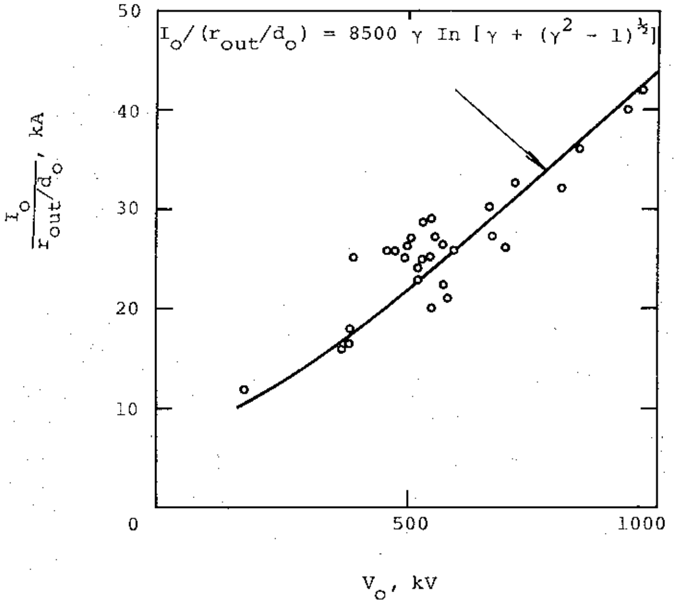

Figure 2.5 Comparison of theoretical (Cf Equation (2-4) and Appendix A) and experimental results for impedance of diode with pinched flow. For this comparison, experimental data are restricted to $dI/dt = 0$: $I_o = I_o(t)_{max} = I_o(t_m)$; $V_o = V_o(t_m)$; each experimental point (I_o, V_o) comes from a single beam pulse.

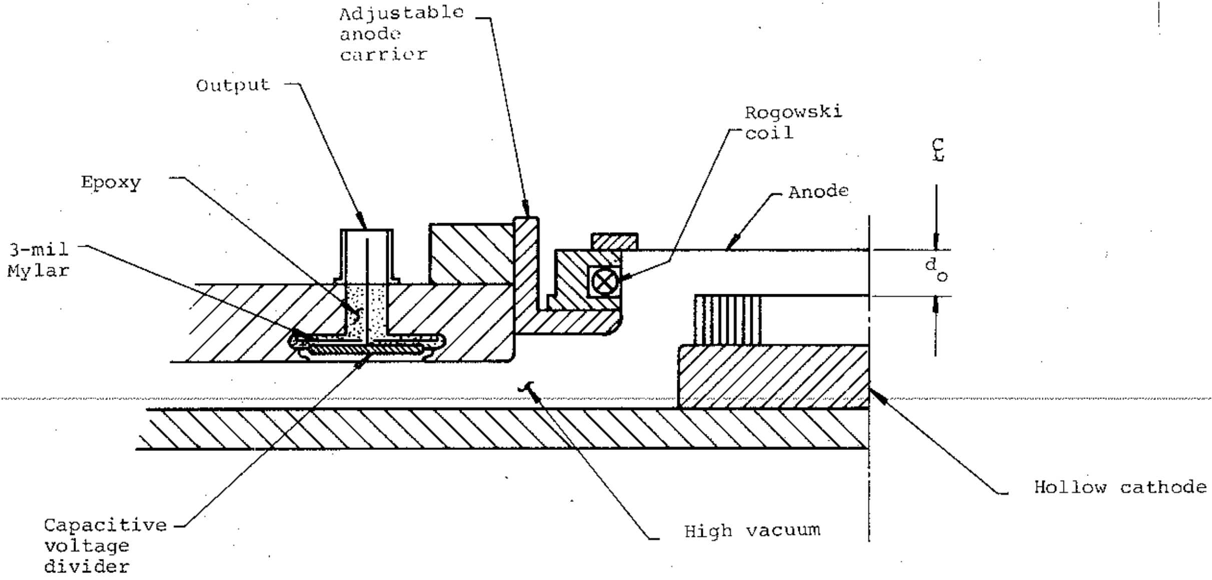

Figure 2.6 Snark anode-cathode configuration showing diode current and voltage diagnostics (not to scale).

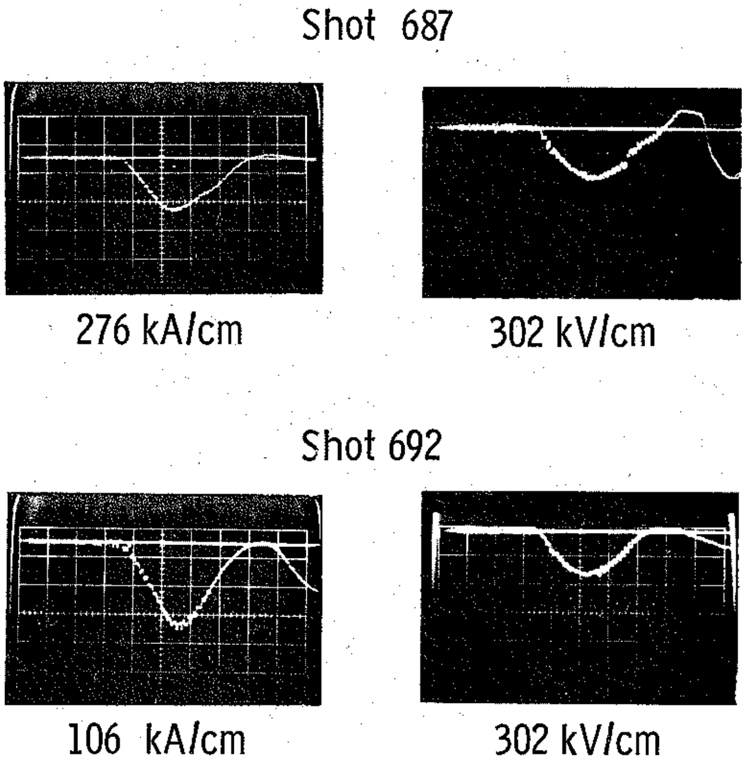

Figure 2.7 Diode current (Rogowski coil) and voltage (annular capacitive divider) waveforms from two Snark pulses. All traces are 50 nsec/cm: (a) Shot 687: $d_o = 4.0$ mm using cathode of Figure 2.8a. Note surge in current beginning at t = 140 nsec, corresponding to a sudden drop in voltage trace. Comparison with Figure 2.3 shows also that impedance begins sudden plunge at this time. All three indications are symptomatic of the late but sudden type of impedance collapse encountered using large, hollow cathodes; (b) Shot 692: $d_o = 6.4$ mm using cathode of Figure 2.8b. Increasing both d_o and r_{in} over the values used in (a).

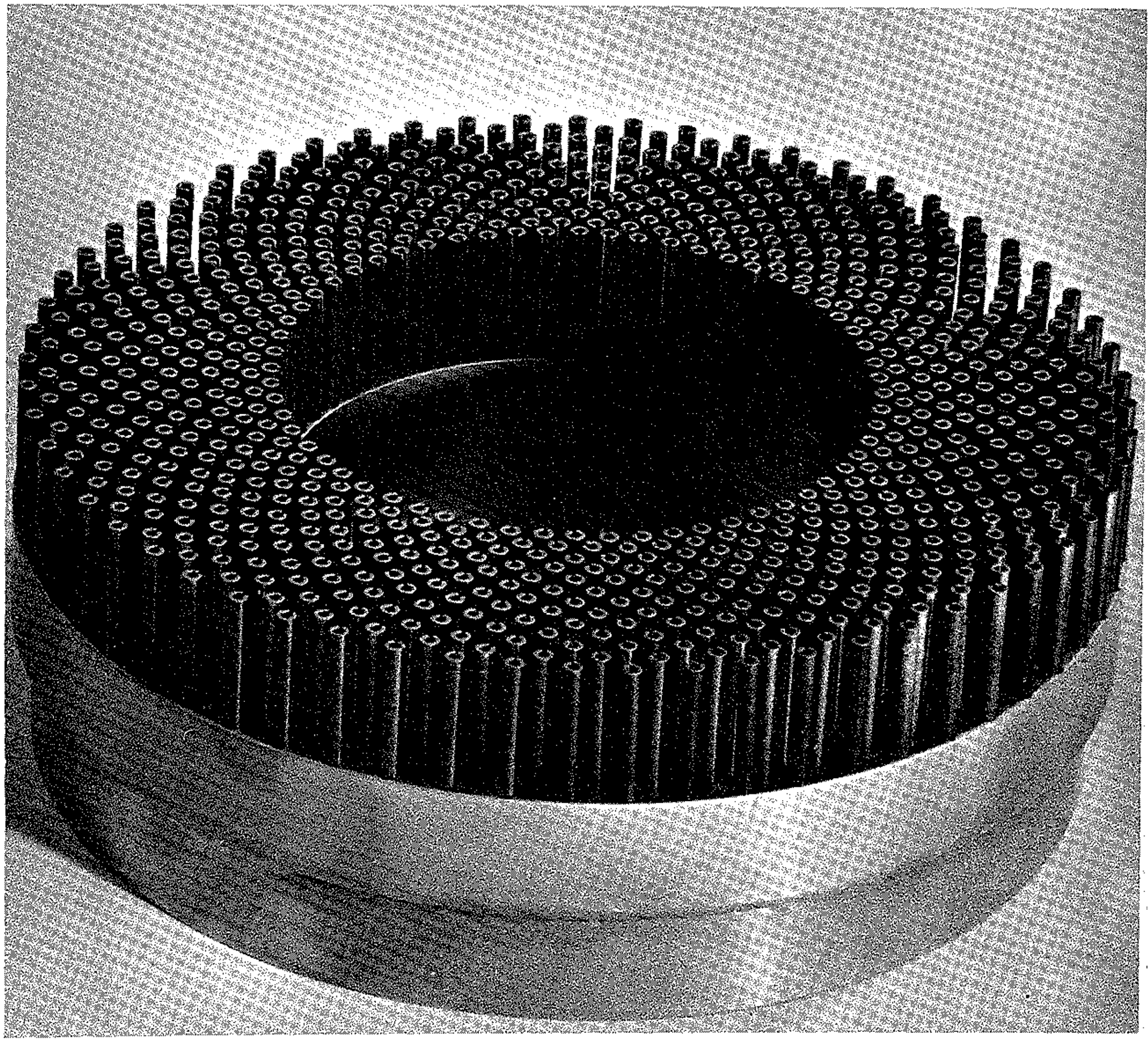

Figure 2.8a Roll pin hollow cathode, where $r_{out} = 7.3$ cm, $r_{in} = 3.9$ cm.

A337

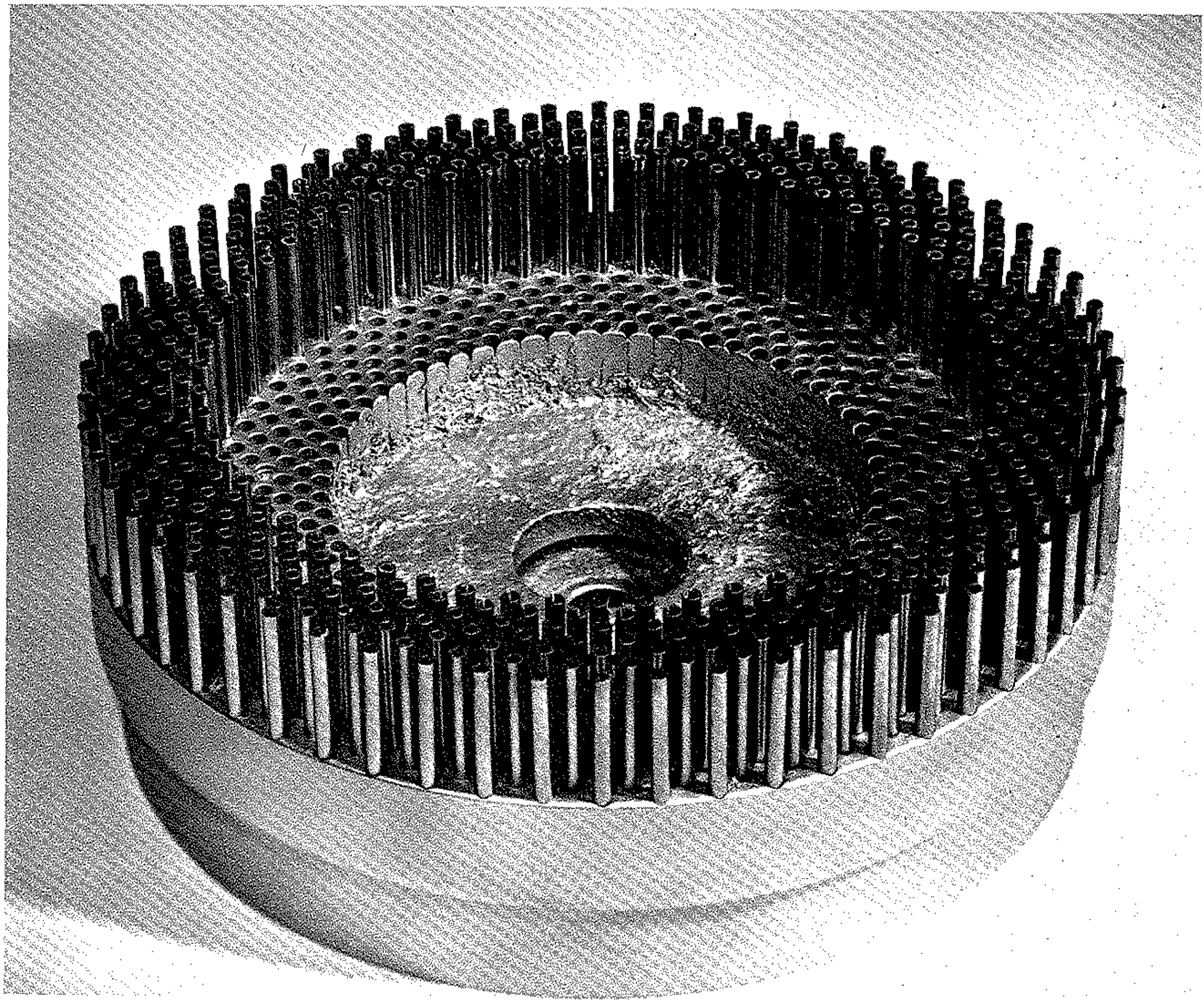

Figure 2.8b Same cathode shown in Figure 2.8a, but with inner roll pins removed to give $r_{in} = 5.5$ cm.

A338

Figure 2.9 Concentric ridge cathode with variable inner and outer radius.

illustrated in Figures 2.10, 2.11, and 2.12, was used on the Snark machine. Cathode shanks were 3 inches in diameter and were 2.86 centimeters apart. As shown in these figures, each cathode was directly exposed to the magnetic field of the other over a 2 centimeter length at the cathode base. The individual anode-cathode gaps were magnetically shielded by the separate 4-inch-diameter cathode enclosures, so the two beams could not directly attract each other. In addition, it can be seen that each cathode in its cylindrical conducting enclosure can be viewed as a coaxial transmission line in that the current flowing along the shank will induce a reverse current in the surrounding wall. For a single-cathode configuration, with the cathode concentric with the tube axis, the induced return current is azimuthally uniform as it leaves the cathode enclosure and flows radially away along the inside surface of the horizontal anode support plate. For a double cathode arrangement, however, the induced return current in each cylinder wall must be peaked opposite the central axis simply because it must be zero near the central axis. Since antiparallel currents repel each other, this effect causes the shank current to flow primarily along the "inside" portion (i.e., near the central axis) of each cathode. The direct exposure of each cathode to the other's magnetic field in the gap D_2 has the same effect, since the parallel shank currents attract each other.

In order to generate unperturbed, uncoupled beams, it is evident that the ratio D_3/D_1 (or D_3/D_2, if D_2 were larger than D_1) must be sufficiently greater than unity, so that the cathode flow perturbations, strongest near the support plate, are negligibly transmitted to the anode-cathode gap where the beam is generated.

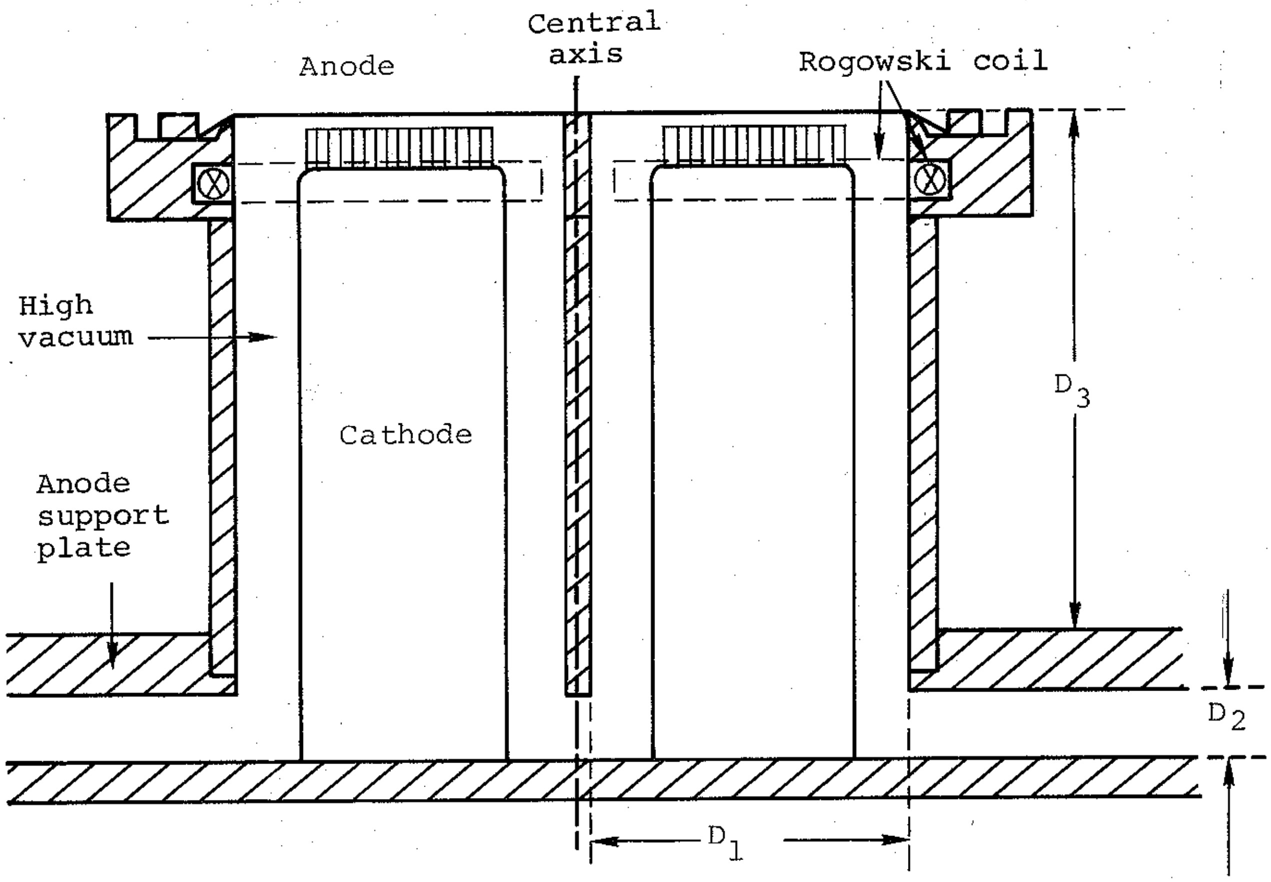

Figure 2.10 Schematic of double-diode configuration. Each Rogowski coil partially surrounds one diode.

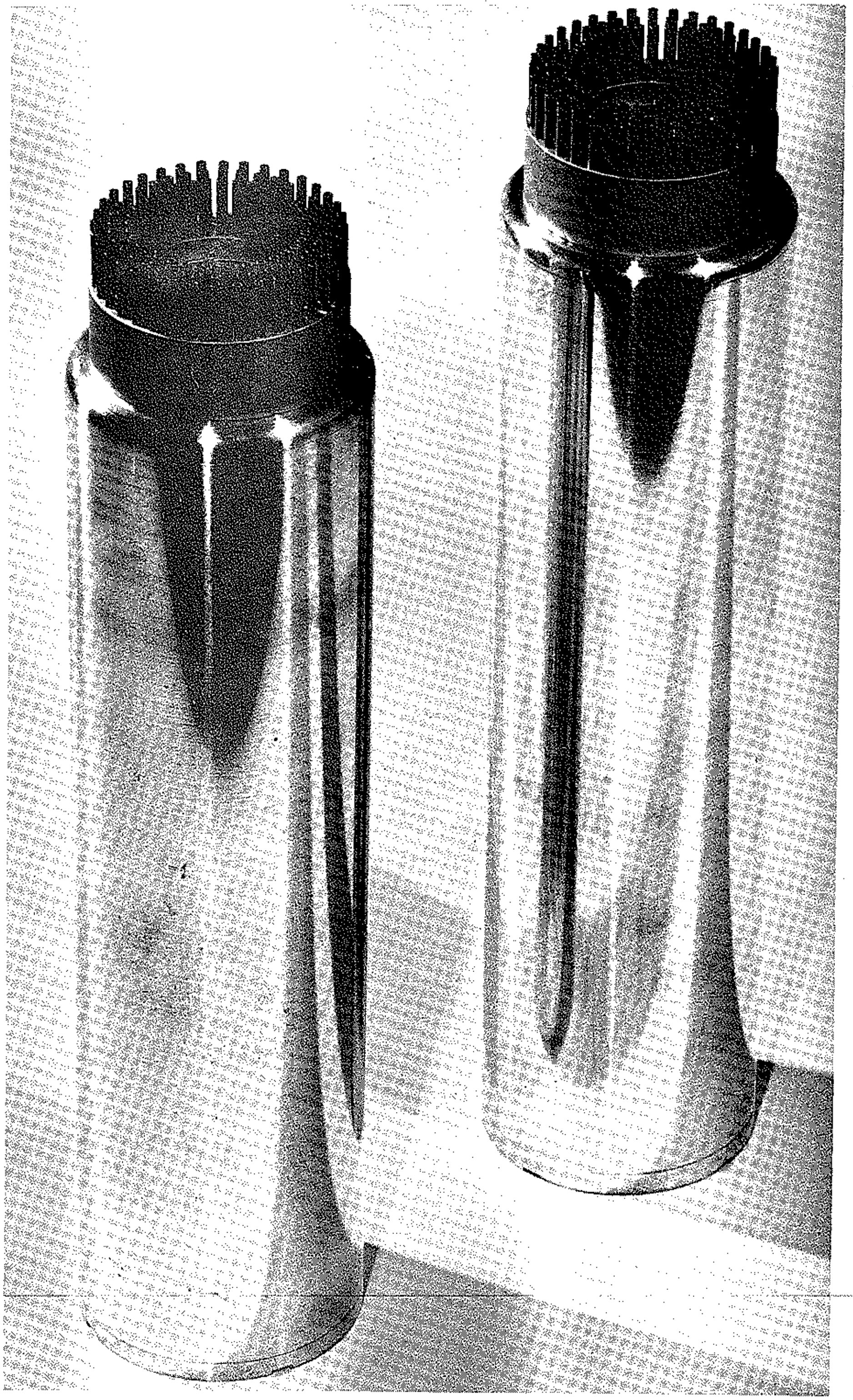

Figure 2.11 Cathode on extended shanks used in double diode experiments to give $D_3/D_1 = 3.12$.

A339

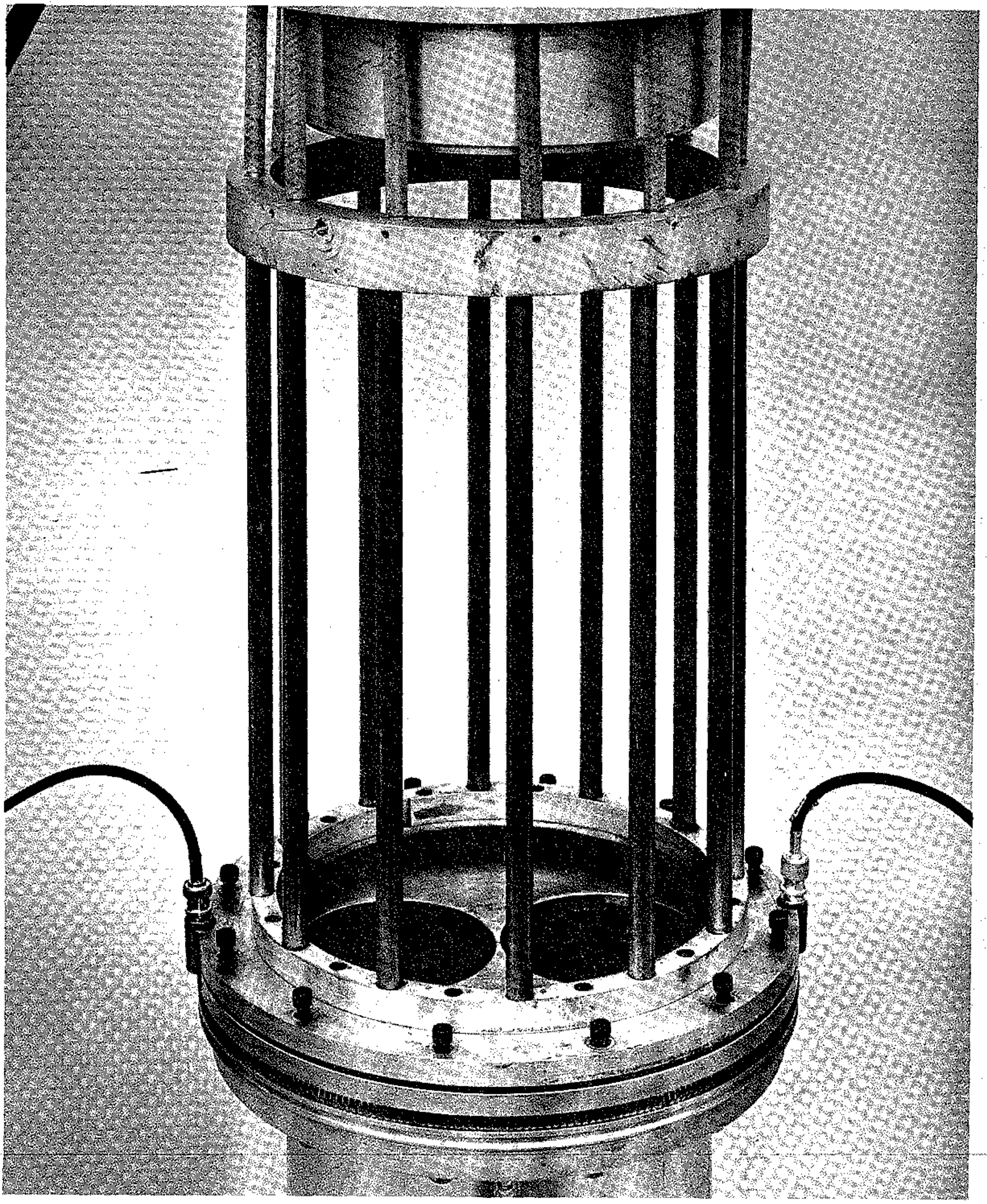

Figure 2.12 Z-pinch apparatus for beam combination experiment. Note dual cathode arrangement with two Rogowski coil cables at base of pinch.

Peak voltage across each diode was typically 800 kV, and peak current in each diode was typically 220 kA, with anode-cathode spacings d_o = 4.0 mm (Figure 2.13). Three set-ups were fabricated and tested, each with a different value of D_3. By changing D_3 we adjusted the ratio D_3/D_1 to be 0.312, 0.625, and 3.12. In the first two cases, graphite witness plates immediately behind each anode foil showed damage craters that were closer together than the cathode axes, with strongest mutual attraction when D_3/D_1 = 0.312. However, D_3/D_1 = 3.12 gave damage craters on line with the respective cathode axes, indicating complete isolation of the beams, as shown in Figure 3.14.

We interpret these results to support the analysis of diode coupling given above, and our conclusion is that uncoupled, unperturbed high-current beams can be generated in the same tube, even at close proximity, by simply extending each cathode on a shank of sufficient length in a cylindrical grounded enclosure.

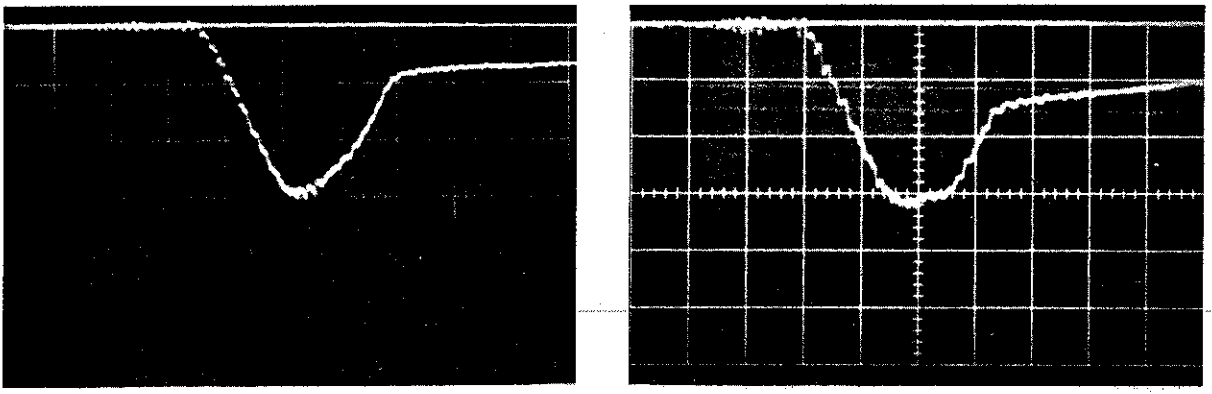

Figure 2.13 Current waveforms from shot 499 using double diode. Peak voltage was 700 kV with anode-cathode gaps of 4.0 mm.

A334

Since no problems were encountered in using this technique with individual currents high enough to pinch (which was obvious from the witness plates), we assume that its only hindrance to generator performance is the extra inductance added to the generator circuit by the long cathode shanks. Using the standard formula for the inductance per meter of a coaxial line with inner radius R_1 and outer radius R_2, the inductance per meter of a number N of parallel coaxes is

$$L = \frac{\mu_o}{2\pi N} \ln \frac{R_2}{R_1} = \frac{2 \times 10^{-7}}{N} \ln \frac{R_2}{R_1}$$

In the configuration tested we had $R_1 = 1.5$ inch, $R_2 = 2.0$ inches, and $N = 2$, so that $L = 0.288 \times 10^{-7} \approx 29$ nH/m; with $D_3/D_1 = 3.12$, the successful case, we had $D_3 = 0.32$ meter, so that the extra inductance from the extended shanks was about 9 nH, a tolerable increment for this study. Of course, the inductance can be decreased by increasing N, the number of diodes. For example, eight diodes instead of two would lower the extra inductance to 2-1/4 nH, a virtually negligible increment; at 250 kA per diode (the level at which we achieved decoupling with $D_3 = 0.32$ meter) this would correspond to a 2 MA total current.

The impedance of the 2-diode load was measured at close to 2 Ω, which is a strong overmatch for Snark and gives somewhat inefficient power delivery. This impedance was due to our use of the relatively small cathode radius of 3.1 cm in each diode, so that the 8-inch-diameter linear pinch tube could encompass the two beams in our B_θ beam combination studies. In a practical system, this overmatch could be easily eliminated. Since the impedance as well as the inductance is inversely proportional to the number of diodes, N, the hypothetical increase to N = 8 in the above example would give a corresponding impedance of about 0.6 Ω, a good match for Snark in this case.

2.4 BEAM RADIAL STRUCTURE AT THE ANODE WINDOW

To measure current density radial distributions at the anode plane, J(r,t), Faraday cups were used at the anode plane which utilized current collector faces of different diameters. By taking a succession of shots with the various collectors, the radial distribution of the current density at the anode plane was measured as a function of time.

2.4.1 J(r,t) Measurements Using the 738 Generator. In connection with our initial experiments on beam propagation in a linear pinch, a 500 keV (mean), 150 kA (peak) beam from the 738 pulser was analyzed for J(r,t). The detailed results were presented in the quarterly report PIQR-226/227-1 (April 1970), on p. 53 and in Figure 25, and will only be summarized here. It was found that even at times when an intense pinch of about 1/2 cm radius existed, measurable current density was observed out to the solid needle cathode radius of 3.2 cm; the measured distribution of current accounted for about 40 percent of the total beam energy being delivered outside the pinch. We refer to this as "wings" in the radial distribution of the current. The verification of these wings was the factor that led to the use of wider linear pinch tubes and resulted in highly efficient beam transport with the B_θ technique.

It is also noteworthy that beam pinch occurred at a time when the total diode current was ~ 105 kA, which is within 10 percent of the critical current $I_c = 8500\ \beta\gamma\ (r_{out}/d_o)$ for the configuration used: the voltage at pinch time was 550 kV, corresponding to $\beta\gamma = 1.82$, and $r_{out}/d_o = 31.8\ \mathrm{mm}/5\ \mathrm{mm} = 6.36$, giving $I_c = 98$ kA.

2.4.2 J(r,t) Measurements Using the DML Generator. Shortly after the J(r,t) results were obtained with the 738 machine, similar measurements were made using the DML pulser with a 3.81 cm radius solid needle cathode to see the effects of increasing ν/γ from about 3.5 (typical of the 738) to about 25. The DML results were presented in quarterly report PIQR-226/227-2 (July 1970), pp. 71-72 and Figures 4.7 and 4.8; the presence of wings containing about 50 percent of the total energy confirmed the earlier findings. In this case, the quantity I_c provided only a qualitative estimate of the current at the onset of pinch, since now it was ~ 30 percent lower than the 300 kA actual value.

2.4.3 J(r,t) Measurements Using the Snark Generator.

Having firmly established the existence of wings in the current distribution containing a substantial portion of the total beam energy, experiments were undertaken on the Snark pulser to examine the effect on the wings of changing the inner radius of a hollow cathode. Our impedance studies had already shown that diode impedance for pinched beams is determined by r_{out}/d_o, and is insensitive to changes in the cathode inner radius r_{in}. Since in practical generator design the quantity r_{out}/d_o will be restricted by impedance considerations, we decided to investigate the possibility of utilizing r_{in} as an independent variable to control the distribution of current at the anode plane.

The cathodes used in these experiments are shown in Figures 2.8 and 2.9. Figure 2.8a shows the 7.3 cm outer radius roll-pin cathode with its initial 13 rings of 60 pins each, giving it an inner radius of 3.9 cm. Figure 2.8b shows the same cathode with the 6 inner rings of pins removed to increase the inner radius to 5.5 cm. J(r,t) analyses were made with each cathode configuration at two different anode-cathode spacings, d_o = 4.0 mm and d_o = 6.4 mm. Figure 2.14 shows the sizes and placement of the annuli corresponding to the cathode dimensions and the Faraday cup dimensions. Instead of presenting the data in terms of current density profiles, as in previous reports, it will be more convenient here to compare the time-waveforms of current entering the three regions measured by the Faraday cups. Region 1 is the annular area directly opposite the roll-pins of the cathode in Figure 2.8. Region 2 is the annular area where $r_3 \equiv 1.85 \text{ cm} \leqslant r \leqslant 4.15 \text{ cm} \equiv r_2$. Region 3 is the central disk $r \leqslant 1.85 \text{ cm} \equiv r_3$.

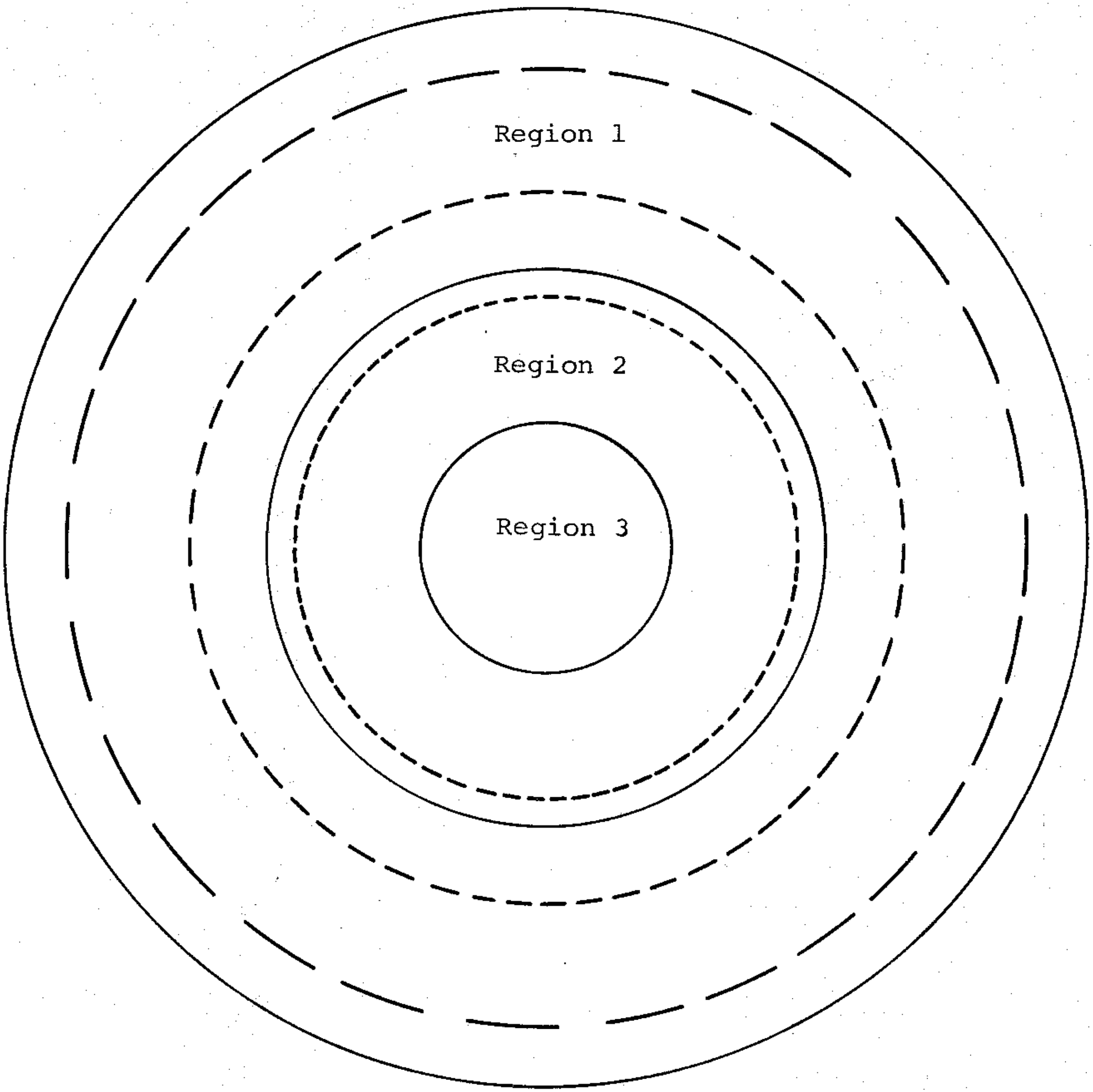

Figure 2.14 Radial design of Faraday cups used for J(r,t) measurements. Solid circles are boundaries of regions 1, 2, and 3 as described in text; outer dashed circle is outer edge (r_{out}=7.3 cm) of hollow cathode, inner two dashed circles are the two inner edges used during experiments. (See Figure 2.8)--Drawn to scale.

Figures 2.15 and 2.16 show the current waveforms in each of the three regions and Figure 2.17 shows diode impedances for the case $d_o = 4.0$ mm. The following features are evident:

a. In each case there are substantial wings

b. Removing the inner pins enhanced the wings at the expense of the pinched core

c. Removing the inner pins had no obvious measurable effect on diode impedance or total current waveforms

d. Removing the inner pins delayed the onset of pinch, although the apparent pinch velocity was unchanged. (The pinch velocity is deduced by dividing the distance r_2-r_3 into the time delay after a sharp current rise occurs in Region 2, until a sharp current rise occurs at Region 3.) The pinch velocity with $d_o = 4.0$ mm is $v_p \approx 1.0$ mm/nsec

e. Increasing d_o delayed the onset of pinch.

The corresponding measurements for the case $d_o = 6.4$ mm, shown in Figures 2.18 through 2.20, also show these effects, but with the pinch velocity increased to $v_p \approx 1.6$ mm/nsec.

These results indicate that the critical current I_c (Equation 2-2) is at best a qualitative estimate that tends to be low. In fact, if by "pinch" we fundamentally mean a concentration of current at the axis, then I_c as given by Equation 2-2 has been too small by a factor of about 2.5, as Figures 2.16 and 2.19 clearly show. Other considerations that emphasize the very approximate nature of Equation 2-2 are:

a. The fact that the pinch time changed noticeably (by 15 to 20 nsec) when r_{in} was changed. Equation 2-2 and its derivation include no effects of r_{in}; and

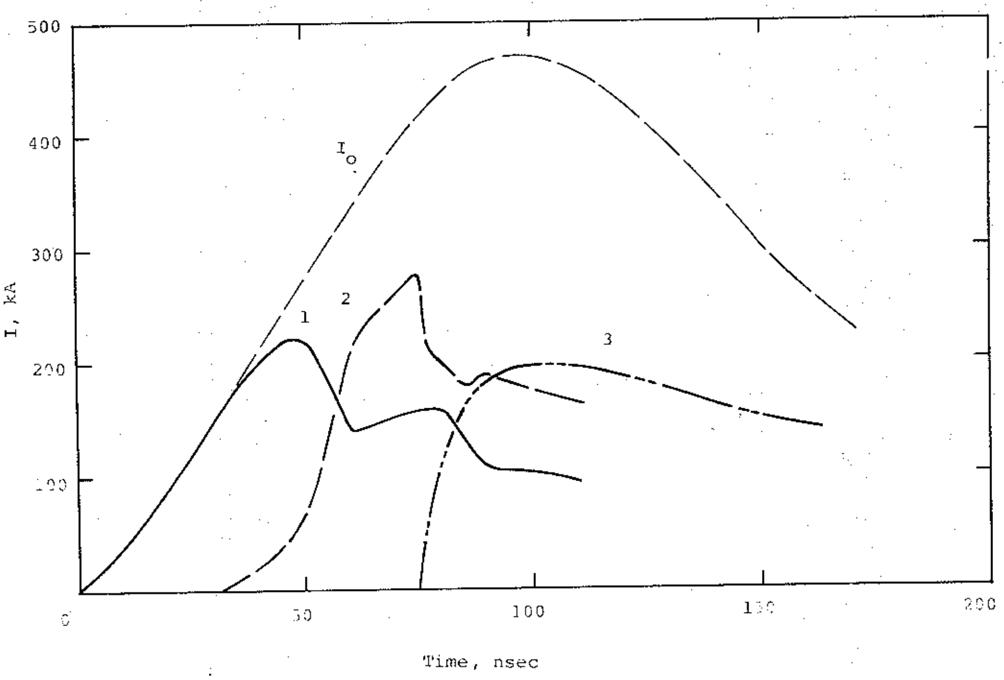

Figure 2.15 Currents in radial regions 1, 2, and 3 using cathode with inner pins; d_o = 4.0 mm, peak voltage = 500 kV.

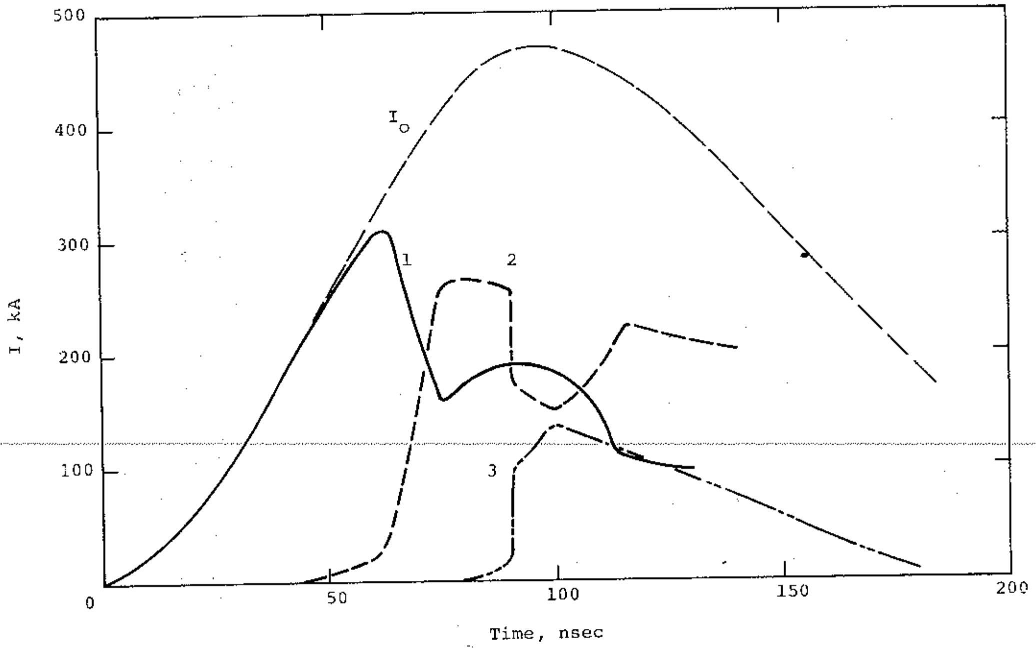

Figure 2.16 Current in radial regions 1, 2, and 3 using cathode without inner pins; d_o = 4.0 mm, peak voltage = 500 kV.

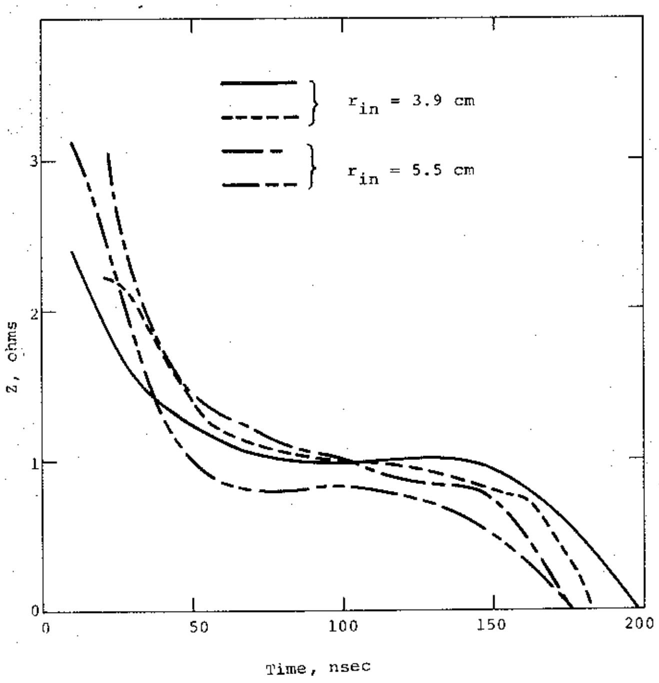

Figure 2.17 Snark diode impedance using d_o = 4.0 mm, r_{out} = 7.3 cm.

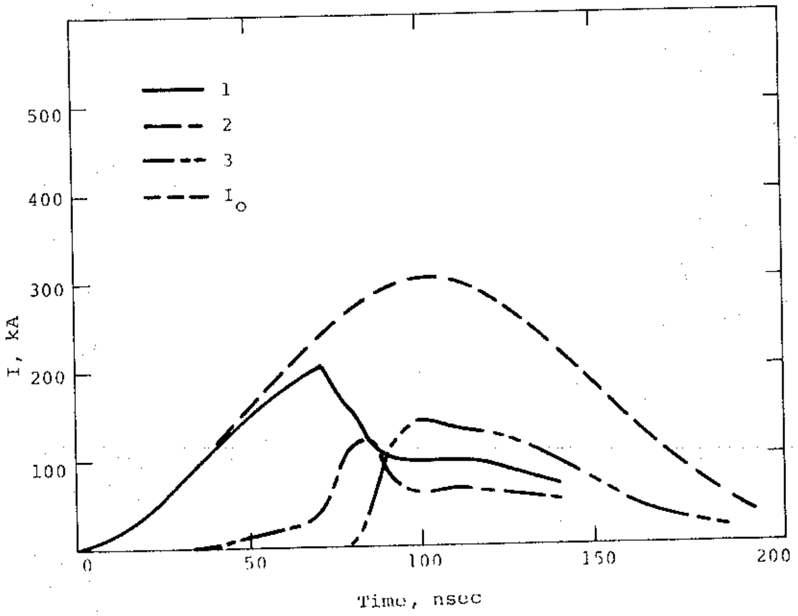

Figure 2.18 Currents in radial regions 1, 2, and 3 using cathode with inner pins; d_o = 6.4 mm, peak voltage = 470 kV.

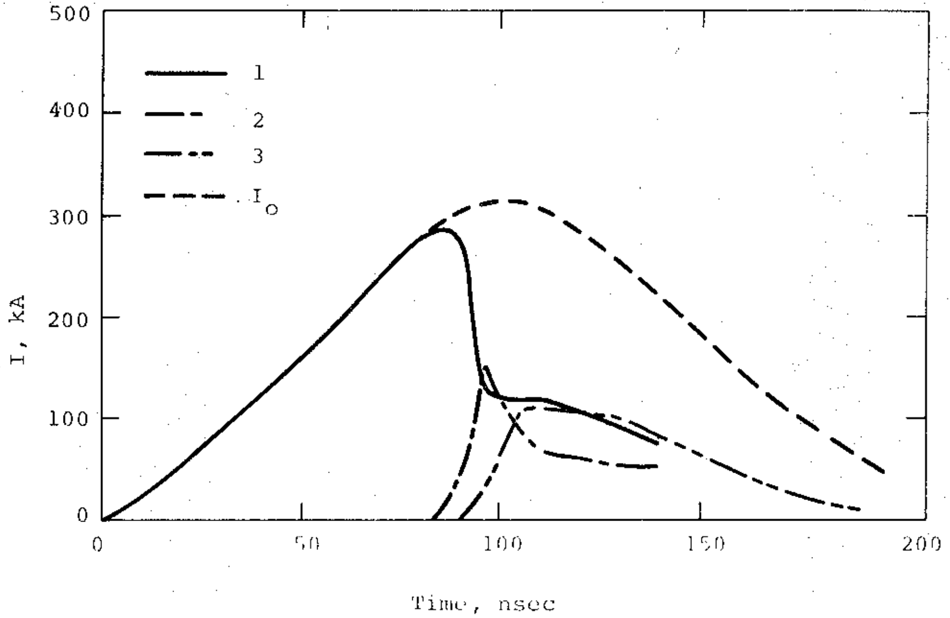

Figure 2.19 Currents in radial regions 1, 2, and 3 using cathode without inner pins; d_o = 6.4 mm, peak voltage = 460 kV.

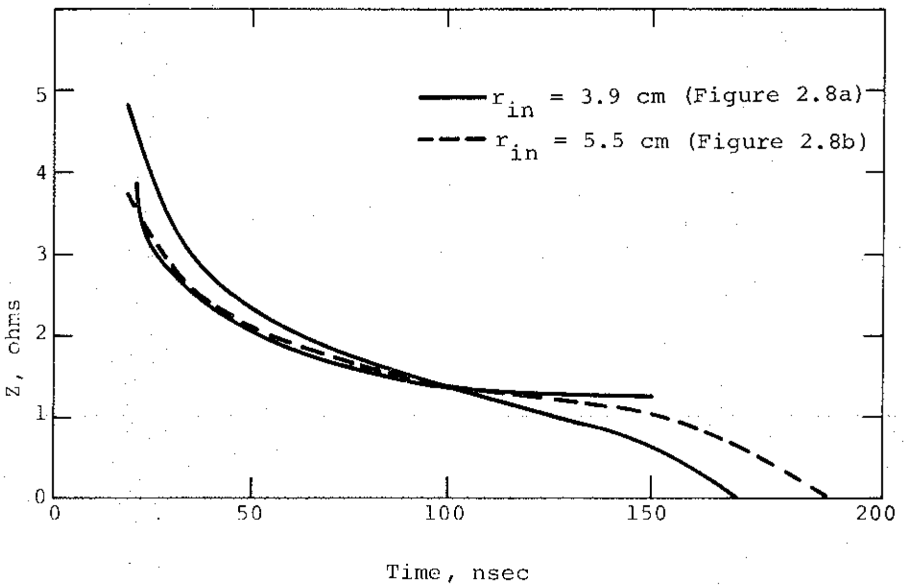

Figure 2.20 Snark diode impedance using d_o = 6.4 mm, r_{out} = 7.3 cm.

b. The fact that with unchanged voltage waveforms the time of pinching changed considerably when d_o alone was changed. By dividing Equation 2-4 by Equation 2-2 we get

$$\frac{I_o}{I_c} = \frac{1}{\beta} \ln \left[\gamma + (\gamma^2 - 1)^{\frac{1}{2}}\right] \qquad 2\text{-}5$$

which is a function of voltage only. Since voltage waveforms of, for example, shots 690 and 692 varied insignificantly (Figure 2.21), Equation 2-5 would predict the pinch time history of these two shots to be unchanged, and yet Figures 2.16 and 2.19 show a shift of almost 30 nsec when d_o was increased from 4.0 mm to 6.4 mm. Since Equation 2-4 for I_o has been upheld in this study, it follows that Equation 2-2 for I_c is the source of the disagreement between Equation 2-5 and experimental results.

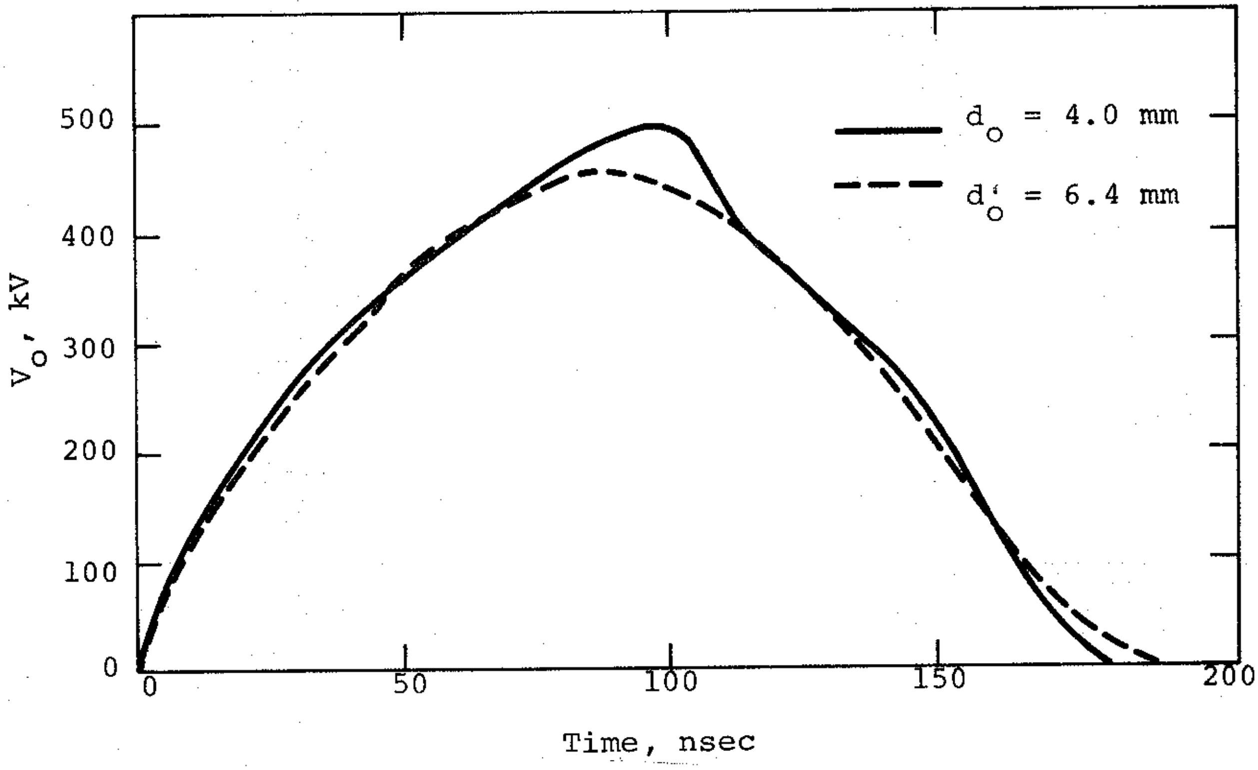

Figure 2.21 Diode voltage waveforms held virtually constant when d_o was changed from 4.0 mm to 6.4 mm.

The fact that the wings in the current distribution intensify when the inner radius is increased suggests that the wings would be minimized when $r_{in} = 0$. However, this was not the case for the 738 and DML studies, which showed substantial wings. We therefore have not been able to demonstrate appreciable control of the wings, although the use of solid cathodes probably minimizes them and optimizes beam pinch. However, with solid cathodes the impedance collapse problem necessitates the use of an anode-cathode gap $d_o \geqslant 3.5$ mm, which in turn demands a large diameter cathode in order to achieve sufficiently low impedances; however this will generate large diameter wings, which is what was to be avoided in the first place. It appears, then, that this problem is insurmountable without substantially more theoretical and experimental effort. Although the analysis of current flow in the pinched beam diode is a very interesting, largely undeveloped, and possibly very fruitful area for further investigation, we are not recommending additional effort in view of the overall goals of the DNA beam program, which we feel should involve the utilization of a B_z beam transport system, with B_z in the diode. Following a review of diode results with $B_z = 0$ we discuss our investigations of diode physics with an applied axial magnetic field.

2.5 CONCLUSIONS, DIODE PHYSICS WITH $B_z = 0$

Our investigations of diodes with $B_z = 0$ can be grouped into the categories of diode impedance, radial structure of the current flow, and decoupling of diodes.

RPN99

Diode impedance prior to beam pinch has been accurately modeled using Child's Law with time-dependent anode-cathode spacing to describe the hydrodynamic expansion of the anode due to beam energy deposition. Using large diameter hollow cathodes, diode impedance under pinched beam conditions has been successfully predicted at the time of maximum current by a specially adapted application of parapotential flow theory. In other words, we have, for the first time, verified a practical scaling law for the design of diodes in the voltage-current regime of prime interest.

Diode decoupling studies were necessary because of the strong mutual magnetic field interaction of high current diodes in the same tube, and because of the current path asymmetries involved in a multiple-diode configuration. Successful decoupling was achieved based on simple geometrical arguments which explain that sufficiently long, individually enclosed cathode shanks provide the needed decoupling of anode-cathode regions, and that impedance and inductance problems are easily avoided by proper choice of the number of diodes.

Studies of the radial structure of pinched beams at the anode plane revealed chronic wings in the radial distribution of current, limiting the current density and energy in the pinched core and necessitating that the linear pinch (B_θ) beam transport option have a beam compression capability that we were unable to achieve during the course of this program.

In view of the latter complication (and other important features relating to B_θ versus B_z transport, elaborated below), we have recommended that emphasis be shifted from diode studies with $B_z = 0$ to diode studies with an applied B_z field. The work accomplished in this area under the projects titled "Development of an Advanced X-ray Source" and "Advanced Photon Source Technology Program" is discussed in the following sections.

REFERENCES

2.1. F. Friedlander, R. Hecktel, J. Jory and C. Mosher, DASA 2173, Varian Associates, 1968.

2.2. D. de Packh, Radiation Project Internal Report No. 7, Naval Research Laboratory, April 1968.

2.3. J. Creedon, "A Quasi-Parapotential Model for the High ν/γ Diode," PIIR-19-70, Physics International Company, San Leandro, California, May 1970.

SECTION 3

BEAM TRANSPORT IN AZIMUTHAL (B_θ) MAGNETIC FIELDS

by J. Benford and B. Ecker

3.1 INTRODUCTION

Previous studies (Reference 3.1) have shown that the propagation of intense relativistic electron beams in neutral gases is accompanied by fundamental loss mechanisms. These losses are substantial and make efficient transport of intense beams with currents greater than 10^5 amperes prohibitive.

The first of the mechanisms is loss due to repulsive electrostatic self-fields. For a beam current density of 10^5 A/cm^2 the electron number density is 2×10^{13} cm^{-3}. Such a beam with a 1 cm diameter has an electric field of 5×10^6 volts/cm at its surface. Under the influence of such a field a beam expands to many times its initial diameter in times of the order of a nanosecond, which precludes the possibility of beam propagation or manipulation. When injected into neutral gas, the beam must first ionize atoms and expel electrons to achieve neutralization of the electrostatic force before it can propagate. Until this neutralization is achieved, (typically a few nanoseconds), the beam is lost by expansion.

The second loss is caused by the rapid rise of beam current (10^{12} - 10^{13} A/sec) which induces a strong back-emf. Beam electrons are decelerated by this electric field and the energy they lose goes into creating the magnetic field of the beam. To estimate this back-emf, consider a uniform beam of radius r_d and infinite extent propagating inside a metal cylinder of radius R. A line integral of Faraday's Law gives the axial field

$$E_z = \frac{1}{c^2} \left[1+\ell n \, (R/r_b)^2\right] \frac{dI}{dt} \qquad (3\text{-}1)$$

Typical values are $dI/dt = 10^{13}$ A/sec, $r_b = 1.25$ cm, R = 5 cm, $E_z = 4 \times 10^6$ volts/meter. MeV electrons in such a high dI/dt beam can thus lose their energy in transport over distances as short as a fraction of a meter.

These two loss mechanisms involve the presence of electric fields, which can be thoroughly quenched by filling the transport region with plasma of high conductivity. Radial electrostatic fields are eliminated by expulsion of plasma electrons from the beam volume, and axial fields are neutralized through the action of plasma electrons inductively accelerated in the direction opposite that of beam propagation. This latter motion results in the net current being less than the beam current, an electrodynamic effect termed current neutralization. The condition for the beam current to be neutralized is $\tau_D >> \tau_B$, where $t_D = 4\pi\sigma a^2/c^2$ is the magnetic diffusion time of the background plasma (a = beam radius, σ = plasma conductivity), and t_B is the beam pulse duration. In highly conductive plasma the beam current is highly neutralized; propagation of a beam through the plasma cannot modify the net magnetic field initially present.

3.2 PREIONIZATION EXPERIMENT

The solution to the two loss mechanisms described above--preionizing the gas in the transport region--introduces another loss mechanism. Because the conductive plasma keeps the beam volume free of both electric and magnetic fields, an injected electron beam must have relatively small radial velocity components if it is not to expand greatly in a short distance. A high ν/γ beam, therefore, should not propagate in a preionized gas if there is substantial transverse beam energy. This transverse energy is due to the interaction of beam electrons with the large magnetic field of the beam (pinch effect), an interaction that occurs in the field-emission diode where the beam is generated. Consequently, beam electrons entering the drift region (through the transmission anode) have a significant fraction of their kinetic energy in transverse motion. Spence et al. (Reference 3.2) have inferred mean angles of 40 degrees in a 160 kA, 550 keV beam ($\nu/\gamma = 4.7$) using transmission foil and dose-depth measurements. Upon injection into a preionized plasma, such a beam should rapidly escape to the walls. We have performed an experiment to check the correctness of these deductions.

The beam utilized in this experiment was produced by the Physics International Model 738 Pulserad which uses a cold field-emission planar diode having a multi-needle 6.4-cm-diameter cathode and a thin foil transmission anode. Beam current and energy were measured in the diode using a resistive voltage monitor and self-integrating magnetic field probe (Reference 3.3). The beam was found to have a peak current of 210 kA and a mean energy of 200 keV during its 85 nsec duration (Figure 3.1). Owing to beam self-pinch in the diode, most of the beam current flowed within a 1 cm radius at the plane of injection.

The experiment consisted of examining beam propagation through two adjacent regions: Region 1 and Region 2 (Figure 3.2), using measurements of net current and observations of witness

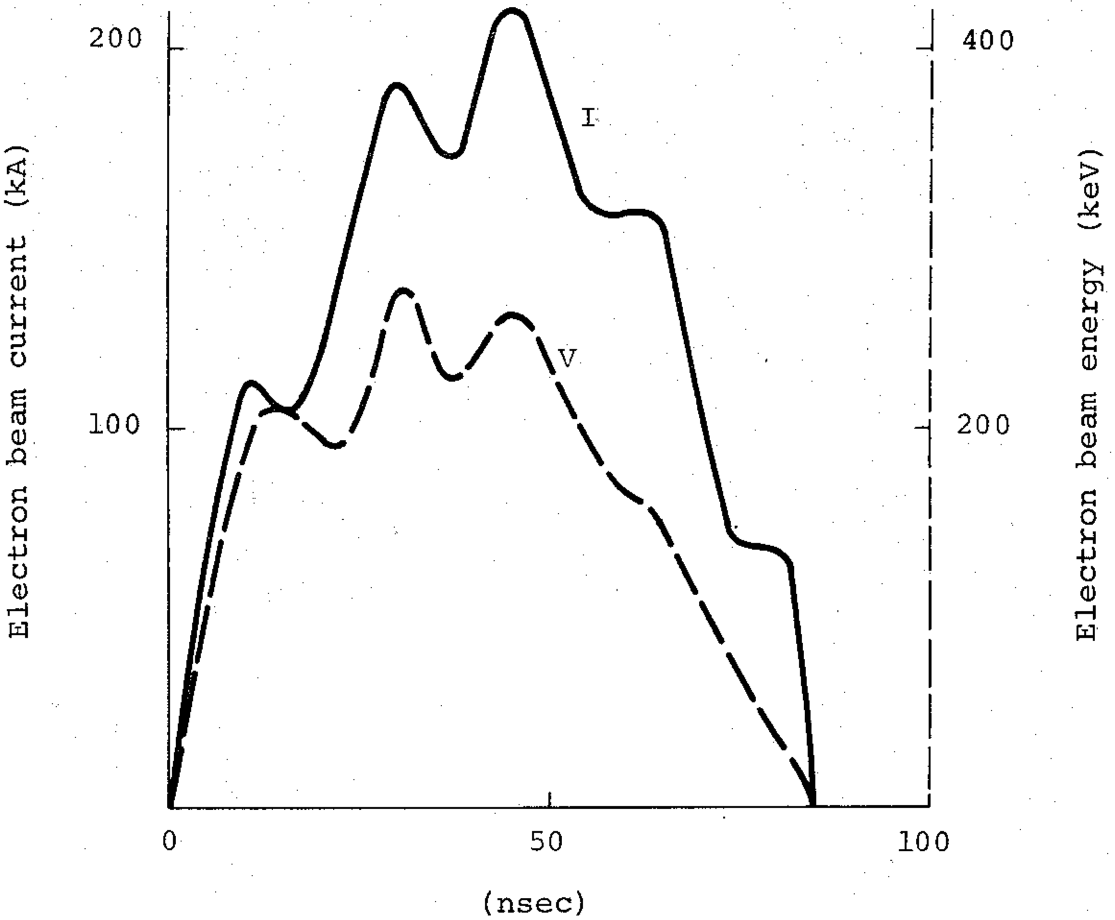

Figure 3.1 Beam current and voltage for preionization experiment.

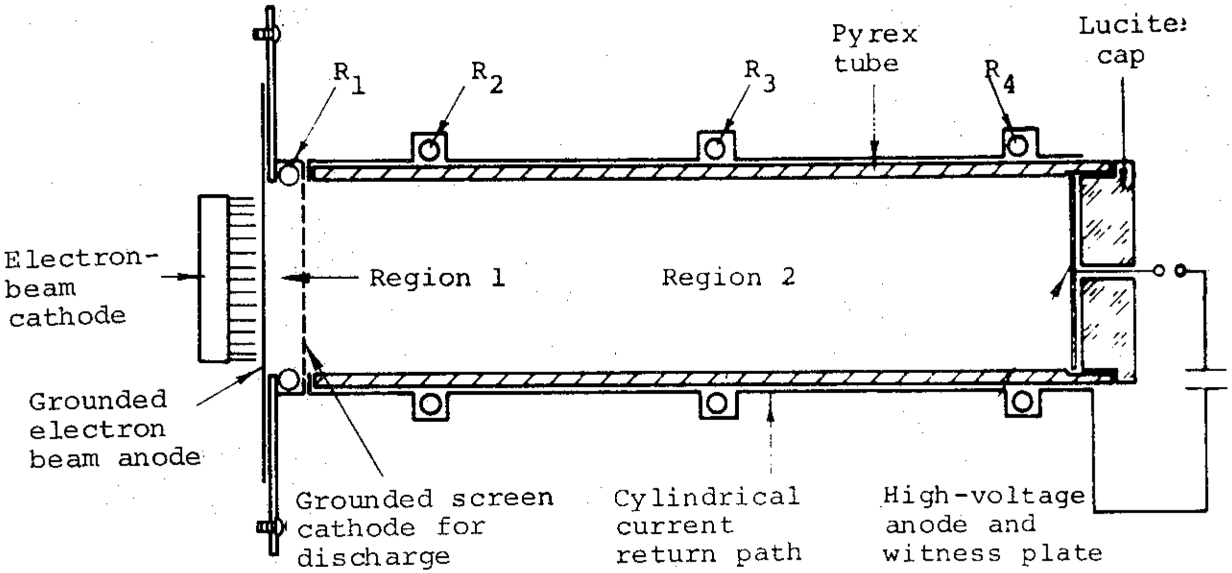

Figure 3.2 Discharge apparatus.

plate damage. A preionizing gas discharge was set up in Region 2 between a stainless steel screen cathode and aluminum plate anode with a separation of 25 cm. The configuration is similar to that of a linear pinch, but the discharge here was approximately uniform through the entire volume because the total inductance of the discharge circuit was high enough to prevent self-pinch of the discharge. There was leakage of ionized gas across the screen into Region 1 due to expansion of the heated plasma in the discharge proper, so that the gas in Region 1 (a 1-cm gap) was partially ionized: Even 0.01 percent ionization gave a free electron density comparable to that of the electron beam. The gas in Region 1, therefore, was preionized--in the sense of this experiment--though its conductivity was probably not as high as that of the gas in Region 2. The beam was injected into Region 1. The screen, a 15 percent mesh, intercepted only a small fraction of the incident beam, which passed into Region 2. The cathode screen and anode plate served as witness plates for damage due to the beam. Four Rogowski coils were used to monitor net current: R_1, R_2, and R_4 had fast risetimes (~ 1 nsec) and their outputs were integrated to measure net beam current, with L/R typically 600 nsec; R_3 monitored the discharge current and was RC-integrated with RC = 103 μsec. The axial positions of the Rogowski coils are indicated in Figure 3.2.

The peak discharge current in Region 2 was 40 kA. Since the current was distributed over the 5-cm-diameter tube, the maximum field in Region 2, about 3 kG, was at the wall. The discharge current had a 5 μsec quarter-cycle time. The beam was injected at peak current using delayed triggers which synchronized the firing of the electron beam and gas discharge. No external voltage was applied across Region 1; and the time scale for hydrodynamic diffusion of the low energy plasma from Region 2 into Region 1 was very long compared with the charge relaxation time, so that it is reasonable to consider Region 1 to have been field-free.

Using air as the background gas, beam propagation was observed under neutral and preionized conditions at 190 μ. In Region 1, screen damage clearly supports the physical picture of beam propagation presented above. Injection into neutral gas always resulted in localized on-axis disintegration of the screen, indicating propagation of some portion of a pinched beam. Preionization always resulted in the bowing of the intact screen away from the diode, indicating that in traveling through 1 cm of plasma the intense pinched beam became a diffuse, locally weak beam.

Net current data for Region 1 is shown in Figure 3.3. In neutral gas the back-emf caused gas avalanche at 8 nsec, at which time current neutralization began. The net current was much lower in the preionized case than in the neutral case. (The early time behavior of the signal in the preionized case is not understood: the measurement indicated the presence of a magnetic field whose sense would correspond to a net current in the upstream direction for $t < 16$ nsec.)

It is seen that current neutralization in preionized gas is not complete, due to the conductivity of the plasma. Although expansion of the beam was great in only 1 cm, some of the beam reached Region 2, where the field due to the on-going discharge was non-negligible, and would tend to limit expansion. It was observed that with preionized gas in Region 2 small portions of the electron beam reached the witness plate/electrode and caused

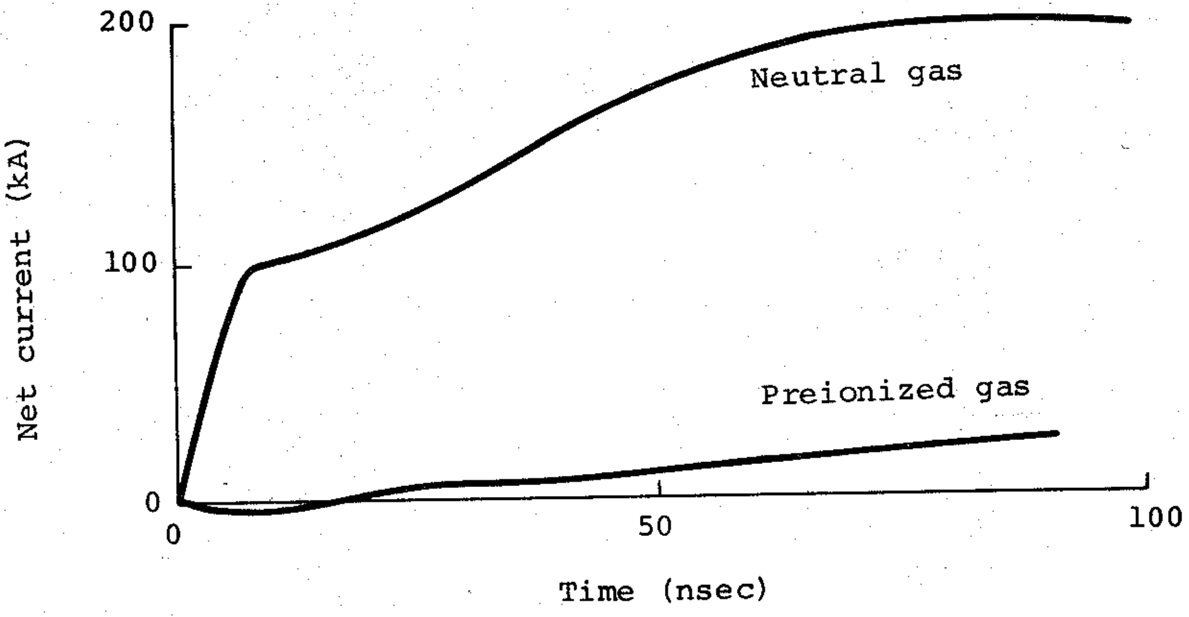

Figure 3.3 Net beam current waveform from Region 1, using neutral and preionized air.

scanty off-axis damage 25 cm downstream from the plane of injection. Propagation through Region 2 in neutral gas was better and witness plate damage was reproducibly on-axis. The net current measurements provide an explanation. Peak values of the net current waveforms for the cases of neutral and preionized gas in both regions are shown in Figure 3.4. The manner in which waveforms diminish drastically with distance in the preionized case but seemingly "stabilize" in the neutral case indicates how the larger self-field in the neutral case results in self-focusing and, therefore, in relatively prolonged propagation.

We conclude that in a preionized gas the propagation losses of a high ν/γ electron beam are rapid and severe if the beam has significant transverse energy content as an initial condition.

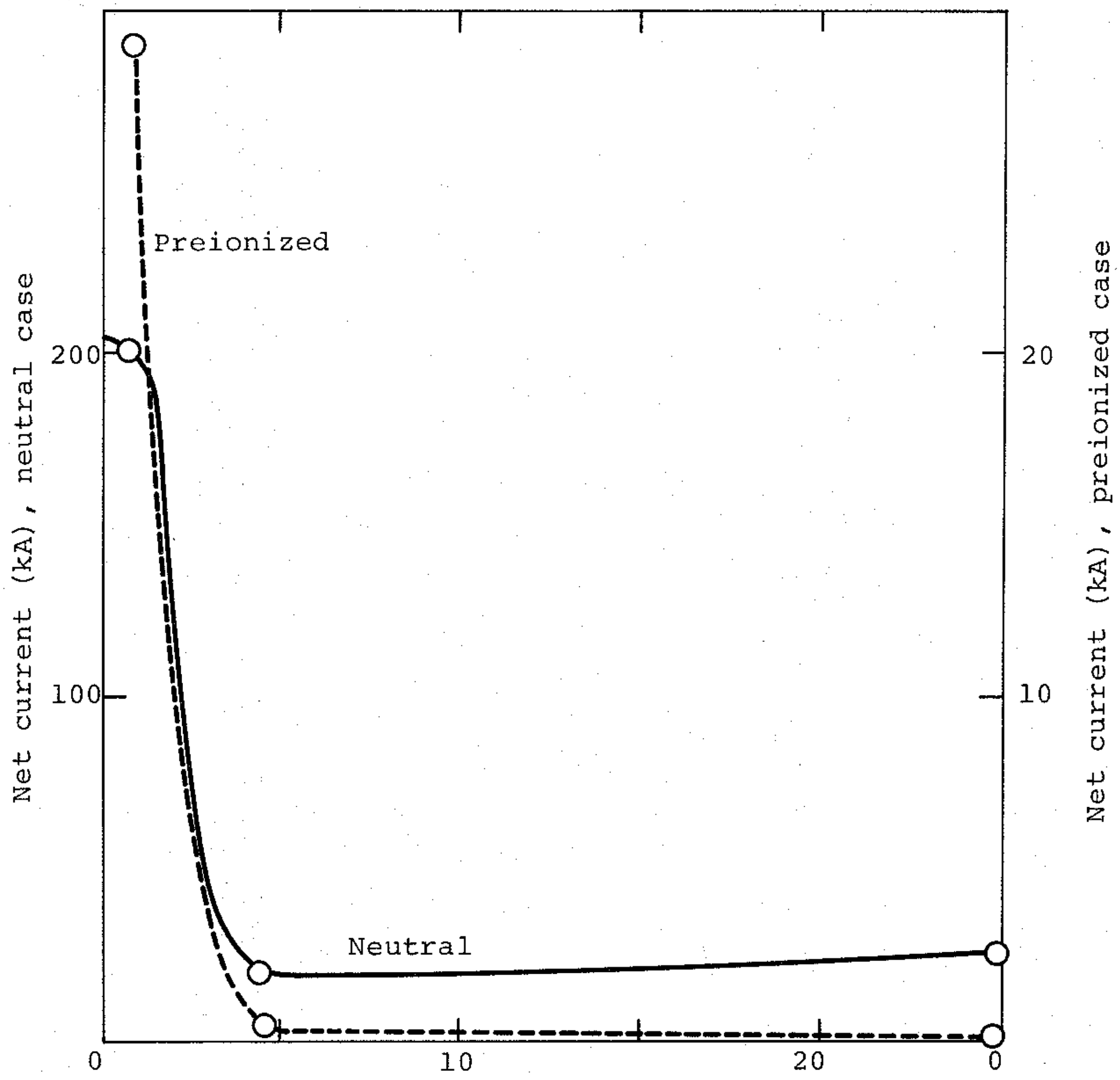

Figure 3.4 Net beam current maximum versus distance along discharge chamber for neutral air (solid line) and preionized air (dashed line). Note order of magnitude difference in scales.

This conclusion is supported by the observation by Kouzes, et al. (Reference 3.4) of efficient transport in preionized gas of beams with little transverse motion. Externally applied forces appear to be necessary for the propagation of high-transverse-energy beams if the advantages of preionization are to be retained. In particular, consider the removal of Region 1 and the intensification of the discharge in Region 2. In such a case the beam would be injected directly into a high conductivity medium with an externally applied guidance field to prevent beam expansion.

3.3 Z-PINCH TRANSPORT

3.3.1 738 Z-Pinch Transport Experiment. The objective of this experiment was to confine and transport a beam by injecting it into a plasma with a trapped azimuthal magnetic field. This field, an externally applied substitute for the beam self-field, would result in radial containment of the beam electrons. Roberts and Bennett (Reference 3.5) have reported the transport in a Z-pinch of a beam with little transverse energy ($\nu/\gamma \approx 0.2$); we extended these results to beams where transverse velocity components contain much of the beam kinetic energy. These beams were transported with negligible loss using magnetic fields substantially less than the self-field of the beam in the diode.

3.3.1.1 Apparatus. The Z-pinch consisted of two plane-parallel, 9.8-cm-diameter, 0.2-cm-thick, circular aluminum electrodes at the ends of a gas-filled 61-centimeter Pyrex cylinder. Discharge return current was carried by six coaxial return current rods to a strip transmission line that was connected to a 42 μF, 13 nH capacitor bank (Figure 3.5).

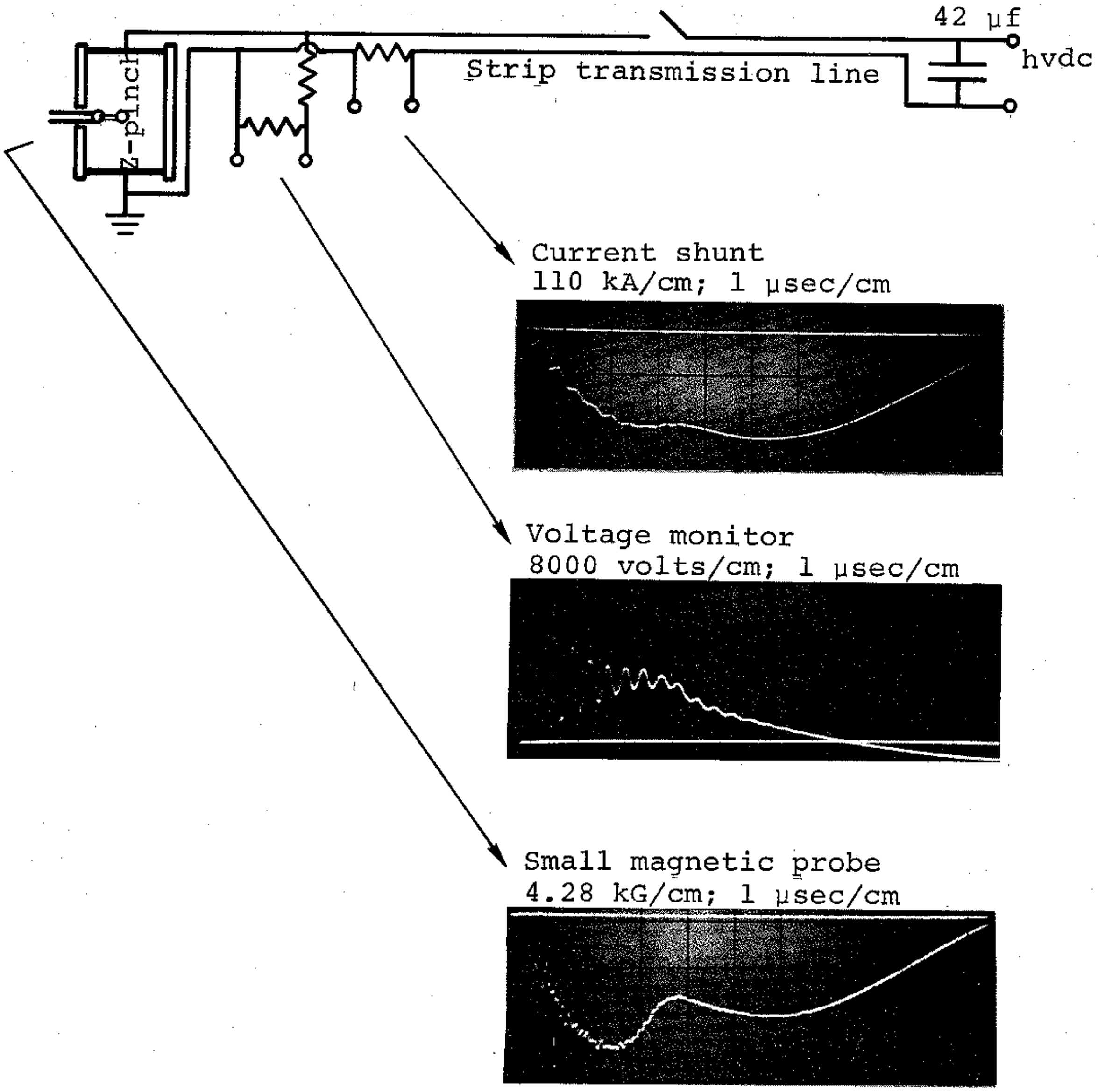

Current shunt
110 kA/cm; 1 μsec/cm

Voltage monitor
8000 volts/cm; 1 μsec/cm

Small magnetic probe
4.28 kG/cm; 1 μsec/cm

Figure 3.5 Z-pinch circuitry and diagnostics.

A726

The firing of a low-inductance (25 nH) rail gap switch caused the bank to discharge through a 12-meter, 30-nH strip transmission line, terminating in the Z-pinch. The length of the line was required in order to delay reflections of the beam-induced voltage signal from the capacitor bank; the double-transit time of the line was greater than the beam pulse width. Figure 3.5 displays circuit diagnostics and typical waveforms. The current shunt was a section of brass foil, 0.025 centimeters thick, 0.8 mΩ, inserted in the transmission line and folded to minimize lead inductance. The voltage monitor was a resistive divider in parallel with the transmission line near the Z-pinch. Calibration tests showed a risetime of 5 nsec. The voltage monitor was used to check discharge reproducibility and to measure beam-induced axial electric fields.

Figures 3.6 and 3.7 show in detail the Z-pinch apparatus and beam-generating diode; these were back to back at a 0.0025 cm aluminum foil electrode which served as the anode for the beam diode and the cathode for the Z-pinch. In this way the beam injected directly into the Z-pinch. A self-integrating magnetic fluxmeter loop (Reference 3.3) in the diode measured the injected beam current waveform on each shot, indicating peak current and overall reproducibility. Beam voltage was measured with a resistively graded voltage divider. Beam and pinch currents were parallel so that the pinch magnetic field acted to contain the beam.

In the Z-pinch the axial current at breakdown flowed in a thin sheath along the tube wall. The rapid current rise caused jxB body forces which collapsed the current sheet to the cylinder axis in 3.6 μsec. Figure 3.8 is a time-exposed photograph of a collapsed pinch. The gas pressure (300 μ argon) was chosen to

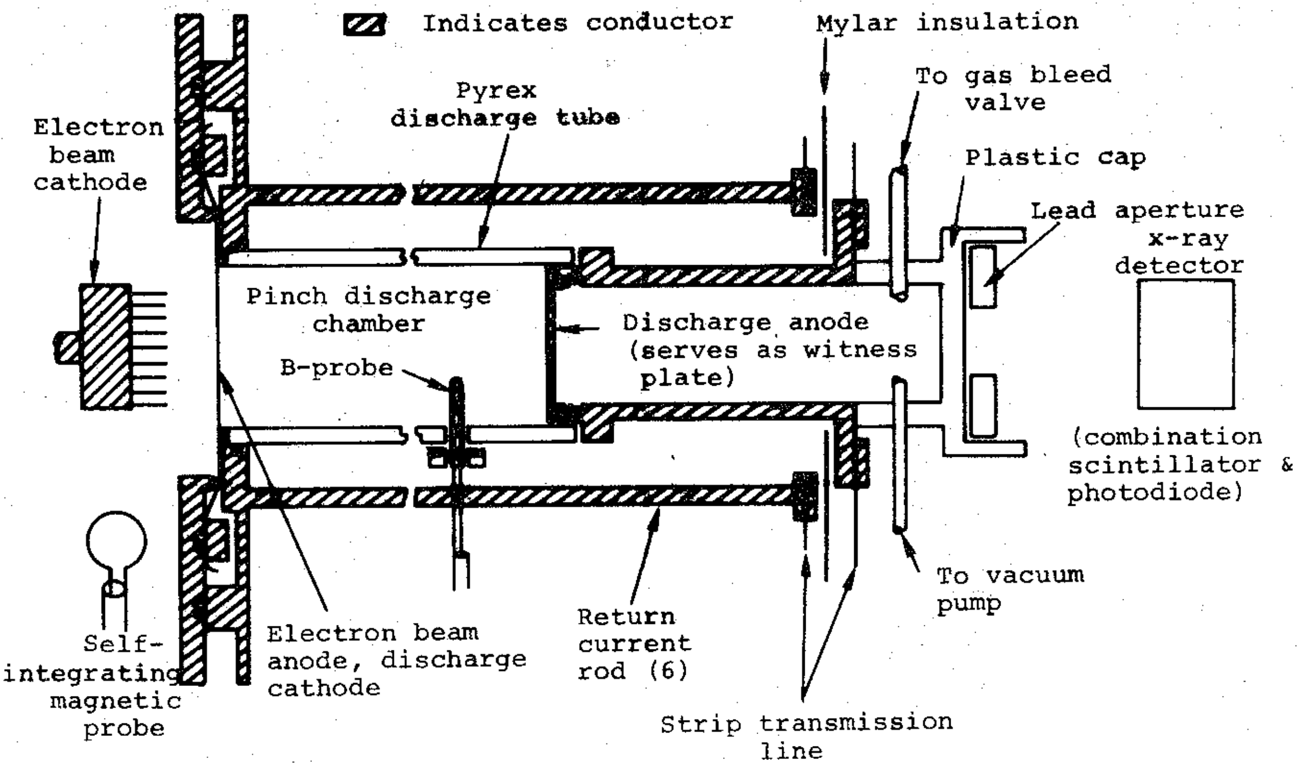

Figure 3.6 Experimental configuration of Z-pinch apparatus and beam-generating diode.

give a collapse time equal to the risetime of the pinch current, ensuring efficient "sweeping up" of plasma. Associated with the collapse was a continuous succession of azimuthal magnetic field profiles. The Z-pinch magnetic field was known for all radii and times from probe measurements made prior to the experiment. The probe consisted of three turns of #38 Formval-coated wire, 0.226 cm in diameter, at the end of a 50 ohm coax. The signal was RC-integrated at the oscilloscope with RC = 264 μsec to give magnetic field versus time. The probe was at the closed end of a thin quartz capillary tube inserted radially into the discharge

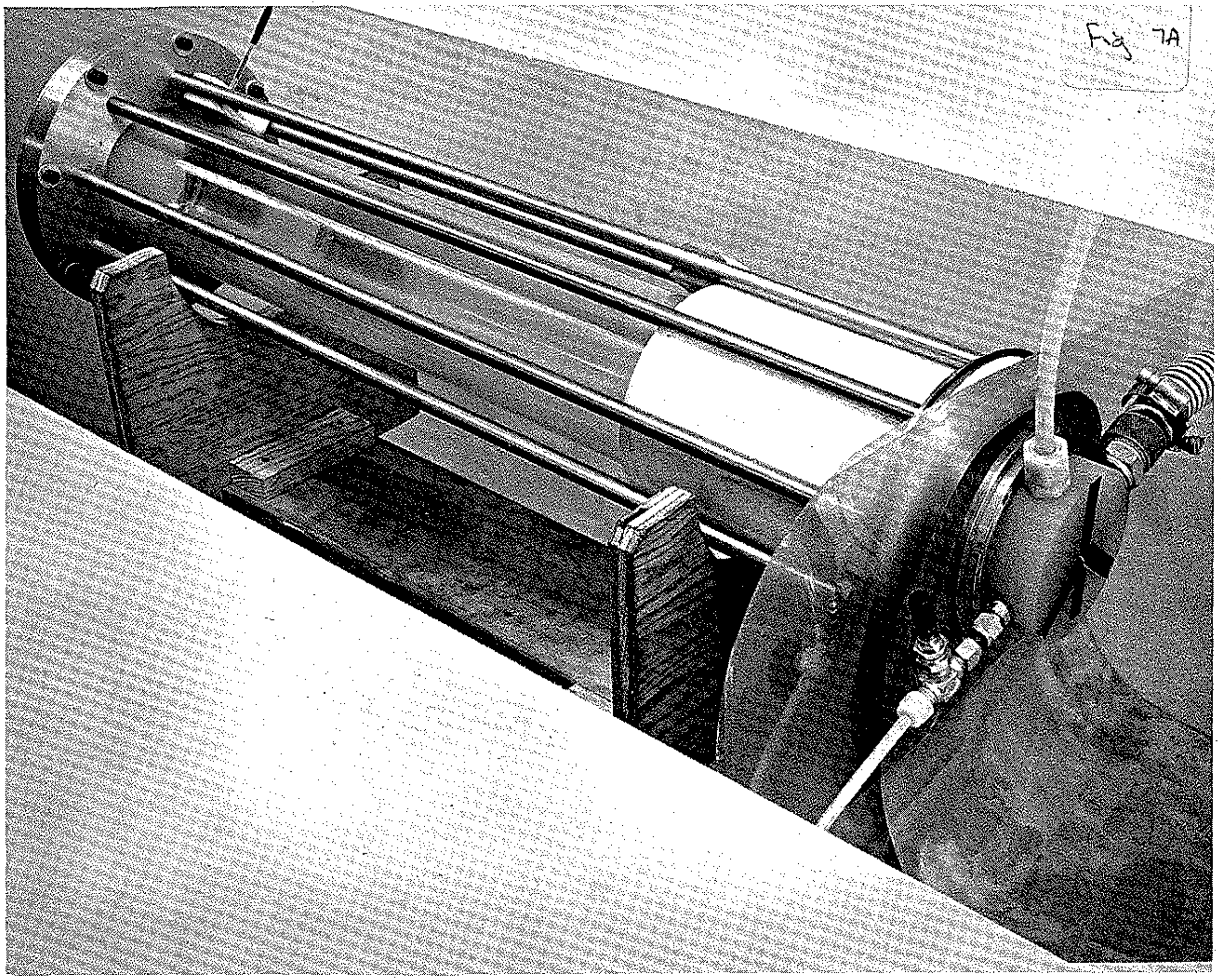

Fig 7A

Figure 3.7 Z-pinch in support stand. Note gas and vacuum feeds in head of pinch and magnetic probe inserted near injection end.

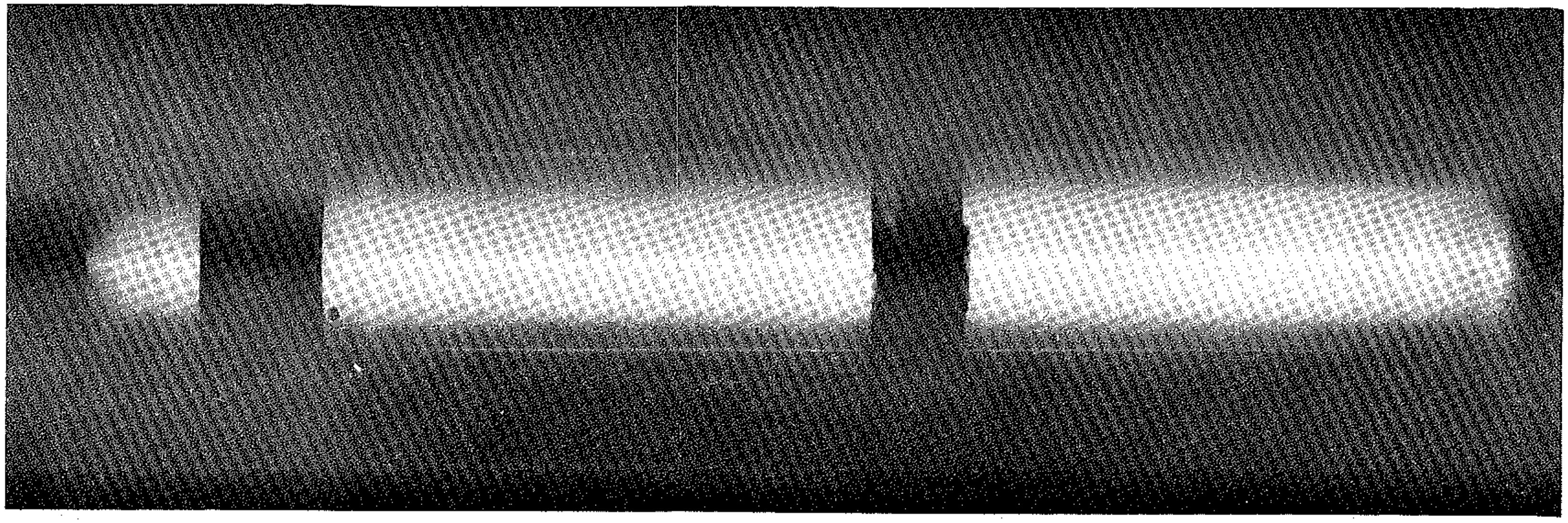

Figure 3.8 Time-integrated (open shutter) photograph of 12 kV, 500 μ Ar discharge. Dark bands are B-probe vacuum seal and Rogowski coil.

region. In any Z-pinch, the sheath has a finite thickness; in our case the gas was ionized at all radii even at early times in the discharge with conductivity highest near the sheath region. Figure 3.9 shows the magnetic field profiles at the times at which the 160 kA beam was injected.

The pulse width of the beam was ~ 50 nsec (FWHM), while the pinch collapse time was 3.6 μsec. Thus, the beam could be propagated through the Z-pinch at a well-defined moment, in a well-defined Z-pinch azimuthal magnetic field. Low-jitter delayed-trigger circuitry was used to preselect the injection time. The time of beam injection was measured by algebraically adding the signal from the current shunt in the Z-pinch circuit to the signal from the current monitor in the beam diode. This sum was displayed using a Tektronix 454 oscilloscope at 0.5 μsec/cm. The beam current waveform appeared as a narrow spike in the relatively slowly varying waveform of the Z-pinch current, defining the time of injection to within ± 0.05 μsec (Figure 3.10).

Beam propagation through the Z-pinch was diagnosed in two ways: damage resulting from beam energy deposition in the Z-pinch anode and time-resolved measurements of bremsstrahlung produced during energy deposition. Bremsstrahlung was detected using a combination scintillator and nanosecond-risetime photodiode. This detector was placed on-axis, 240 cm downstream from the target anode. A lead aperture shielded the detector from any bremsstrahlung produced in the Pyrex wall. A disk of nylon 1 cm thick stood between the target and detector as part of the Z-pinch vacuum system.

The propagation measurements just described supplied half of the data required to ascertain propagation efficiency. The other half of the data consisted of the same measurements made

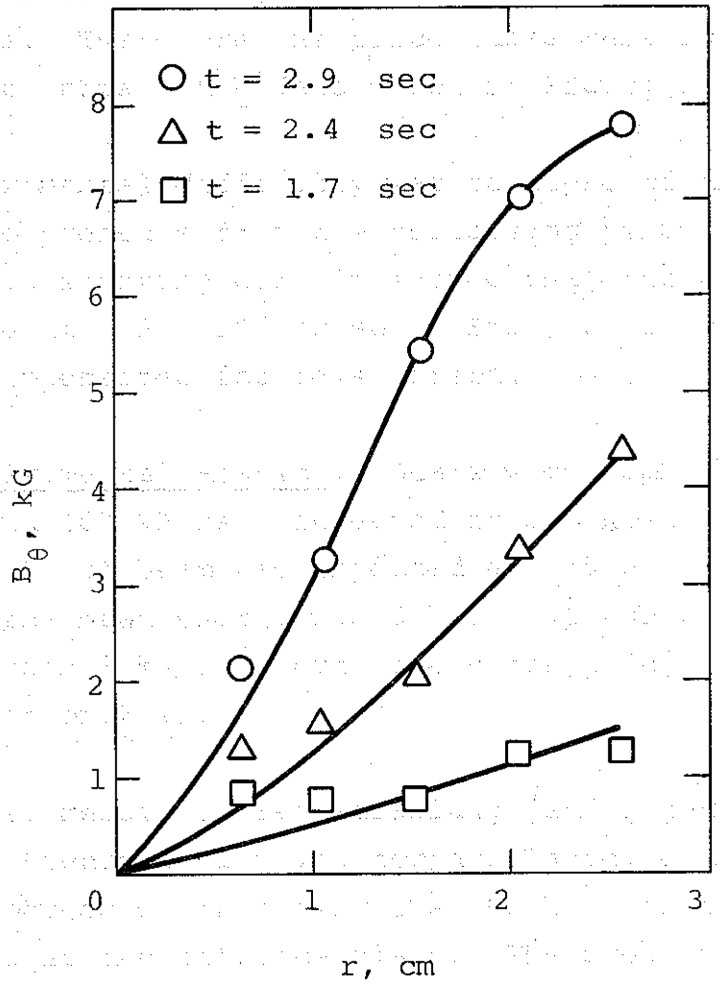

Figure 3.9 Profiles of azimuthal magnetic field at times of injection of 160 kA beam. Perturbation of plasma by probe was large nearest the axis, distorting measurements there.

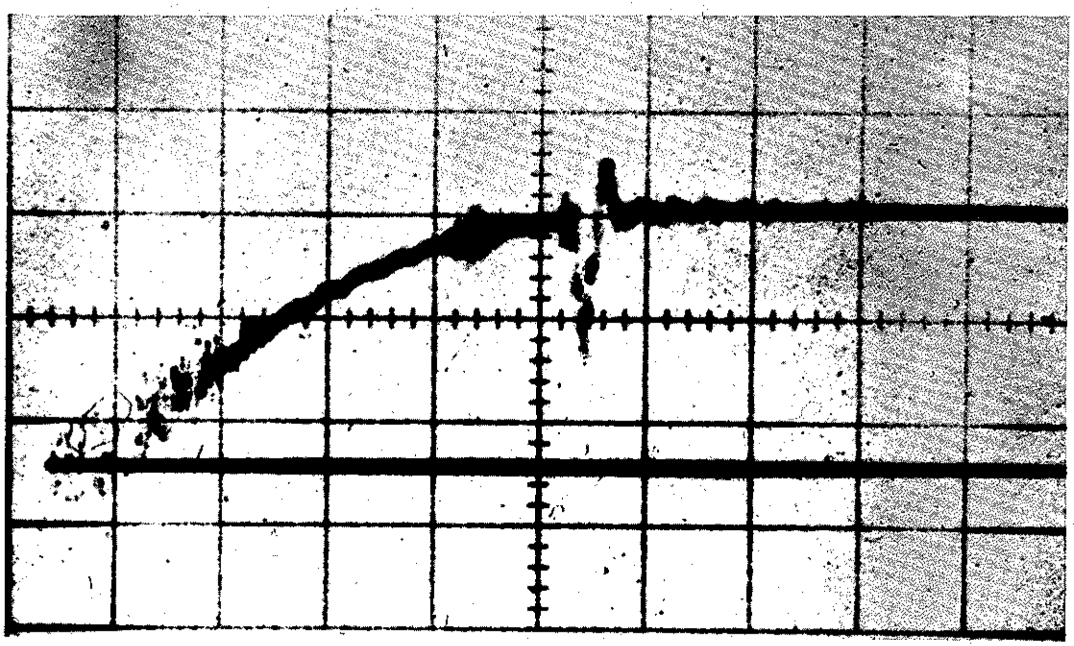

Figure 3.10 Beam current subtracted from pinch current, sweep 0.5 μsec/cm, injection at 2.1 μsec.

at the Z-pinch entrance plane: a Z-pinch anode plate was positioned 0.05 cm behind the foil electrode and damage and bremsstrahlung measurements were made as before. When the diode current monitor indicated that matching shots had been made, the entrance and exit plane data were compared to provide information about propagation efficiency.

It should be noted that a high degree of relative accuracy was obtained with this procedure. This was due both to our ability to accurately determine injected beam reproducibility to almost arbitrary precision using the diode current monitor, and to the sensitive dependence $(I_b V_b{}^{2.5 \pm 0.5})$ of the bremsstrahlung waveform on the beam energy waveform.

The various electron beams used were selected by adjusting the anode-cathode gap in the diode. Pinch pressure was stabilized with a calibrated needle valve and monitored with a McLeod vacuum gauge on each shot. Pyrex discharge tubes were reused after mild etching in strong acid and alkaline solutions to remove the aluminum anode and cathode material deposited on the walls. Since the Pyrex absorbed gas vapor between shots, the magnetic field data taken prior to the experiment had to be obtained under similar conditions. Therefore the pinch tubes were replaced after every shot to obtain the data shown in Figure 3.9.

Another experimental difficulty was collapse of the anode-cathode gap due to pressure from the collapsing pinch. Measurements with a simple shorting circuit showed that the anode moved toward the cathode at $\sim 2 \times 10^5$ cm/sec. Small corrections to the gap spacing compensated for this effect.

3.3.1.2 Experimental Results. Beams with peak currents of 120 kA, 140 kA, and 160 kA were injected at 2.9 μsec ± 0.05 μsec. In addition, the 160 kA beam was injected at 0.5 μsec, 1.7 μsec, and 2.4 μsec. Total beam energy was 3 kJ. Average current density was less than 8 kA/cm^2, but core current density exceeded 100 kA/cm^2 (see Section 2.4).

Target damage, measured bremsstrahlung, and injection current are given in Figure 3.11 which compares anode damage and bremsstrahlung produced by injecting the 160 kA beam at 2.9 μsec with that produced at the entrance plane. The preservation of both the amplitude and shape of the X-ray signal and the quite comparable degrees of beam-produced damage indicate complete efficiency of transport, which was also observed with the 120 kA and 140 kA beams. (In the pulses shown in Figure 3.11 the difference in X-ray signal at late times was caused by imperfect beam reproducibility.) Guidance of the beam was quite good, as the well-centered circular damage attests. In view of the great sensitivity of the bremsstrahlung waveform to beam voltage and

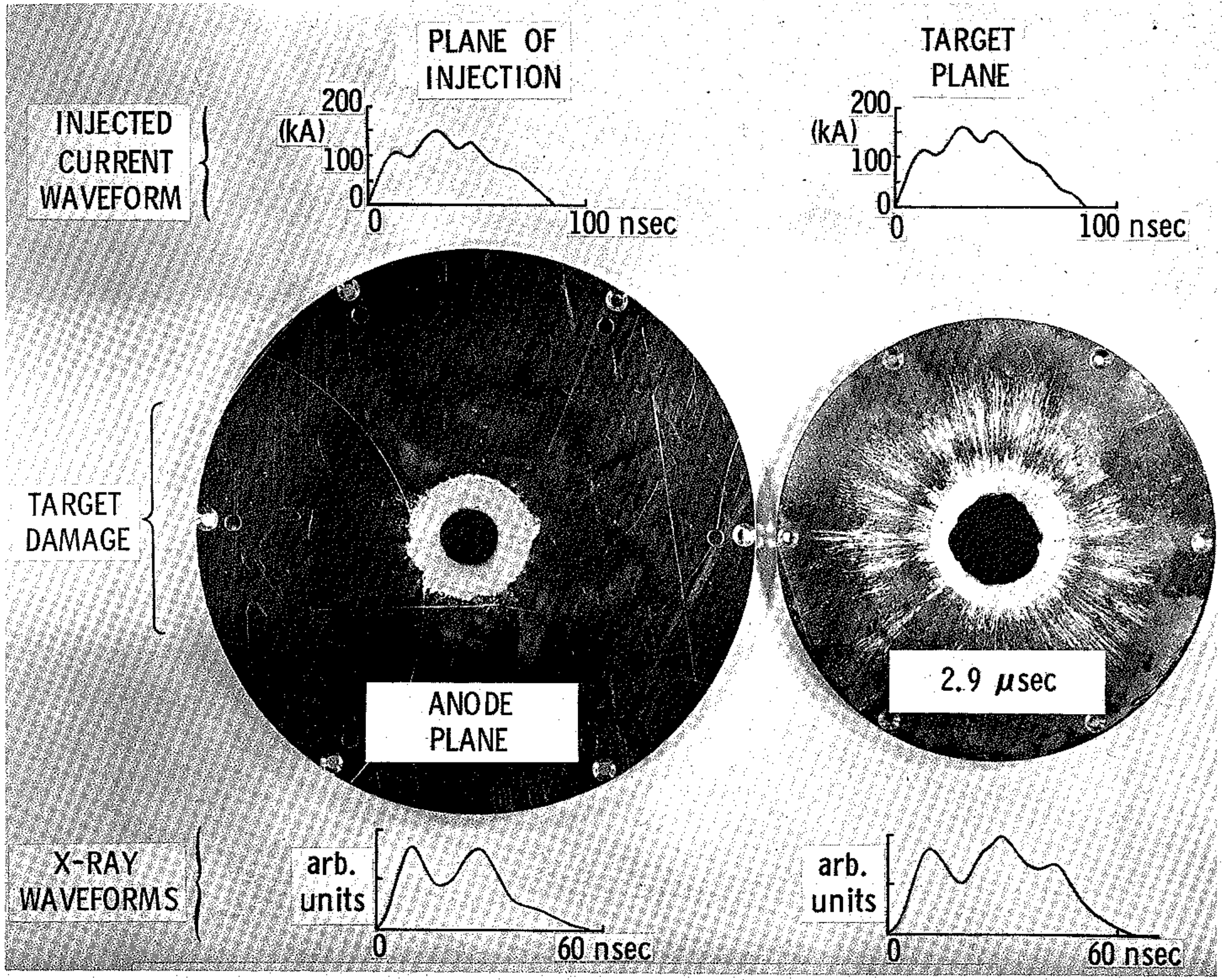

Figure 3.11 Target damage resulting from transport of 160 kA electron beam along a two-foot Z-pinch.

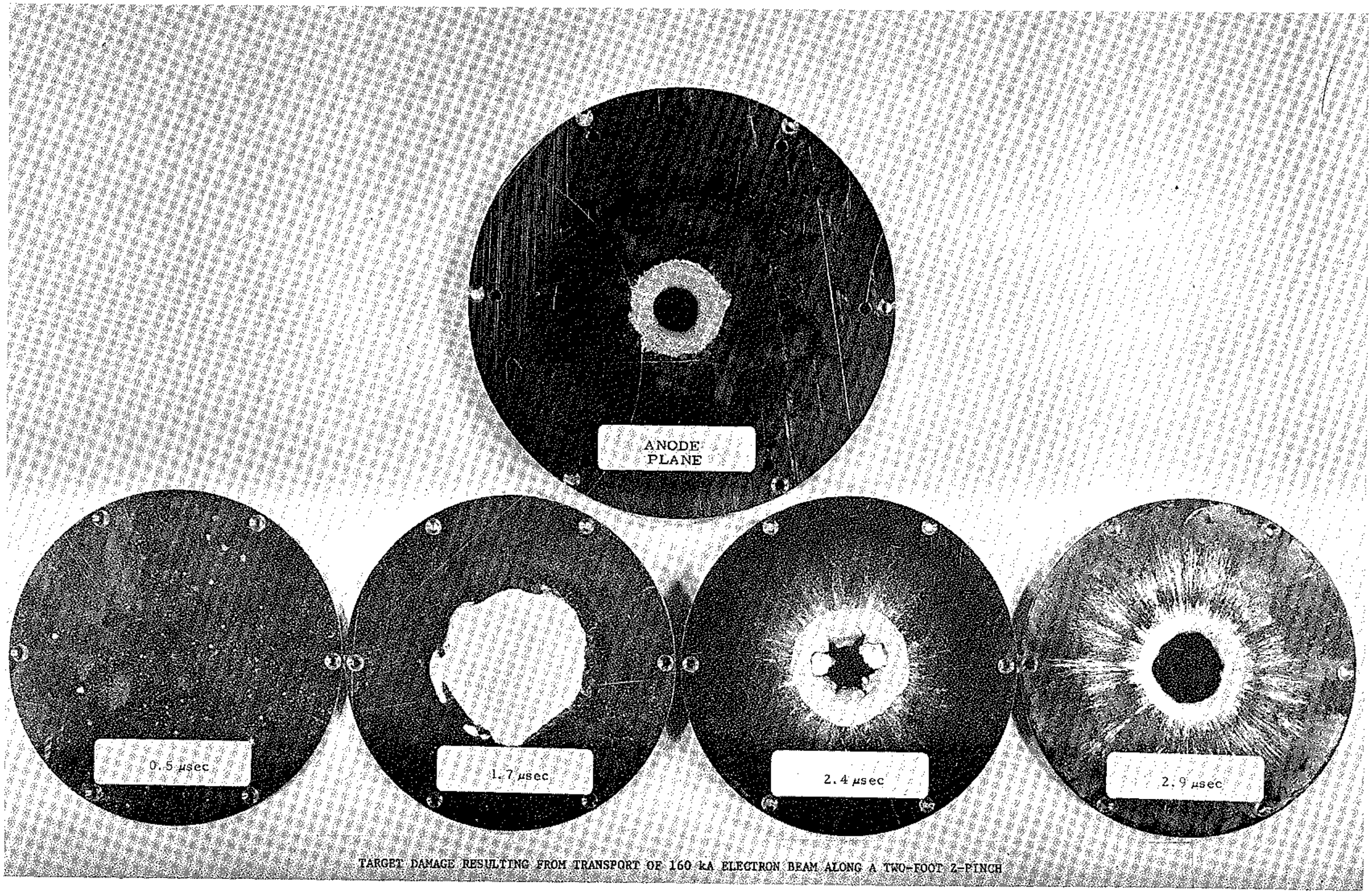

Figure 3.12 Target damage resulting from transport of 160 kA electron beam at four times in the collapse of a Z-pinch.

current, the high degree of preservation indicates that the voltage and current waveforms were not appreciably dispersed, attenuated, or otherwise altered during propagation, when injection occurred at 2.9 μsec. This suggests that in these cases there was no important coupling, energy exchange, or collective interaction between the beam and the plasma through which it traveled.

The most striking feature of the pinch anode damage is the contraction of the damage pattern for beam injection at later times. Figure 3.12 shows damage patterns produced by 160 kA beams for four injection times. At the earliest time, 0.5 μsec, the pinch magnetic field had not risen to a high enough value to contain the beam. This shot was much like the preionization experiment and here too transport was poor. For other injection times the damage was extensive and covered a smaller area at later times. Figure 3.13 displays the damage radii graphically, as well as those of other shots. The trajectory of the pinch current maximum is also shown. The damage is always within the current sheet during the collapse phase of the pinch. From the field measurements (Figure 3.9) and the damage radii we have determined that the pinch current contained within the damage radius was always small compared with the transported beam current, and was smallest in the case of largest damage radius (Figure 3.13). In other words, the amount of pinch current coextensive with the transported beam was found to decrease with increasing beam expansion.

Injection of 120 kA, 140 kA, and 160 kA beams at 2.9 μsec resulted in expansion of the damage pattern with increasing beam current (Figure 3.14). Since magnetic self-interaction in the generating diode presumably increases with current (due to the concomitant increase in magnetic field), it is probable that

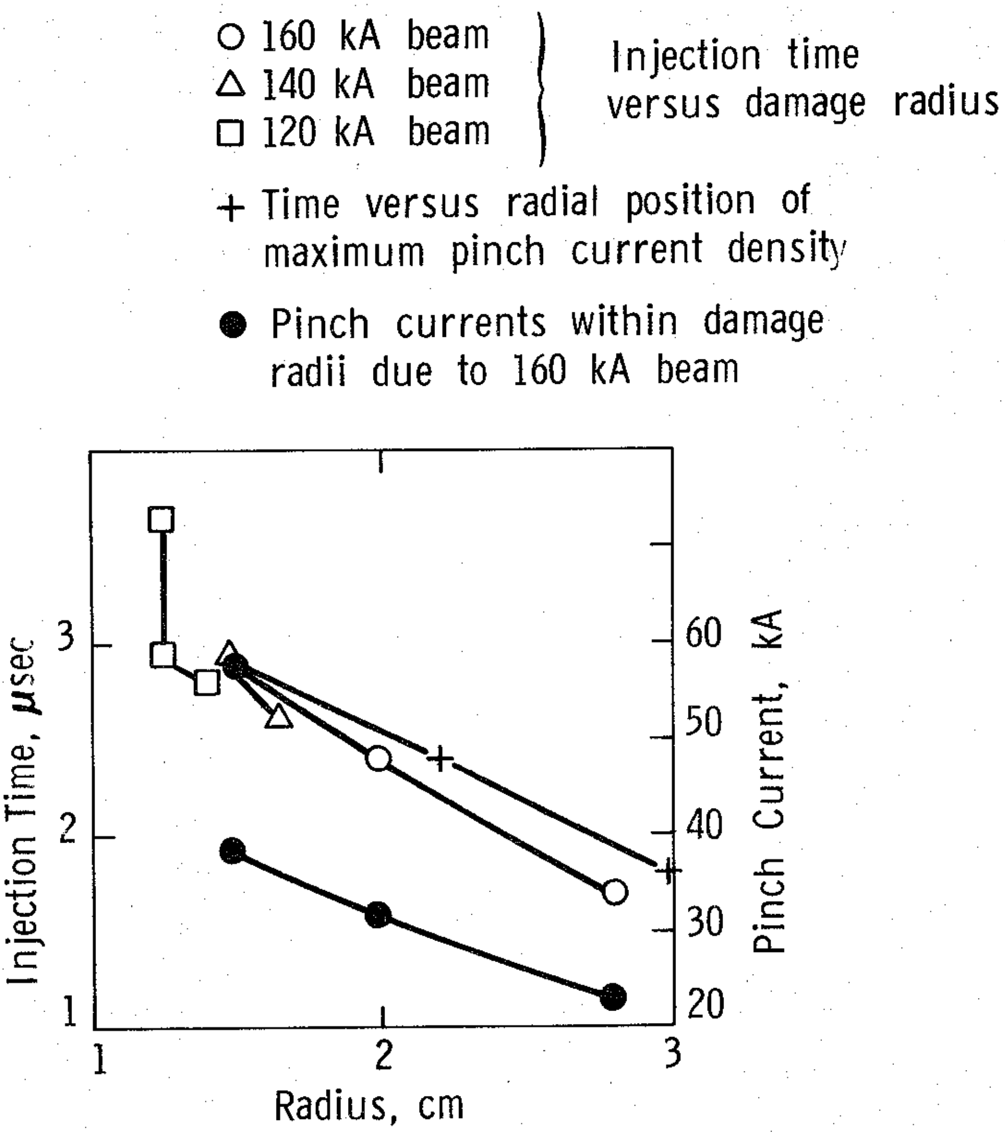

Figure 3.13 Graph showing damage radii, injection times, collapse trajectory of pinch current sheet, and amounts of pinch current inside damage radii of 160 kA beams.

these increases resulted in increasing deviation from paraxial trajectories at injection. Electrons from these "hotter" beams underwent larger excursions from the axis during transport, causing an expanded damage pattern.

The potential difference between the Z-pinch electrodes was time-resolved during beam propagation using the fast risetime voltage monitor with an Tektronix 519 oscilloscope at 20 nsec/cm. The voltage waveform during beam propagation showed no measurable deviation from the "background" Z-pinch voltage waveform (as in Figure 3.5). This was the case for all shots. In this way an upper limit of about 1000 volts was established as the maximum value of the induced Z-pinch interelectrode potential, corresponding to an induced axial electric field of, at the most, 17 volts/cm.

From this measurement, a lower bound on the current neutralization can be obtained by using Equation 3-1. Using $(E^{\mathrm{induced}})_z \leqslant 17$ volts/cm, $R = 7$ cm (the radius of the return current rods), and $r_b = 1.5$ cm (a typical transported beam radius), we see that $\dot{I}_{\mathrm{net}} \leqslant 4.2 \times 10^9$ A/sec. If this time derivative persisted for most of the beam pulse duration, the maximum net current due to the beam can be conservatively set at $I_{\mathrm{net}}^{\mathrm{max}} = 0.5$ kA. In the case of the 160 kA electron beam, this represents current neutralization of no less than 99.7 percent. No measurements were made to determine whether beam current density was locally cancelled to within 0.3 percent, (i.e., the inequality $\sigma >> \tau_c^2/4\pi L^2$ is satisfied), but conservative estimates of the plasma skin depth of the relevant frequencies yield values much less than the beam radius. This calculation suggests that beam current neutralization was locally maintained in the plasma volume co-extensive with the beam.

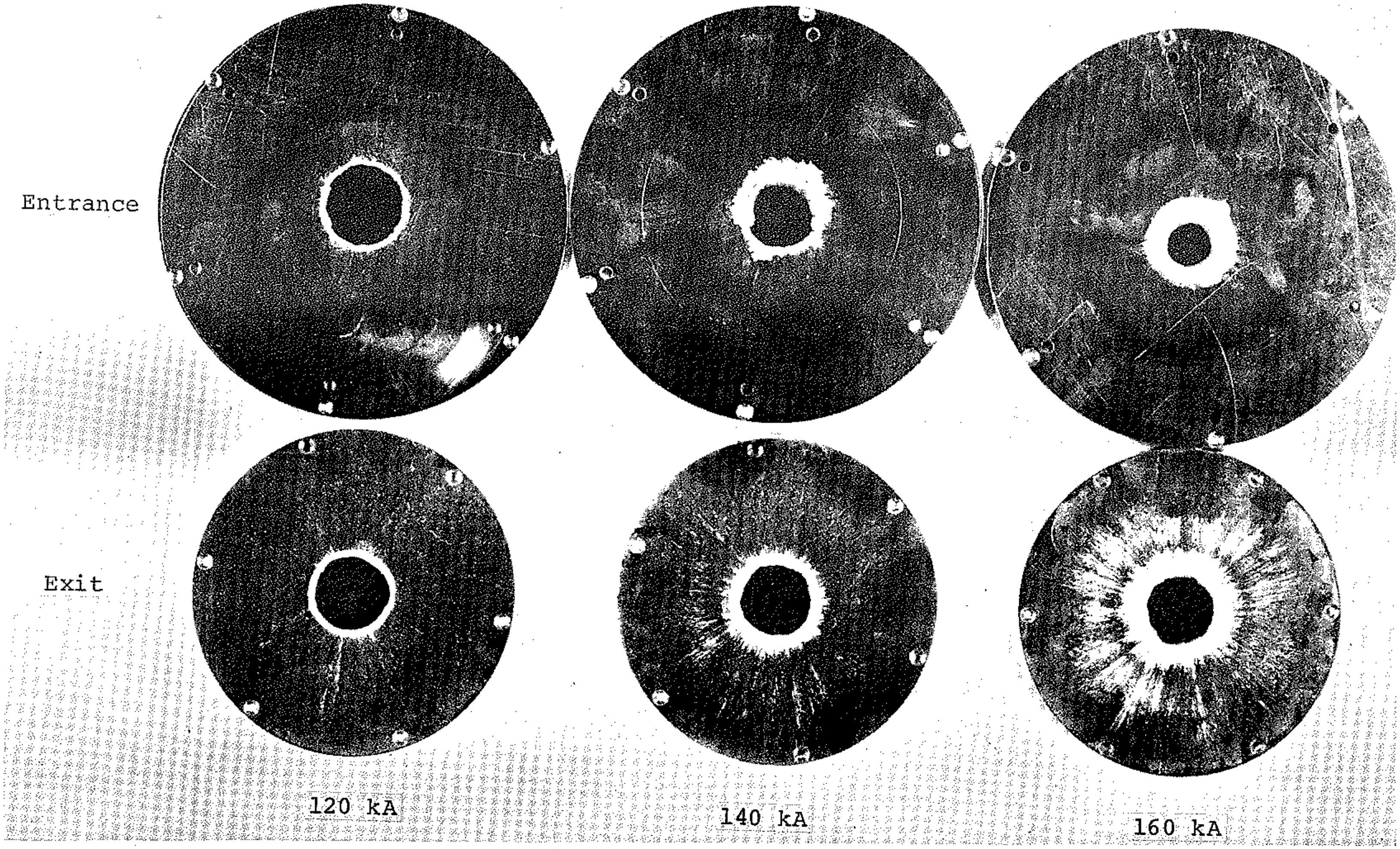

Figure 3.14 Anode and target plane damage patterns for beam injection at 2.9 μsec.

Using the inferred value of I_{net}^{max}, Ampere's law, and r_b = 1.5 cm, we estimate that perturbations of the Z-pinch magnetic field could have amounted to no more than 100 gauss during beam propagation. From Figure 3.9 it is apparent that such fields must have had little influence on propagation, which is to say that the Z-pinch magnetic field was to a good approximation an unperturbed external field in which beam electrons followed single-particle trajectories.

The Z-pinch magnetic field was also measured during the experiments. Using the magnetic probe, the azimuthal field was displayed on an oscilloscope at 1 μsec/cm and measured field before and after beam propagation on each shot. (Noise precluded measurements of B_θ during the beam pulse.) Identical measurements had been made prior to the beam propagation experiments. These corresponding pairs of magnetic field waveforms, with and without beam injection, were obtained at three radii: 1.9 cm, 2.5 cm, and 3.8 cm. The time derivative and magnitude of the field were the same before and after beam transport. Beam propagation had no effect on the time history of the magnetic field, indicating no gross perturbation of the discharge by the passage of the beam.

Other experimental work included the injection of 175 kA, 425 keV and 250 kA, 200 keV beams at various times in preliminary tests. Neither bremsstrahlung measurements nor entrance-plane damage references were obtained. However, target damage was comparable to the 160 kA shots at 1.7 and 2.9 μsec, and we tentatively concluded that these beams were efficiently propagated.

3.3.1.3 Modeling. In view of these observations we have interpreted beam transport in the Z-pinch as follows: The virtual absence of beam magnetic field decouples beam electrons from each other and they follow single-particle trajectories in the pinch magnetic field. This explains the relatively low magnetic fields that contained the beams. In the azimuthal field of the pinch a beam electron moves in an r-z plane along a trajectory that repeatedly intersects the pinch axis. Such motion has been described by Alfven (Reference 3.6) who showed that uniform beams cannot propagate with current greater than $I_a = 17{,}000\ \beta_{\|}\gamma$, for the case where the beam is influenced only by its self-magnetic field. In this experiment the field configuration is determined by the pinch, not by the beam itself. Hammer and Rostoker (Reference 3.7) and Benford et al., (Reference 3.8) have shown that "hollow" beam structures, with magnetic fields reduced at small radii but strongly peaked at the beam edge, enable beams to propagate at currents greater than I_A. Thus, for the 1.7 and 2.4 μsec injection times (where the magnetic field configuration closely approximates that due to a uniform beam, Figure 3.9) the enclosed pinch current is less than 17,000 $\beta_{\|}\gamma \approx 39$ kA. The field configuration at the 2.9 μsec injection time varies more steeply than the $B \alpha r$ dependence of a uniform beam and in this case the enclosed pinch current is greater than I_A.

To obtain quantitative understanding of the beam electron orbits, consider for example a 500 keV electron (mean energy of the 160 kA beam) in a field of 2 kG (representative of the case of injection at 2.9 μsec). Its Larmor radius is 1.5 cm, which was roughly the damage radius. To get better estimates of single-electron motion, we have numerically calculated electron trajectories in the measured magnetic field profiles (Figure 3.15). The computer program used finite differences in the radial coordinate, with radius intervals always much smaller than the local

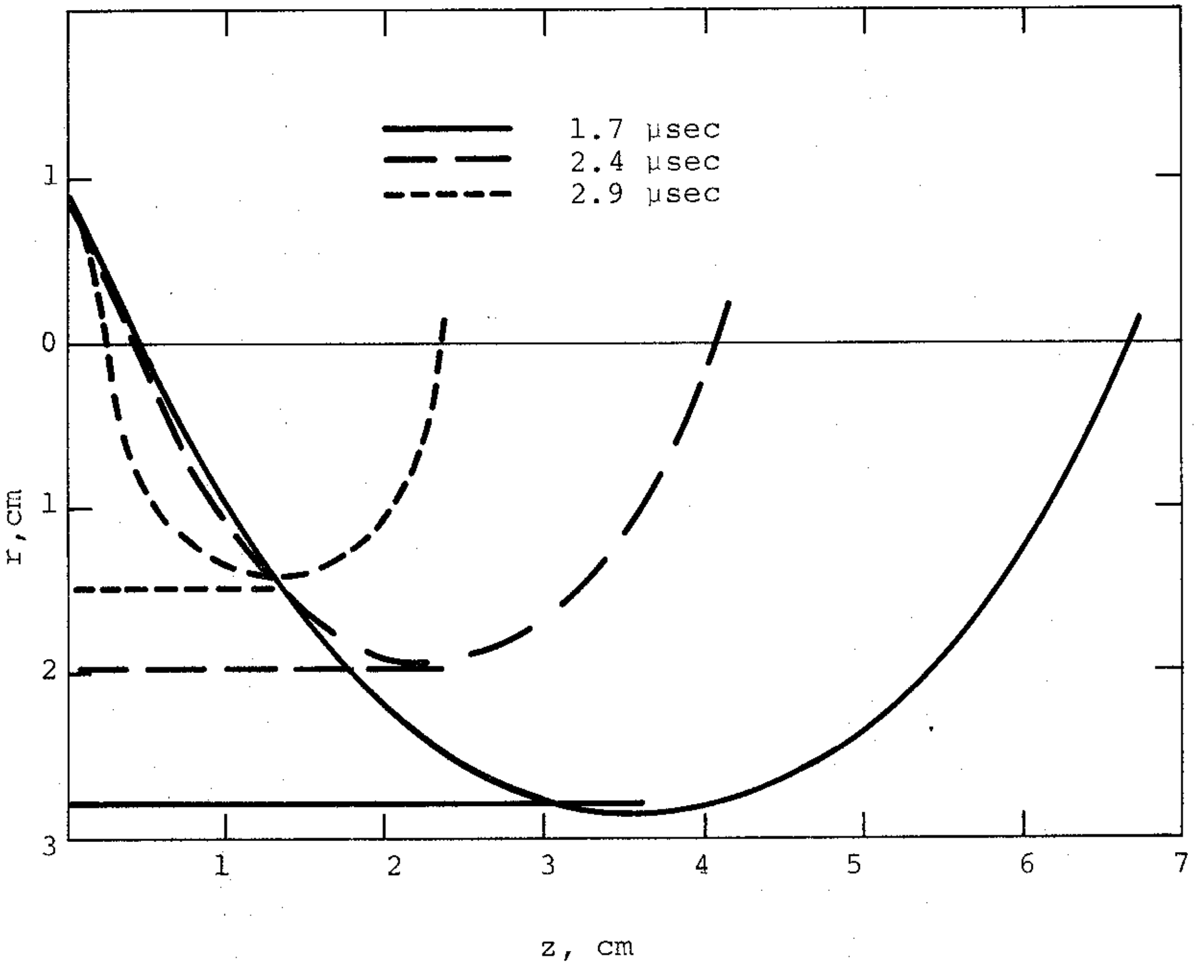

Figure 3.15 Calculated electron trajectories in field profiles at 1.7, 2.4 and 2.9 μsec. Assumed entrance (Z=0) conditions: kinetic energy = 750 keV (peak energy of 160 kA beam), radius = 0.9 cm, velocity vector (in r-z plane) makes 60° angle with Z-axis.

Larmor radius. For each radius interval, the program calculated a circular arc in the r-z plane with radius of curvature equal to the local relativistic Larmor radius and subject to the conditions that slope and position be continuous at arc junctions. We emphasize that these trajectory calculations are strictly hypothetical trajectories because of our incomplete knowledge of the actual electron entrance conditions. However, the ranges over which the entrance parameters individually varied during a pulse can be reasonably well identified. Incident radii are no greater than the cathode radius; incident energies are known from cathode voltage measurements; and incident angles are known to reach large values (Reference 3.8) with a time-integrated average of 40 degrees inclination to the propagation axis when current and energy waveforms are close to those of the 160 kA beam used here. Angles somewhat greater than 40 degrees could therefore be anticipated during the beam pulse. Trajectories were computed using values for the incident electron's radius, energy, and angle within the limits just delineated. The kinds of trajectories described above resulted, and the excursions from the Z-axis were consistent with the observed radial containment of the beam. In particular, the most favorable results are in Figure 3.15, where three orbits are shown that were computed from identical entrance parameters: $\gamma = 2.5$ (peak energy of 160 kA beam), $r_o = 0.9$ cm (compare with 1.25 cm cathode radius), $\alpha = 60$ degrees (angular deviation from beam axis). The field profiles for which these trajectories were computed are those into which the 160 kA beam was injected (1.7, 2.4, and 2.9 μsec). A consistent correlation between target damage diameter and trajectory width is apparent. These results serve to demonstrate the compatibility of our single-particle analysis with the quantitative features of the transport system and electron beam.

However, this is not the only mode of transport possible. In Figure 3.16 a typical magnetic profile for a linear pinch is shown. In Region I, beam electrons execute periodic orbits about the axis of the pinch as described above. Region I is bounded by that radius wherein the enclosed pinch current is just sufficient to turn a beam electron. In Region II of Figure 3.16, where the enclosed pinch current is greater than I_A and $\partial B_\theta/\partial r > 0$, beam electrons undergo a ∇B drift type trajectory which turns them back into the diode. On the other hand Region III, where enclosed current is greater than I_A but $\partial B_\theta/\partial r < 0$, should transport beam current because the ∇B drift is in the right direction. Evidence for this can be seen in Figure 3.13 (120 kA beam) where injection at 3.6 μsec, such that much of the beam is injected into a $\partial B/\partial r < 0$ region, allows transport without expansion of

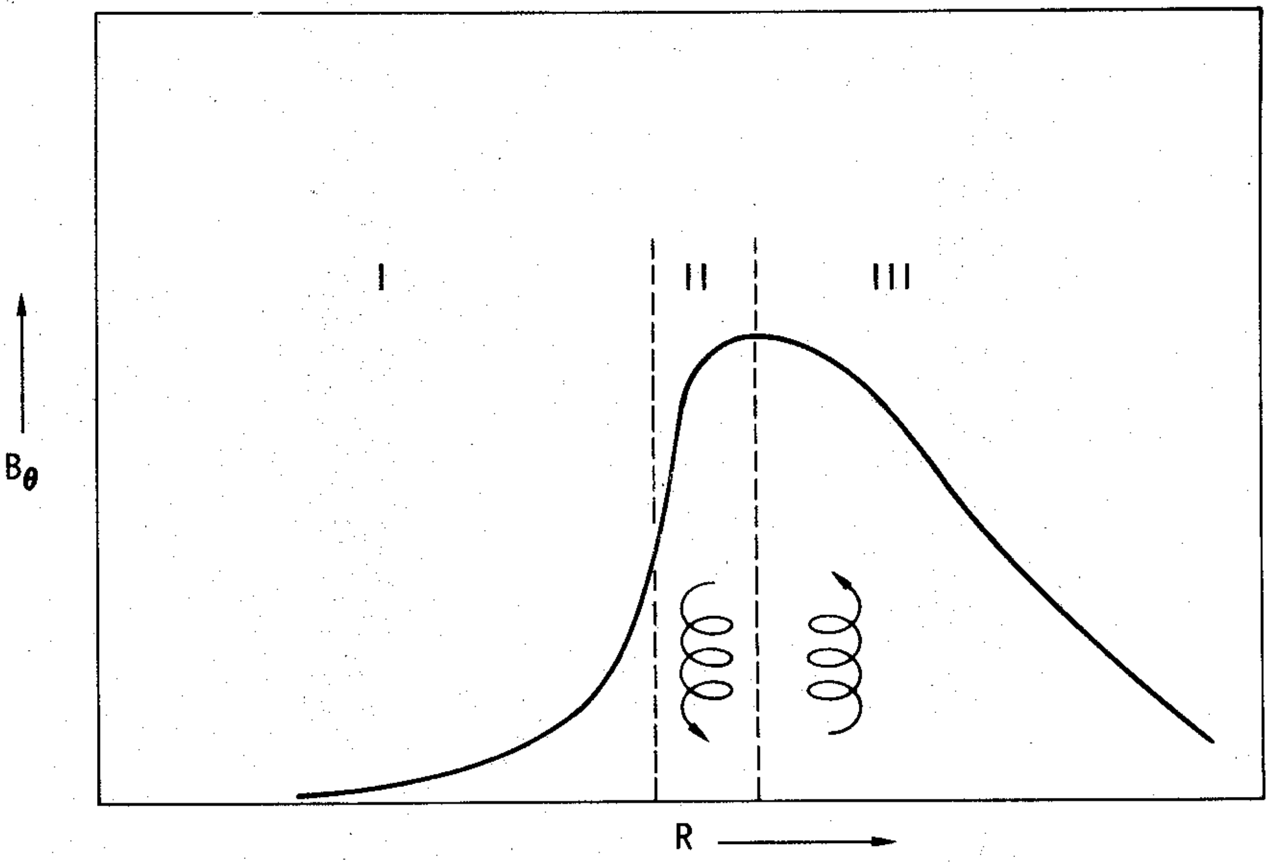

Figure 3.16 Typical field profile for collapsing linear pinch current sheet.

the beam. Observation of the existence of Region II would be difficult in that damage to the pinch anode in Regions I and III would essentially obliterate any annulus undamaged by the beam itself. Also, the spread of injection angles of beam electrons would tend to smear out the boundary between Regions II and III. X-ray pinhole photographs are a promising way of recording this structure.

3.3.1.4 Conclusions. The linear pinch was able to transport beams over 60 cm without loss with currents $\lesssim$ 160 kA, voltages $\lesssim$ 750 kA, beam energy ~ 3 kJ at mean current densities of 8 kA/cm^2, and peak injected current densities of 100 kA/cm^2. The beam propagated inside the collapsing current sheet, which allowed some control over the beam fluence. Pinch currents substantially smaller than the beam current were sufficient to contain the beams. Virtually complete neutralization of the beam current occurred. A model based on single-particle motion of beam electrons in the pinch magnetic field describes the phenomena.

3.3.2 Snark Z-Pinch Transport Experiment. This experiment was conducted to investigate Z-pinch transport of intense beams. These beams were generated on Snark and had peak beam currents of 310 kA, peak voltages of 570 to 670 kV, and total beam energy of 11 to 13 kJ. The ν/γ of these beams was 14, twice that of the 738 beams.

A pinch system of larger energy was used for this experiment. The bank consisted of sixteen 15.8 μF capacitors, connected in parallel, with a peak voltage of 20 kV. Total bank energy was 48 kJ. Twelve Belden 198 low-inductance cables connected in parallel led from the bank to the pinch head. The pinch was 45 cm long and was 20 cm in diameter (Figure 3.17). Construction

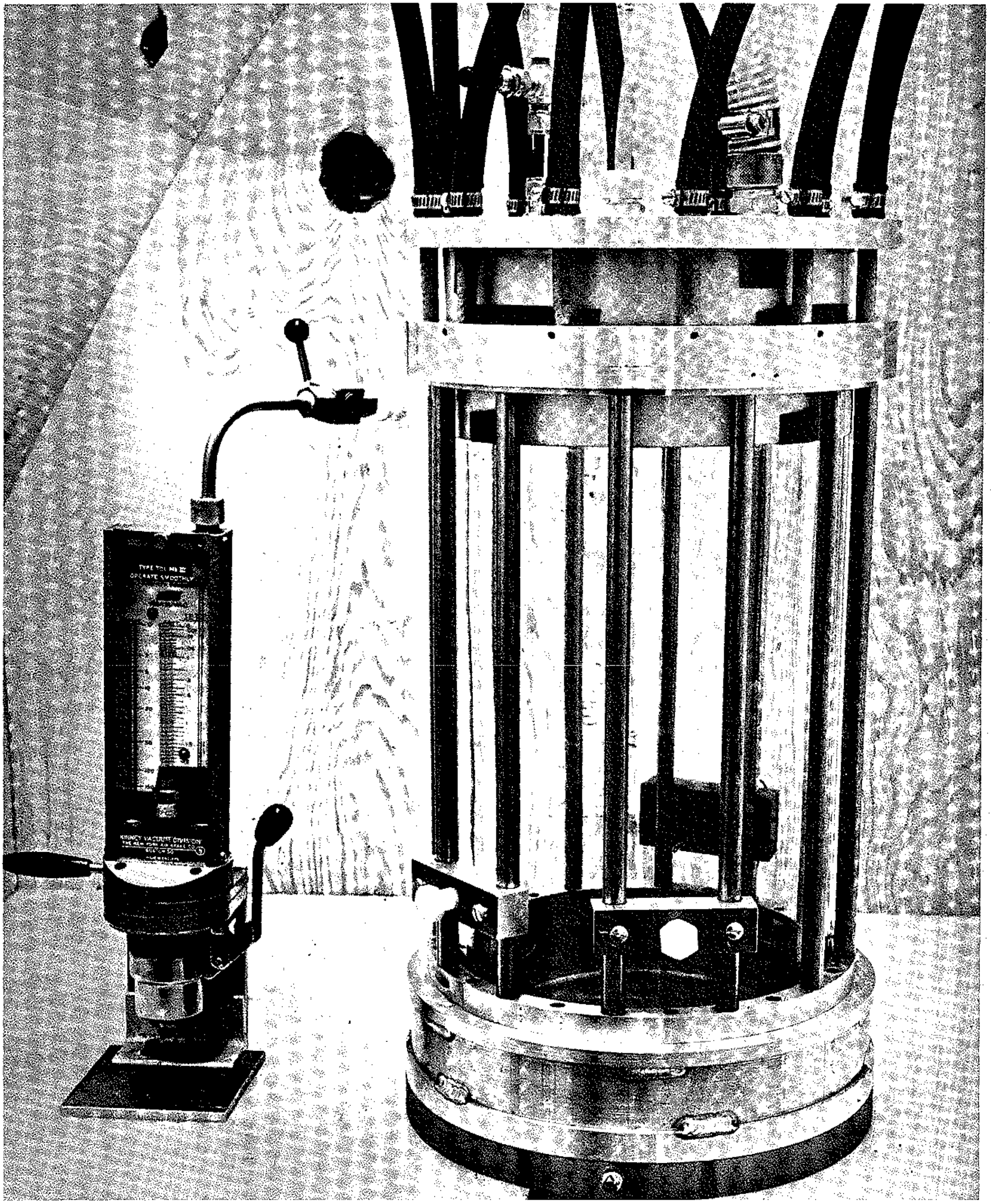

Figure 3.17 Snark Z-pinch with cable, gas, and vacuum connections. Note magnetic probe inserted through far side of discharge tube.

and operation of the Snark pinch was similar to that of the 738 pinch. Pinch voltage was monitored at the point where the 8 foot cables connected to the bank. Pinch current was monitored by a pickup coil at this point. With charging voltage of 20 kV the peak pinch current was 850 kA; 18 kV was used in the experiment to reduce the probability of bank failure. At 18 kV the peak pinch current was 750 kA. The operating pressure was 300 μ argon, which was chosen (as for all pinches in this study) for rapid gas breakdown and reproducible probe traces. The pinch reached maximum compression at 5.5 μsec. Magnetic probes of the same design as used in the 738 experiment were used to map the discharge. Figure 3.18 displays four magnetic field profiles during the collapse. The current sheet had a much sharper rise than the 738 pinch; this was due to the considerably higher rate of rise of the pinch current.

The anode of the pinch was an aluminum plate with a 10 cm diameter, 0.0025 inch thick tantalum foil stretched over the center by a clamping ring. This foil was used to enhance X-ray production by the transported beam. Its size was limited by the small gas and vacuum inlets which were also located in the head of the pinch. A 10 cm recess in the pinch head allowed the X-ray diagnostics to be placed directly behind the aluminum 0.6 mm plate anode. The diagnostics were a scintillator-photodiode combination, a Compton diode, and a thermoluminescent detector (TLD) array spaced over the 10-cm-diameter circle. Operating procedure and beam injection timing were the same as in the 738 experiment.

Snark beams were emitted by the Mark IV cathode, (a rollpin cathode with a 6.5 cm i.d., 11.85 cm o.d.), using a 0.00125 cm titanium anode to help prevent collapse of the anode-cathode gap by impulse from the pinch discharge.

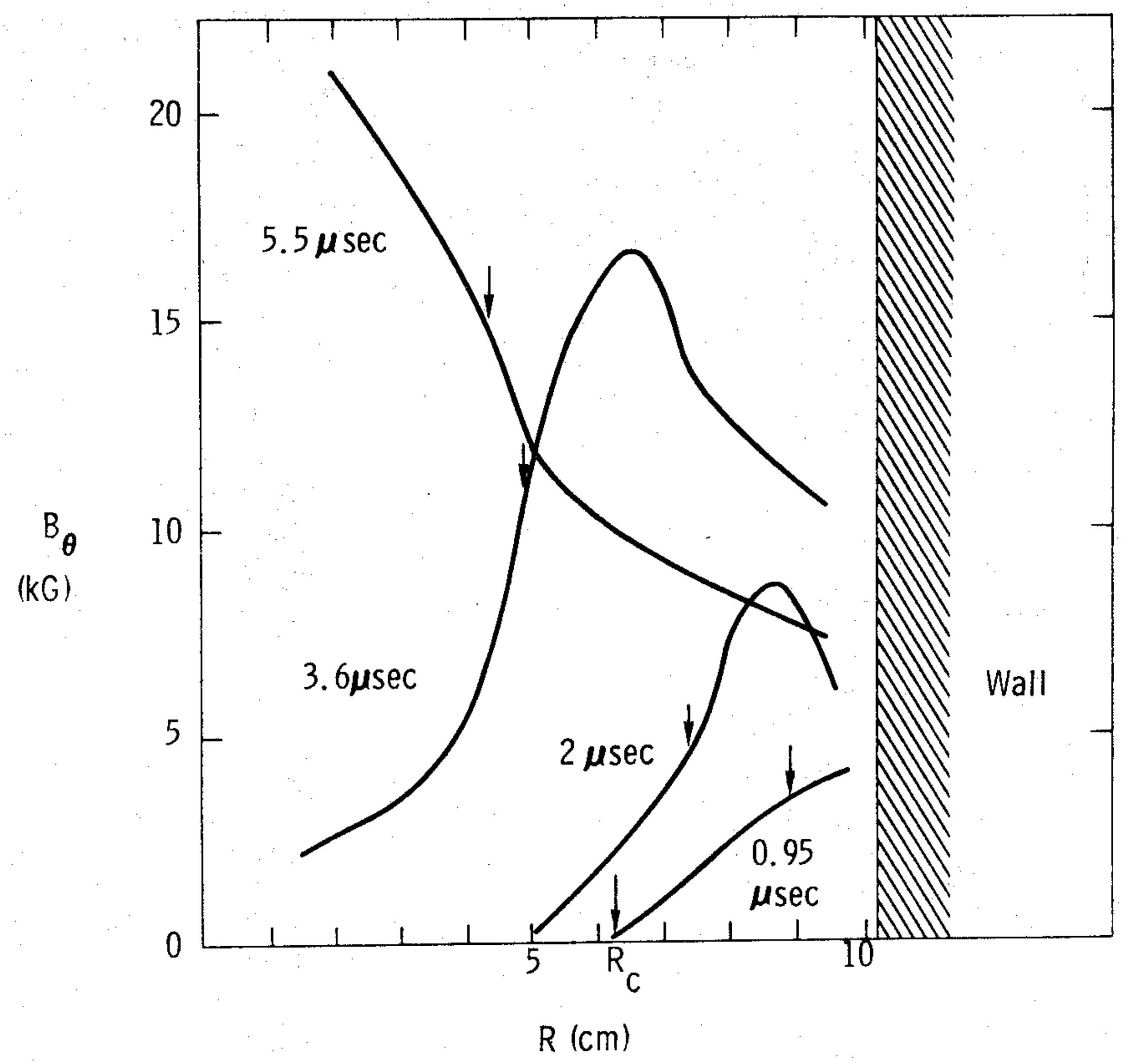

Figure 3.18 Magnetic field profiles at times of beam injection. R_c is beam cathode radius, arrows indicate damage radii of transported beams.

Beams were injected at several times in the pinch collapse, as shown in Figure 3.18. The arrows indicate the radii of the damage patterns on the pinch anode. For 0.95 μsec, 2 μsec, and 3.6 μsec (collapse phase) the beam clearly propagated on the inside of the current sheet as shown in Figure 3.19. At 5.5 μsec, when the pinch was at maximum compression, the damage extended some distance into the region of declining field. The considerable fluence control available with Z-pinch transport is evident from this figure: varying the time of beam injection from 0.95 μsec to 5.5 μsec changed the damage pattern area from 250 cm^2 to 60 cm^2. The beam damage patterns were not uniform at the early times, but became progressively more uniform at later injection times. This is consistent with the single-particle analysis developed earlier: Beams expand to fill the cross section of the current sheet, but reflect from the current sheet more often and have their azimuthal velocity components randomized if injected into a smaller diameter pinch sheet.

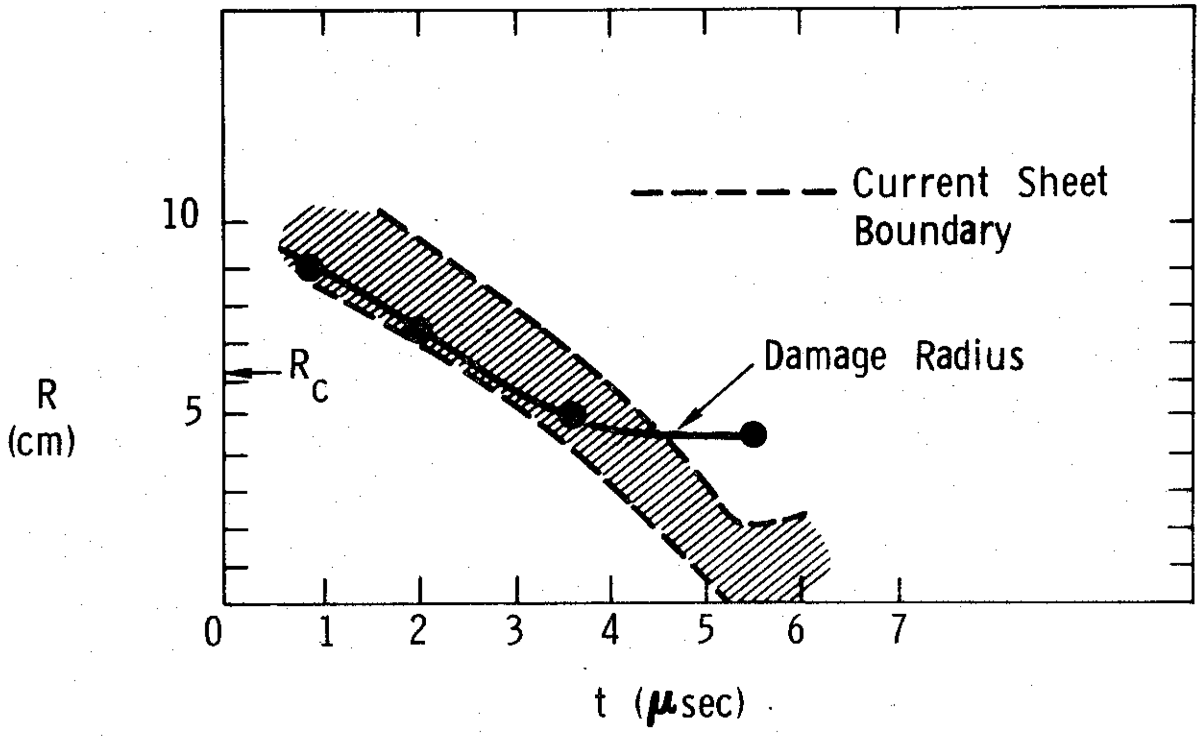

Figure 3.19 Pinch anode damage radii as a function of beam injection time.

The beams transported at 0.95, 2.0 and 3.6 μsec clearly propagated inside the current sheet in the Region I mode discussed previously. In contrast to the 738 experimental results, the pinch current enclosed by the beam channel was much greater than the Alfven current. The enclosed currents were 156 kA, 173 kA, and 288 kA for the three injection times. The Alfven current for the beams was less than 35 kA, so that I/I_A varied from 4.5 to 9 for these shots. In this case the field profiles were much like those associated with "hollow" beams, (i.e., low fields at small radii and a steep $\partial B/\partial r$ gradient at the current sheath) which allowed beam currents in excess of I_A to propagate (see paragraph 3.3.1.3). The beam injected at 5.5 μsec propagated in the Region III drift mode, much like the 120 kA beam shot in the 738 experiment.

Transport efficiency was diagnosed by comparing transported beam photodiode, Compton diode and TLD measurements with those taken at the anode. Correlation between the three diagnostics was found to be more reliable than any single diagnostic. The 0.95 μsec shot could not be analyzed because most of the beam was incident upon the aluminum area of the pinch anode. Some, but not most, of the 2 μsec beam impinged on the aluminum as well, giving a reduced efficiency measurement, 70 ± 15 percent, because of the reduced X-ray production. The shots at 3.6 μsec and 5.5 μsec created damage totally within the 10-cm-diameter tantalum and were transported with efficiencies of 93 ± 15 percent and 82 ± 15 percent respectively. The reduction in transport efficiency at 5.5 μsec was perhaps due to injection of parts of the beams into Region II field geometry. Although many of the beam electrons were injected into Region III field geometry ($\partial \beta_\theta/\partial r < 0$), some beam electrons injected near the axis were in

Region II field geometry ($I > I_A$, $\partial\beta_\theta/\partial r > 0$) and drifted back into the diode. Reentry of beam electrons into the diode is a complex phenomena; it is quite possible that the process is lossy. This would explain the reduced efficiency of the 5.5 μsec shot.

The Snark Z-pinch transport experiment shows that the physics of the interaction does not change with increasing beam current. Transport efficiencies were high and a considerable degree of fluence control was demonstrated. The single-particle model developed previously is adequate to explain the damage patterns and efficiency measurements.

3.4 BEAM COMBINATION EXPERIMENT

The transport mechanism discussed in the preceding section offers a simple way to combine beams while transporting them. When a beam is injected into a Z-pinch, the beam electrons are decoupled from one another by the neutralization of their net current. The beam expands to fill the inside of the current sheet and a second beam, injected inside the current sheet at the same time, will do the same (Figure 3.20). There will be no interaction between the beams because their fields are suppressed by the conducting plasma. Beam electrons follow single-particle orbits to the target. The θ-components of velocity resulting from off-axis injection of the high ν/γ beams result in their azimuthal mixing, so that the combination beam is soon azimuthally symmetric. The advantage of this scheme is that the beams are mixed, not merely brought into proximity, and cannot be separated later. An experiment was performed to test this model; the collapsing current sheet successfully combined two beams while retaining high transport efficiency.

The methods used to extract two beams while preventing any magnetic interaction between their diodes is discussed in the section on diode studies, Section 2. Two 6-cm-diameter rollpin hollow cathodes were extended on stalks and the anode-cathode gap (0.45 cm for this experiment) was adjusted by using shims at their bases. The cathode centers were 10 cm apart (Figure 3.21). The anode (0.0025 cm aluminum) was stretched over both diodes and clamped at the edge of the pinch tube. The two 700 keV beams injected into the pinch were not precisely identical; they differed in peak current by ~ 20 percent on each shot. Their sum varied from 365 kA to 375 kA. Total beam energy was 16 kJ. The two diode currents for the beams injected at 2.6 μsec are shown in Figure 3.22(a). The pinch was a modified version of that used

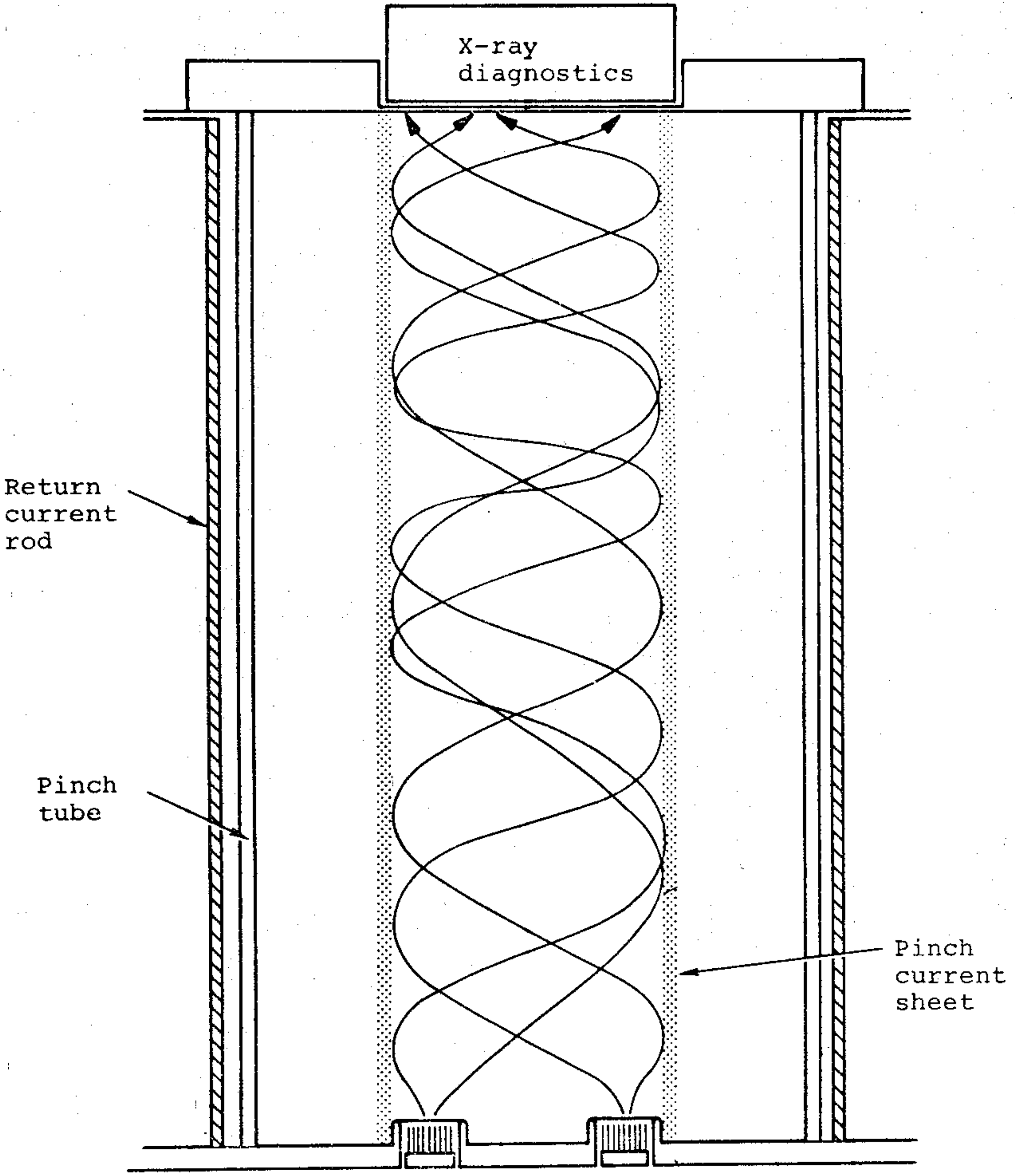

Figure 3.20 Beam combination in a Z-pinch.

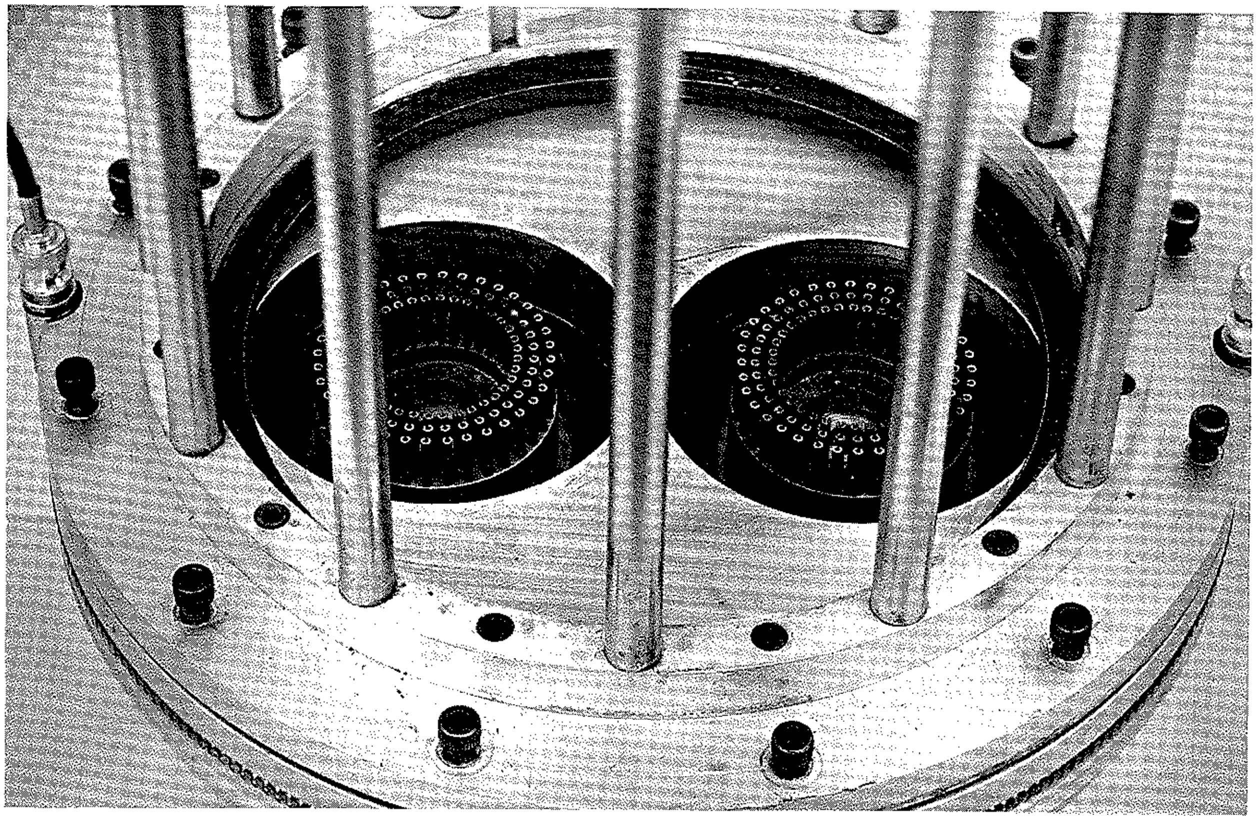

Figure 3.21 Photo of pinch base with dual cathodes. Note cable connections to Rogowski coils around each cathode.

A326

a. Currents in the two diodes 50 nsec/cm. Upper peak current 168 kA, lower 205 kA.

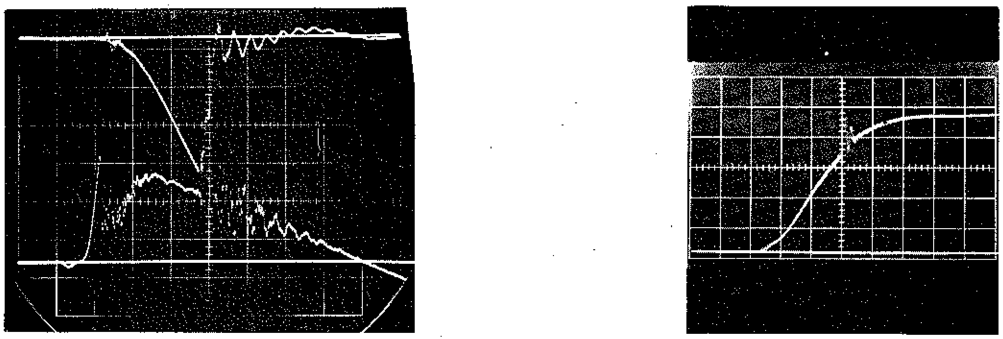

b. Snark Marx pulse charge voltage (upper) and pinch voltage (lower), sweep 1 μsec/cm.

c. Pinch current plus beam current, 1 μsec/cm. Peak current 650 kA.

Figure 3.22 Pinch and beam waveforms for beam combination.

for the Snark transport experiment. Since the primary indicator of beam combination was the damage produced in the pinch anode, the head of the pinch was altered to maximize the anode plate area from which X-rays could be detected and to minimize the anode plate surface used for gas and vacuum parts. This was accomplished by placing the gas and vacuum ports at the periphery of the plate and enlarging the recession behind the plate to a 15 cm diameter. Voltage and current for the 15 kV discharge are shown along with the pulsed charge voltage of the Snark Marx in Figure 3.22b and c. On the shot shown, the pinch and Snark Marx were triggered at appropriate times to give beam injection at 2.6 μsec into the discharge. The pinch voltage rose rapidly until breakdown, then fell and remained low until the pinch inductance had risen enough (by current sheet collapse) to cause a higher voltage drop across the discharge. Meanwhile the Marx voltage rose, the master switch fired, and the beam was injected. Noise on the voltage monitor signal precluded any determination of the degree of current neutralization by measurement of the change in voltage across the pinch. Current sheet profiles for the times of beam injection ascertained by the same probe technique described earlier are shown in Figure 3.23 along with the radial location of a cathode. The current sheet velocity was low at early times (because of the low dI/dt), but increased after 0.8 μsec; maximum compression occurred at 6.5 μsec.

Damage to the pinch anode clearly indicated the mixing of the two beams. Figure 3.24 shows damage to four anode plates produced by transported beams. For comparison, a witness plate placed behind the anode demonstrates the distinct separation of the two beams at the injection plane. The transported beams clearly had combined in propagating down the 45 cm length of the discharge tube. The damage patterns for 2.7, 3.1, and 3.9 μsec

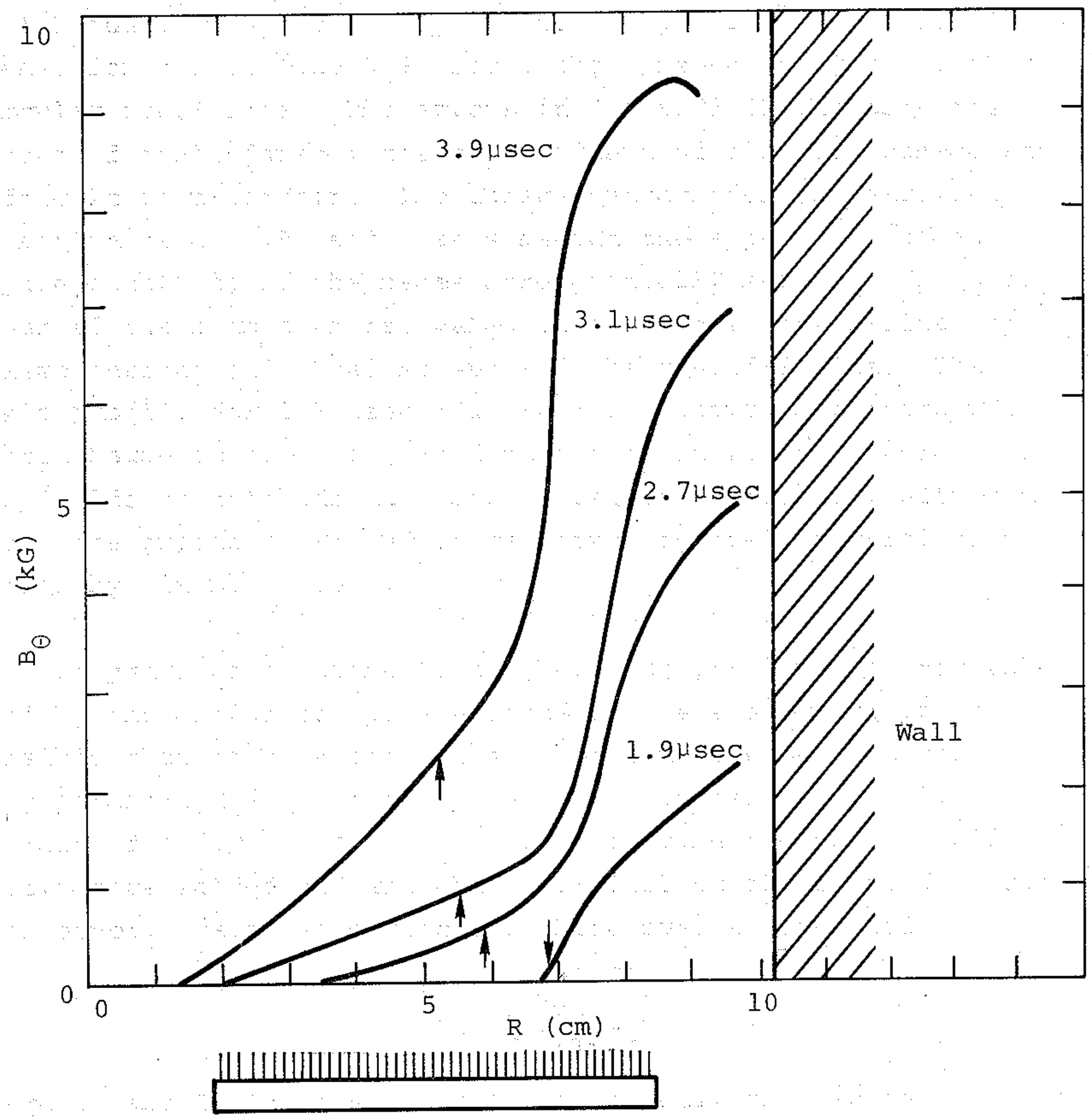

Figure 3.23 Magnetic field profiles for beam injection times. The location and size of one cathode is shown. Arrows indicate outer limit of spall damage.

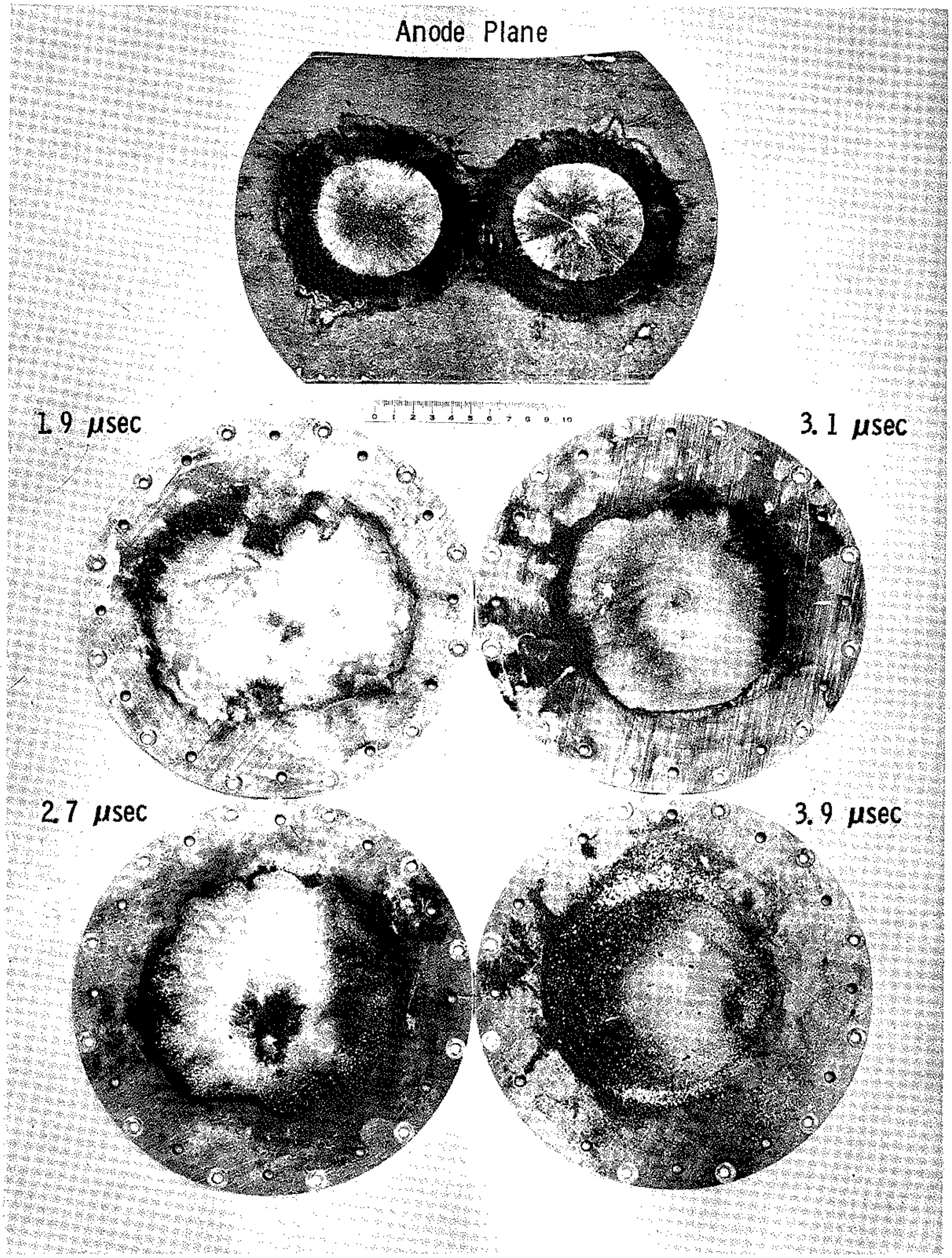

Figure 3.24 Damage produced at anode by two separate beams and at target by combined beams for four injection times.

show no sign that they were caused by two separate beams. Damage at 1.9 and 2.7 μsec was composed of irregular melt and spall areas; for the 3.1 and 3.9 μsec shots, the damage was a uniform circular spall area. The arrows in Figure 3.23 indicate the extent of spall damage; the outer extent of all beam damage was difficult to ascertain. The damage pattern for the earliest injection time, 1.9 μsec, has somewhat the appearance of a figure eight, as if the beams were partially merged. This could occur if the beam currents were not completely neutralized by plasma current and retained some of their self-fields. The field profile for 1.9 μsec (Figure 3.23) shows that there was little magnetic field in the damage pattern region (inside 7 cm). The fields of the beam may have helped to contain it, although they were probably limited in magnitude by their partial neutralization by plasma current.

In previous experiments the beam current has been neutralized by the preionized plasma ahead of the sheet, but it is possible that at this early injection time the beam current was only partially neutralized by weakly prionized plasma (i.e., instead of $\tau_D \gg \tau_B$, $\tau_D \sim \tau_B$). In this case the beams would retain some self-field and their parallel currents would attract each other. Parallel currents combine over a time scale,

$$\tau = r_o \sqrt{\frac{mc^2 \pi}{4I_1 \; I_2}}$$

where I_1 and I_2 are the currents, m is their reduced mass per cm, and r_o is their initial separation. For the beams in this experiment this time is short ($\sim 10^{-15}$ sec) if the reduced mass is just that of the beams themselves. However, the conductive plasma will retard the combination time of the beams to that of magnetic

RPN 99

diffusion. This occurs because the fields are "frozen" in the plasma and cannot change over times less than τ_D. Since $\tau_D \lesssim \tau_B$ for partial current neutralization, the partial beam combination evident in the damage pattern is expected.

Transport efficiency was diagnosed by TLD arrays and scintillator photodiode signals. Efficiency decreased with injection time. The 1.9 μsec and 2.7 μsec shots were transported completely, 104 ± 15 percent and 87 ± 15 percent respectively. Inadequate diagnostics were recorded on the 3.1 μsec shot and the 3.9 μsec shot tranported poorly: 60 ± 20 percent. The reason for this decrease in efficiency is simple: the current sheet swept in, causing less of the beam to be injected inside the current sheet at the later time. This agrees with the decline of the damage radius as injection time increased (Figure 3.23).

The model discussed above predicts that each beam spreads to fill the inside of the current sheet; this was checked by injecting a single beam. One cathode and its shank were removed and the pulse charge lowered to compensate for the impedance increase. The resulting beam closely resembled each of the beams used for the two-beam shots. It was injected at 1.2 μsec (Figure 3.23) and filled the inside of the current sheet, in agreement with expectations. The single beam was not energetic enough to cause spall over the entire anode plate, but less prominent damage extended out to 9 cm on the surface. The area of most intense spall was on the opposite side of the pinch tube from the point of injection, indicating a great deal of beam spreading. Transport efficiency was 90 ± 15 percent, consistent with the 1.9 μsec shot.

This experiment demonstrates that beams can be mixed by injecting them inside a collapsing current sheet. The two 8 kJ beams spread to fill the sheet and mixed while propagating down the sheet without substantial loss. Although these beams were injected directly from the diodes, this experiment is physically equivalent to the combination of two beams transported some distance from the generating diodes and injected through a foil into the pinch. Therefore this combination scheme could be used in conjunction with a transport stage.

3.5 BEAM COMPRESSION (TAPERED PINCH) EXPERIMENT

The problem of beam compression was addressed under the B_θ studies by injecting a high ν/γ (PIML) beam into a tapered Z-pinch. If the current sheet of a pinch is inclined to the axis of a beam, the beam electrons should reflect from the sheet at increasing angles as they go down the pinch (Figure 3.25). This should reduce the beam diameter and increase the current density. However, a beam electron injected at a large angle should be reflected after a few bounces; this also is shown in Figure 3.25. The number of electrons which compress and then pass through the tapered pinch should depend upon the angles at which they were injected. Since the ν/γ of the beams used in this experiment varied from 3.5 to 7 and the peak currents exceeded the critical current, pinching of the beam in the diode could be expected to introduce high transverse velocity components. At early injection times (before the pinch collapses at the small diameter end), these "hottest" components of the beam should propagate. Beam injection at later times in the pinch, however, should result in increasing reflection of the "hot" beam components and reduced transport efficiency. At even later times, all of the beam should be reflected from the strong field

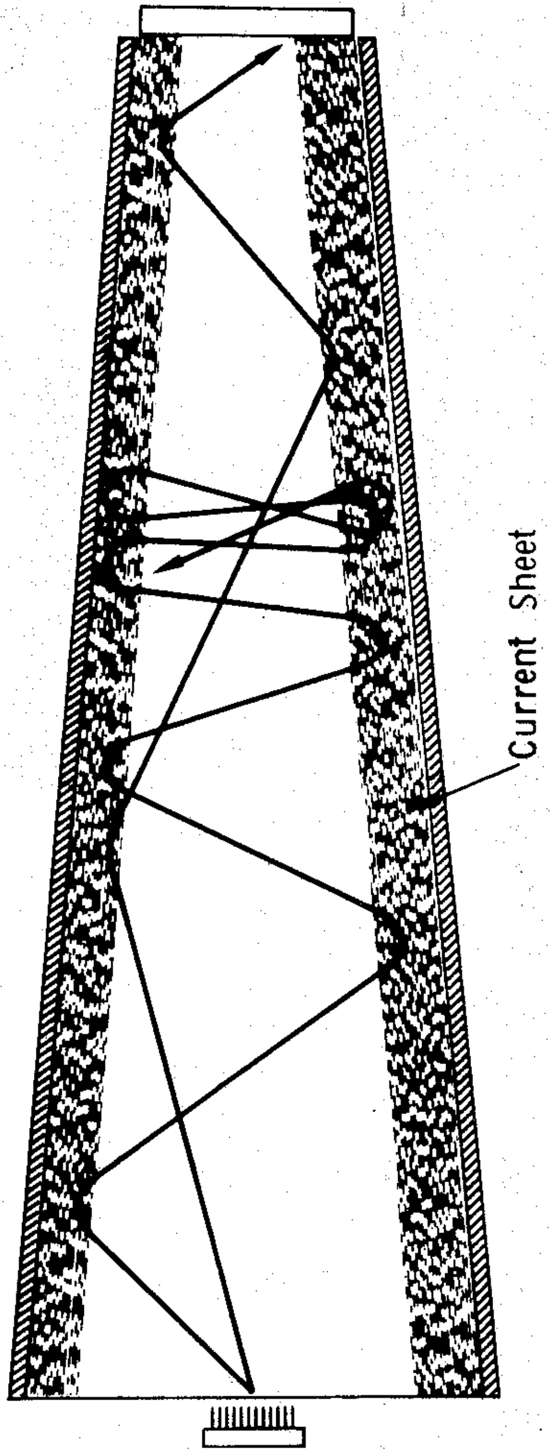

Figure 3.25 Transmission and reflection of beam electrons in a tapered Z-pinch with a sharp current sheet.

at the end of the pinch. In this regard, the tapered pinch should be similar to the magnetic mirror, in that "hot" beams will be reflected rather than transported. The experiments reported here were directed at determining if this picture is true by measuring beam size and transport efficiency after passage of the beam through a tapered Z-pinch.

The pinch used in this experiment is shown in Figure 3.26. The capacitor bank was the same 20 kV, 9 kJ unit used in the 738 pinch experiments. Voltage was applied to the pinch anode by a 8-cable (Belden YK 198) extension of the transmission line. Pinch voltage was diagnosed with a resistive current shunt, and current was monitored with an inductive pickup coil. Magnetic field probes were used to map the collapse of the pinch current sheet at four axial locations. Magnetic field profiles 3 cm from the pinch anode are displayed in Figure 3.27. The 30 cm discharge tube was tapered from a 10 cm diameter at the base to 5 cm at the top, a taper angle of 4 degrees 45 minutes. In tapering the discharge tube, two additional dynamic effects were introduced into the collapse history of the current sheet. First, the current sheet velocity was higher at the narrow end of the pinch, but this was determined from probe measurements to be a small effect. Second, due to the smaller pinch diameter at the top end, the pinch current density was higher there. This caused the sheet to be steeper at the top, as shown in Figure 3.28. The "bounce" model (Figure 3.25) would then be more valid at the top of the pinch than at the bottom.

The tapered pinch experiment was conducted on PIML, using a 3.8-cm-diameter cathode and A-K distances of 2 to 3 mm. The base plate of the pinch was a 0.3 cm aluminum plate with a central 5-cm-diameter hole. An anode (0.0025 cm foil) was

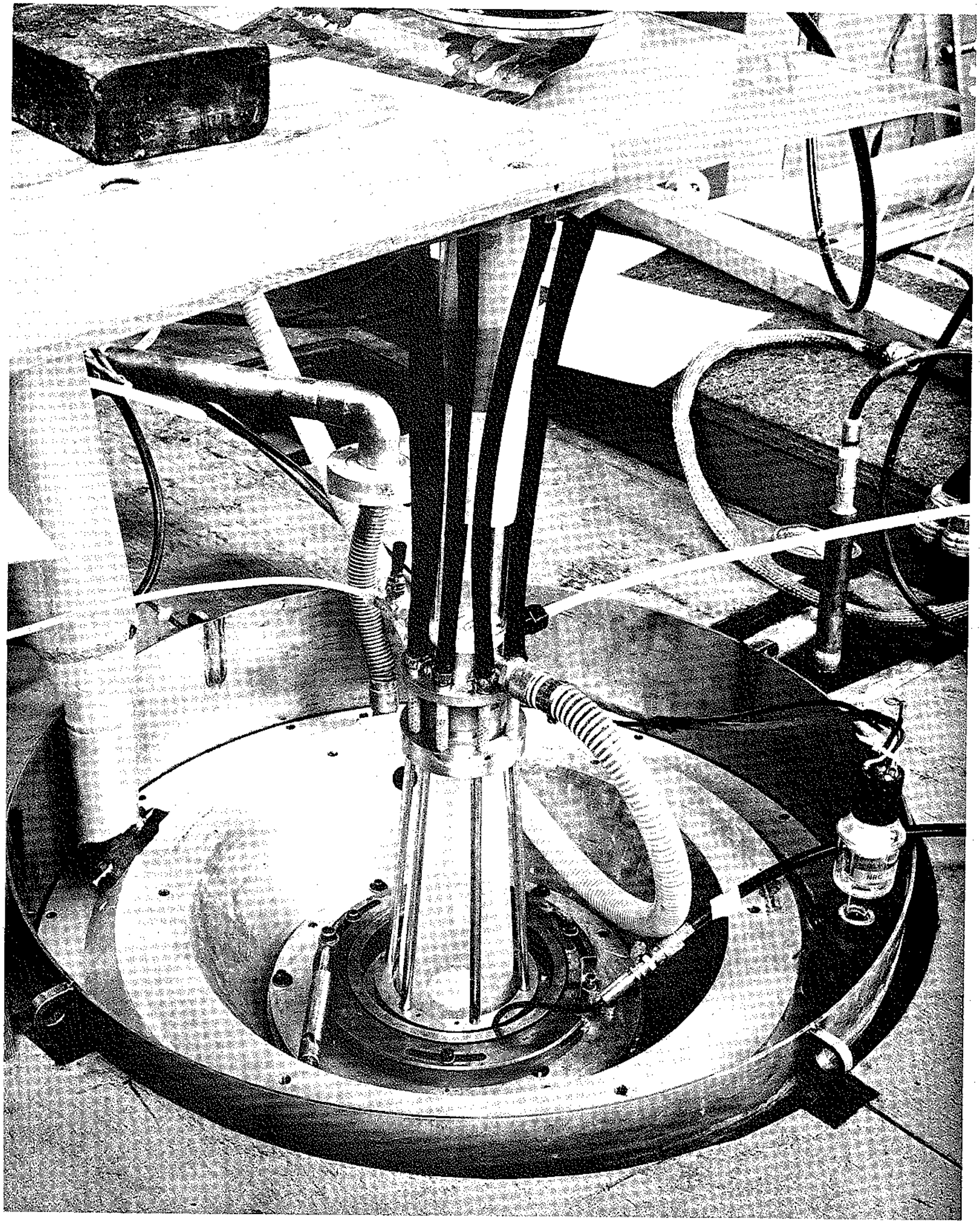

Figure 3.26 Tapered pinch on PIML. Note central anode foil at base pinch.

A325

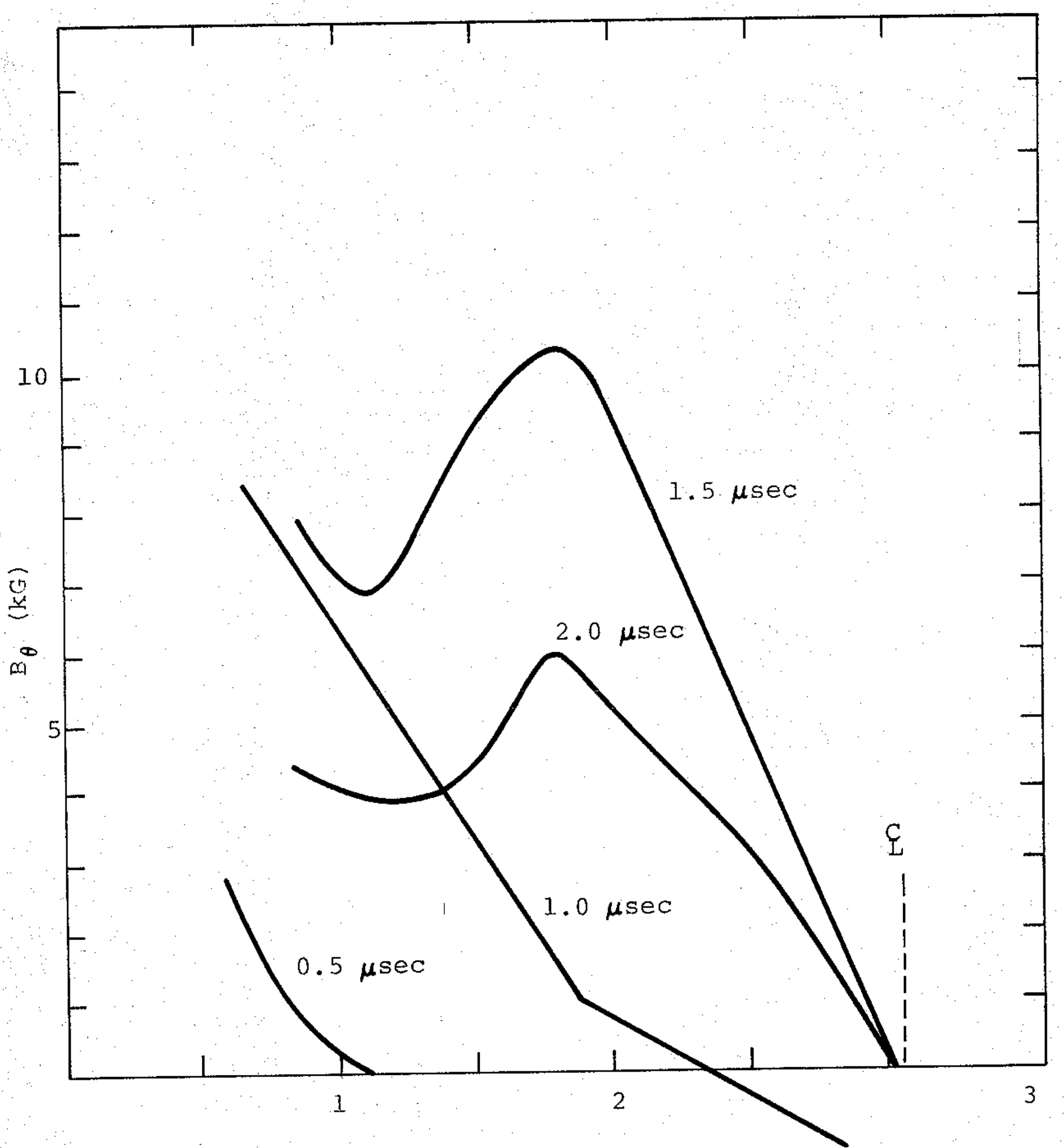

Figure 3.27 Magnetic field profiles 3 centimeters from top of pinch.

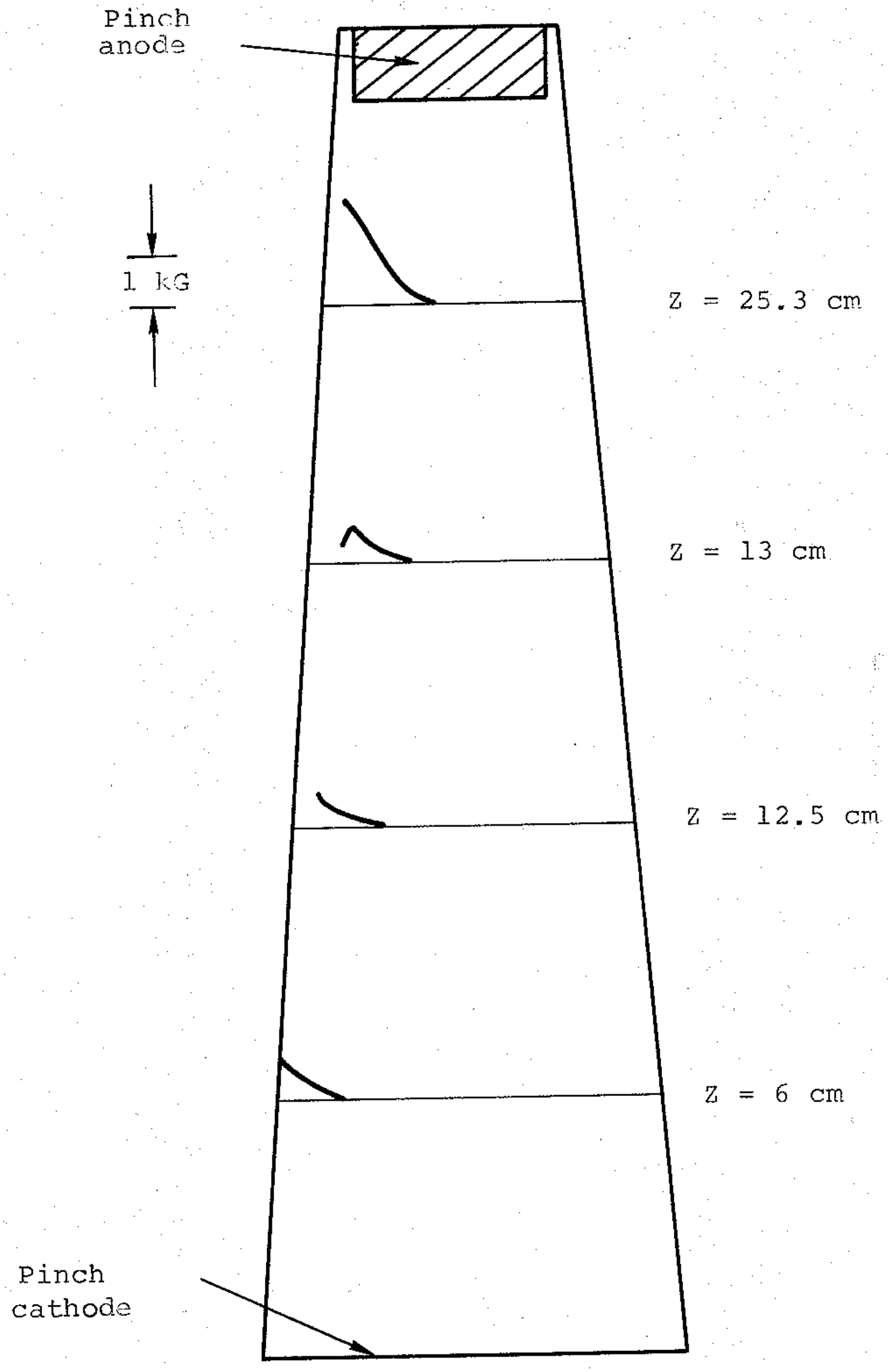

Figure 3.28 Cross section of pinch showing magnetic field structure at four axial locations. Current sheet is sharper nearer top.

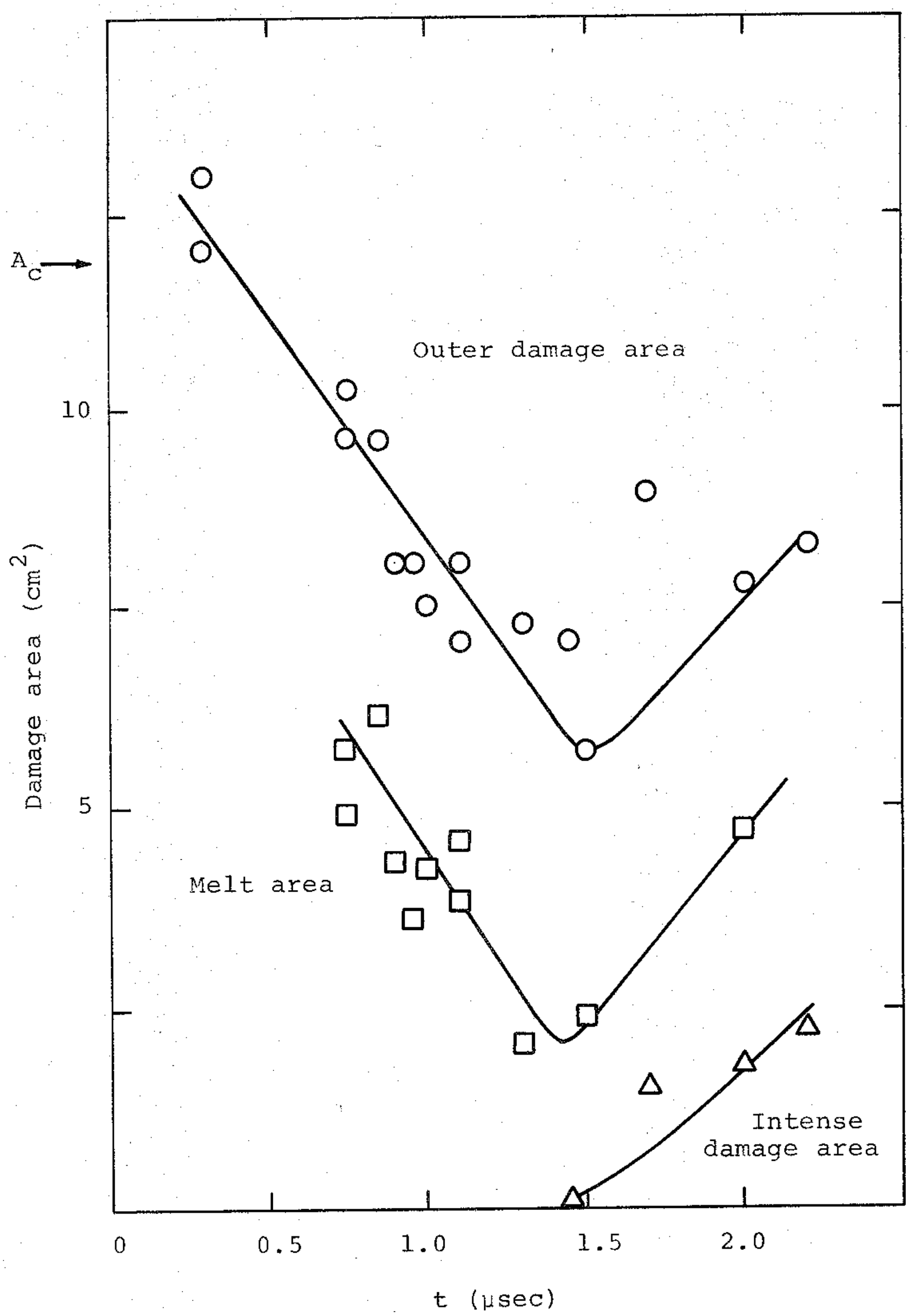

Figure 3.29 Damage to pinch anode versus beam injection time. A_c is the beam-generating cathode area.

stretched over a supporting assembly beneath the pinch base and filled the 5-cm aperture in the base plate. The injected beams had peak currents of 90 to 160 kA, peak voltage of 310 to 460 kV, and a total energy of 1 to 2 kJ. Magnetic probe profiles (Figure 3.27) near the top of the pinch indicated that the pinch should shut off beam transport at ~ 1.5 μsec, when the collapse was ending.

Damage patterns on the face of the 1 mm thick aluminum pinch anode indicated the radial extent of the transported beam as well as the dose level. X-rays generated by the beam in the anode were monitored with TLDs and a scintillator photodiode located behind the anode.

The PIML beams were injected into the collapsing tapered discharge at 13 times up to 2.1 μsec, when anode foil motion shorted the diode. Results of the analysis of pinch anode damage are shown in Figure 3.29. The area damaged by the beams diminishes until ~ 1.5 μsec, in agreement with expectations. However, after 1.5 μsec, the damage area increases. For injection times greater than 0.7 μsec there was an area within the damage where the dose was sufficient to cause melting of the aluminum. This area also decreases until 1.5 μsec, then increases. The most intense dose levels splattered the melted aluminum; this dose level is not reached until 1.5 μsec and the corresponding area increases in the same manner as the other areas.

Analysis of the efficiency of beam transport for the 16 shots shown in Figure 3.30 is complicated by the variation of beam parameters from shot to shot. Efficiency was roughly 50 percent for all shots. Five shots of $\nu/\gamma = 5$ beams were chosen

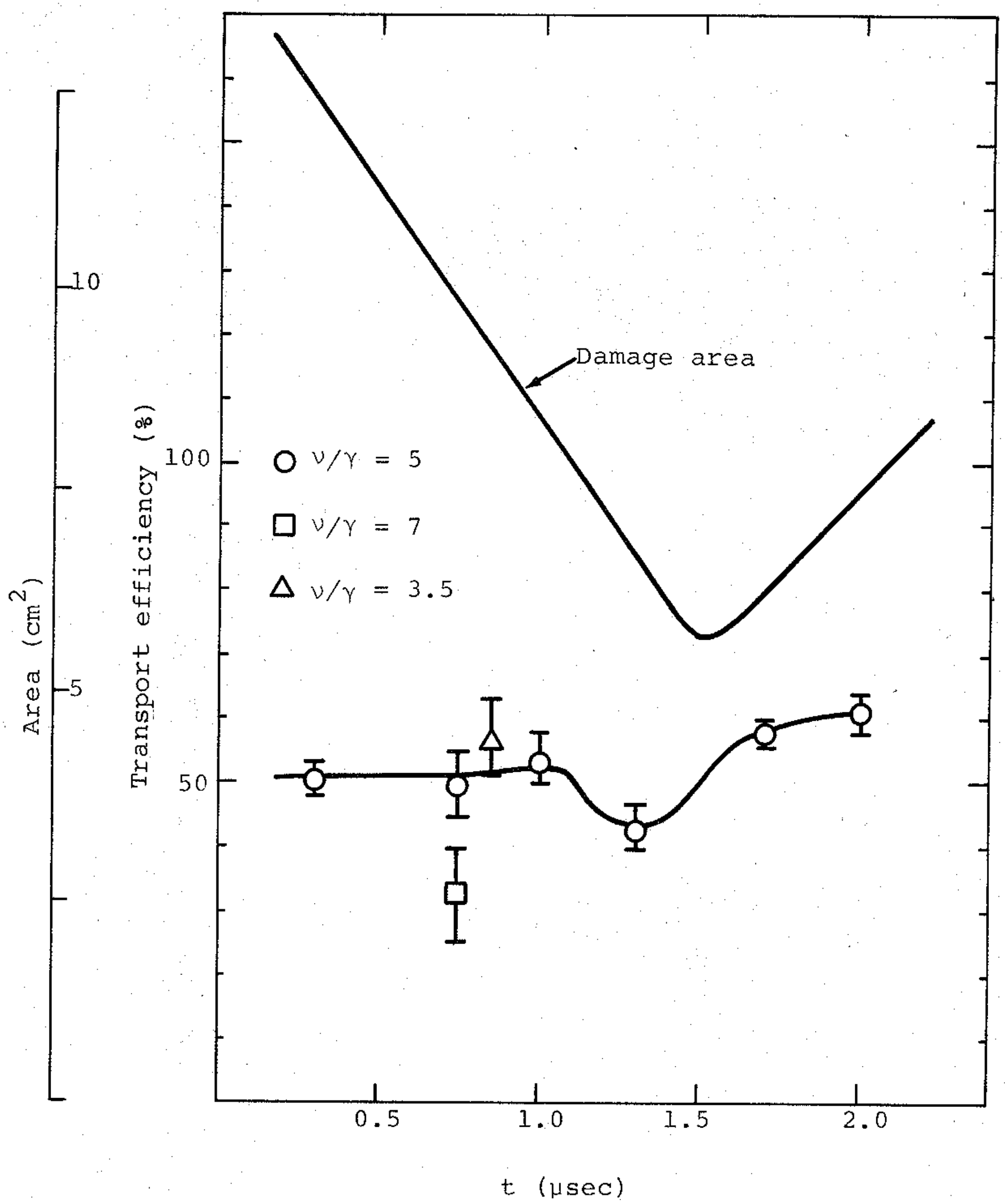

Figure 3.30 Efficiency of beam transport versus injection time. Outer damage area is also shown.

for their reproducibility and their transport efficiency analyzed using TLD readings and photodiode trace peak and area. Figure 3.30 displays these efficiencies as well as those of $\nu/\gamma = 3.5$ and 7 beams. Transport efficiency for $\nu/\gamma = 5$ beams is constant until 1 μsec, then drops slightly and rises. These variations are small and are almost washed out by the experimental uncertainties. Transport efficiency for the higher ν/γ beam is lower, which is consistent with the greater transverse energy that should be present. Likewise the lower ν/γ beam transports with slightly improved efficiency.

The low efficiency of transport is due to the operation of two loss mechanisms. The first, already mentioned, is the reflection of beam electrons from the narrow end of the pinch discharge. This effect should cause a lowering of efficiency as the beam is injected into later stages of the collapsing discharge. At early times, loss is due to escape of beam electrons to the walls. The weak magnetic fields at the base of the pinch (from the diffuse current structure mentioned earlier) are insufficient to turn back beam electrons. Operation of these two loss mechanisms cause the low efficiency of transport.

Since the transport efficiency changes little with injection time while the damage area declines, the average current density of the transported beams increases (Figure 3.31). However, even with this increase the average current density never exceeds that at injection.

These results show the essential correctness of the proposed model of beam compression in the tapered pinch until 1.5 μsec. However, beam transport does not cut off or even decline after that time. This indicates the occurrence of new phenomena, not included in the above analysis.

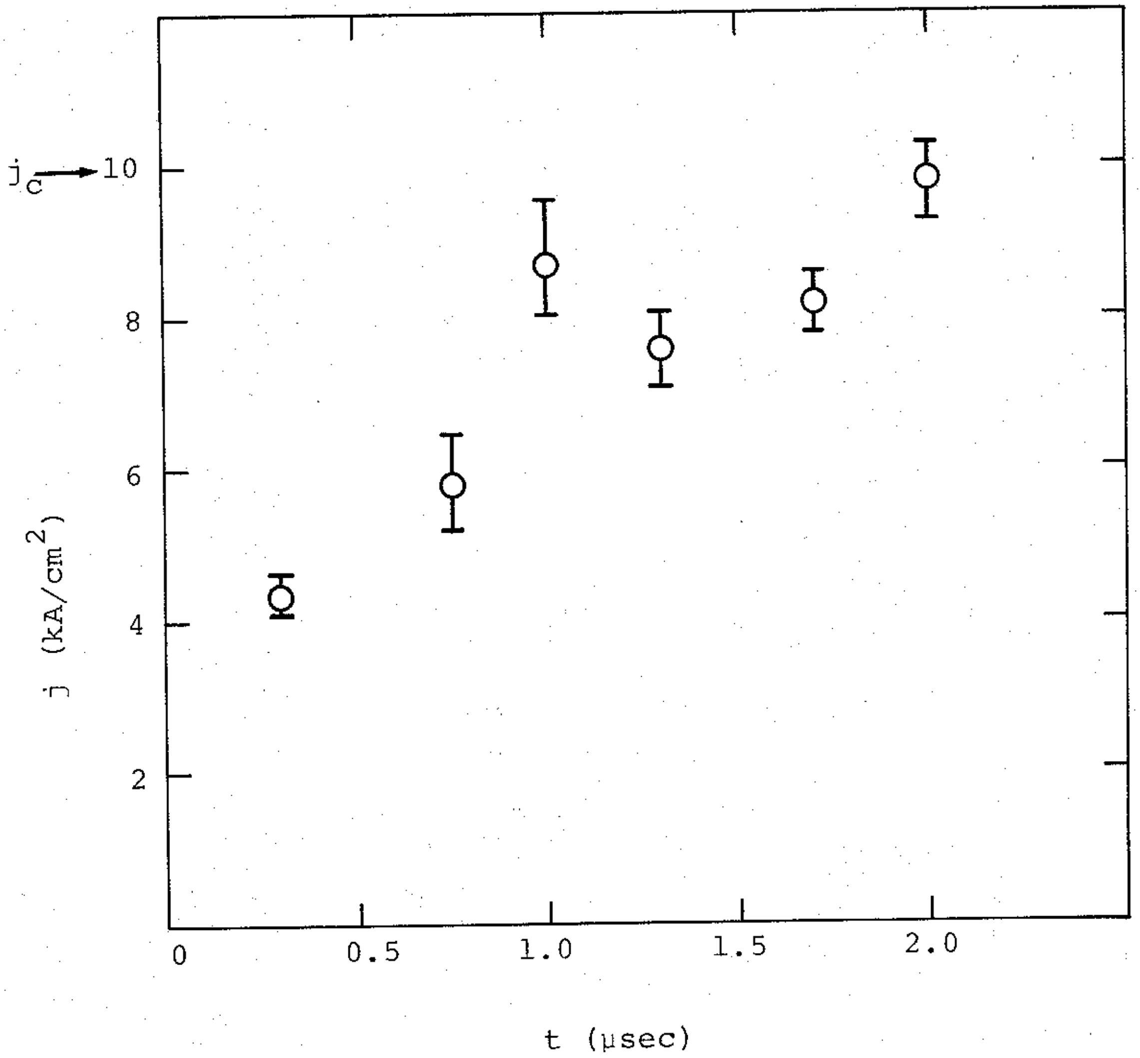

Figure 3.31 Transported beam mean current density versus injection time. j_c is the mean current density at the cathode.

It is clear from the field profiles near the top of the pinch that beam electrons would be reflected if they followed single-particle orbits. At 1.5 μsec, the field profile 3 cm from the pinch anode is that of a uniform current (Figure 3.27). The damage radius at the anode for this injection time is 1.35 cm and B_θ at that radius is ~ 10 kG. Therefore, the enclosed pinch current is $I = 5\ Br = 67$ kA. The Alfven limiting current for this beam is $I_A = 17{,}000\ \beta\gamma = 24$ kA. This means that the beam could not propagate through the field configuration because the curvature of the beam electron orbits as a function of r is great enough to turn them around. Yet the beam is observed to transport with fair efficiency even after the critical pinch field has been reached. Guillory (Reference 3.9) has suggested that E x B drift near a region of charge buildup at the collapsed portion of the pinch allows electrons to penetrate. The charge buildup is assumed to result from reduced cross-field plasma conductivity and reflection of beam electrons $(\nabla \cdot J)$ in the high field region of the pinch, to the point where charge neutralization is no longer complete. A qualitative picture of electron trajectories in the region is given in Figure 3.32. The beam flows around the charge and this produces enlargement of the damage pattern. When the E x B drift motion around the charge cloud is slow compared with the axial velocity of the unimpeded beam, this would be observed as a delay of some beam electrons, i.e., as dispersion in the pulse shape of the X-rays at the downstream target. For some injection times, such dispersion is observed, as discussed below.

Another possible explanation is that the single particle orbit model may not be a valid description of electron motion and that the pinch motion may be important. In cases where the

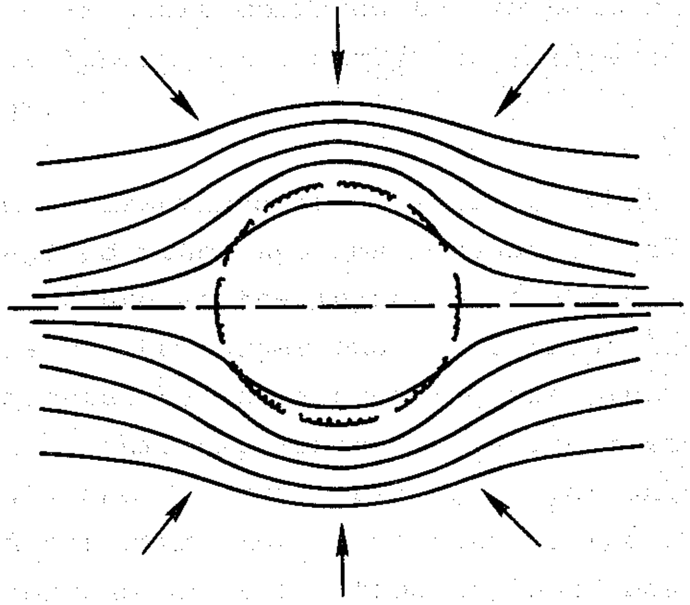

Figure 3.32 Flow of electron beam around charge clump. Arrows indicate electric field.

inward pinch velocity is small, the pinch might not be able to contain the high transverse pressure beam.

Figure 3.33 displays the X-ray pulses from the pinch anode for the $\nu/\gamma = 5$ shots. The leading edge of the X-ray pulse is relatively unaltered by change in injection time, but the X-ray intensity 15 nsec into the pulse is reduced and the peak intensity is increased at 0.75, 1.0 and 1.3 μsec. This distortion could be interpreted as a delay in transport of the portion of the beam at ~ 15 nsec caused by the charge cloud model described above. The pulse shape at 1.7 and 2.0 μsec injection times returns to the normal shape, which could be because the charge

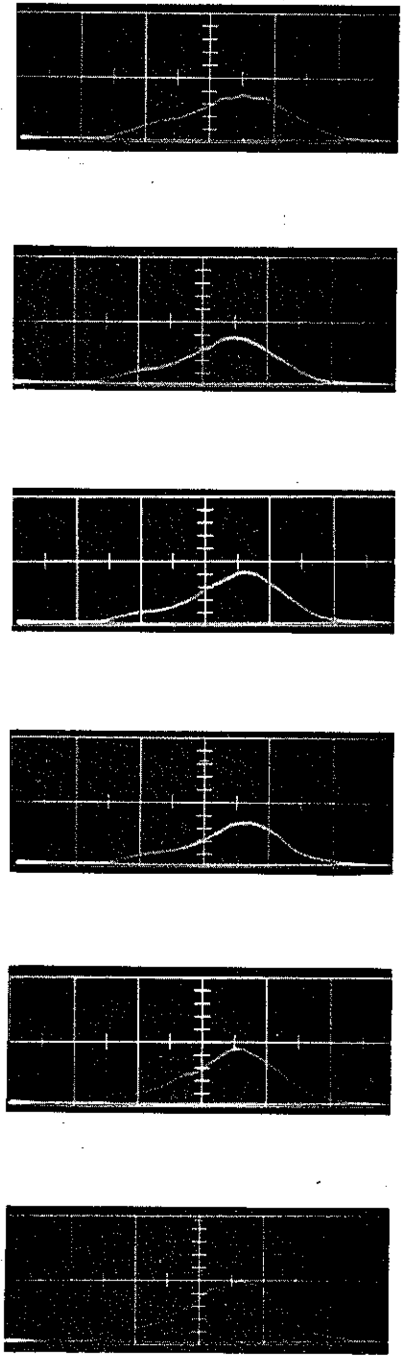

a. 0.3 μsec

b. 0.75 μsec

c. 1.0 μsec

d. 1.3 μsec

e. 1.7 μsec

f. 2.0 μsec

Figure 3.33 X-ray signal from pinch anode for six injection times. Sweep speed 20 nsec/cm.

is greater for these injection times so that the transit time around the charge is short compared to the beam pulse. This interpretation is tentative; clearly the interaction is an area for further study.

The experiment described above suggests that "hot" beams are lost from tapered pinch systems because of (a) diffuse current sheet structure at the injection end and (b) reflection of beam electrons at the target end. The first loss can probably be eliminated by (a) increasing the pinch current above the 200 kA level of this experiment, thus increasing the magnetic field strength and (b) using smaller taper angles, thereby making the field structure more like that of the straight pinch. The second loss mechanism, reflection of "hot" beam electrons, can only be overcome by injecting "cool" beams. For example a large diameter annular cathode (chosen to give $I < 8500\ \beta\gamma\ r/d$ to prevent pinch) or an array of magnetically isolated cathodes could be used for injection into the base of a tapered pinch. This combination-compression-transport system would eliminate the problem of an external magnetic field fringing into the sample volume, which can occur in B_z systems.

3.6 CONCLUSIONS

It has been shown that the losses attendant with beam propagation in neutral gases and preionized field-free gases can be avoided by transporting beams in Z-pinches. Efficient transport has been demonstrated for beams with currents from 120 kA to 375 kA at voltages of 500 keV to 750 keV, containing total energies from 3 kJ to 17 kJ. The injected mean current densities were as high as 8 $\mathrm{kA/cm^2}$; peak current density was 100 $\mathrm{kA/cm^2}$. The beams were transported down pinches from 45 cm to 60 cm in length. A considerable degree of fluence control was demonstrated by varying the time of beam injection into the pinch. Two 8 kJ beams were efficiently combined and well mixed. A tapered pinch was employed for beam compression, but losses due to pinch current sheet structure and reflection of beam electrons prevented any increase in current density upon transport.

The physics of beam transport in the linear pinch has been successfully modeled as single-particle motion of beam electrons in the magnetic field of the pinch. Two transport modes have been predicted and strong evidence for their existence has been obtained. The successful combination of two beams provides additional support for the model which predicted their mixing. Beam transport in the tapered pinch also agrees with prediction but only up to a point. The failure of transport to cut off at late stages in the discharge does not agree with single-particle modeling. Further investigation of this phenomenon may provide insight into other processes occurring in Z-pinch transport.

Scaling of Pinch Systems. The scaling of Z-pinch transport systems for very high current beams requires:

a. A plasma medium of sufficiently high conductivity for plasma current to neutralize the beam current. This is equivalent to requiring that the magnetic diffusion time of the plasma be long compared to the beam pulse length ($\tau_D = 4\pi\sigma a^2 >> \tau_B$ where σ = plasma conductivity and a = beam radius).

b. Azimuthal magnetic fields strong enough to turn back beam electrons before they reach the discharge tube wall. For electron energies less than a million electron volts, this means fields of several kilogauss for tube diameters a few centimeters greater than the cathode diameter.

c. Beam injection into a region of favorable electron drift motion. Transport can occur by electron motion along Alfven type trajectories or by ∇B drift motion (Regions I or III in Figure 3.15).

When these three conditions are met, the injected beam will propagate to the end of the pinch with little or no loss, expanding to fill the current sheet if the injection area was inside the sheet. The feasibility of transporting beams over distances greater than a meter is determined by the voltage required for development of a well-defined current sheet. From the experiments performed in this study, it appears that at least a 5 kV/ft potential gradient is required for production of sharp current sheets. Therefore long-distance transport requires pinch voltages substantially higher than those used in these experiments. However, high-energy high-voltage capacitors are available and the construction and operation of pinches at the 100 kV level is feasible. An alternative to high voltages is the staging of pinches with a foil interface between the discharge tubes to allow beam transport. Each stage would then have to "float" relative to ground.

The use of linear pinches with Marx generators in this program has shown stringent requirements on the triggering ability of both systems. Since both the Marx and the pinch bank operate on microsecond time scales, jitter in either system will seriously affect beam transport efficiency and beam fluence at the pinch anode. The combined Snark Marx-pinch bank system was found to exhibit ± 500 nsec jitter during transport and beam combination experiments. This jitter frequently resulted in failure to obtain the desired injection time and lowered the useful shot rate to about one-half that of B_z transport experiments. Therefore low timing jitter must be considered a prerequisite for application of B_θ transport stages to any multiple-module system.

The replacement of the discharge tube in the Z-pinch constitutes an operational disadvantage of the system. Although recycling of the Pyrex glass by cleaning reduces the expense somewhat, the procedure has limited usefulness. After two or three cleanings the surface properties of the glass are modified and the tube must be discarded. Taking account of both the initial cost of the glass and the labor to clean it, each pinch shot costs approximately $25.00. While this cost is not prohibitive, it must be considered when comparing to neutral gas and B_z transport systems, which do not require such replacement expenses.

In conclusion, the scaling of Z-pinch systems to multi-stage transport combination and compression appears technically feasible. The time phasing and operational features of the system would make it a complex one; however, these complications may be justifiable depending on the status of other transport techniques.

REFERENCES

3.1 G. Yonas, P. Spence, B. Ecker, and J. Rander, "Dynamic Effects of High ν/γ Beam Plasma Interactions," DASA 2426, August 1969.

3.2 P. W. Spence, G. Yonas, and D. K. Dean, "Shock Generation in S-200 Beryllium Using a Pulsed Electron Beam," SCL-DC-69-152, Sandia Laboratories, Livermore, California, January 1970.

3.3 D. Pellinen, Rev. Sci. Instr. 42, 667 (1971).

3.4 R. Kouzes, L. Levine and I. Vitkovitsky, Bull. Am. Phys. Soc. 14, 1012 (1969).

3.5 T. G. Roberts and W. H. Bennett, Plasma Phys. 10, 381 (1968).

3.6 H. Alfven, Phys. Rev. 55, 425 (1939).

3.7 D. A. Hammer and N. Rostoker, Phys. Fluids 13, 1831 (1970).

3.8 G. Benford, D. Book and R. Sudan, Phys. Fluids 13, 2621 (1970).

3.9 J. Guillory, private communication.

SECTION 4

INVESTIGATION OF BEAM TRANSPORT IN AXIAL (B_z) MAGNETIC FIELDS

by C. Stallings

4.1 INTRODUCTION

B_z systems are defined as those experiments with an externally applied magnetic field which is parallel to the desired beam transport direction. The external magnetic field is usually applied by a solenoid. The primary advantage of this type of system is that the magnetic field and the plasma parameters can be controlled independently.

When intense electron beams propagate in a neutral gas with no externally applied fields they have an electrostatic force tending to blow the beam apart, a self-magnetic field that exerts a compressive force on the beam and, while the beam current is rising, there is an inductive electric field that degrades the energy of the electrons. In practice, the beam ionizes the background gas in a few nanoseconds and propagates in a plasma. Expulsion of plasma electrons rapidly charge-neutralizes the beam so the electrostatic force disappears. However, the inductive electric field and the self-magnetic field are coupled. When the plasma conductivity is sufficient to eliminate the inductive electric field, there cannot be a self-magnetic field because the net current is zero. For high ν/γ beams, the transverse velocity of the electrons will then cause the beam to blow up (Reference 4.1). However, when a B_z field is applied, the electrons are constrained to follow the magnetic field. This allows the possibility of efficient transport of high ν/γ beams over a few meters.

4.2 DIODES

When a B_z field is applied to a diode, the dynamics are changed both quantitatively and qualitatively (References 4.2 and 4.3). Experiments were carried out to study the effect of this applied, longitudinal magnetic field in the diode. Figure 4.1 is a comparison of X-ray pinhole photographs of a 3-inch-diameter rod cathode with three different field strengths. Two observations can be made: first, the cathode structure is discernible in even the lowest external field; second, the current density appears higher near the cathode center at all field levels studied. Because of the first observation, the second cannot be explained by the assumption of beam self-pinch, since the latter characteristically does not preserve cathode surface structure. To explain the observed effects, we propose an explanation of diode behavior when B_z is of the same order as $(B_\theta)^{max}$. The magnetic field in the diode is the sum of the applied uniform axial field and the azimuthal self-field, which increases with radius. The net field, therefore, is helical, and the pitch decreases as radius increases. Assuming that the electrons in some sense follow the field lines, the electron axial velocity is a decreasing function of radius, and the time spent in the diode by an electron is an increasing function of radius. The space-charge-limited current density would therefore decrease with increasing radius for a given anode-cathode voltage. To test this hypothesis, a hollow-core, multi-rod cathode with a 3-inch outer-diameter and a 1-inch hollow-core-diameter was tested. If the beam were pinching due to its own self-field, the highest current density would be at the central axis; but if the above arguments apply, then the current density would be highest directly over the innermost emitters and would be zero over the 1-inch-diameter hollow core. The latter type of behavior is evident in Figure 4.2, an X-ray pinhole photograph

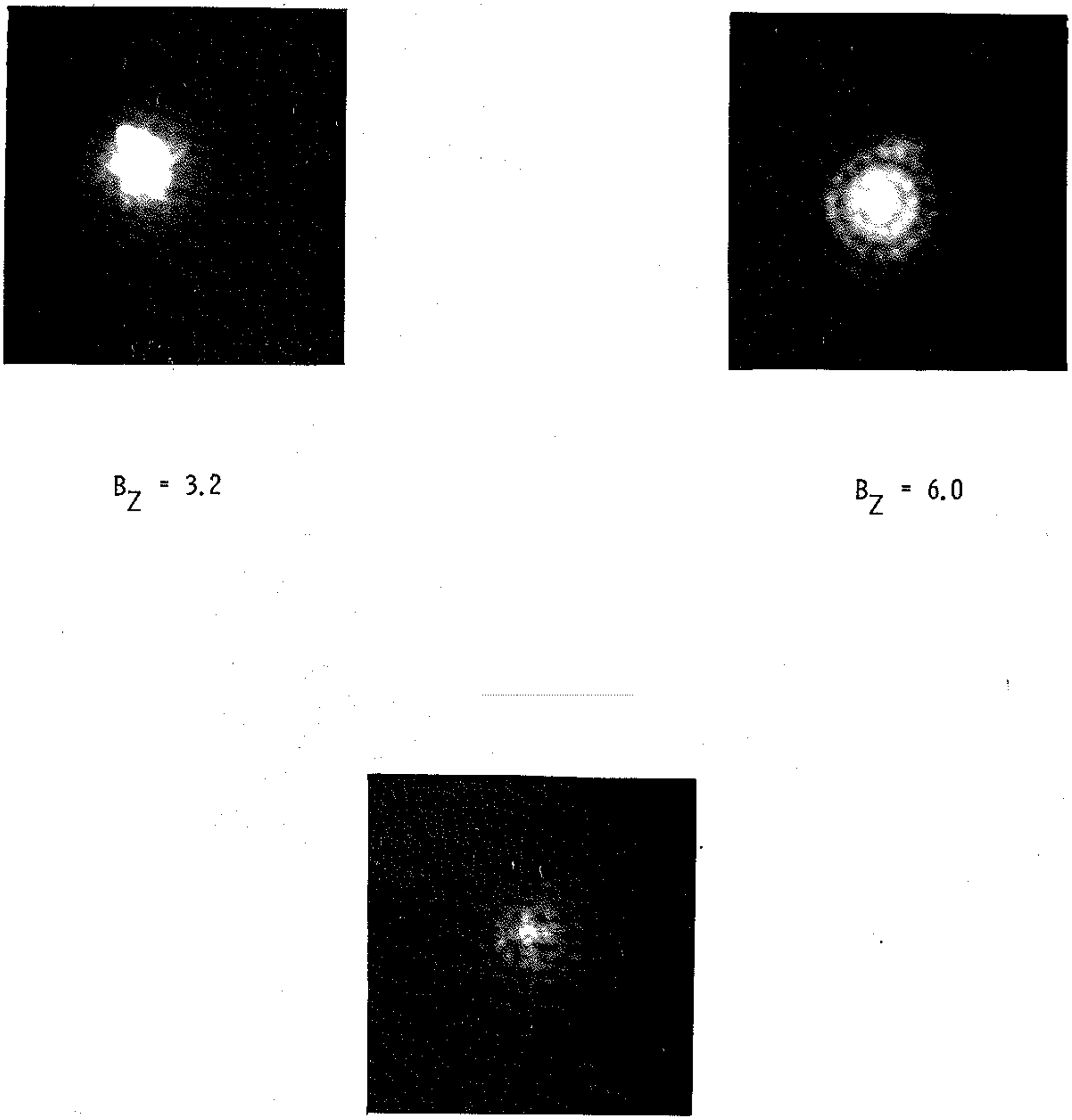

B_Z = 3.2

B_Z = 6.0

B_Z = 7.9

Figure 4.1 X-ray pinhole photographs of the anode using a 3-inch-diameter rod cathode.

A212

taken using this hollow cathode. The self-field of the beam at the edge of the cathode was 10 kG and the longitudinal magnetic field was 11.8 kG. This supports the model presented above.

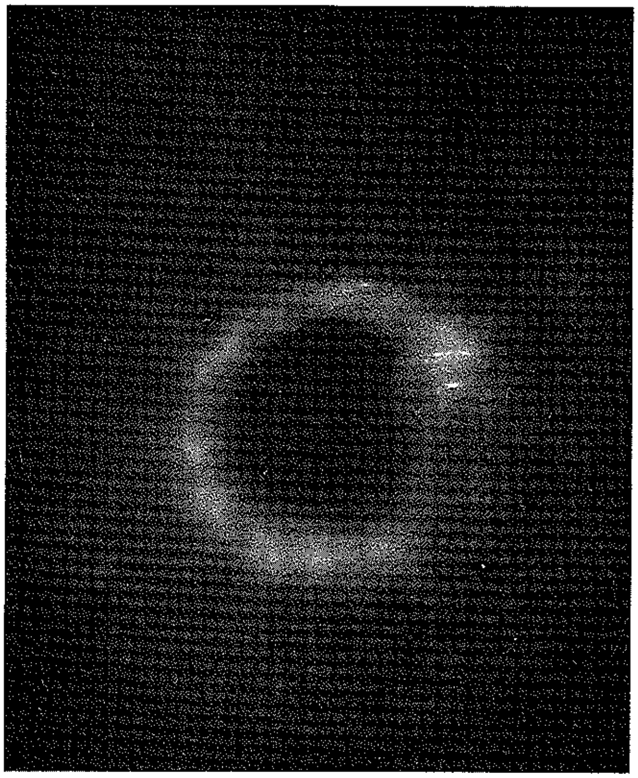

Figure 4.2 X-ray pinhole photograph of the anode using a hollow cathode three inches in diameter with a 1-inch-diameter hole in the center.

Since the current density is highest at the innermost cathode emitters, the diode impedance should not be sensitively dependent upon cathode area (when the latter is above a certain critical value). Figure 4.3 shows impedance as a function of time for a 3-inch-diameter cathode and 3-inch by 1-inch rectangular cathode. Even though their areas are different by a factor of 2.3, their impedances are approximately equal. In

A344

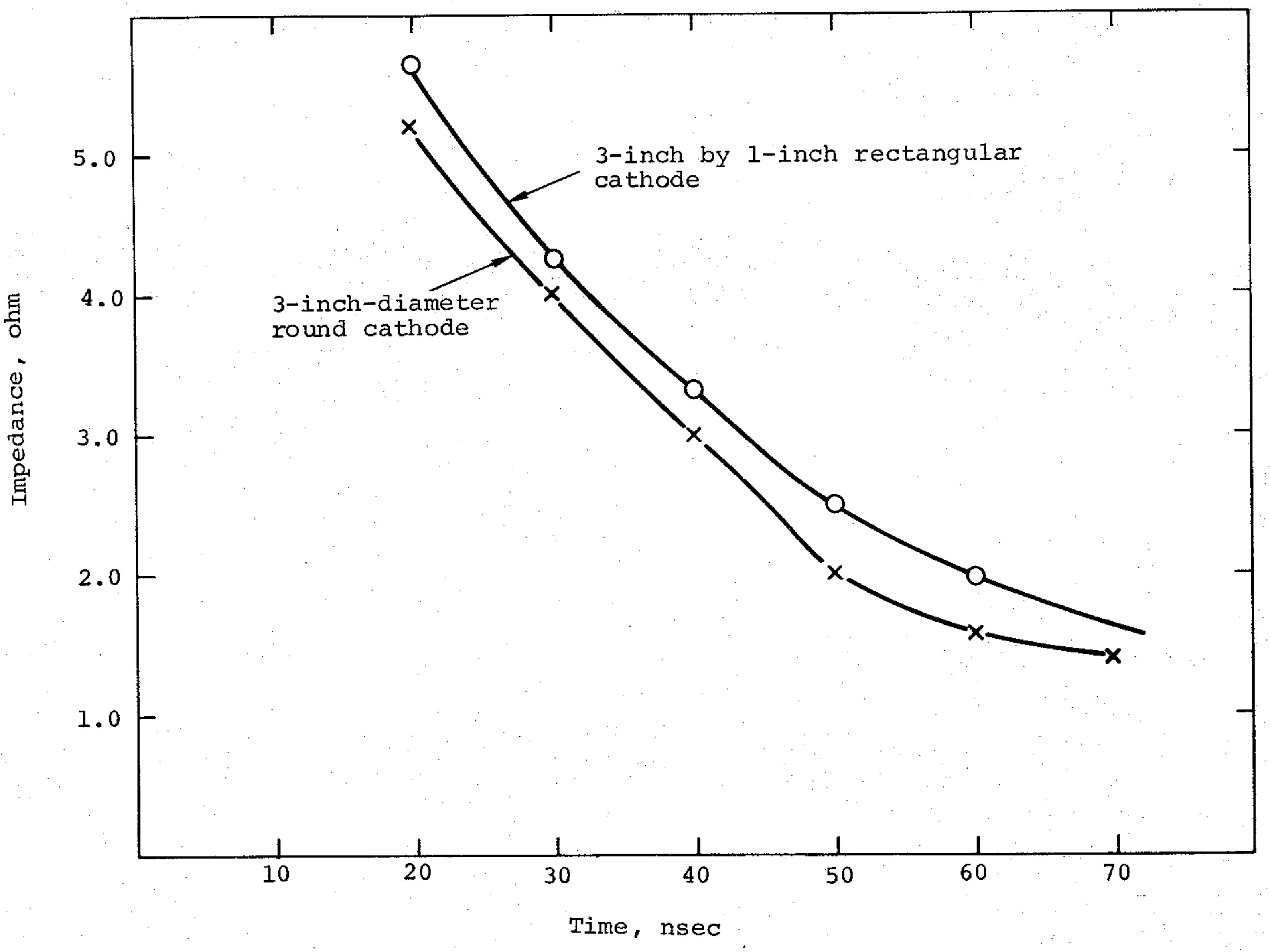

Figure 4.3 Impedance as a function of time for two cathodes.

the limit $B_z \gg B_\theta$, the field is approximately axial over the entire cathode and emission is approximately uniform, so that the impedance is sensitive to the cathode area.

When the B_z system was used on Snark (Reference 4.4), the most striking result was that the diode impedance, on the average, held up longer before shorting. However, as the current density increased, a larger magnetic field was needed to make the diode hold up for the duration of the pulse. These data are summarized in Figure 4.4. The impedances were taken when dI/dt = 0. The parapotential and Langmuir-Childs impedances are given for reference.

4.3 LINEAR TRANSPORT EXPERIMENTS

The simplest B_z transport experiments have a uniform B_z field throughout the diode and transport regions (Reference 4.5). A diagram of the apparatus used for these uniform B_z experiments is shown in Figure 4.5. The cathode and anode stalks were made from stainless steel rods buried in epoxy. This construction made the diode region transparent to pulsed magnetic fields. The main coil was 1.1 meter long and 5 inches in diameter. The coil was driven by a 252-μF, 20-kV capacitor bank. During the first half-cycle the magnetic field was

$$B_z \text{ (Gauss)} = (148 \times 10^{-2})\ V_o \sin\left(\frac{2\pi t}{8 \times 10^{-4}\ \text{sec}}\right)$$

where V_o is the charging voltage on the bank. Figure 4.6 is a photograph of this system on the Snark machine.

A small amount of preionization could be added in the solenoid by placing small resonant capacitors in parallel with

Cathode Area	60 cm^2	20 cm^2	11 cm^2
A-K	3.0 mm	2.75 mm	4.0 mm
Parapotential impedance	1.8 Ω	2.5 Ω	4.8 Ω
Langmuir-Childs impedance	1.1 Ω	2.1 Ω	7.8 Ω
Typical impedance	5.6 kg 1.9 Ω 8.9 kg 1.3 Ω 14.8 kg 1.3 Ω	8.9 kg 3.1 Ω 14.8 kg 1.3 Ω	7.5 kg 2.5 Ω
Typical shorting time	5.6 kg 70 nsec 8.9 kg 118 nsec 14.8 kg 118 nsec	8.9 kg 60 nsec 14.8 kg 92 nsec	7.5 kg 80 nsec

Figure 4.4 Impedance summary.

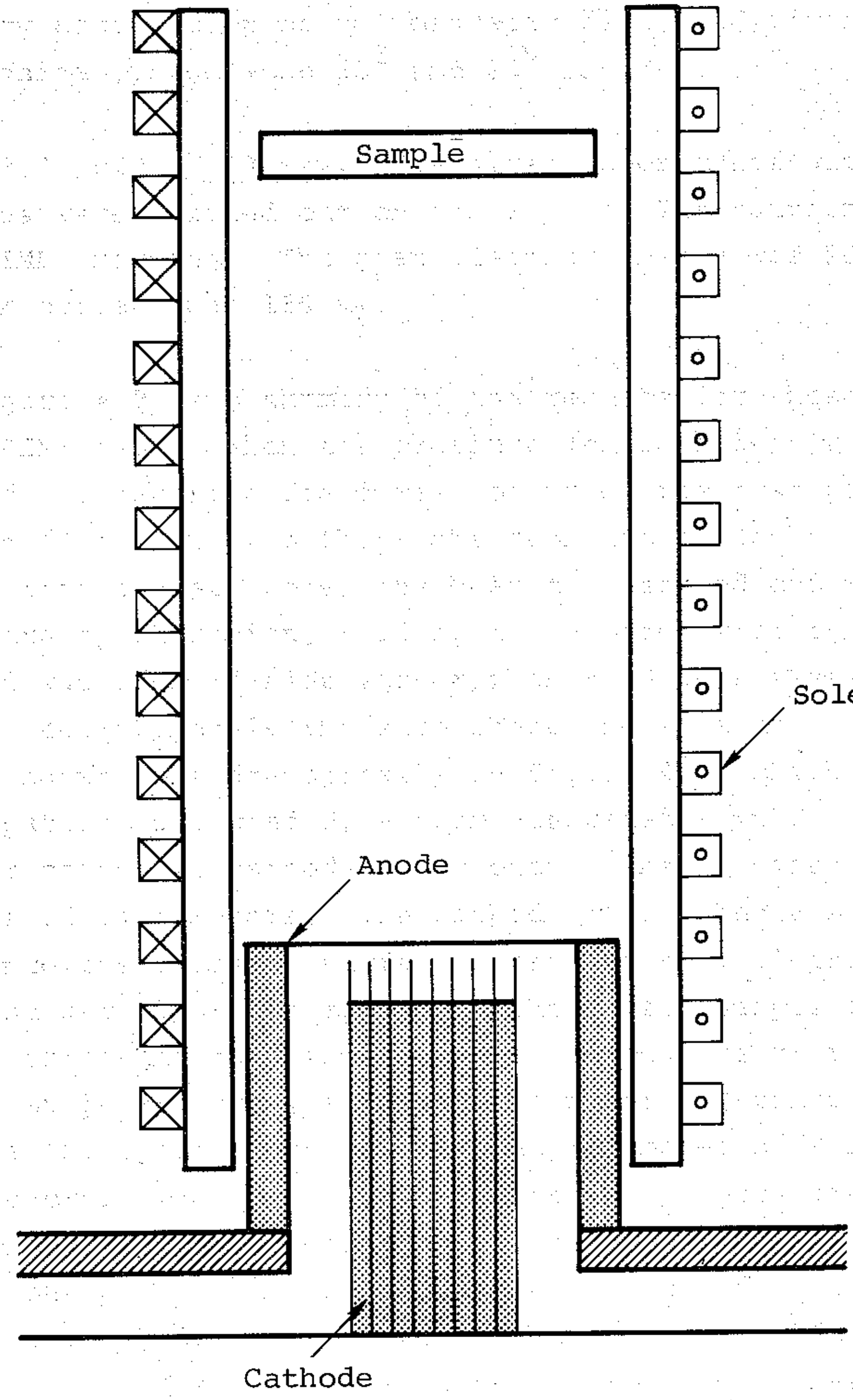

Figure 4.5 Diagram of the solenoid transport system.

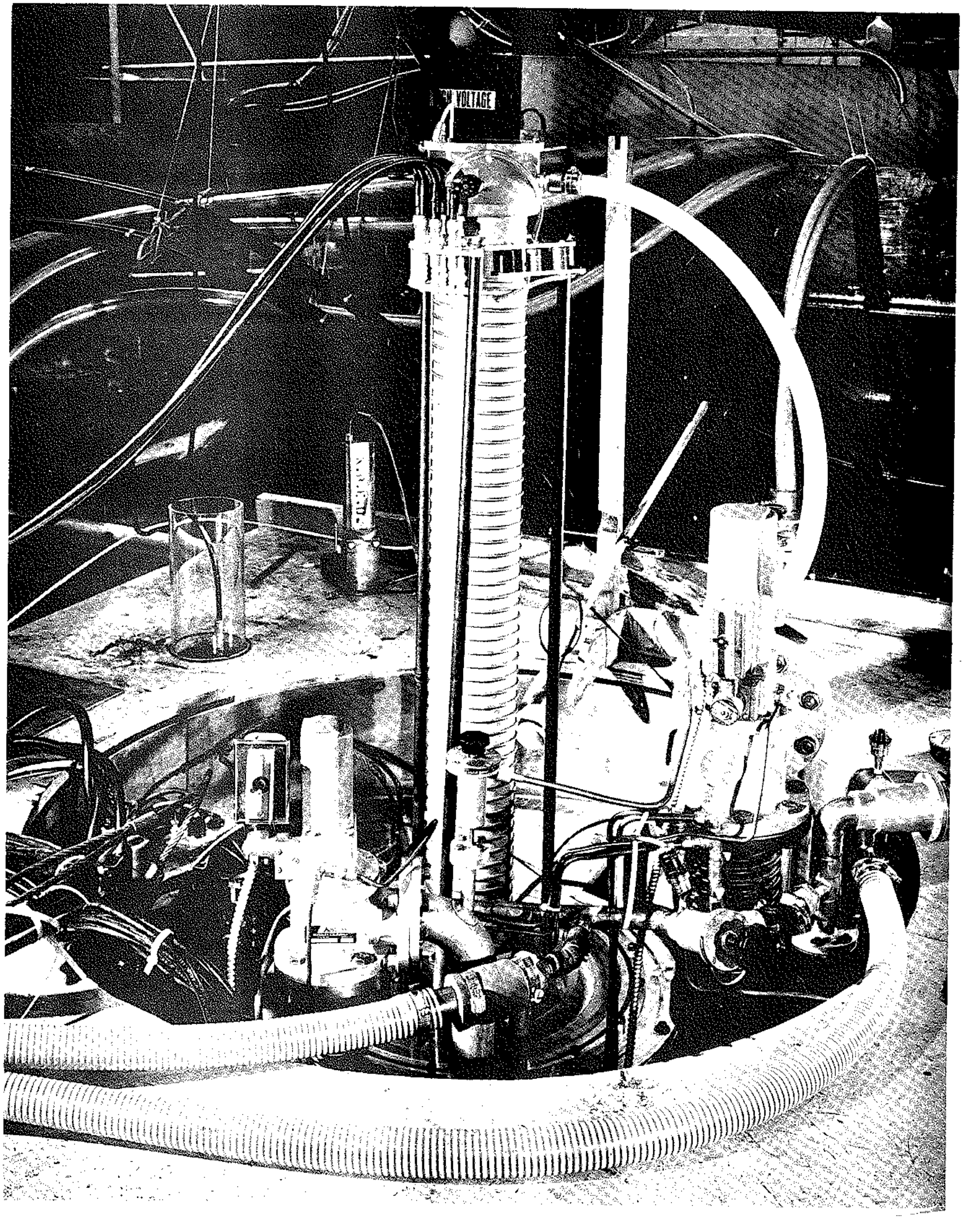

Figure 4.6 Solenoid on Snark measuring 1.1 meters.

the solenoid (Reference 4.6). This superimposes a small high-frequency oscillation on the magnetic field and gives a low level of preionization between 10^8 and 10^9 ions/cc.

4.3.1 PIML, 300 keV. The first experiments with this apparatus were carried out on the Physics International Mylar Line (PIML) machine. The mean electron energy was 200 keV and the peak current was 180 kA.

Figure 4.7 is a summary of the results for those experiments on the PIML beam. When the pressure in the solenoid was 600 millitorr and the magnetic field was not used, the transport efficiency was 42 ± 10 percent. Without the magnetic field, the diode region pinched into a small core; the beam then spread and was diffused in the transport region, filling the entire drift tube. When a B_z field was used (fields larger than 4 kG were tested) the beam retained approximately the same shape and size as the cathode. This is shown most dramatically in Figure 4.8, which pictures the damage pattern produced by a beam generated with a ~ 3-inch by 1-inch rectangular cathode. The beam transport distance for this shot was 25 centimeters. The cathode itself had a somewhat wavy edge since the emission surface consisted of 1/16-inch-diameter rods that were 1/4-inch apart. Although the sample damage area is more irregular than the cathode, the obvious reproduction of cathode shape and area, even after 1 meter of transport, indicated that the transport process can be approximated by a single-particle-orbit theory in which collective effects are ignored in the transport region. This is not to say that collective effects do not take place, but only that they are not the dominant processes in these experiments. Further evidence for a single-particle model was that local non-uniformities in beam fluence at the target were obviously present until the magnetic field was

TRANSPORT EFFICIENCY FOR 0.5 METER
(errors are ± 10%)

t = 150 μsec

Pressure, millitorr

B_z, kgauss	200	600	1000
4.1	65%	92%	93%
8.25	92%	98%	100%
13.7	69%	72%	75%

t = 240 Msec

Pressure, millitorr

B_z, kgauss	200	600	1000
8.4	100%	98%	93%
14.0		100%	

t refers to the time after the start of the applied B_z field.

Figure 4.7 Beam transport at 0.5 meters for the PIML electron beam. The peak current was 200 kA and the mean energy was 250 kV.

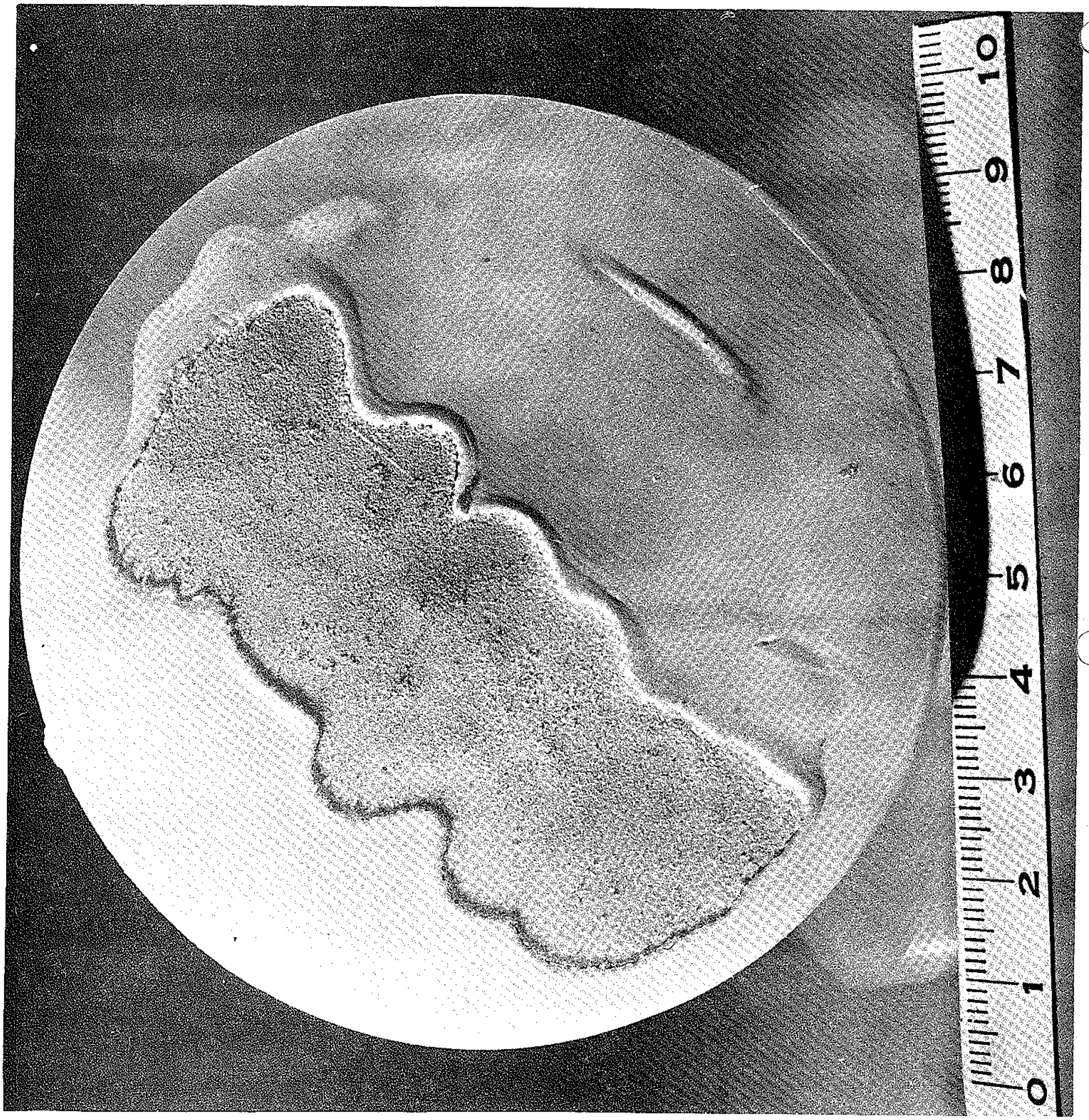

Figure 4.8 Damage crater in polyethylene produced by a beam generated with a 3-inch by 1-inch rectangular cathode. The beam transport distance was 25 centimeters.

A262

lowered enough for the electron gyro diameter to equal the cathode inter-rod distance. When this condition was satisfied, the sample appeared very uniform. When the beam transport distance was increased from 0.5 meter to 1 meter, the transport efficiency changed by less than 10 percent.

4.3.2 Snark, 800 keV. The majority of experiments were carried out on the Snark machine. These experiments used exactly the same equipment as the PIML experiments. The first experiments were used to test the length, pressure, and magnetic field scaling. The major improvements over the PIML experiments were higher current density and Faraday cup diagnostics, instead of the X-ray diagnostics used on PIML. This Faraday cup, like the diode, was transparent to a pulsed magnetic field.

These initial experiments were carried out with a mean energy of about 600 keV and a peak current of 550 kA. This was an average current density of 9 kA/cm^2. However, as was pointed out in Section 4.2, the diode emission was not uniform. The current density in the center 5 cm^2 was 36 kA/cm^2. In other words, at the anode plane, about one-third of the total current flowed in the center 5 cm^2. The transport efficiency could not be determined just by measuring the relative currents in the diode and at the Faraday cup at the end of the transport section. Pulse dispersion changed the shape of the current waveform as it propagated. Since there was a spectrum of angles, some electrons traveled down the solenoid faster than others and the peak current could be altered even though all of the energy was transported. Transport efficiency was measured by integrating the Faraday cup signal and determining the total charge transported. This was then compared to the total injected charge. Calorimetry and bremsstrahlung measurements were also used to determine efficiency, but a Faraday cup was normally used because it gave information on the current as a function of time as well as the transport efficiency. When the energy transport efficiency was compared to that of charge, the calorimeters gave an efficiency of 80 percent ± 20 percent, while the total Coulomb efficiency was 90 percent ± 10 percent. This difference was smaller than the experimental error, so it was impossible to say if the energy loss was due to a degrading of the energy of the electrons, or the loss of individual electrons from the beam channel.

Figure 4.9 is a plot of transport efficiency as a function of distance for two different pressures. Both conditions show a smooth decay of efficiency. This shows that the energy loss did not occur primarily near the anode, but instead was reasonably distributed throughout the transport region.

Transport efficiency was also scanned as a function of pressure to determine the optimum region. Figure 4.10 shows these data for a 3-inch-diameter cathode on the Snark machine with 550 kA peak current. The optimum pressure was about 1.0 torr, the same as the PIML experiments (Figure 4.7) with a lower current density. This optimum pressure is somewhat higher than the optimum pressure in neutral gas without any externally applied field.

The most surprising result of these initial experiments is shown in Figure 4.11, i.e., with no preionization there is an optimum value of the applied magnetic field. In addition, Figure 4.12 shows that the optimum B_z is rather insensitive to changes in the current density and that the optimum field is a rather modest 7 to 8 kgauss. For high current density, the transport efficiency drops off rapidly with increasing B_z (above 8 kgauss); while at the lower current density, the transport efficiency drops off much more slowly.

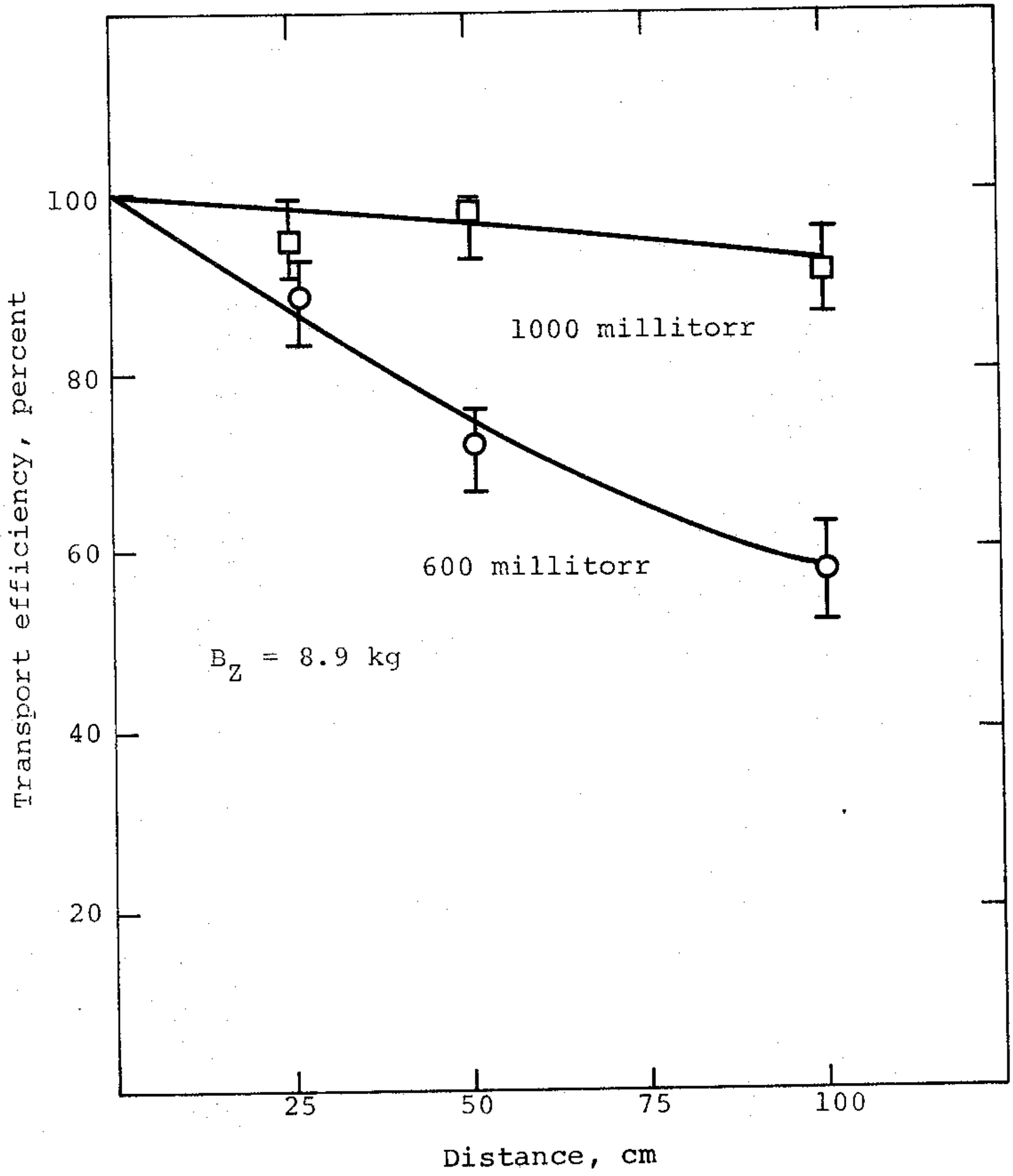

Figure 4.9 Charge transport efficiency as a function of distance.

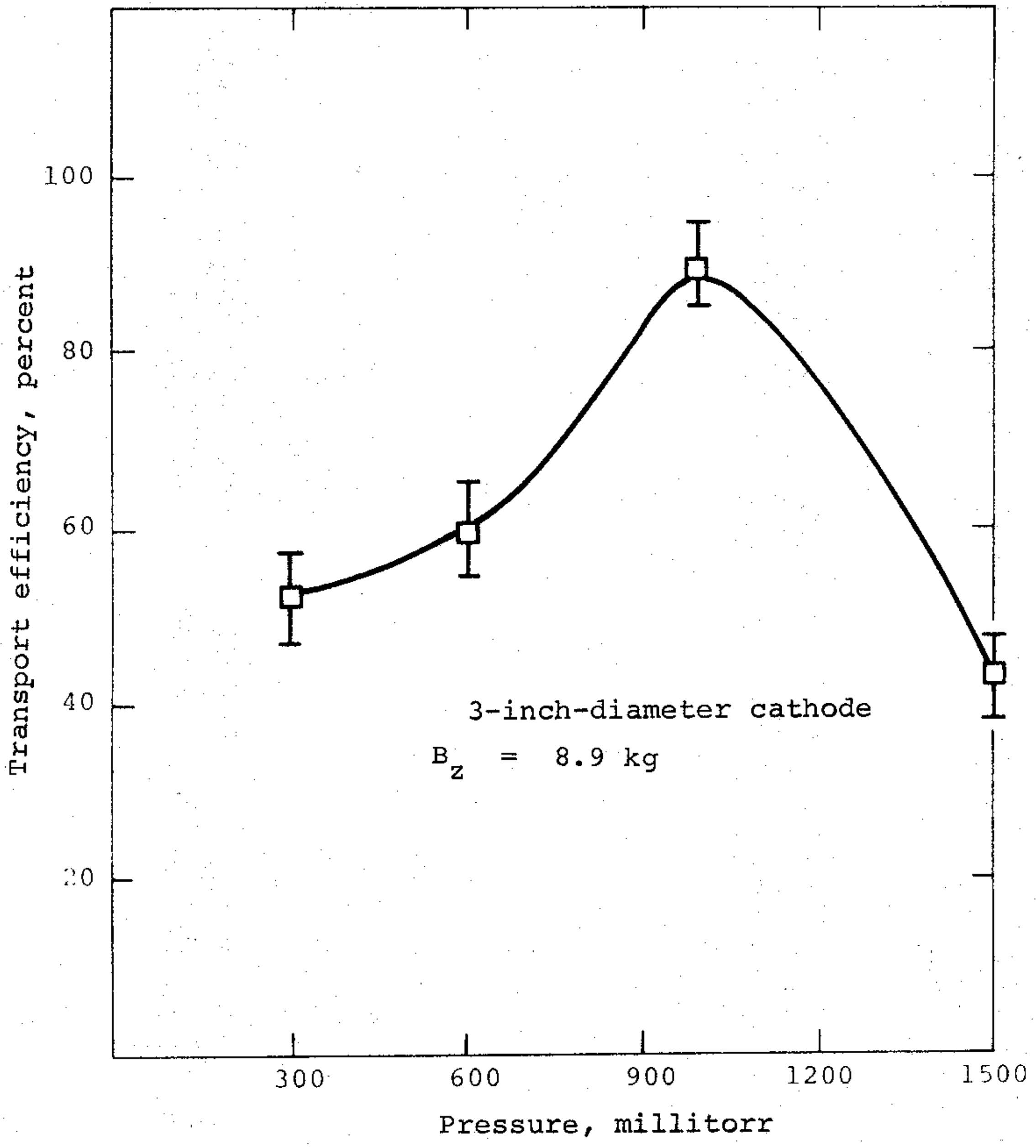

Figure 4.10 Transport efficiency at 1 meter.

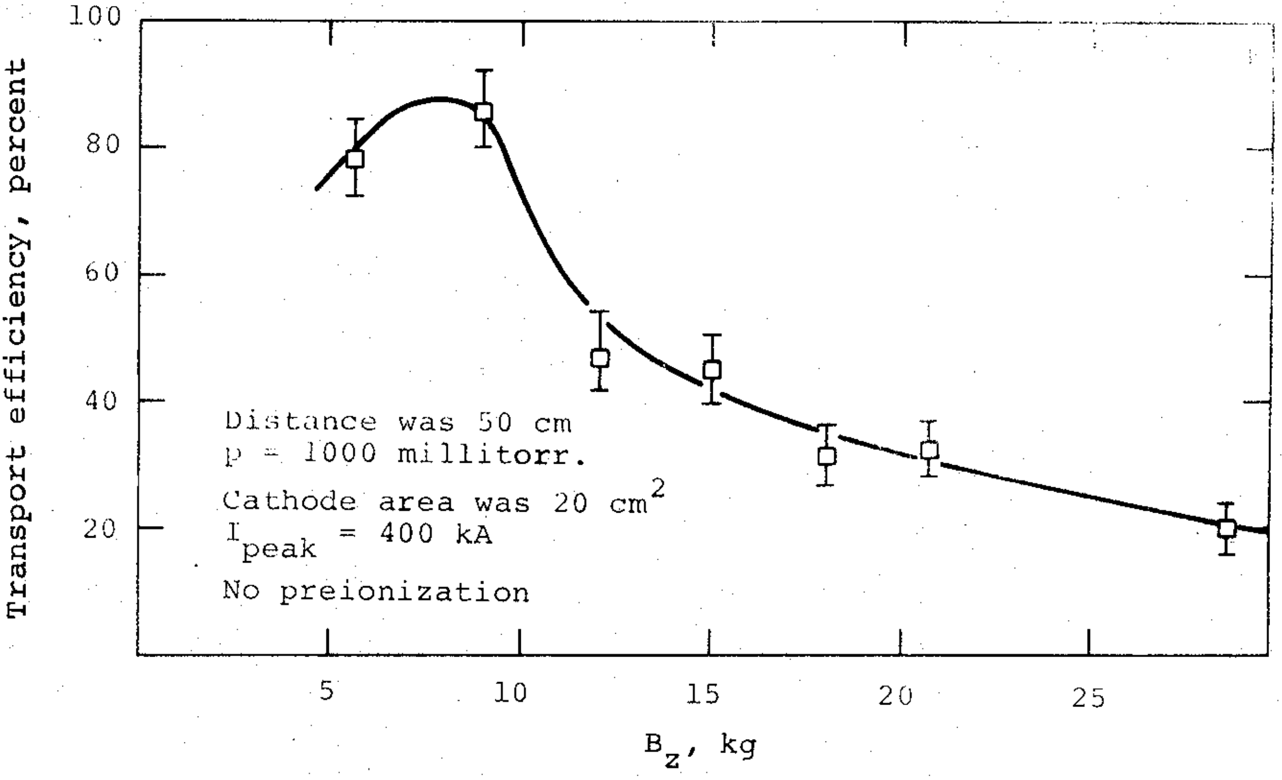

Figure 4.11 Transport efficiency as a function of B_z.

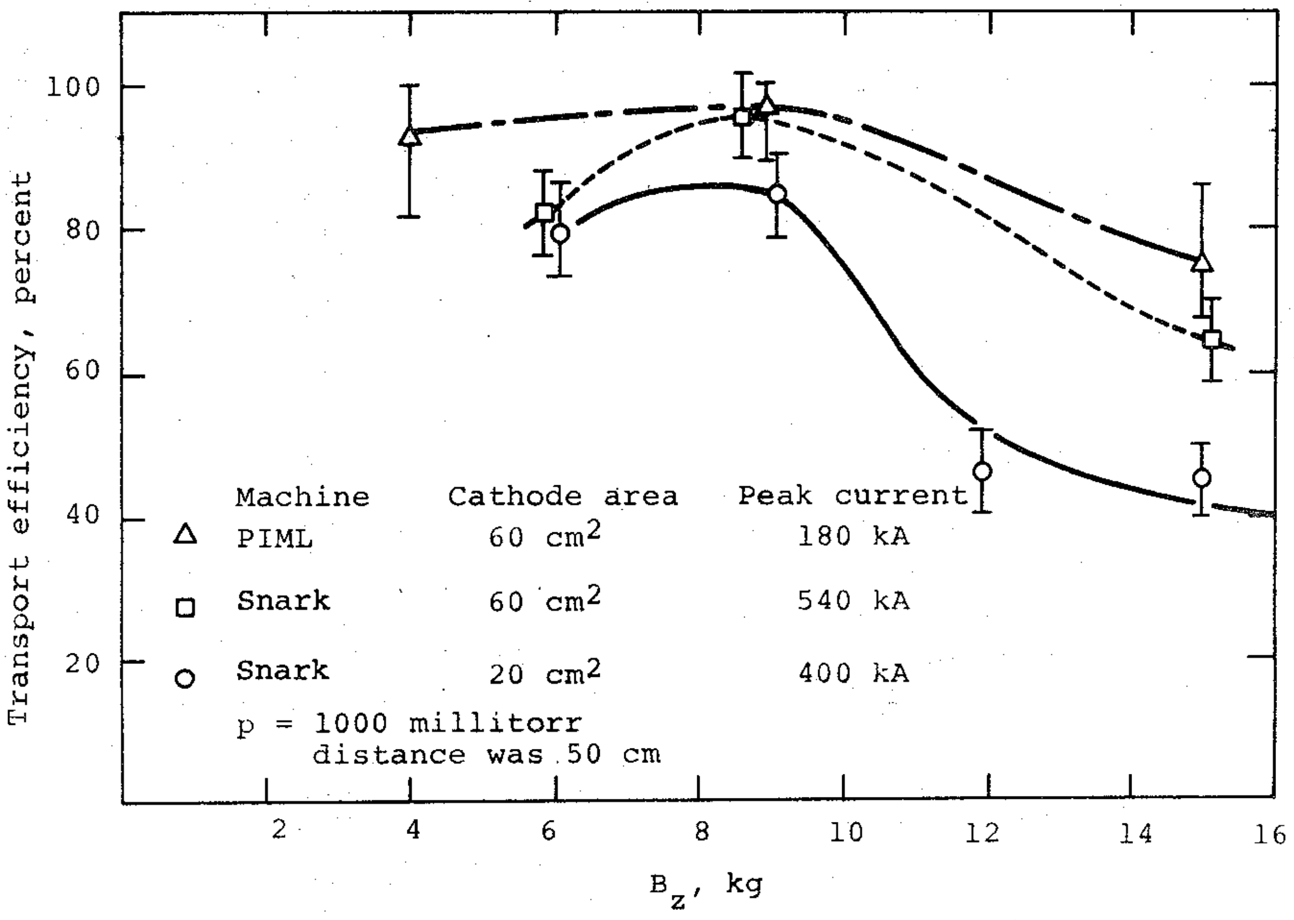

Figure 4.12 Charge transport efficiency at 1/2 meter for three current densities.

4.3.3 DML, 100 keV. During this program we did not study the effect of preionization in detail; however, some work has been done and preliminary conclusions can be drawn. Work was done on the 100-keV DML using a quasi-theta-pinch (these experiments will be described later in this section). This work used magnetic fields up to 50 kgauss and plasma densities of up to 10^{15} ions/cc. In some cases, when the plasma density was on the order of 10^{14} to 10^{15} ions/cc, transport efficiency was better than 90 percent even for 100 kA/cm^2 and B_z = 50 kgauss. When rf preionization (10^9 to 10^{11} ions/cc) was used in the Snark experiments, transport efficiency at 18 kgauss and 1 torr or 9 kgauss and 1/2 torr was not improved enough to make a definitive statement. There did appear to be an increase of about 5 percent but this is within the experimental error. The interesting point is that almost all of the apparent increase in efficiency occurred early in the pulse with very little change in the later portion of the pulse which has most of the power and charge. This is consistent with a model in which a small amount of preionization shortens the effective breakdown time of the gas but has no other major effect. When the same rf preionization was used with a 12 kgauss field but at the optimum pressure of 1 torr, the transport efficiency was increased by 20 percent. Again this was due to an increase in efficiency early in the pulse with no measurable change in the efficiency of the latter portions of the pulse.

The current densities that have previously been used in describing the beam were determined simply by dividing the current by the cathode area. As was shown in Section 4.2, the current density was not uniform but varied with radius. The peak current density with a 60-cm^2 cathode of 550 kA was 36 kA/cm^2 over the center 5 cm^2; with a 20-cm^2 cathode of 400 kA, it was 46 kA/cm^2 over the center 5 cm^2. Therefore, the average current densities are 9 kA/cm^2 and 20 kA/cm^2, while the peak current densities are 36 kA/cm^2 and 46 kA/cm^2, respectively. The current density was measured on the anode using apertures on the Faraday cup; it was measured 1 meter downstream by using a multiple block calorimeter. The results of these two measurements are shown in Figure 4.13. To increase the average current density, an 11-cm^2 cathode was constructed. The diode parameters were approximately 400-kA peak current and 650-kV mean energy, corresponding to an average current density of 36 kA/cm^2. This beam was transported without any measureable loss for one-half meter.

The net current was measured by the voltage drop across a stainless steel resistor in the return current piece that connected the sample to the anode plane. The measurements were taken across two 1-inch-long, 3-7/8-inch-diameter shunts, placed 5 centimeters and 95 centimeters from the anode; a 3-inch-diameter cathode was used.

The net current traces near the anode were reasonable and similar to those obtained without B_z, except that the magnitude was smaller (see Figure 4.14). However, the net current 95 centimeters from the anode showed a great deal of structure and no discernible behavior that could be related to the diode parameter. This behavior will be discussed further in a following section.

Figure 4.15 gives the net current as a percentage of the primary current for several magnetic fields and pressures. A following section will discuss these in a detailed analysis. The primary features are that the net current has a slight minimum at about 5.6 kgauss and then increases with increasing B_z and with increasing pressure, except for pressures below a few hundred millitorr.

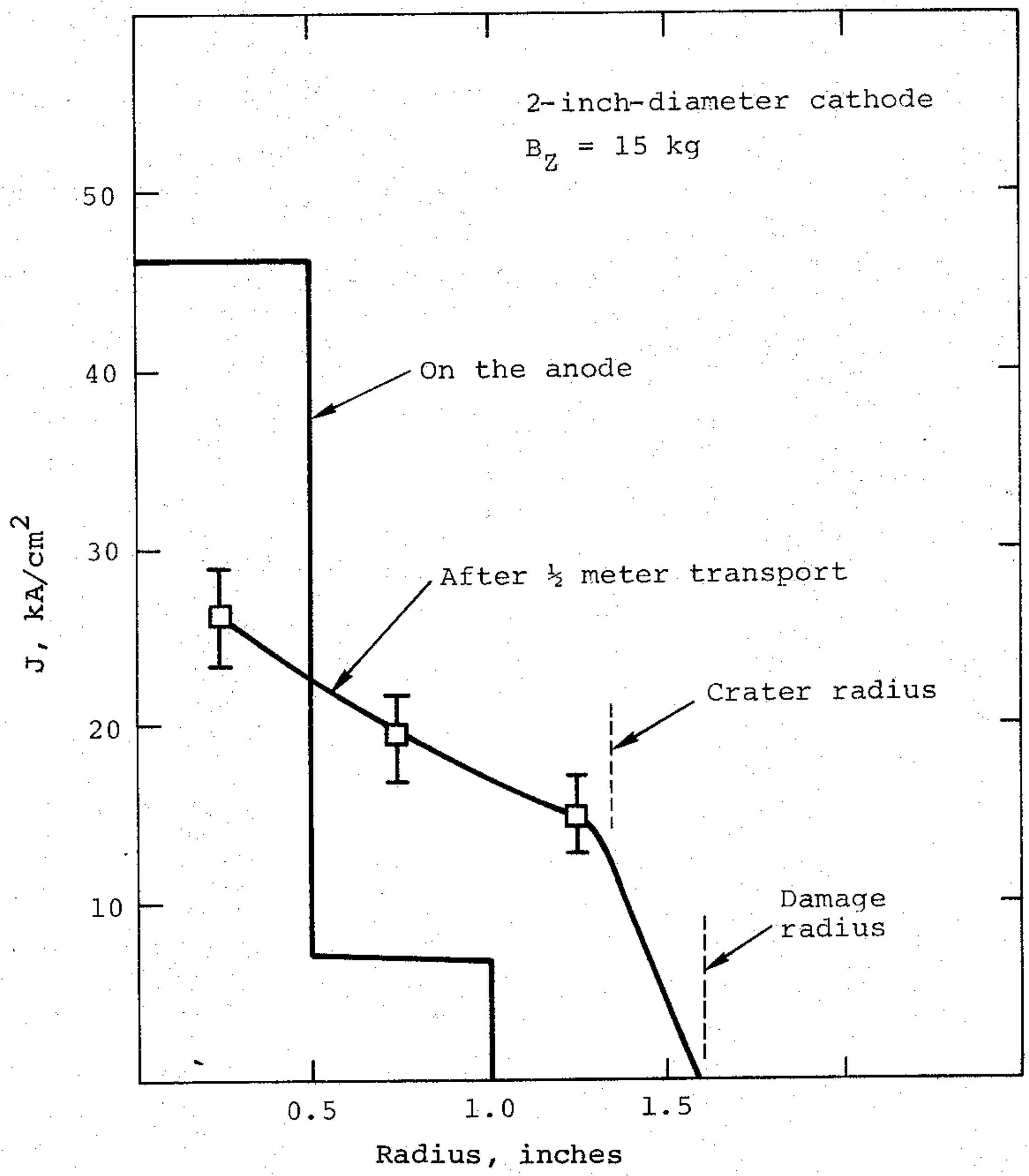

Figure 4.13 Current density.

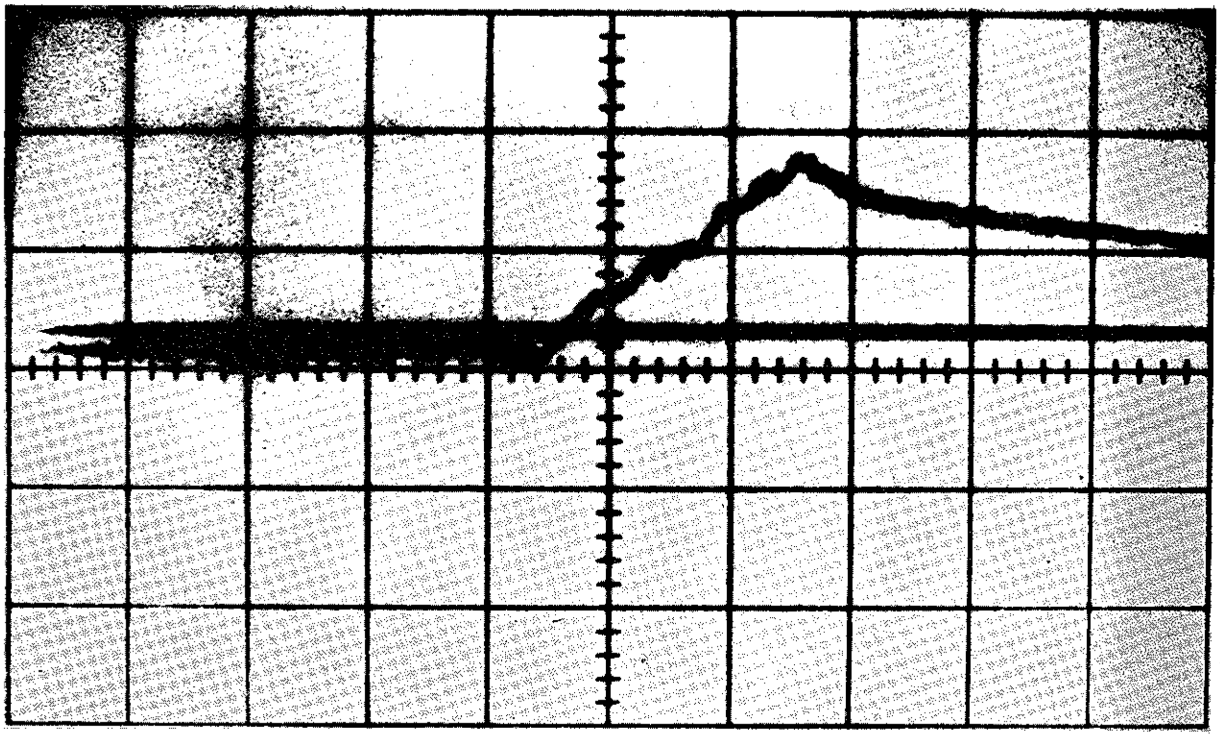

a. 5 cm from the anode; 50 nsec/cm and 16.5 kA/cm

b. 95 cm from the anode; 50 nsec/cm and 16.0 kA/cm

Figure 4.14 Net current traces.

A343

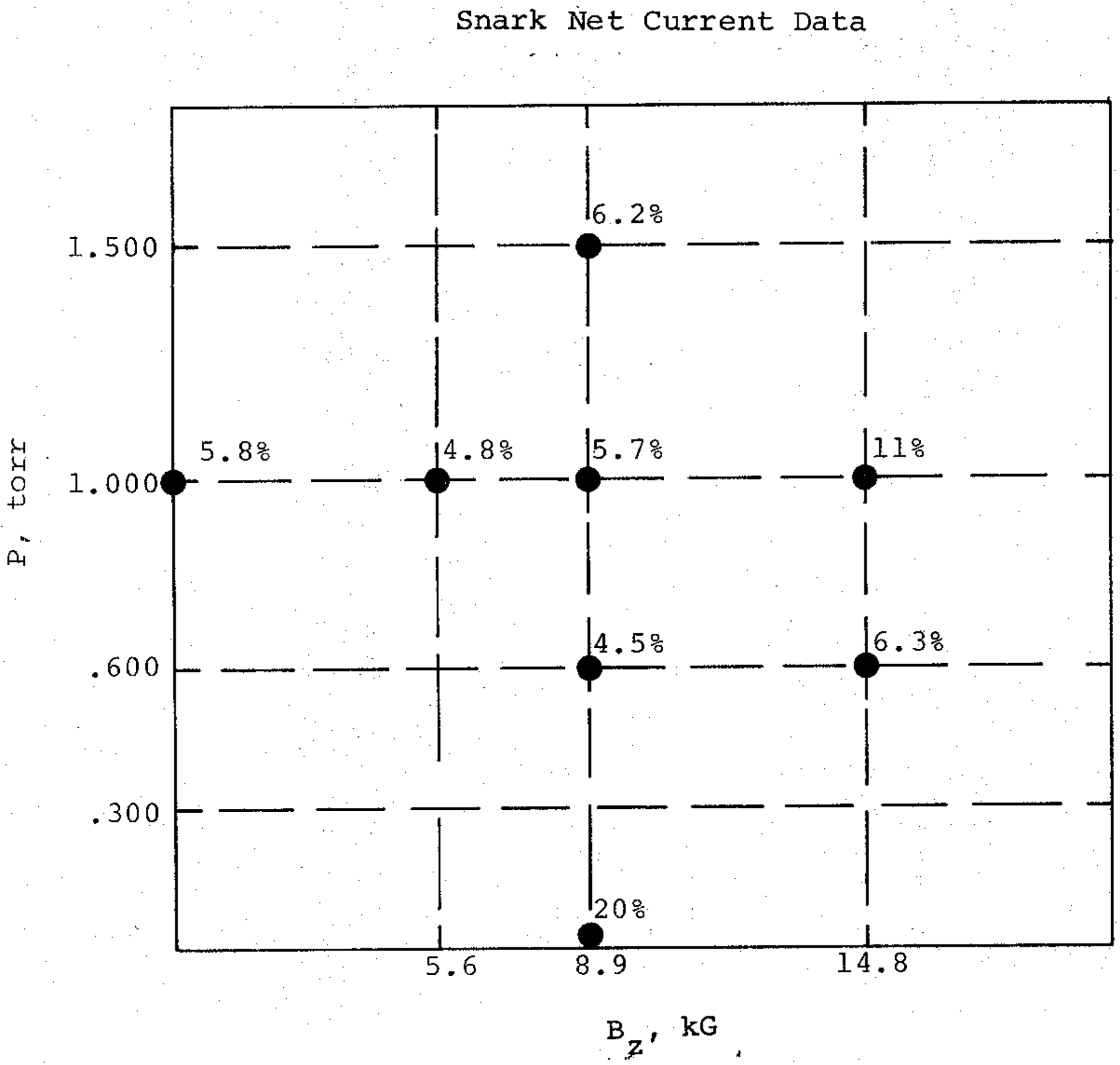

Figure 4.15 Net current as a percentage of primary current.

There was evidence from the Naval Research Laboratory that the electron beam rotated with respect to the cathode (Reference 7). As a check on where this rotation takes place, an experiment was carried out using a 7-inch by 2-1/4-inch cathode and $B_z \approx B_{\theta max}$. A sample with a rectangular hole in the center was placed on the anode and another sample was placed 10 inches downstream from the anode. The sample on the anode (Figure 4.16) showed a rotation of about 9 degrees, while the sample 10 inches downstream did not show any measurable rotation with respect to the hole in the anode sample.

A high current density, high B_z experiment was performed earlier with IR&D funding on the 100-keV DML (Reference 4.8). Some of the results are given here because they pertain to the questions of high current density, preionization, and field strength that were addressed by this contract.

The apparatus used for these experiments was a theta pinch-like plasma device (Figure 4.17). This device had a large B_z field (up to 56 kgauss with present equipment) as well as a large dB/dt, which could be used to preionize gas in the drift region of the electron beam.

The equipment consisted of four basic parts: (1) a 56-μF, low-inductance capacitor bank, (2) a 5-nH spark gap to switch the current, (3) a low-inductance transmission line from the capacitor bank to the field coil, and (4) a single-turn field coil around the electron-drift region.

The drift region was 1.5 inches in diameter and 8 inches long. When the electron beam filled the entire 1.5 inches and was not current neutralized by a reverse plasma current, it had

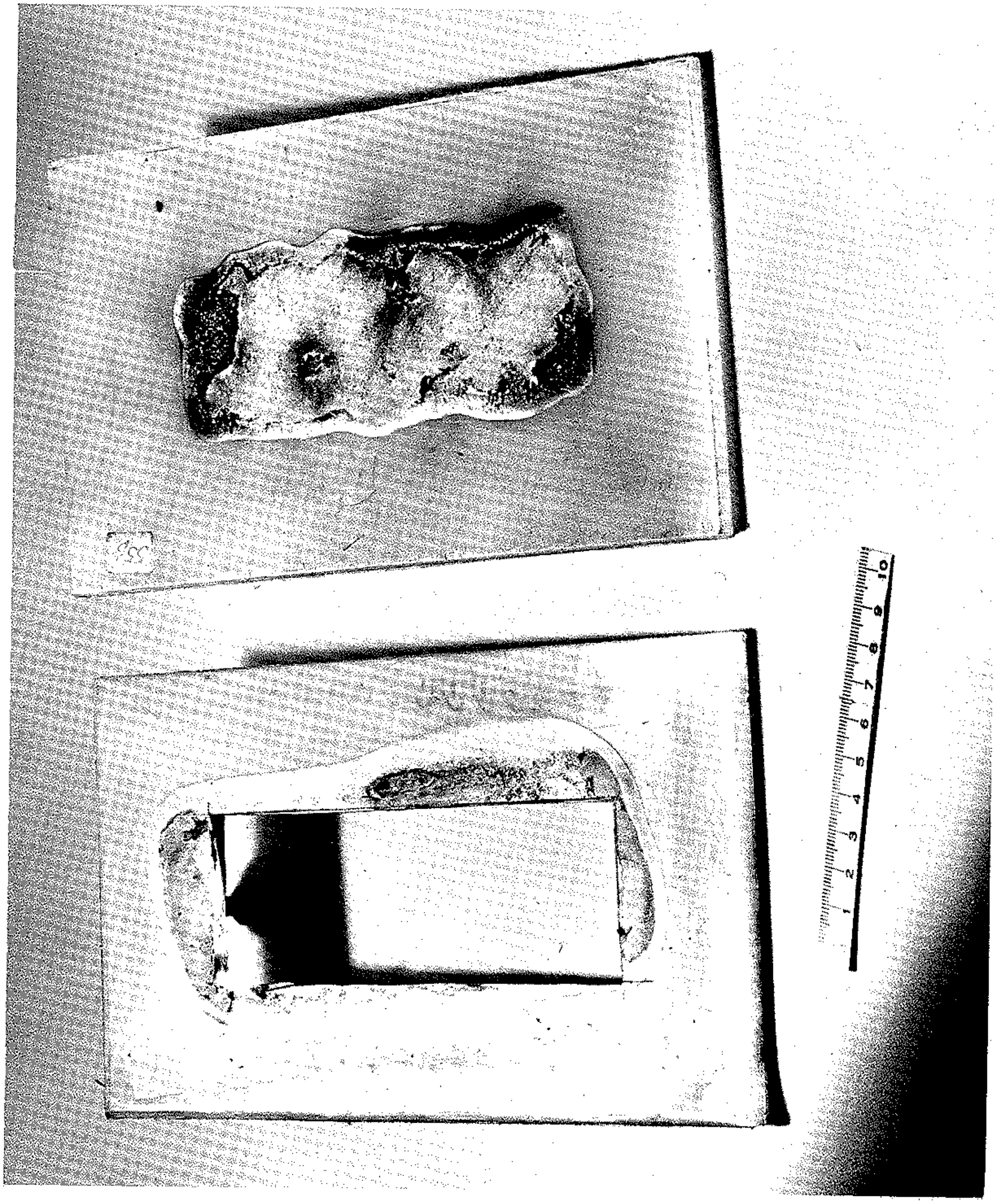

Figure 4.16 Rotation of the beam. Top sample was on the anode, bottom sample was 10 inches from the anode on the same spot.

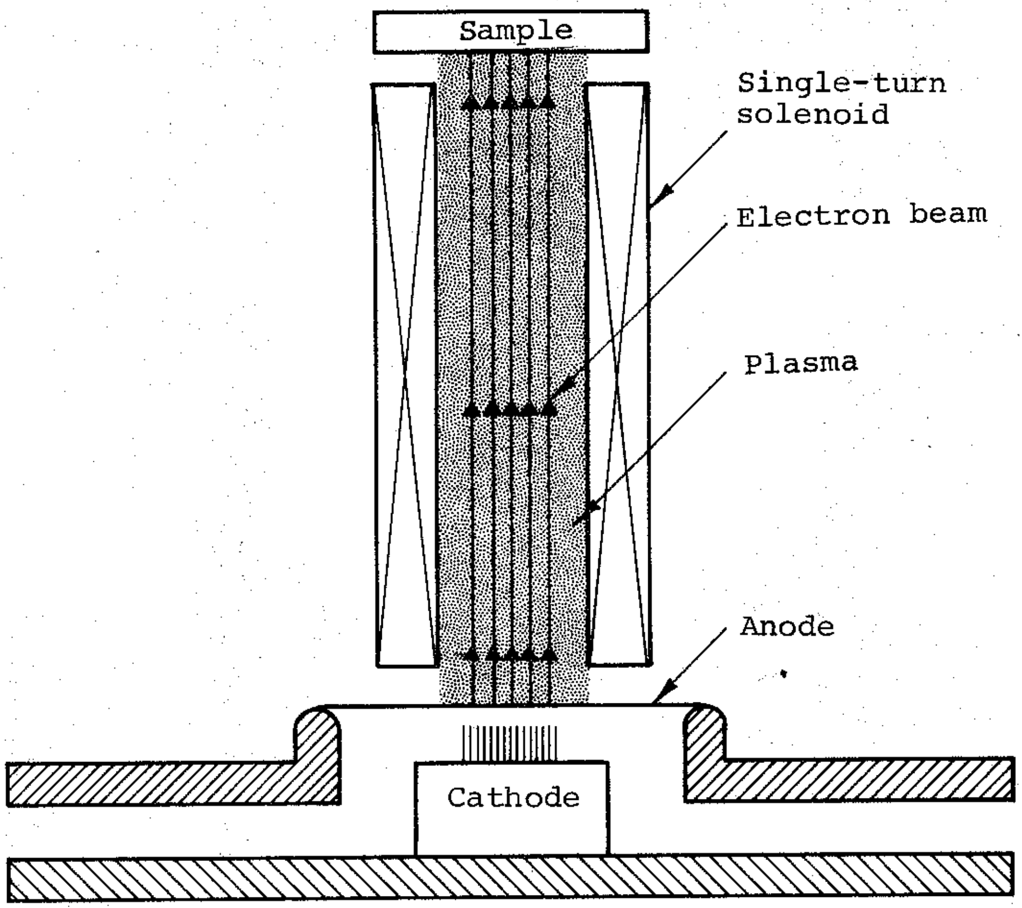

Figure 4.17 Diagram of experiment.

a self-field that was about 15 kgauss. The maximum B_z that could be applied by the external circuit was 56 kgauss.

The same field coil could be used to ionize the gas in the drift region. Since the plasma was a good conductor, the net current was small. Therefore, the B_θ in the drift region due to the presence of the electron beam was also small.

If the plasma was allowed to pinch into a small dense core, the diagmagnetic properties of the plasma would tend to exclude the B_z from this core. This means that the electrons would have to pass from a region of low magnetic field in the cathode into a higher magnetic field at the anode and then into a lower field in the plasma. To minimize the possible problems arising from two field transitions, the apparatus was operated as a preionized solenoid rather than as a theta pinch. This means that the electron beam was fired after the gas was ionized but before it had formed a current sheet.

The field coil was designed so that a relatively large magnetic field leaked into the anode-cathode gap. However, the electron gyroradius was small compared to the characteristic distances of the B_z field. This means that $(W_\perp/|B|)$ was approximately an adiabatic invariant for each electron ($W_\perp$ is the transverse energy of the electron and $|B|$ is the magnitude of the magnetic field). If the cathode was in a weak field, B_1, and the maximum field in the field coil was B_o, then only those particles with initial angles of

$$\frac{W_\perp}{W} \leqslant \frac{B_1}{B_o}$$

could move into the region of maximum field (W is the total energy of an electron).

The X-ray flux coming from a thin tantalum target was used as a measure of the electrons striking the target. A photodiode (always in the same geometry with respect to the target) was used to measure the X-ray flux. The skin depth for the external magnetic field was 0.8 mm for tantalum and 4.0 mm for graphite. Therefore, 0.025-mm-thick tantalum targets and 0.5-mm-thick graphite targets could be used without seriously distorting the applied B_z field.

The first experiments were performed with the field coil 3/4 inch away from the anode. This meant that the anode-cathode gap was in a weak fringing portion of the applied magnetic field. The beam propagation was very poor. The target plate showed only slight damage and the photodiode showed very little X-ray flux coming from a tantalum target placed 2 inches from the anode (1.25 inches inside a 7.25-inch-long field coil). This indicated that almost all electrons were lost in the first two inches. High ν/γ beams, such as the ones used in this experiment, in Snark, and in larger machines, have most of the energy in a transverse component. The previous adiabatic invariant argument leads one to expect difficulty in transport when the cathode is purposefully in a weak fringing portion of the magnetic field.

The magnetic-field topology was changed by using a special return-current insert. This insert (Figure 4.18) served a dual purpose; it carried any net current that may exist in the beam-plasma system back to ground, and it extends the magnetic-field lines so the single-turn solenoid appears to be at the anode instead of 3/4 inch away. Therefore, by using this geometry, a large magnetic field could be applied in the diode and mirroring effects could be minimized. This produced a dramatic improvement in beam transport. When the pressure in the drift chamber was

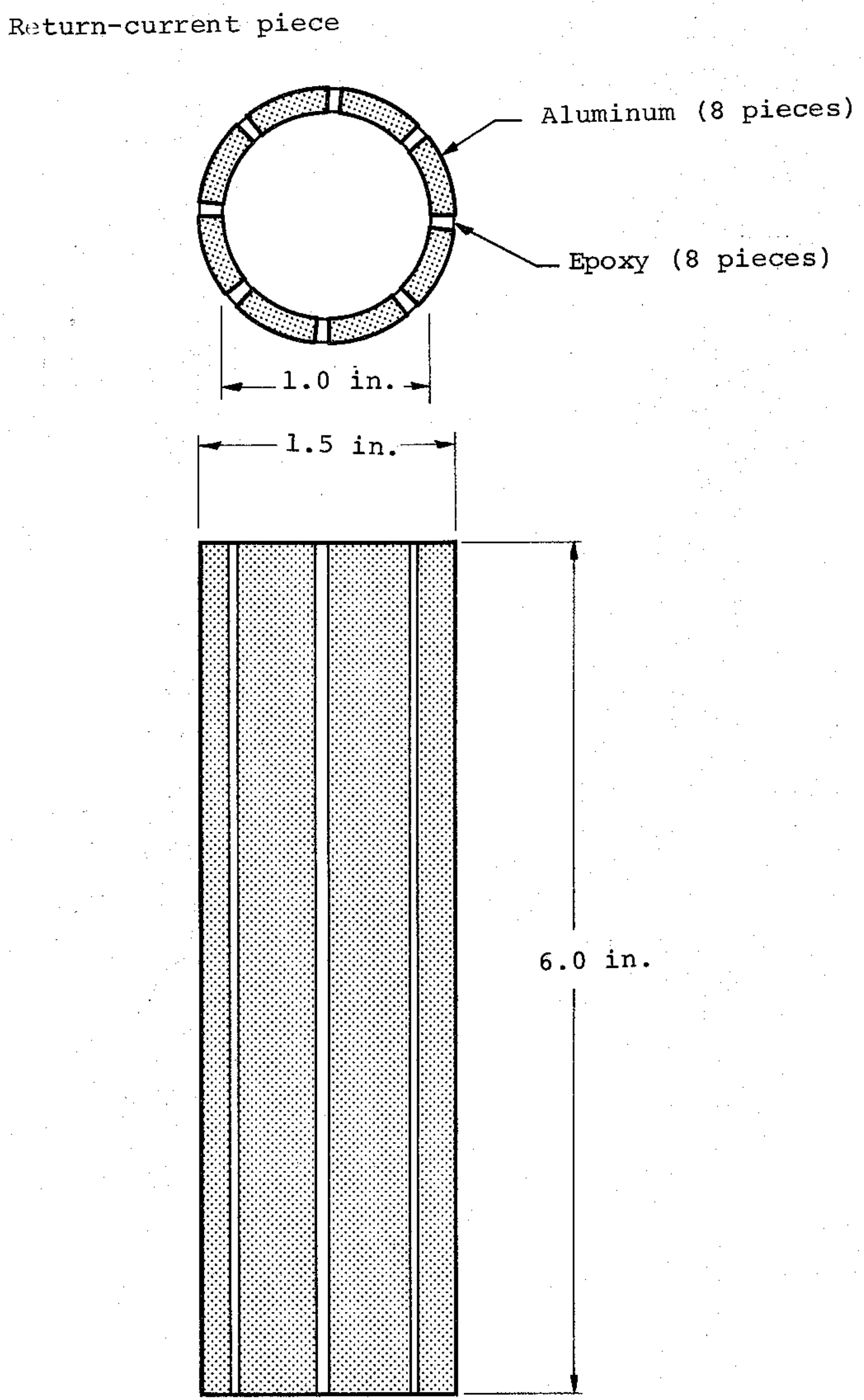

Figure 4.18 Return-current insert.

Sample on anode.

Sample 6.0 inches from
anode; solenoid on the
anode. B_z is 50 kilogauss
and pressure is 1 torr:

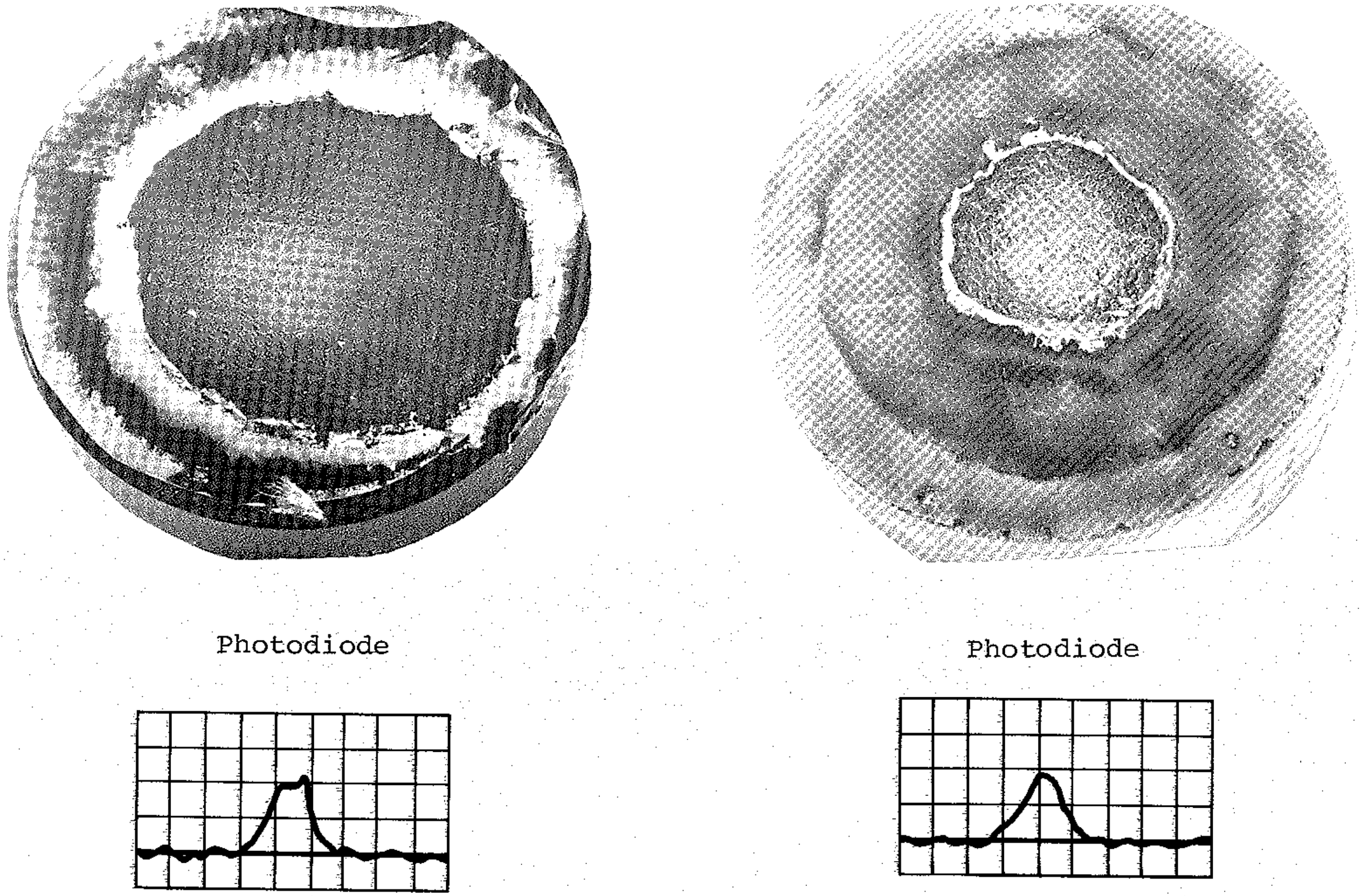

Photodiode

20 nsec/cm
6.7 V/cm

Photodiode

20 nsec/cm
6.7 V/cm

Figure 4.19 Beam propagation with the solenoid on the anode.

1 torr and the peak applied field was 50 kgauss, approximately 100 percent of the beam was transported (Figure 4.19). Although this was the only condition which gave 100 percent transport, a large range of conditions gave transport between 50 to 75 percent (Figure 4.20). For example, approximately 70 percent of the beam was transported using a pressure of 0.2 torr and a B_z field of 28 kgauss.

	Pressure (millitorr)		
Magnetic Field (kilogauss)	200	500	1000
20	35%		
28	70%	40%	50%
42	50%	80 to 90%	60%
50	40%		95 to 100%

All percentages are ± 5 percent

Figure 4.20 Percentage of beam transported.

The symmetric return-current piece was used with a thin graphite sample to confirm the fluence arriving at a sample 6 inches from the anode. The crater produced in the graphite sample was one centimeter in diameter and about 2.5 mils deep. This correlates very well with the 100 percent transport determined by photodiode measurements of the bremsstrahlung produced in the tantalum targets. This implied that 100 calories were delivered to the target in a 120-keV beam with a fluence of 125 cal/cm^2. The graphite was removed for essentially the entire electron range. This means that the dose was at least 2000 cal/g, 2.5 mils into the sample, and the front-surface dose was in excess of 6000 cal/g (computed for an assumed incident angle of 60 degrees).

Some experiments were done to measure the plasma density inside the solenoid using a coaxial Langmuir probe. Because of the probe saturation at high density (greater than 5×10^{14} ions per cubic centimeter), a definitive correlation with beam transport was not obtained; however, when the plasma density was greater than 10^{13} ions/cc, at least 50 percent of the electron beam was transported the length of the solenoid. When the magnetic field was too low (below 50 kgauss at 1000μ and below 25 kgauss at 200μ) a dense plasma was not formed and the beam did not transport efficiently. At 200μ, when the plasma was formed at fields above 25 kgauss, the transport efficiency decreased with increasing B_z just as it did in the PIML and Snark experiments. The optimum pressure again appears to be about 1000μ but the issue was clouded by the close coupling between the magnetic field and plasma density.

The important conclusions of these 100-keV experiments are that current densities in excess of 100 kA/cm^2 can be efficiently transported with B_z, even at 100-keV mean energy, but the initial plasma density must be of the order of 10^{13} or 10^{14} ions/cc. In addition, B_z can be used efficiently at values greater than 50 kgauss, but again only when the preionized plasma density is greater than 10^{13} ions/cc.

4.4 BEAM CONVERGENCE (CONE EXPERIMENT)

Two of the problems associated with high beam currents are inductance in the diode and high transverse energy in the electron beam. Both of these problems are directly related to the large self-magnetic fields produced when a high current beam is generated. When the diameter of the cathode and beam are increased, the inductance is reduced and the electrons probably have less transverse energy. The drawback to this approach is that a large diameter cathode usually means a large area, low fluence beam.

The cone experiment made a large diameter beam in the form of an annulus with a relatively small area. The magnetic field was generated by a conical solenoid with a conducting cone in the center to exclude magnetic field from part of the volume (Figures 4.21 and 4.22). The property of this field configuration was that field lines converge and the diameter of the electron beam was reduced, but the field strength was not increased so the area and temperature of the beam were not changed. In practice, the beam was expected to remain as an annulus because the magnetic field was excluded from part of the volume by resistive diffusion. This meant that the innermost field lines actually went into the solid aluminum cone, and consequently these field lines could not be used to transport electrons.

A typical sample is shown in Figure 4.23. The cathode diameter was slightly larger than the entire sample. As predicted, the diameter of the beam was reduced while the width of the annulus increased and the area remained constant. The hole in the center corresponded to the magnetic flux that passes into the solid aluminum cone.

The energy transported to the sample appeared to be at least 90 percent of the injected energy; however, the injection was very inefficient and erratic. An average of about 40 percent of the energy entering the diode arrived at the anode and there was a large amount of shot-to-shot scatter in this number.

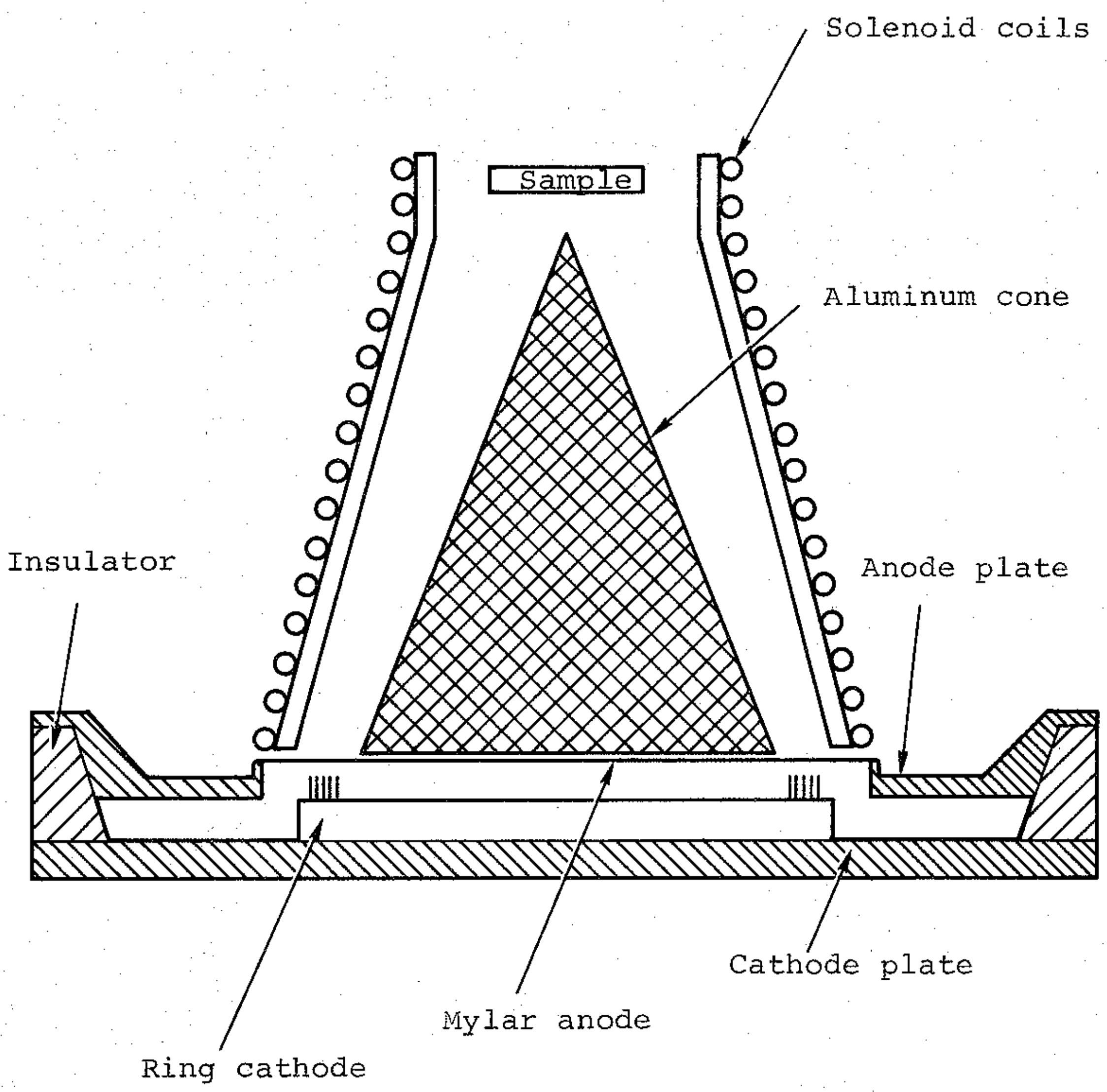

Figure 4.21 Task 3.5 - annular cathode with conical preionized channel and B_z.

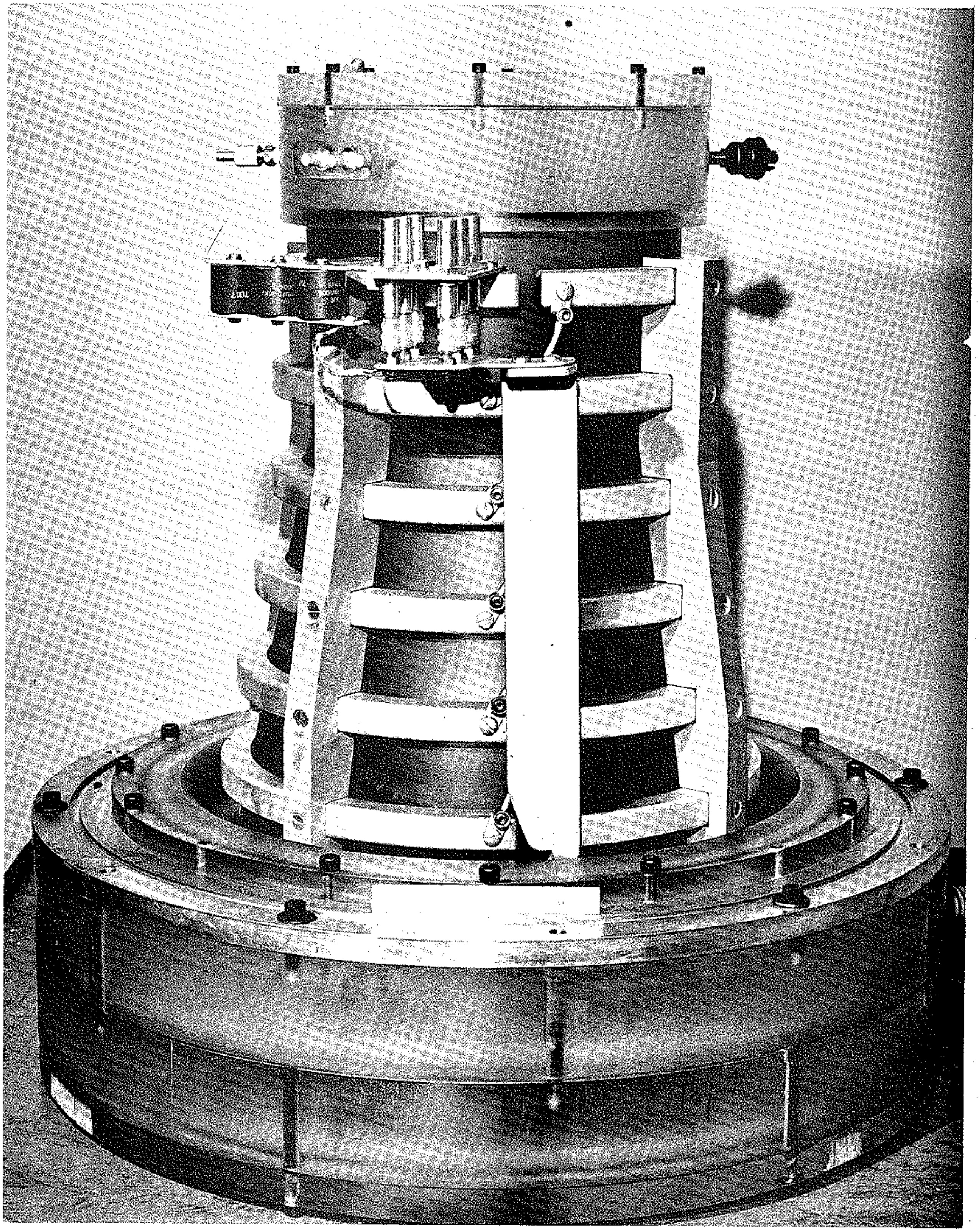

Figure 4.22 Completely assembled cone system.

A348

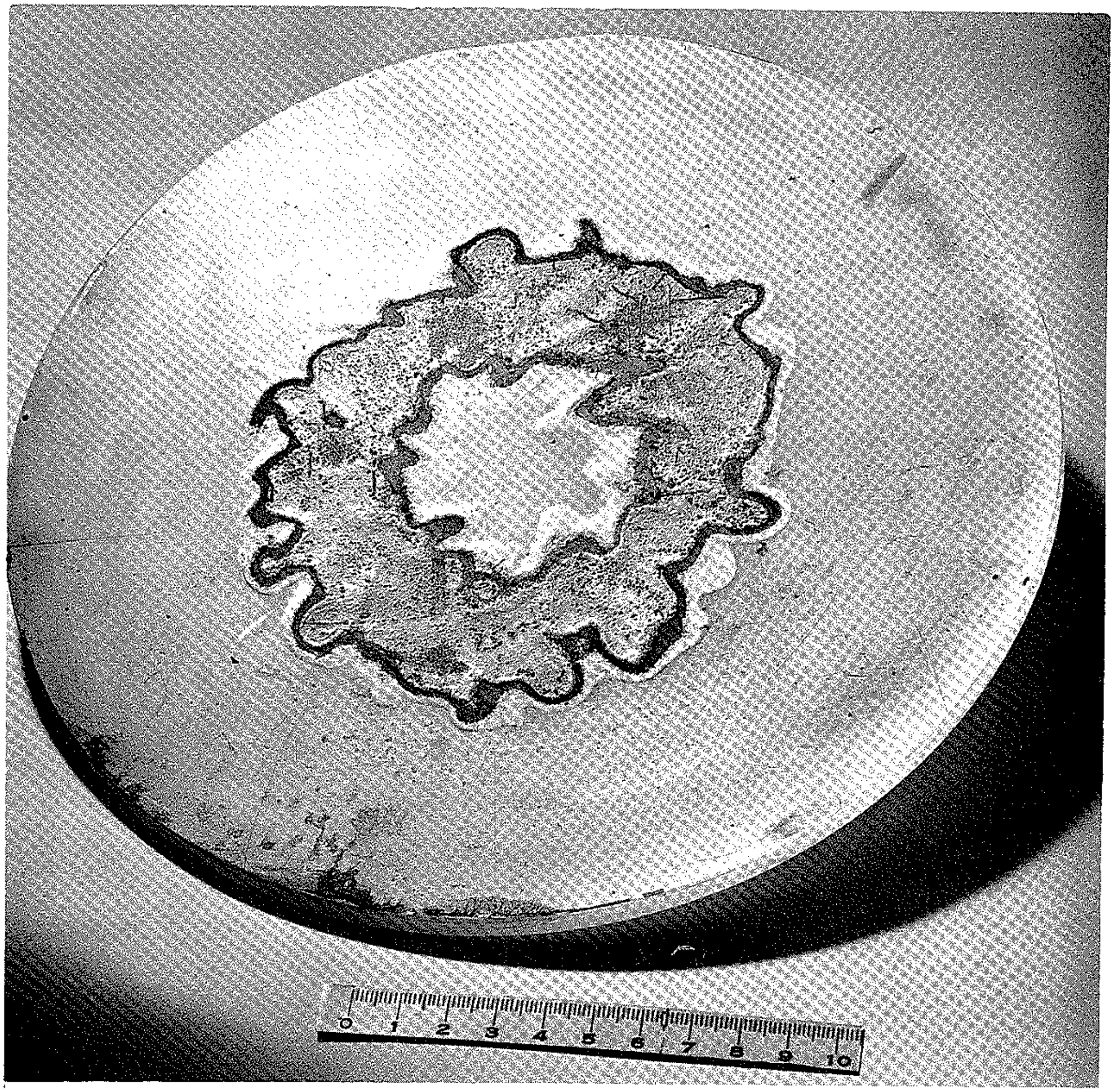

Figure 4.23 Sample at the end of the cone system. The cathode was the diameter of the entire system.

A352

An instability was observed in the propagated beam. This instability was observed as a wavy nonuniform damage pattern (note that the aluminum cone was supported by six legs that intercepted part of the beam and these are also evident in the sample). The growth of this instability was observed on a single shot by dividing up the beam into six segments and observing each segment at a different distance downstream (Figure 4.24). The growth appears to be approximately linear.

The important conclusion that can be drawn from these experiments is that the transport region behaved as expected except for a non-catastrophic instability; however, an unresolved problem remains in the construction of the diode.

4.5 CONCLUSIONS

The B_z systems were operationally very simple. The period of the magnetic fields were long enough to make timing and jitter problems insignificant, and the system could be readied for the next shot almost as rapidly as a similar neutral gas system. In particular, the liners did not have to be cleaned after each shot as they did with the linear pinch.

A planar cathode did not emit uniformly. The current density was peaked in the center, but it could be made more uniform by increasing the applied B_z field. The diode did not short as early when a B_z was applied, but as the current density was increased a larger B_z was needed to have the diode hold up for the duration of the pulse.

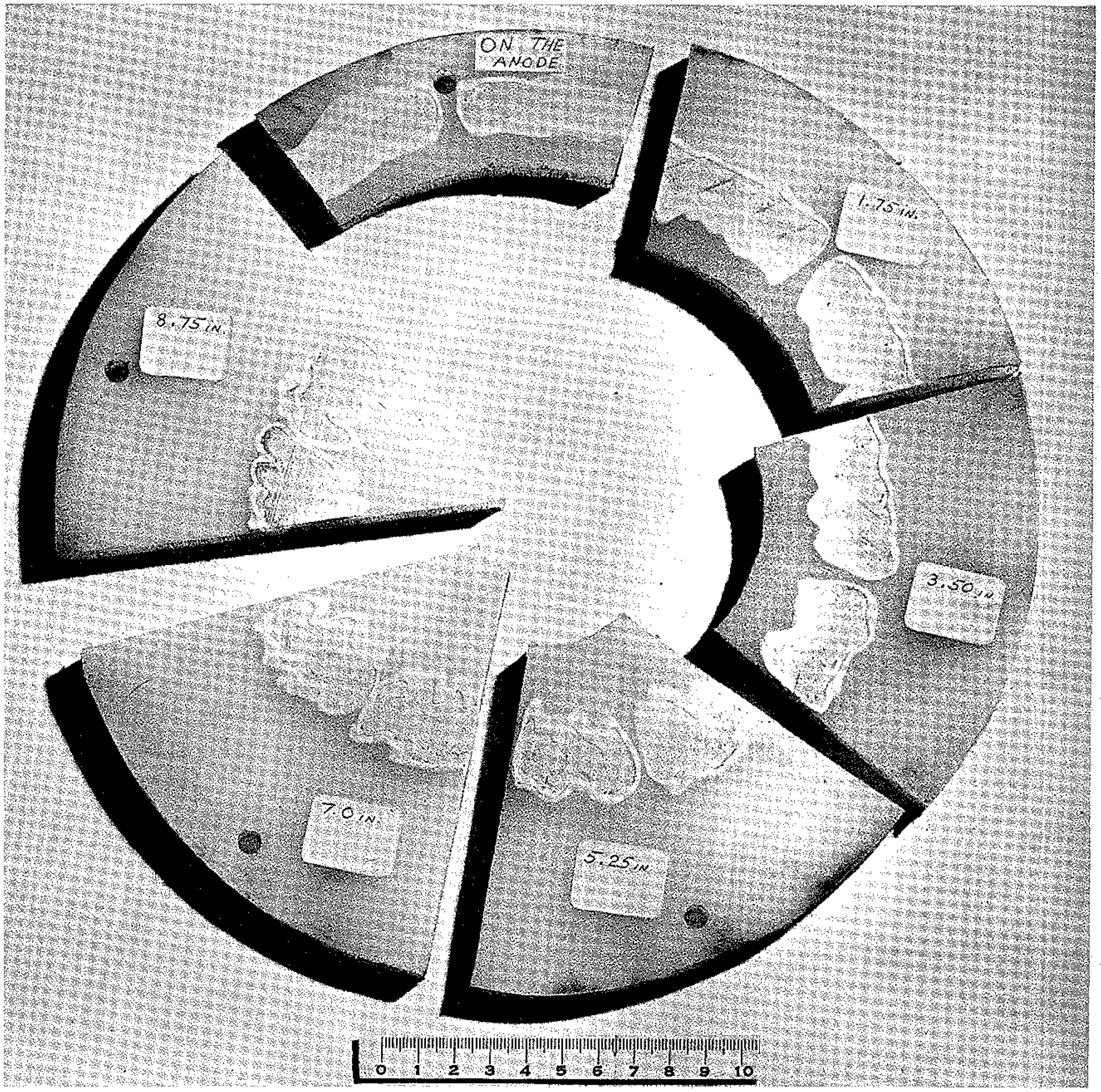

Figure 4.24 Growth of an instability as a function of distance from the anode.

A353

There is an optimum B_z for beam transport at about 7.5 kgauss. This optimum is very broad for current densities of about 3 kA/cm^2 and a wide range of conditions will give transport efficiencies in excess of 75 percent, but as the current density was increased the optimum became more pronounced. This optimum can probably be broadened by better preionization. Even without preionization, current densities of 36 kA/cm^2 averaged over an 11-cm^2 cathode were transported efficiently at the optimum B_z. When a 20-cm^2 cathode was used, the current density in the center 5 cm^2 was 46 kA/cm^2; this beam was also transported 0.5 meter with 90 percent efficiency.

Feasibility was shown for using a double cone type geometry to reduce the diameter of an annular beam without changing its area. An unexpected problem arose with diode construction and all of the beam was not injected, but this does not appear to be a fundamental problem.

In general, the behavior of intense electron beams in a longitudinal field is more complicated than originally anticipated; however, it has been shown to be an efficient means of transporting these beams over 1-meter distances.

REFERENCES

4.1 B_θ systems discussed in Section 3.2 of this report.

4.2 B. Bzura, J. Linke, R. Rostoker, "Propagation of Electron Beams I - Energy Transfer in Neutral Gases in the Presence of an Axial Magnetic Guide Field," Cornell University, Laboratory of Plasma Science, Internal Report.

4.3 D. A. Hammer, B. Oliphant, I. Vitkovitsky, and J. Fargo, "Effects of External Magnetic Field on Accelerating High-Current Electron Beams," Naval Research Laboratory, Washington, D.C., Internal Report.

4.4 I. Smith *et al.*, "Development of an Advanced X-ray Source," PIQR-226/227-2, Physics International Company, San Leandro, California (July 1970).

4.5 D. A. Hammer and N. Rostoker, *Phys. Fluids*, **13**, 1831 (1970).

4.6 B. Ecker, J. Benford, C. Stallings, S. Putnam, and P. Spence, "Proceedings of the Eleventh Symposium on Electron, Ion and Laser Beam Technology," Boulder, Colorado (May 1971).

4.7 David Hammer, NRL, private communication.

4.8 C. Stallings and P. Spence, *Bull. Am. Phys. Soc.* 15:1501, 1970.

SECTION 5

BEAM TRANSPORT IN AXIAL (B_Z) MAGNETIC FIELDS--CALCULATIONS

by J. Guillory

5.1 DEPENDENCE OF NET CURRENT ON MAGNETIC FIELD

Two theoretical models predict an increase of net current with increasing magnetic field. One, due to Guillory, is presented and discussed in some detail here; the second, due to Lee and Sudan, has recently been published (Reference 5.1), and its applicability is discussed here. The first model agrees roughly with our experimental data if the plasma density, n_p, is of the order of 10^{15} to 10^{16} cm^{-3}. The second model agrees roughly with the data if $n_p \sim 10^{13}$. We feel that the first of these theories gives predictions somewhat more in accord with the limited net current data of our experiments.*

The net current traces near the downstream target are erratic both during and after the passage of the beam. The net current near the anode is more reproducible; it has a linear rise throughout the beam pulse (unlike the behavior reported in DASA 2426 for $B_z = 0$ and lower beam power). Superimposed upon this linear rise are small oscillations or steps with periods on

---

*The data consists of net current traces near the anode and target ends of the transport region for each of eight shots, all at different values of B_z (the applied magnetic field or P (pressure). See Figure 4.15.

the order of 5 to 10 nsec, near the limits of resolution of the traces. Similar fast fluctuations appear with larger amplitude on the downstream net current.

The linear rise of net current is relatively well understood in terms of a Boltzmann equation with time-dependent plasma density and self-consistent induced electric field. The peak value (or, if one prefers, the slope) can be interpreted in terms of an effective conductivity.

However, the oscillations or steps in the net current at the anode and the erratic behavior of the downstream traces even long after beam turnoff strongly suggest the presence of instability, probably involving the streaming of background plasma electrons. The instability appears to be convective (Reference 5.2) with amplification anti-parallel to the streaming velocity of the plasma electrons. The increase of the upstream net current with increasing B_z and P suggests that the resistivity, due to the instability (and probably the growth rate), increases with B and P. The plasma density probably increases with P; thus we expect an instability which, if its growth rate does not explicitly involve collisions, goes as ω_c and probably ω_p (cyclotron frequency and plasma frequency) to some positive powers. The two-stream cyclotron instability (Reference 5.3) appears not to behave in this way. The ordinary-mode instability (Reference 5.4) behaves correctly but is ruled out because it occurs only when the plasma energy density exceeds twice that of the magnetic field. The whistler instability (References 5.5 and 5.6) has a growth rate proportional to $\omega_c\omega_p$ and can apply to plasmas of moderate density if there is a high energy "tail" on the distribution function in parallel (or perpendicular) velocities (Reference 5.6).

5.1.1 Presentation of the Instability Model. The model given here will have two basic features:

a. A simple description of net current in terms of effective resistivities averaged over spatial coordinates and beam duration

b. Assumption of instability (unspecified), as just discussed, to explain increasing net current with B_z at high plasma density

Justification of the first of these model assumptions will largely be left to a later discussion. Pressure dependence of the net current is due to changes in both the collision rate and the plasma density. We now present the model and fit it to the data, after which we will evaluate the model of Lee and Sudan.

5.1.1.1 Net Current in Terms of Axial Conductivity. If the axial plasma current density is related to the induced E_z field by

$$J_{zp} = E_z/\eta_{tot} \quad (\eta_{tot} = \text{total effective resistivity})$$

then we can show that the ratio of net current to beam current

$$j \equiv |J_{znet}|/J_B$$

is given by $$j = (Z/\eta_{tot} + 1)^{-1}$$

where Z is a dynamic beam impedance, dependent only on beam radius and risetime:

$$Z \approx \frac{\pi a^2}{c^2}\,\omega \quad (\omega \equiv \text{inverse risetime of beam})$$

Comparison of the actual net and primary (beam) current traces at the anode shows that the ratio j is approximately constant throughout the beam pulse (with slight jitter), and this can be predicted theoretically for times longer than a collision time (which is typically less than 1 nsec).

During the beam pulse, a typical value for the self-magnetic field is

$$B_\theta = \frac{2I_{net}}{ca} \approx \frac{\pi a}{c} J_{znet},$$ with J_{znet} evaluated on the axis.

Then $\nabla x E = 1/c\ dB_\theta/dt$ gives as a typical value of E_z:

$$E_z \approx \left(\frac{\pi a^2}{c^2}\ \omega\right) |J_{znet}|$$

and this supplies the desired Z. It is assumed that the beam is well charge-neutralized so that there is no space charge contribution to E_z, and it is assumed that the net electron flow is forward, i.e., $J_{znet} < 0$.

The relation $j = (Z/\eta_{tot} + 1)^{-1}$ then follows simply from $J_{zp} = E_z/\eta_{tot}$ and the definitions.

In our experiments the ratio $J_{znet}/J_B \equiv j$ was always small, so that approximately

$$j \approx \frac{\eta_{tot}}{Z} << 1$$

5.1.1.2 Net Current in the Presence of Instability. As discussed previously, we now assume that electrons scatter off of unstable waves at a rate ν^* proportional to the growth rate of the instability, assumed to increase with B. The effective parallel resistivity $1/\sigma_{\|}$ now has a classical part, $1/\sigma_o$, and a contribution η from the instability. Thus

$$j \approx \frac{\sigma_o^{-1} + \eta}{Z}$$

Here σ_o and possibly η depend on P, and η depends on B. If the scattering of electrons by the turbulent waves proceeds at roughly the linear growth rate, as in some streaming instabilities (Reference 5.7), then,

$$\eta \sim 4\pi \mathrm{Im}\ \omega/\omega_p^2$$

with $\mathrm{Im}\omega$ as the growth rate. However, when the collisionless plasma theory indicates $\mathrm{Im}\omega = \kappa\omega_c$, we must expect to find $\mathrm{Im}\omega = \kappa\omega_c - \nu$ because when the collision rate exceeds the linear collisionless growth rate there is usually no growth of the waves.

With this simple model we have

$$j \approx \frac{1}{\sigma_o Z} + \frac{\eta}{Z}$$

with $\eta \sim 4\pi/\omega_p^2\ (\kappa\omega_c - \nu)$ when this is positive, and equal to zero otherwise. We leave κ to be determined by fitting the data, then check the acceptability of the empirically derived value.

5.1.1.3 Numerical Evaluation of Instability Model. If we assume ν (sec^{-1}) $\sim 7 \times 10^9$ P(torr) for electrons in nitrogen gas of ionization $\lesssim$ 40 percent, and if we take $1/\sigma_o \sim 4\pi\nu/\omega_p^2$ (which is probably good for $P \geqslant 1$ torr), then a beam with a risetime of 100 nsec and a radius of 3.8 cm gives

$$\frac{1}{\sigma_o Z} \approx 0.6 \; P \times \frac{10^{14}}{n_p}$$

and

$$\frac{\eta}{Z} \approx 0.84 \times \frac{10^{14}}{n_p} \; (1.7 \; \kappa B - 0.7 \; P)$$

when this is positive. (Here P is in torr, n_p in cm^{-3} and B in kG.)

From the data we have dj/dB(kG) $\sim 0.8 \times 10^{-2}$ at $P = 1$ torr. This would require

$$\kappa \sim 0.55 \; n_p/10^{16}$$

and the instability would take hold at

$$B(\text{kG}) \sim 0.7 \times 10^{16}/n_p$$

The value $n_p = 1.2 \times 10^{15}$ gives $\text{Im}\omega \sim 0.07 \; \omega_c$ $(\kappa = 0.07)$ and the model estimate of j is shown in Figure 5.1. If n_p is higher than this at $P = 1$ torr, the horizontal portion of the curve becomes shorter and lower (instability sets in at lower B_z), and the value of κ required to fit the data increases as n_p. In the "low-frequency whistler" instability of Reference 5.6, $\text{Im}\omega$ is between ω_{ci} and ω_{ce}, and $\text{Im}\omega \sim 0.07 \; \omega_e$ is thus quite

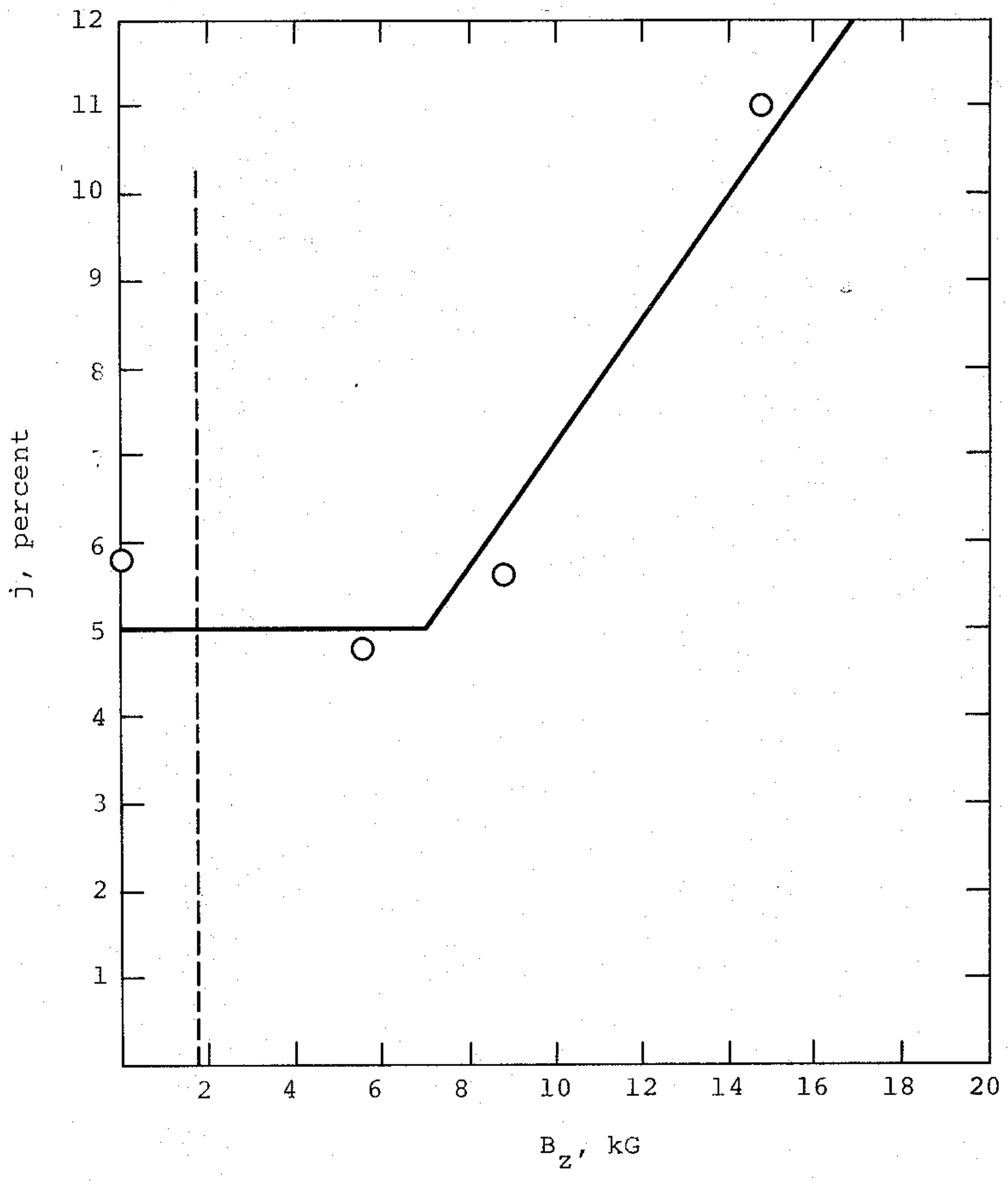

Figure 5.1 Net current data at P=1 torr, compared with instability theory for $n_p = 1.2 \times 10^{15}$ and growth rate $0.05\,\omega_c$. Theory does not apply to left of the dashed line.

reasonable. But if n_p is as high as 10^{17} at 1 torr, then the κ required becomes larger than unity, implying $\mathrm{Im}\omega > \omega_c$, an unlikely situation. The data point at $B_z = 0$ also becomes harder to explain, although the model does not strictly apply for very low B_z. Actual prediction of n_p from ionization rates is possible in principle if the plasma density at breakdown or pulse onset is known; but because n_p exponentiates with the ionization time, the appropriate average value of n_p cannot be calculated to within a factor of three. Our model thus seems to apply if $n_p \sim 10^{15}$-10^{16} cm^{-3}.

The actual transition from the stable to the unstable regime is somewhat rounded by the statistical nature of the collisional damping, but this is a minor refinement. Another refinement is that at low applied B_z where the self-field B_θ exceeds B_z, a geometrical effect of anisotropic conductivity enters: the axial conductivity has an increasing contribution from the small cross-field component of the conductivity tensor. Diamagnetic effects previously neglected also become important because of the larger azimuthal plasma current. These combined effects are expected to produce somewhat larger axial net current, which could explain the slightly high value of j observed at $B_z = 0$.

5.1.1.4 <u>Pressure Dependence of Net Current</u>. The pressure dependence is not easily explained. If $n_p \propto P$, then the smaller value

$$dj/dB\ (\mathrm{kG}) \sim 0.4 \times 10^{12} \text{ at } P = 0.6 \text{ torr}$$

indicates that κ varies with n_p to some power larger than unity, say $\kappa \propto n_p^2$. There is no known model for this in the instability behavior, and it is not clear that $n_p \propto P$. A further complication is that n_p may depend on beam current density J_B. In the experiments, J_B was consistently higher for the 8.9 kG shots than for those at 5.6 or 14.8 kG, and this may affect the model because n_p is assumed fixed when fitting the data.

The observed net current for zero applied B_z is not constant but has a minimum at $P \sim 1$ torr. But the relation between this data and what one would expect for $B_z > B_\theta$ is clouded by the fact that when $B_z = 0$ the perpendicular conductivity

$$\sigma_\perp = \sigma_o \ (1 + \omega_c^2/\nu^2)^{-1}$$

is involved. The increase in net current (for $B_z = 0$) at lower pressures is explained by the decrease of $\sigma_\perp$ as ν decreases. The increase of net current with P when $P > 1$ torr is attributed to the fact that collisions increasingly impede the flow of the plasma return current. Greater ionization from avalanche apparently does not compensate for this, indicating that n_p varies slower than P, or that electron-ion collisions dominate and the electron temperature T_e is decreasing with increasing P.

5.1.2 Comparison with the Theory of Lee and Sudan.

The model of Lee and Sudan (Reference 5.1) predicts an increase of net current with B_z although it takes no account of rising plasma density or of the finite length of the transport region. In the regime where the net current is still small, they give

$$j = \frac{c}{2a\omega_p} \left[(1 + i\zeta)^{1/2} + (1 - i\zeta)^{1/2} \right]$$

where $\zeta \equiv \omega_c(B_z)/\omega_p$. This is plotted in Figure 5.2 for two quite low values of plasma density, $n_p \sim 10^{13}$ cm^{-3}. For higher n_p, j is smaller and increases more slowly with B_z, and thus cannot explain the data.

If the density really is as low as 10^{13} cm^{-3} then the instability model probably cannot explain the data, mainly because $\sigma_o Z$ is not large enough ($\sigma_o Z = 1.6 \times 10^{-14}$ n_p/P, with P in torr).

From previous studies of ionization rates in the presence of the beam (Reference 5.8) we estimate that n_p is at least 10^{15} cm^{-3} when most of the beam current passes, but measurements have not been made. For further investigation of these effects, it is imperative that plasma density be measured, at least upon beam turnoff.

5.2 DIAMAGNETISM OF A WARM BEAM PENETRATING A UNIFORM PLASMA WITH AXIAL MAGNETIC FIELD

5.2.1 Effect of Incomplete θ-Current Neutralization: Equation for B_z Neglecting B_r. We shall now consider a hot (large thermal spread) beam in a plasma with $B = B_z \hat{1}_z$ along the direction of propagation. Let us take the case where beam current I_z and beam surface current I_θ (from diamagnetic and ∇B drifts) is rising. We shall assume that I_z is completely neutralized by infinite conductivity σ_z of the plasma along magnetic field lines. The θ current is only partially neutralized because of finite plasma conductivity $\sigma_\perp$ normal to the magnetic field. Thus B_θ is zero because the net Z current is zero, but B_z and dB_z/dt are nonzero because of finite $\sigma_\perp$. The dB_z/dt produces a θ electric field, driving the plasma J_θ current density. We neglect radial plasma mass flow due to $E_\theta \times B_z$ and the radial dependence of $\sigma_\perp$.

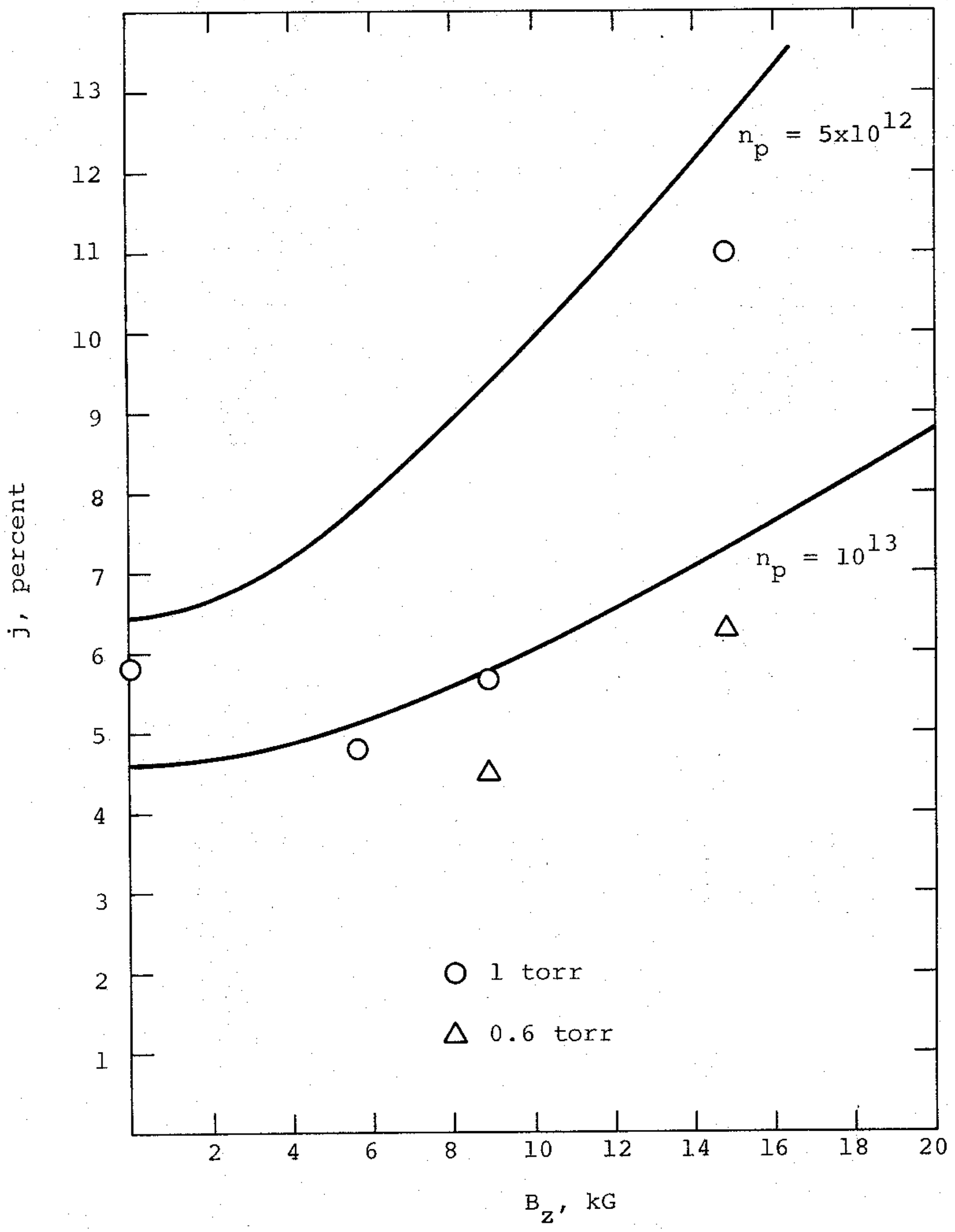

Figure 5.2 Net current versus magnetic field as predicted by Lee and Sudan (Reference 5.1), evaluated for two different plasma densities (solid curves). PI data is shown as circles (for P=1 torr) and triangles (for P=0.6 torr).

The beam surface θ current is $\vec{J} = \frac{4\pi c}{B}\frac{d}{dr}(n\varepsilon_\perp)\hat{1}_\theta$ (5-1)

where $\varepsilon_\perp$ is the perpendicular energy per electron for the beam plus plasma (usually the plasma pressure $n_p\varepsilon_{p\perp}$ is smaller than the beam pressure $n_b\varepsilon_{b\perp}$ even though $n_p >> n_b$).

The plasma θ current is $J_{p\theta} = \tilde{\sigma} \cdot E$, where $E = E_r\hat{1}_r + E_\theta\hat{1}_\theta$ and $\tilde{\sigma}$ is the plasma conductivity tensor:

$$\begin{array}{cc} \begin{pmatrix} \sigma_\perp & -\sigma_H & 0 \\ \sigma_H & \sigma_\perp & 0 \\ 0 & 0 & \sigma_\parallel \end{pmatrix} & \begin{array}{c} (r) \\ (\theta) \\ (Z) \end{array} \end{array}$$

If the radial electric field is zero, then $\tilde{\sigma} \cdot \vec{E} = \sigma_\perp E_\theta$. We assume that this is the case and we assume $\partial\sigma/\partial r = 0$. Then putting the total current

$$J = \frac{4\pi c}{B}\frac{d}{dr}(n\varepsilon_\perp) + \sigma_\perp E_\theta \qquad (5\text{-}2)$$

into the Maxwell equation for ∇xB (neglecting the displacement current $c^{-1}\partial D/\partial t$), we get

$$-\frac{\partial B_z}{\partial r} = \frac{4\pi}{B}\frac{d}{dr}(n\varepsilon_\perp) + c^{-1}\sigma_\perp E_\theta \qquad (5\text{-}3)$$

But the Maxwell equation for ∇xE,

$$\frac{\partial}{\partial r}(rE_\theta) = -\frac{r}{c}\frac{\partial B_z}{\partial t}$$

can be combined with Equation 5-3 after multiplying Equation 5-3 by r and differentiating:

$$-\frac{\partial}{\partial r}\left(r\,\frac{\partial B_z}{\partial r}\right) = 4\pi\,\frac{d}{dr}\left(\frac{r}{B}\,\frac{d}{dr}\,n\varepsilon_\perp\right) - (r/c^2)\sigma_\perp\,\frac{\partial B_z}{\partial t} \qquad (5\text{-}4)$$

Using $n\varepsilon_\perp = P_\perp$ and rearranging, we have the diffusion-like equation:

$$\frac{\partial^2 B}{\partial r^2} + \frac{1}{r}\,\frac{\partial B}{\partial r} - \frac{\sigma_\perp}{c^2}\,\frac{\partial B}{\partial t} = -\,4\pi\left(\frac{1}{rB} - \frac{1}{B^2}\,\frac{\partial B}{\partial r}\right)\frac{\partial P_\perp}{\partial r} - \frac{4\pi}{B}\,\frac{\partial^2 P_\perp}{\partial r^2} \qquad (5\text{-}5)$$

where B refers to B_z only. The right-hand side of the equation is a source term (nonlinearly dependent on the solution B) for the radial diffusion operator on the left-hand side.

Because $\partial P_\perp/\partial r$, as a function of r, changes with time (the beam is slowly being compressed by the magnetic field), one must actually include B_r and the beam input distribution to solve the problem rigorously. Even without that difficult program one can see the physics of the solution to Equation 5-5. The initial condition is that $B = B_o$, uniform everywhere, at time zero. The source term, concentrated near the pressure gradient (beam "edge") and pressure second derivative, causes a reduction in B to diffuse inward from the source region on a magnetic-diffusion time scale. This change in B propagates a distance proportional to

$$c(t/\sigma_\perp)^{\frac{1}{2}}$$

in a time t; but note that B jumps discontinuously at the source location (wherever $\partial P_\perp/\partial r$ and $\partial^2 P_\perp/\partial r^2 \neq 0$) when the beam is introduced. For a rectangular profile of P (r), this means a sudden change in B at the beam edge only, which then propagates diffusively to larger and smaller r.

While we have not examined the motion of the beam envelope as B changes there, it is reasonable to suspect that when $B_r \neq 0$ is included in the treatment, the beam will constrict, probably on a magnetic-diffusion time scale, to the radius required by pressure balance, and the beam edge will become less sharp.

5.2.2 Radial Fields Included. In a medium of uniform constant tensor conductivity $\tilde{\sigma}$, the vector potential, $\vec{A}$, satisfies

$$\nabla \times \nabla \times \vec{A} + \frac{1}{c^2}\frac{\partial^2 \vec{A}}{\partial t^2} + \frac{4\pi}{c^2}\tilde{\sigma}\cdot\frac{\partial \vec{A}}{\partial t} = \frac{4\pi}{c}\vec{J}_B - \frac{4\pi}{c}\tilde{\sigma}\cdot\nabla\phi - \nabla\frac{1}{c}\frac{\partial \phi}{\partial t}$$

where J_B is the beam current; (plasma currents are in the σ terms). We assume azimuthal symmetry in r, θ, Z coordinates and choose as gauge $A_r = 0$. Then when σ_{zz} is very large we have

$$-\frac{\partial}{\partial r}\left[\frac{1}{r}\frac{\partial}{\partial r}(rA_\theta)\right] + \left[-\frac{\partial^2}{\partial Z^2} + \frac{1}{c^2}\frac{\partial^2}{\partial t^2} + \frac{4\pi}{c^2}\sigma_{\theta\theta}\frac{\partial}{\partial t}\right]A_\theta = \frac{4\pi}{c}J_\theta$$

and
$$\frac{1}{c}\frac{\partial}{\partial t}A_Z = -\frac{\partial \phi}{\partial z} + 0\,(J_z/\sigma_{zz})$$

where J_θ and J_Z refer to the beam current. If we assume $\vec{A}$ and ϕ are functions only of r and $u \equiv \gamma\,(vt - z)$, and let $k \equiv 4\pi\beta\gamma\sigma_{\theta\theta}/c$ ($\beta \equiv V/c$, $\gamma^{-2} = 1 - \beta^2$) we have from the A_θ equation

$$-R\,A_\theta + \left(k - \frac{\partial}{\partial u}\right)\frac{\partial A_\theta}{\partial u} = \frac{4\pi}{c}J_\theta$$

RPN 99

where R is the radial operator $\partial/\partial r\,[1/r\;\partial/\partial r\;(r\,\cdot)]$. Note that

$$\frac{\partial A_\theta}{\partial u} = \frac{B_r}{\gamma}$$

with B_r the radial magnetic field perturbation.

For order-of-magnitude estimates we assume a solution of the form

$$\left.\begin{aligned} A_\theta &= rF(u) \\ J_\theta &= rj(u) \end{aligned}\right\}\quad \text{for } r < R$$

where R is the beam radius, and take $j(u) = j_o \sin su$ for $0 < u < \pi/s$. (This defines s in terms of the beam duration τ: $s = \pi(\beta\gamma c\tau)^{-1}$.) With this model of the solution we have $RA_\theta = 0$ and

$$B_r \approx -\frac{4\pi}{c}\,\gamma j_o (k^2 + s^2)^{-\frac{1}{2}}\; r \sin(su + \phi) \qquad (5\text{-}6)$$

for $r < R$ and $0 < u < \pi/s$, where $\phi \equiv \tan^{-1}(s/k)$. Since $B_z = 1/r\;\partial/\partial r\;(rA_\theta) = 2F(u)$ and $r\partial F/\partial u = \partial A_\theta/\partial u = B_r/\gamma$, we have

$$\frac{\partial B_z}{\partial u} = \frac{2B_r}{\gamma r}$$

and if $B_z = B_{zo}$ when $su \approx -\phi$, then the diamagnetic perturbation is

$$\Delta B_z = \frac{8\pi}{c}\, j_o s^{-1} (s^2 + k^2)^{-\frac{1}{2}}\,[\cos(su + \phi) - 1] \qquad (5\text{-}7)$$

for $r < R$ and $0 < u < \pi/s$. Note that $s/k = [(\beta\gamma)^2 \sigma_{\theta\theta}\tau]^{-1}$, so that when $\beta\gamma \sim 1$ one has $s/k \sim (\sigma_\perp \tau)^{-1}$, which is usually small.

Without attempting to refine these solutions by matching inner and outer radial solutions or those inside and outside the beam region $0 < u < \pi/s$,* we have from Equations 5-6 and 5-7 a qualitative picture of the perturbed magnetic field, as in Figure 5.3.

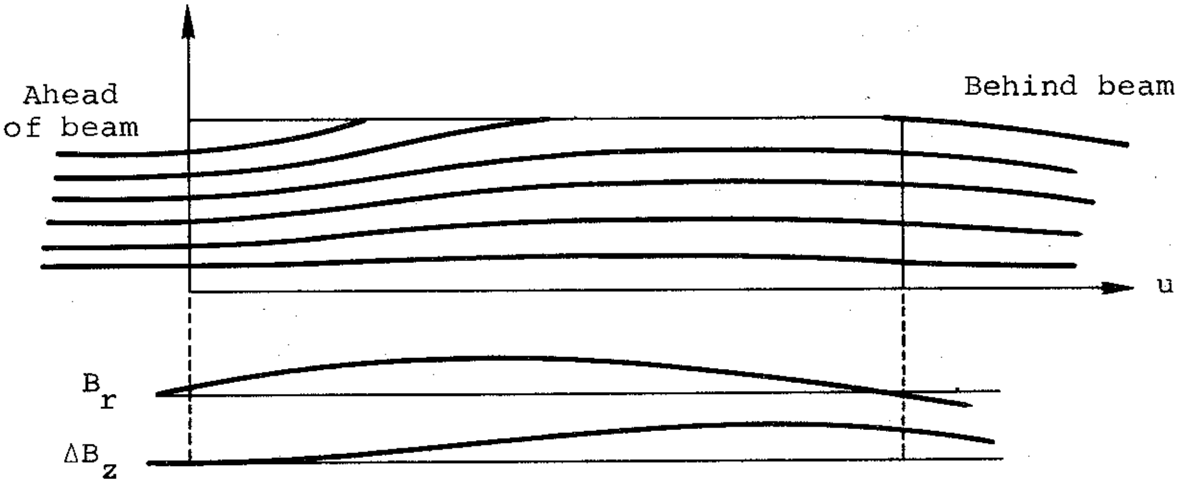

Figure 5.3 B_r, B_z profile for beam diamagnetism.

---

*Solutions ahead and behind the beam decay exponentially.

If one puts

$$J_\theta = \frac{4\pi c}{B} \frac{dP_\perp}{dr}$$

from the preceding section into this model with $J_\theta = rj(u)$, it becomes clear that the model represents a beam pressure $P_\perp = P_o - \alpha r^2$, i.e., a parabolic profile. In this sense the present model is more restrictive than that of the preceding section, but it is less restrictive in having the Z-dependence and radial magnetic field included. It is easy to show that with the parabolic density profile the solution of Equation 5-7 is approximately a solution of the diffusion equation: Equation 5-5, discussed earlier, provided $\sigma_\perp \tau$ is large and ΔB_z is small. The source term in that case is proportional to r for $r < R$, and the solution ΔB_z is constant with r for $r < R$. If the beam pressure is not monotonically decreasing with $r < R$, there are paramagnetic as well ad diamagnetic source terms.

5.2.3 Discussion. The consequence of these equations is that the beam is slightly diamagnetic when the beam pressure decreases monotonically with radius; for the Snark beam, with most of its 500 keV energy assumed to be in transverse motion, typical current densities of 10^4 A/cm^2 would cause a 10 to 20 percent reduction in field strength when the applied field is 10 kG. Yet this does not mean that pressure balance determines the beam radius. Since the transport region is short compared with the beam length $\beta c \tau$, the actual beam radius can be determined more by new incoming beam electrons than by the response of a beam electron to the pressure gradient. The forces on the beam electron are such as to make it drift primarily in the θ direction, thus reducing B_z. Radial motion due to $E_\theta \times B_z$ causes a radial drift of [0.1 E_θ (kV/cm)] cm in the time (~ 10 nsec) required to traverse the 1 meter drift region.

5.3 REDUCTION OF TRANSPORT EFFICIENCY WITH INCREASING NET CURRENT

In order to reach the end of the transport region, a beam electron must have sufficient parallel energy to overcome the retarding E_z electric field induced by imperfect current neutralization. The magnitude of E_z becomes larger at higher magnetic field (above about 8 kG) as indicated by the net current increase. We might therefore expect poorer transport at higher B_z because those electrons which cannot overcome the higher retarding voltage will either return to the diode or arrive downstream very late in the pulse, after the class of electrons which are counted as transported charge.

Because there is evidence that most of the beam energy at these current densities is in transverse motion (References 5.9, 5.10, and 5.11), these moderate E_z fields over a length of about 1 meter may cause reflection of a considerable part of the pulse. The fraction of total energy to be found in transverse motion increases with increasing current (if the energy, γ, is held fixed); therefore, we expect the fraction of parallel energy to be smaller late in the current pulse, where the current is larger.

Figure 5.4 shows a typical diode current and voltage trace and gives a rough estimate of the parallel energy of a typical electron* as a function of time during the pulse. The actual time history of the parallel energy is probably determined by conditions in the diode and at the diode-plasma interface (which

---

*A radial average, weighted by current density.

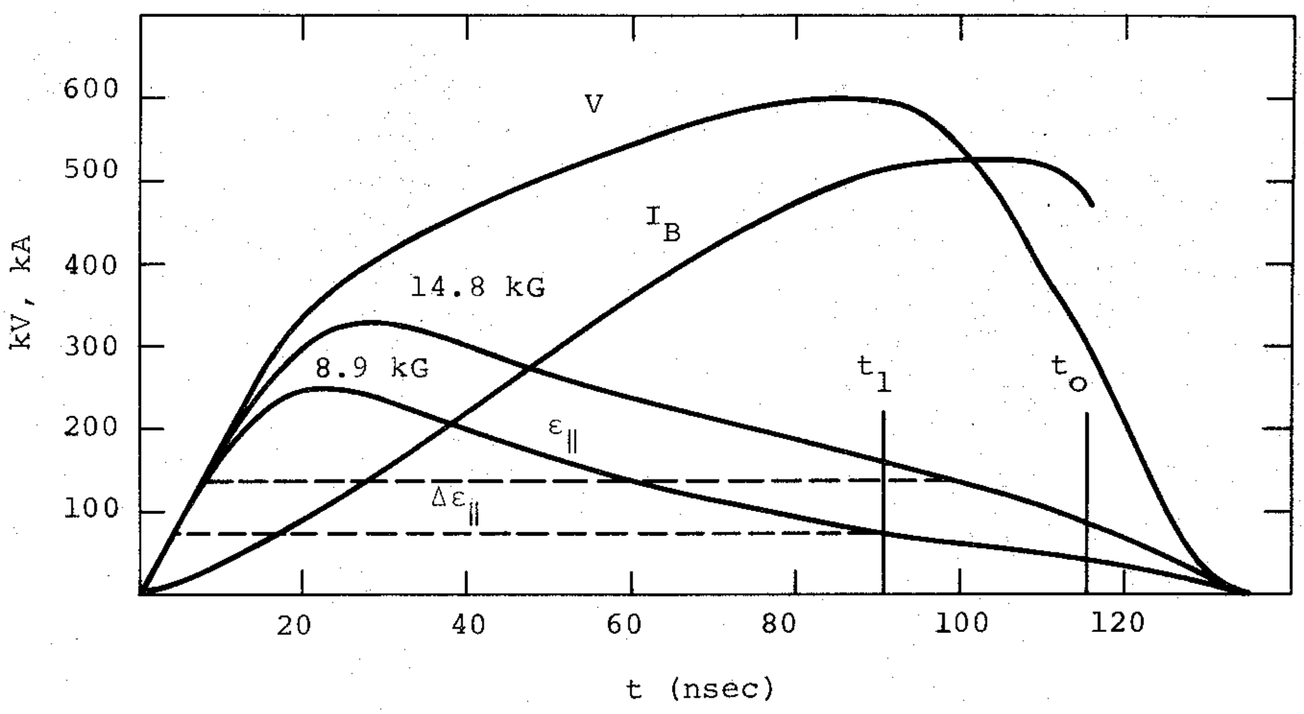

Figure 5.4 Time history of beam voltage and current, and estimated parallel energy $\varepsilon_\parallel$ for 3-inch-diameter cathode and two values of B_z. Parallel energy loss $\Delta\varepsilon_\parallel$ (dashed) is estimated from the measured net current by assuming E_z constant with z and t. Charge transport begins to break down at $t \approx t_1$ (shown for B_z = 8.9 kG), and emission stops at $t \approx t_o$.

may be a region of nonadiabatic motion). As yet there is no satisfactory theoretical model which predicts the pitch-angle distribution of the electrons leaving the diode, as a function of current and applied B_z magnetic field, although some steps have been taken toward such a theory (Reference 5.12). For applied B_z fields larger than the self-field, B_o, of the beam without current neutralization, the particle orbits should begin to "straighten out," tending toward paraxial orbits as $B_z \rightarrow \infty$. However, the fields used so far have provided $B_z \lesssim B_o$. (This is perhaps fortunate for transport because of the violent instability that can set in when the parallel energy distribution becomes sharp, Reference 5.13.)

As a rough model, suppose that all the θ-motion in the diode becomes perpendicular motion in the transport region. Suppose further that the motion in the diode is along the field lines $B_\theta \hat{1}_\theta + B_z \hat{1}_z$, and neglect the radial (pinching) velocities. (These assumptions are probably not realistic; they are made only to provide a working model.) This model gives the parallel energies shown in Figure 5.4:

$$\varepsilon_{\|}(t) = \frac{eV(t)}{1 + (B_o(t)/B_z)^2} \tag{5-8}$$

with V(t) the beam voltage. Diamagnetic effects on B_z are neglected.

The parallel deceleration is given by

$$m \frac{d}{dt}(\gamma u_{\|}) = - eE_{\|} + m\gamma u_E \cdot db/dt - \gamma^{-1} M \partial B'/\partial s \tag{5-9}$$

where $u_{\|}$ is the guiding center velocity along field lines (approximately the particle velocity V_z),

$$\vec{u}_E = c\vec{E} \times \vec{B}/B^2, \quad B' = B\sqrt{1 - E_{\perp}^2/B^2}$$

$$M = P_{\perp}^2/2mB'$$

with $P_{\perp}$ the perpendicular momentum observed from the frame moving with u_E. The unit vector in the direction B is indicated by $\hat{b}$, and the path length along field lines by s.

The last two terms in Equation 5-9 represent magnetic mirror forces due to diamagnetism of the beam. If this is a slight effect as implied in Section 5.2, we expect the dominant effect in determining charge transport to come from $E_{\|} (\simeq E_z)$. This E_z is roughly constant during the pulse[*] but scales with the rise rate of the net current when $B_z \gtrsim 7$ kG, as observed in Section 5.1. The magnitude of the net current is not dramatically different at large and small distances, so while reflection of beam electrons is negligible we may take $\partial E_z/\partial z \approx 0$. Neglecting diamagnetic effects, the degradation of parallel energy during transit is

$$\Delta\varepsilon_{\|} = e \int E_z dZ + \Delta_a \varepsilon_{\|}$$

where $\Delta_a \varepsilon_{\|}$ is the parallel energy loss in the anode foil and in the screening foil of the Faraday cup. When $\Delta\varepsilon_{\|} \approx \varepsilon_{\|}$ for a typical electron leaving the diode, it is expected that the charge will not reach the detector. It will return to the diode and, if the voltage there has decreased, it will fall into the cathode (this is the case for the final portion of the pulse in Figure 5.4). Charge transport thus greatly diminishes at the time, t_1, at which $\Delta\varepsilon_{\|} \approx \varepsilon_{\|}$. (Some transport persists because electrons near the beam axis have most of their energy in parallel motion.) Because the beam current is a rising function of t, this near termination of transport can significantly affect the Coulomb transport efficiency, ξ, even if t_1 is not much less than t_o, the time at which energetic emission ceases in the diode.

---

[*] Actually, during that portion of the pulse which is being transported. This is deduced from the fact that both J_{net} and J_B increase more or less linearly.

If t_1 occurs when the beam voltage V is nearly constant, then the model Equation 5-8 gives

$$B_o^2(t_1) = B_z^2\,[eV/\Delta\varepsilon_{\parallel} - 1]$$

If the beam current I_B is still linearly rising, and if

$$\Delta\varepsilon_{\parallel} \approx LeE_z + \Delta_a\varepsilon_{\parallel},$$

with

$$L \equiv \text{transport distance}$$

$$\Delta_a\varepsilon_{\parallel} \sim 10\ \text{keV}^*$$

and

$$E_z \sim \eta dJ_B/dt$$

as discussed in Section 5.1, this gives

$$t_1 \sim (caB_z/2\dot{I}_B)^2 \left[\frac{eV}{e\dot{I}_B R(B_z) + \Delta_a\varepsilon_{\parallel}} - 1\right] \tag{5-10}$$

where $R(B_z) = \eta L/\pi a^2$ is the turbulent resistance.

This approach gives magnitudes of the charge transport efficiency which agree moderately well with the data at higher B_z where the model Equation 5-8 is expected to apply; (certainly it does not apply for $B_z \approx 0$). However, $\partial\varepsilon_{\parallel}/\partial t$ is small as shown in Figure 5.4, and this means that t_1 is a sensitive function of the model and of E_z. For this reason Equation 5-10

---

[*] (0.5 mil titanium anode.)

should not be used for quantitative predictions; only the underlying idea is to be applied. (For instance Equation 5-8 gives the efficiency ξ increasing with B_z up to $\sim B_o$, while the real optimum B_z is much lower.)

A consequence of this model is that when the pulse shorts early, ξ should be large. This is in agreement with the data, which show t_o increasing with increasing B_z.

REFERENCES

5.1. R. Lee and R. N. Sudan, Phys. Fluids 14, 1213 (1971).

5.2. R. J. Briggs, Electron-Stream Interaction with Plasmas, MIT Press, Cambridge, Massachusetts (1964).

5.3. K. N. Stepanov and A. B. Kitsenko, Zh. Tekh. Fiz. 31, 167 (1961).

5.4. R. C. Davidson and C. S. Wu, Phys. Fluids 13, 1407 (1970).

5.5. M. M. Shoucri and A. B. Kitsenko, Plasma Phys. 10, 617 (1968).

5.6. C. F. Kennel, Phys. Fluids 9, 2190 (1966).

5.7. S. M. Hamberger and M. Friedman, Phys. Rev. Letters 21, 674 (1968).

5.8. S. Putnam, "Theoretical Electron Beam Studies," PIFR-105, Physics International Company, San Leandro, California, April 1970.

5.9. J. Benford and B. Ecker, Bull. Am. Phys. Soc. 14, 1070 (1969).

5.10. G. Yonas and P. Spence, in Record of Tenth Symposium on Electron, Ion and Laser Beam Technology, edited by L. Marton (San Francisco Press, 1969) p. 143.

5.11. J. J. Clark and S. Linke, Cornell University Laboratory for Plasma Studies Report LPS 23, August 1969.

5.12. D. C. de Packh, Radiation Project Internal Report #13, Naval Research Laboratory, March 1970.

5.13. H. Bohmer, J. Chang, and M. Raether, Phys. Fluids 14, 150 (1971).

SECTION 6

BEAM TRANSPORT IN NEUTRAL GAS, NO EXTERNAL MAGNETIC FIELDS

by D. Pellinen

6.1 INTRODUCTION

The least complex system of transport and combination for a multi-megampere machine involves subdividing the output current into separate magnetically isolated beamlets. If the beam self-pinches in the diode, current densities of 100 $\mathrm{kA/cm^2}$ are achievable. Transport in a thin-walled array of separate guide pipes could be carried out at this current density. It has been known for some time, however, that there are competing mechanisms which prevent efficient transport of pinched high ν/γ beams, when they are injected into a neutral gas without externally applied field (Reference 6.1). Since such beams are characterized by highly nonparaxial electron motion, a large fraction of the total beam current is lost over the first few centimeters of transport if the gas is preionized or if it is at a pressure appropriate to rapid breakdown--approximately 0.75 torr in nitrogen. After these high-angle components are lost, the remaining portion of the beam propagates relatively efficiently; (an e-folding distance of approximately 250 centimeters has been observed for a 250 kV beam propagating in a 1-1/4-inch-diameter pipe). On the other hand, if gas breakdown is delayed by use of sufficiently low-pressure gas (less than 0.5 torr in nitrogen), then the net current can equal the primary current for a larger fraction of the pulse duration, resulting in better containment of the transverse energy components by the azimuthal self-magnetic field. In this case, however, the rapidly rising current creates a back emf which decelerates the energetic electrons.

Consider, for instance, a 6-MA pulser with the current of the machine subdivided into N separate beamlets. Then, for a risetime of 20 nsec, we get E_z (V/m) = 10^{-7} dI/dt (A/sec) = $10^{-7} \times 6\times10^{6}/N \times 1/20\times10^{-9} = 30/N$ MV/m. If the beam is propagated at pressures below 1 torr, the breakdown time will be relatively insensitive to E/P and will be equal to approximately 10^{-9} seconds divided by the pressure in torr (Reference 6.2). If the pressure is chosen sufficiently low to prolong the breakdown time but high enough to give collisional charge neutralization, then a reasonable value for pressure would be 0.1 torr, giving a breakdown time of 10^{-8} seconds. If we assume that the characteristic breakdown time controls the velocity of the beam front, then we can approximate the beam-front velocity by $v_f \approx V/E_z t_B$. This gives $\beta_f = 10^{-2}$ N. By comparing the beam-front velocity with the velocity of propagation of high ν/γ electrons within the beam and by requiring negligible erosion over distances of roughly 2 meters, we see that at least thirty separate beams are required. In addition, the allowable pipe diameter for efficient transport of the self-pinched beam is questionable. Previous experience (Reference 6.3) indicates that the low-pressure beam behavior is subject to even greater losses than that from erosion alone when the beam is contained within a relatively small-diameter conducting pipe. As a result, one is not able to closely pack the transport beams over a small output area. By creating a beam which has minimal transverse energy, many of the problems previously discussed can be eliminated. Transport of such a "cold" beam has been suggested by J. C. Martin (Reference 6.4).

Assuming uniform current density from a disk cathode of radius, r, anode-cathode distance, d, and no diode impedance collapse during the pulse, beam pinch (and the resulting generation of large transverse-energy components) can be avoided if the diode current (assumed here to be the Langmuir-Child's Law current) is less than the critical value given in Reference 6.5:

$$I_{L-C} = \frac{V^{3/2}}{136} r^2/d^2 < 8500\ \beta\gamma\ (r/d)$$

The current for each beamlet at 1 MeV must then be less than 85,000 amperes. The hypothetical 6-MA pulser would require, for example, 90 separate 65,000-ampere beams for a diode r/d of 3.

The approach for the neutral gas experiments in this program was to generate small area beams (with $I < I_{critical}$) and to investigate their transport efficiency in small-diameter guide pipes.

6.2 EXPERIMENTAL DIODE BEHAVIOR AND TRANSPORT EFFICIENCIES

The experiment was performed on the 738 Pulserad (which was operated at 600 to 800 kV peak voltages) using two cathodes mounted on a low inductance dome inside the tube. Total currents as large as 150 kA could be generated in this configuration (75 kA per beam) and lower currents could be obtained by reducing the pulse charge voltage. The experimental configuration is shown in Figure 6.1. Diode current and voltage waveforms were measured with Rogowski coils surrounding each cathode and an annular capacitive voltage divider. Guide pipes were built ranging from 1.9 to 2.54 cm in diameter and with lengths ranging from 4 cm to 1 meter. Two types of cathodes were also

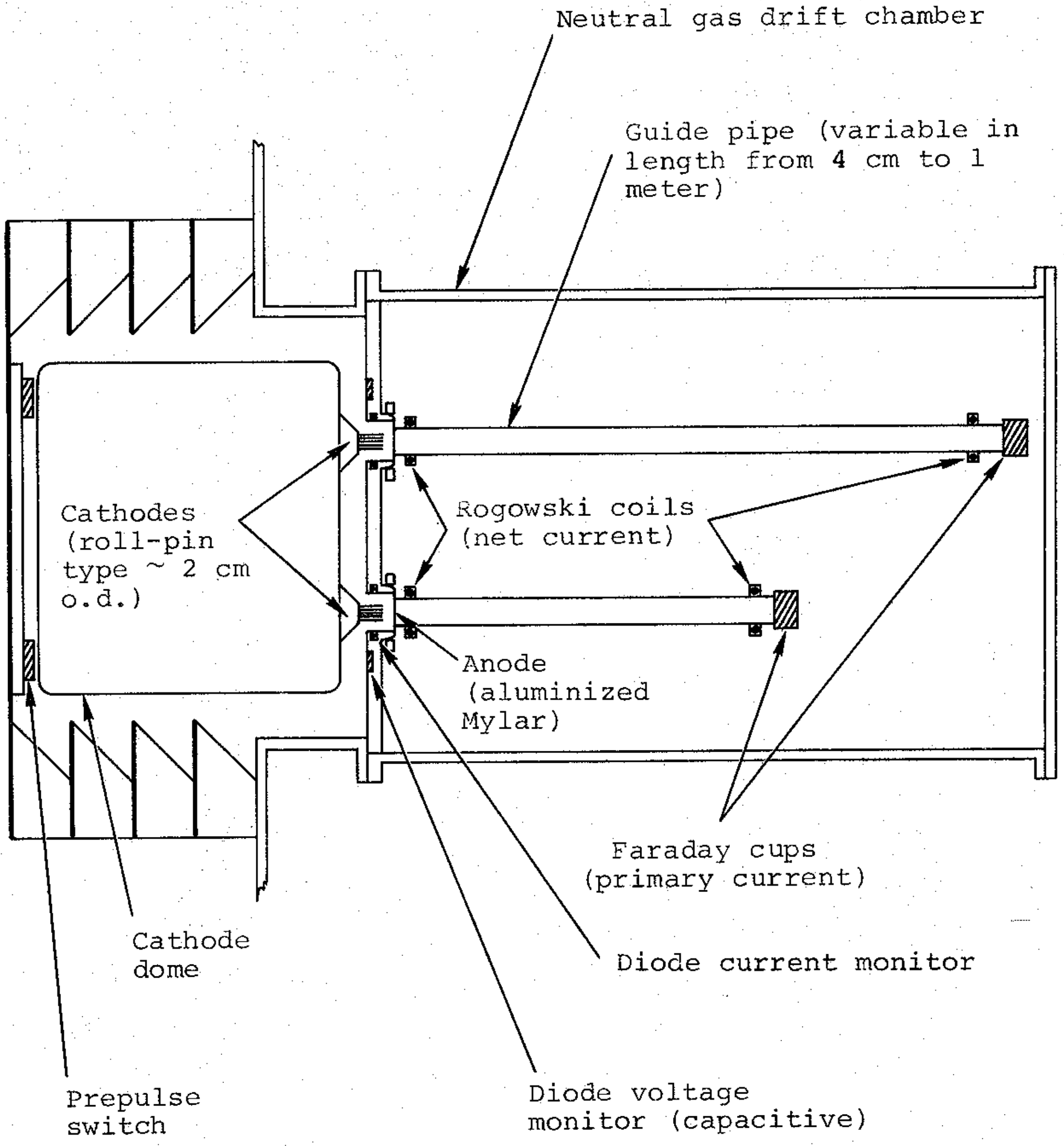

Figure 6.1 Experimental configuration for neutral gas transport experiments.

developed; a 2-cm-diameter flat cathode and a 1.76 cm hollow annular cathode. Both used hollow roll pins as their emitting surface. Figure 6.2 shows a photograph of the two diodes mounted on the pulser. An instrumentation package consisting of a self-integrating Rogowski coil to measure net beam currents and a high-current Faraday cup was made to snap on the end of each guide pipe. The Rogowski coil was located 0.95 cm in front of the Faraday cup collector face. Anode-cathode spacing and guide pipe length and diameter were independently variable. Data were simultaneously taken on both transport systems with parameters being independently varied.

Two pulsing sequences were made with the following goals:

a. Determine diode impedance as a function of anode-cathode spacing and determine the effect of self-pinching on each cathode. Determine the attractive effect of the two cathodes on each other and determine injection efficiency.

b. Optimize injection efficiency and measure transport efficiency as a function of pressure, anode target distance, and injected current.

Phase one was accomplished with the 2-cm flat cathodes. The initial pulsing was done using the tube voltage monitor and the two anode current monitors as impedance diagnostics. The effect of beam self-attraction was qualitatively checked by open shutter photography and calorimetry. Injection efficiency was measured by mounting a Faraday cup at an anode target distance of 8 cm and taking the ratio:

$$\frac{I_{\text{FC (peak)}}}{I_{\text{Diode (peak)}}}$$

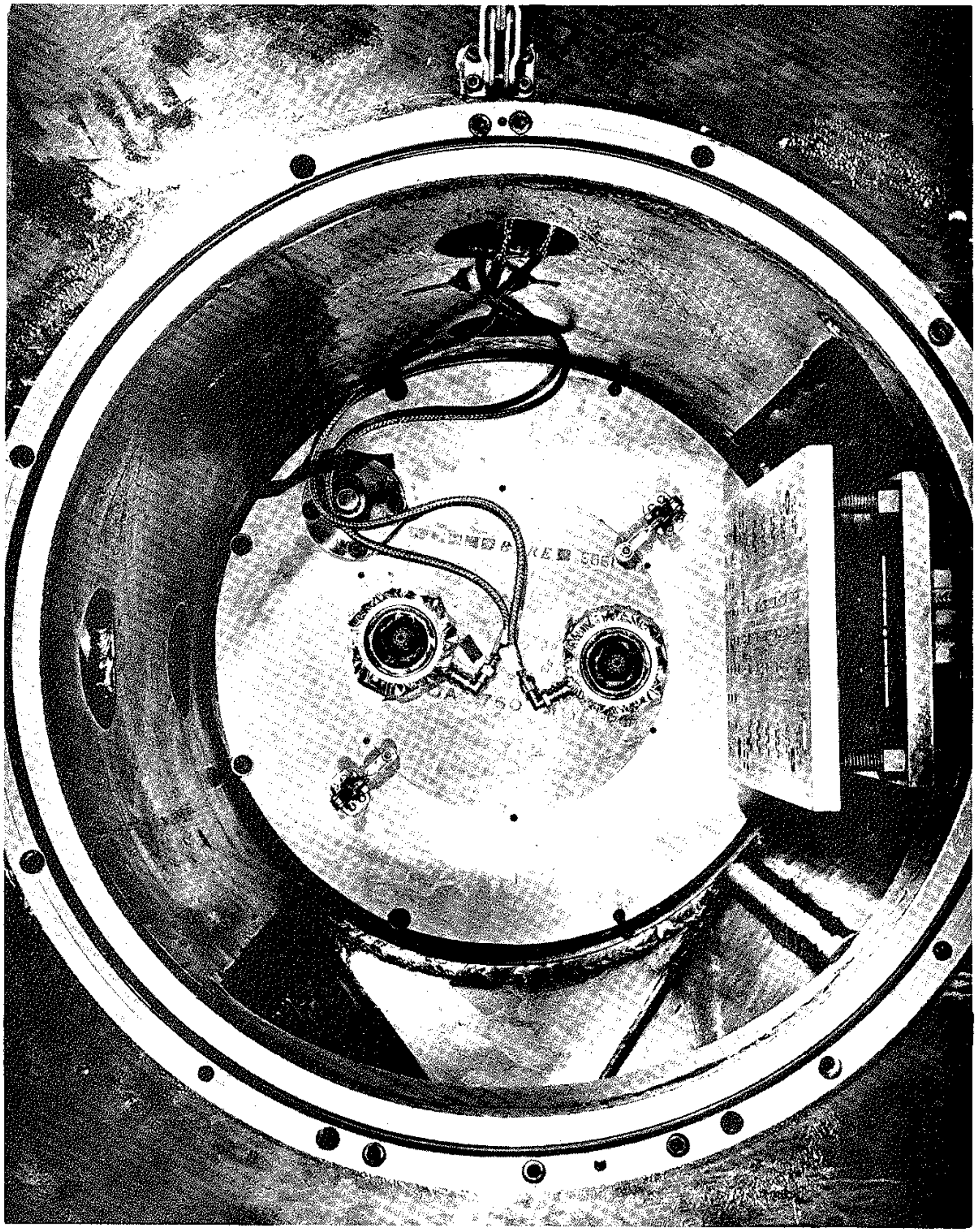

Figure 6.2 Photograph of double-diode setup used for neutral gas transport tests.

Conclusions drawn from the first shots were

a. Two independent beams could be generated and the beams did not seem to perturb each other.

b. The diode current could be described by Child's Law where the constant was on the order of 50.

c. Injection efficiency, i.e., I_{FC}/I_{Diode}, was on the order of 30 to 40 percent, at Z = 8 cm.

d. A cool beam was not generated; pinching in the diode could not be avoided.

In an attempt to improve injection efficiency by lowering the degree of diode pinch a new pair of cathodes were built to raise the diode impedance at the same A-K gap. The cathodes were annular in shape (1.76 cm o.d.) and roll pins formed the emission surface. Further minor improvements were made in the hardware and testing was again begun. Twenty-four pulses were taken with mean energies ranging from 0.446 MV to 0.730 MV with peak currents of 70 kA to 31 kA per cathode. Injection efficiency was monitored with a Faraday cup at 4 cm and was found to be approximately 65 to 70 percent relatively independent of injected current. Transport efficiency versus drift pressure was measured at Z = 0.5 meters (see Figure 6.3); it was found to peak in the range of 0.4 to 0.6 torr and was in the range of 50 to 60 percent of the measured diode current, corresponding to transport of 80 to 90 percent of the injected current, i.e., the current that reached Z = 4 cm. Transport was measured at Z = 86 cm at a pressure of 0.5 torr and transport efficiencies of 40 percent of the diode current or 60 percent of

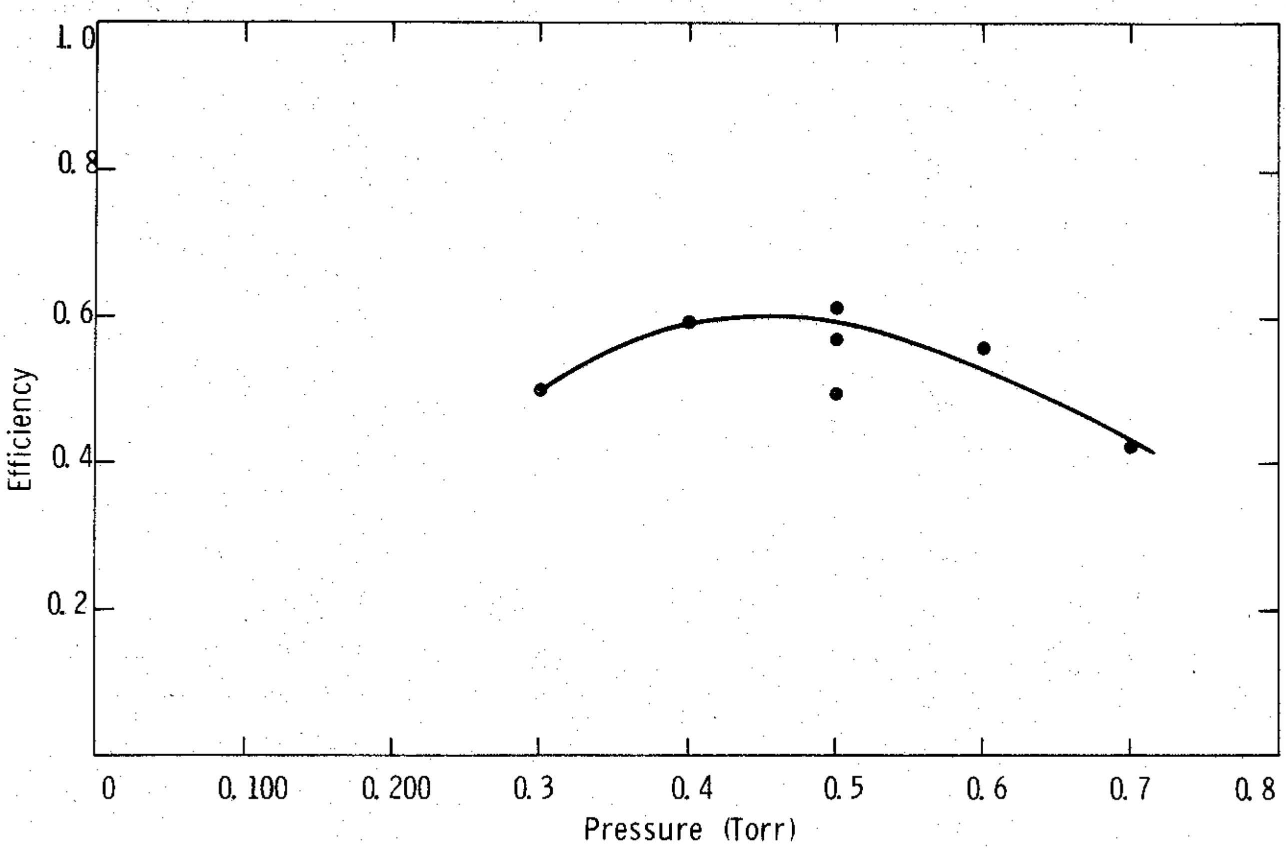

Figure 6.3 Transport efficiency versus pressure at Z = 0.5 meter - 1.25 cm radius guide pipe--peak Faraday cup current versus peak diode current.

the injected current were measured. Transport efficiency versus distance is plotted in Figure 6.4 and typical data (showing injected and transported current waveforms) is given in Figure 6.5.

6.3 CONCLUSIONS

The results of the neutral gas transport work have shown that the suggested approach (namely generation of small diameter 50 to 80 kA beams and transport in small diameter guide pipes) is unfeasible because of the inability to prevent beam pinch (high transverse energy) in the circular and annular diodes. The Langmuir-Child's Law constant, describing the impedance behavior of the diodes appeared to be in the range 40 to 50 which implies currents:

$$I = \frac{V^{3/2}}{50} r^2/d^2 < 8500\ \beta\gamma\ r/d$$

or $I \lesssim 25$ kA at 1 MV would be required to prevent diode pinch.

Beam injection efficiency was definitely improved by use of a hollow (annular) cathode. Beams from the 2-cm-diameter solid cathode showed loss of 50 percent over the first 8 cm of transport, while the loss for beams generated by a similar diameter hollow cathode was 30 percent over the same distance.

There appear to be several directions for neutral gas transport that may yet show promise for application to multi-megampere machines:

a. Generate beams with lower current density to avoid diode pinch.

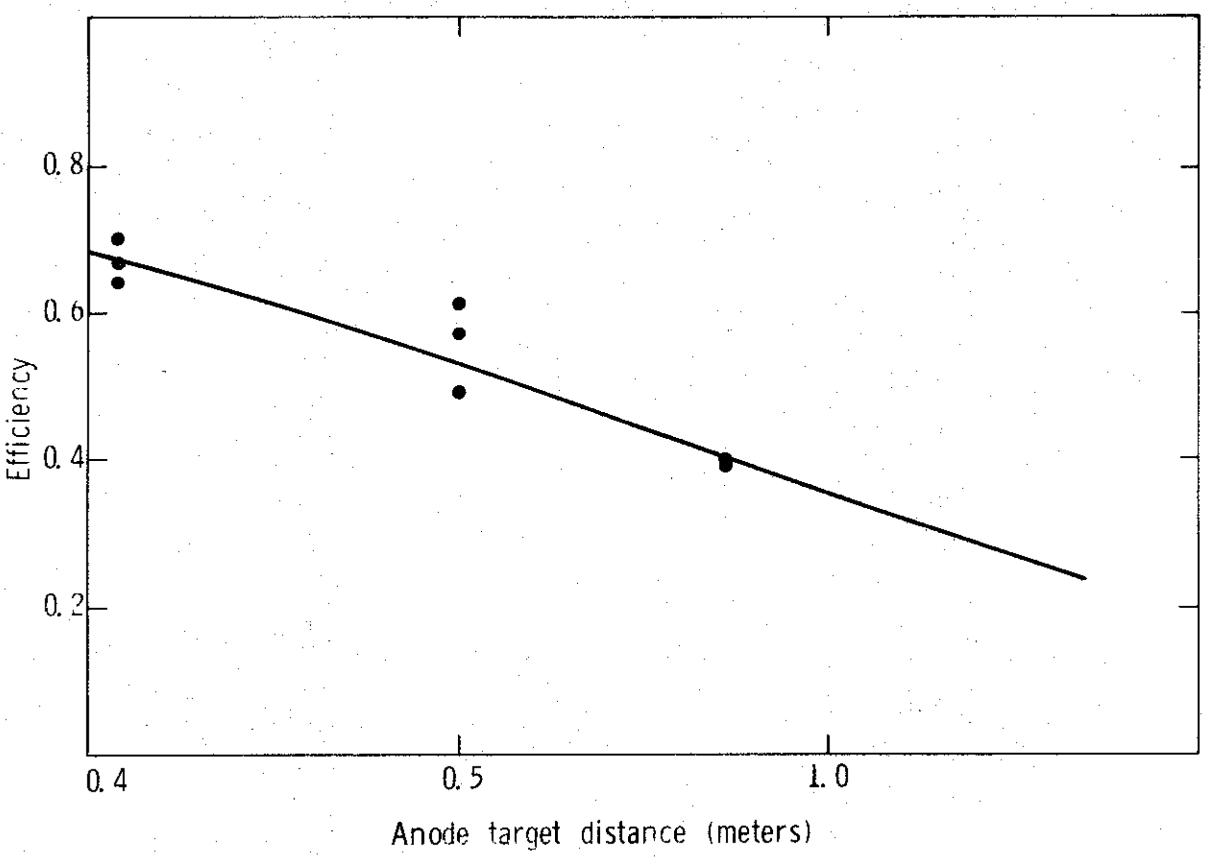

Figure 6.4 Transport efficiency $\nu/\gamma \overset{\approx}{>} 1.5$ (P = 0.5 torr) 1.25 cm radius guide pipe.

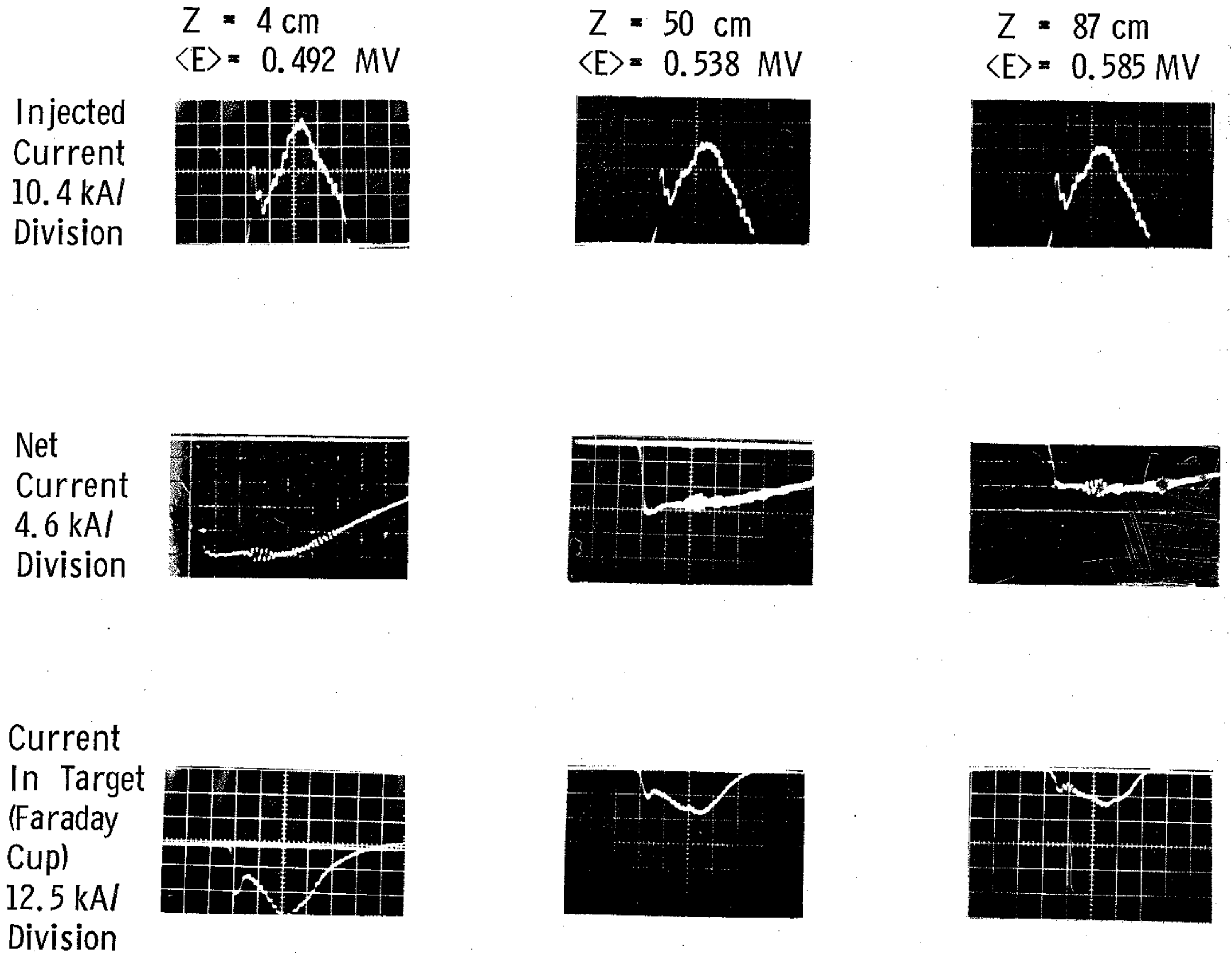

Figure 6.5 Transport versus distance (0.500 torr) (current waveforms).

b. Use annular or strip cathodes to achieve higher current densities without pinch.

c. Couple the separate beams in a final combination/ compression stage.

The prospects for neutral gas transport systems operating in the range 20 to 50 kA/cm^2 are not, however, promising.

REFERENCES

6.1. G. Yonas, P. Spence, B. Ecker, "Current Neutralization in High ν/γ Relativistic Electron Streams," Bull. Am. Phys. Soc. 14, 1070 (1969).

6.2. G. Yonas and P. Spence, "Experimental Investigation of High ν/γ Beam Transport," Proc. 10th Symposium on Electron, Ion, and Laser Beam Technology, L. Marton, editor; San Francisco Press, Inc., 1969.

6.3. G. Yonas, et al., "Dynamic Effects of High ν/γ Beam Plasma Interactions," DASA 2426, August 1969.

6.4. J. C. Martin, paper presented at the DASA Simulator Design Conference, Washington, D. C., January 26-28, 1971.

6.5. F. Friedlander, R. Hectel and J. Jory, Technical Report No. 1 for Contract DASA 01-68-C-0025, January 1968.

SECTION 7

DIAGNOSTICS DEVELOPMENT

by D. Pellinen and D. Wood

7.1 INTRODUCTION

Instrumentation for the measurement of electron beam and X-ray output parameters was developed on this program as an extension of a wide base of existing voltage, current, and X-ray diagnostics developed at Physics International over the last decade.

Diagnostics specifically developed or modified for use on the Mylar lines included capacitive voltage monitors for the tube and line, a large self-integrating Rogowski coil (current monitor) surrounding the cathode emission area, Faraday cups (to measure injected and transported current), and X-ray fluence and depth-dose calorimeters. The diode and electron beam diagnostics are described in Section 7.2. Section 7.3 outlines the X-ray diagnostics.

7.2 ELECTRON BEAM AND DIODE DIAGNOSTICS*

7.2.1 Voltage Monitors. Voltage measurement near the field emission diode of any high current pulser is desirable

---

*By D. Pellinen.

since the magnitude of the inductive portion of the voltage waveform is minimized. The restrictive geometry of the low inductance tubes used on the Mylar line facilities precluded the use of graded resistive monitors of the type developed for use on the more spacious (higher inductance) tubes used on PI's oil dielectric machines; for this reason an annular capacitive voltage monitor, recessed into the anode plate, was developed and tested for use on the 0.3 Ω/100 kV Mylar line and on Snark.

The physical location of the capacitive monitor was shown in Figure 2.6. A detailed view of the monitor construction is given in Figure 7.1; (this particular version was used on the 0.3 Ω/100 kV line in field gradients ≈ 300 kV/cm). A 3-mil Mylar insulator was used between the annular plate and ground. A shielding ring was employed to minimize electric field at the epoxy-metal joints. This version employed a spark gap set to prevent excessive voltage application to the output cable should an arc occur between the capacitor plate and the anode plate; no such arcing occurred during use, so the spark gap was not used on subsequent monitors. An electrical schematic is given below:

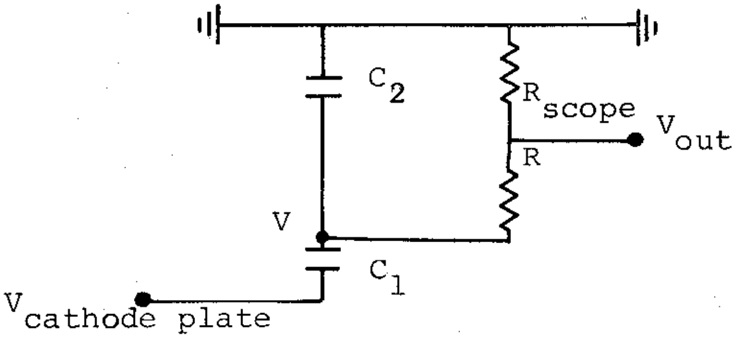

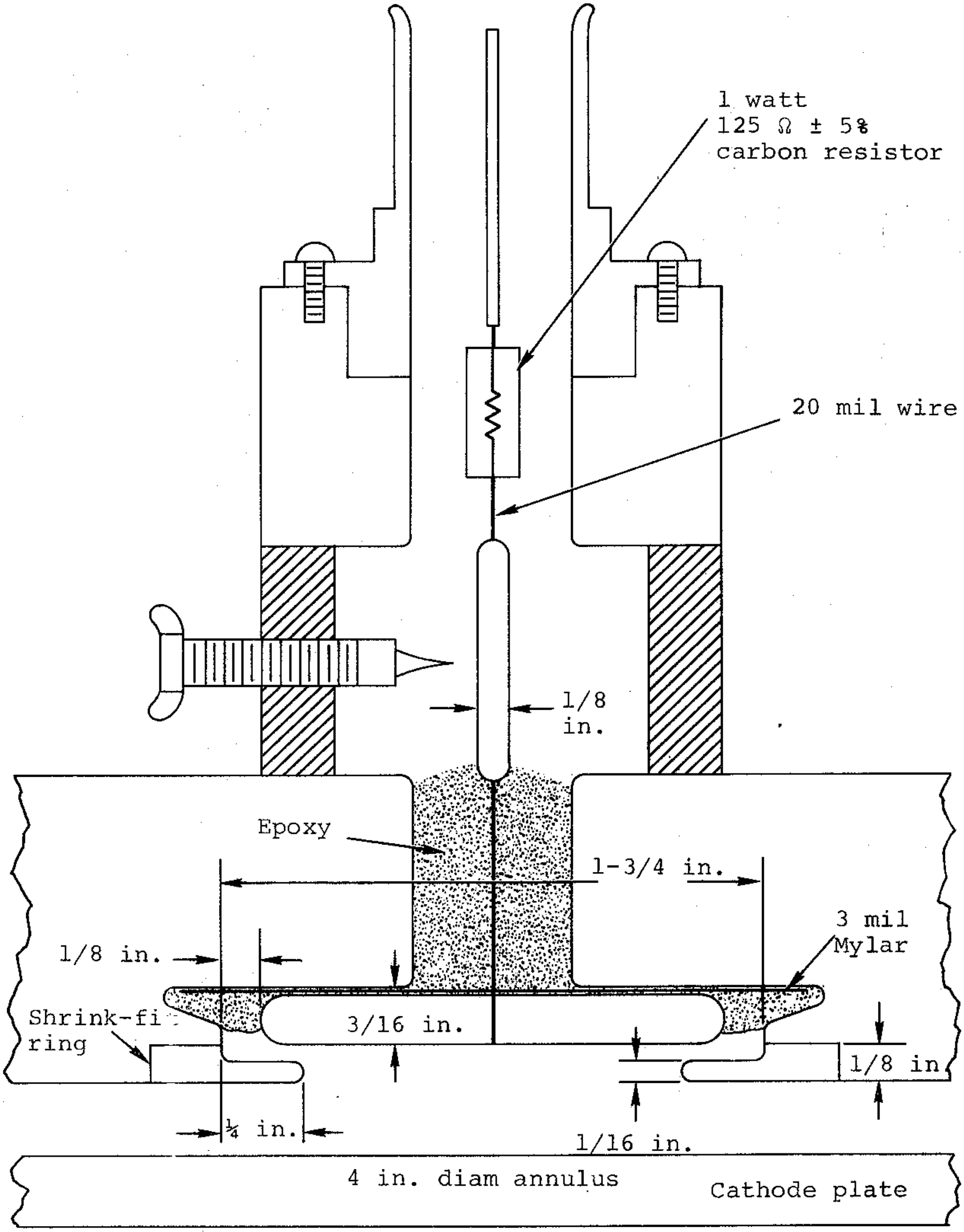

Figure 7.1 Capacitive monitor construction.

The ratio of voltage at the cathode plate to the voltage on the capacitor plate, $\approx V_{\text{cathode plate}}/V = C_2/C_1$ was kept in the range of 200-400/1 with C_1 several tens of picofarads, and C_2 a few nanofarads. Further attenuation was given by the ratio $R_{\text{scope}}/(R_{\text{scope}}+R)$, where the total resistance in the monitor circuit $(R_{\text{scope}}+R)$ was chosen to given an RC time constant $\sim 1\ \mu\text{sec}$. To avoid unnecessary loss of signal, a 125 Ω cable was used and fed directly into a 519 scope; extra resistance was added near the monitor itself (typically a few hundred ohms). This configuration minimized reflections in the monitor circuit and gave total attenuation values $V_{\text{cathode plate}}/V_{\text{out}}$ of 300 to 800/1.

Calibration of the monitors was performed in situ by one of two techniques: (a) When the tube assembly was removed (0.3 Ω/100 kV line) a pulsed voltage was applied to the cathode plate using an external 50 Ω cable pulser. Capacitive monitor output was then calibrated against a resistive monitor placed external to the tube. (b) The monitor was calibrated against line voltage monitors by firing low voltage open-circuit shots.

Performance of this voltage monitor on the 0.3 Ω/100 kV line (and on the PI Mylar line, 1.0 Ω/300 kV) has been good. A similar monitor installed on the Snark tube has performed erratically. At voltage levels across the anode and cathode plates of $\lesssim$ 500 kV we have successfully used the monitor, (see Figure 2.7 in Section 2); however at higher voltage levels the waveform shows nonreproducible behavior occurring after 50 or 60 nsec into the pulse. A possible explanation is the formation of a plasma sheath near the cathode plate which could effectively change the capacitance between the active monitor element and the cathode plate.

7.2.2 Current Monitors. Faraday cups have been used extensively for measurement of primary (energetic) electron current. A description of the original monitor (used at the anode plane) is given in Appendix B. The modification to this basic cup allowing measurement of propagated current is described in Reference 7.1. A similar cup was constructed on this program to be transparent to pulsed magnetic fields for use in Stalling's B_z transport experiments.

Rogowski coils were used to monitor diode current. The monitors are described in Appendix C.

7.3 X-RAY DIAGNOSTICS*

Much of the X-ray diagnostic equipment used in the performance evaluation of the Snark machine has been under continual development at Physics International Company (PI) for several years. The often times unique diagnostic requirements encountered on other PI machines such as, for example, the 738 Pulserad in the low-impedance photon mode, have necessitated the development of sophisticated but reliable equipment that can be used in a routine manner on the different machines. Included are both time-resolved and time-integrated diagnostics.

The time-resolved diagnostics include commercial scintillator photo diodes and special photoelectric diodes manufactured by Physics International. These detectors were used on Snark to provide the time history of the radiation pulse and other qualitative information.

---

*By Don Wood.

The time-integrated diagnostics included conventional thermoluminescent dosimeters (TLD) and calorimeters. In materials suitable for use in calorimetry the absorbed radiation is converted entirely to thermal heat energy so that the measurement of the temperature rise of the irradiated material provides a fundamental and direct method of determining the absorbed dose. The temperature rise is also independent of photon energy and dose-rate. Used on Snark were tantalum-foil depth-dose calorimeters and a totally absorbing tungsten fluence calorimeter. Thermoluminescent dosimeters were used on all shots to provide normalization of the calorimetry between successive shots to account for nonreproducibility and to map the radiation field.

Characterization of the Snark X-ray output with the time-integrated dosimetry included the following steps: (a) determining the rate of fall-off in the X-ray intensity as a function of distance from the source point with TLD's, (b) measurement of the X-ray deposition in the tantalum-foil depth-dose array that is corrected for the rate of fall-off determined from the TLD's in step (a), and (c) measurement of the X-ray fluence. The time-resolved diagnostics were used to determine when the radiation pulse terminated so that accurate calculations of total energy could be made from the diode diagnostics. The results of these calculations were then used to determine the yield and efficiency of X-ray conversion.

The following sections briefly describe the depth dose and fluence calorimetry and the last section discusses the results of the measurements on Snark. Also included is a comparison with the low impedance output from the 738 Pulserad using thin beryllium debris catchers.

7.3.1 Tantalum Depth Dose Calorimeter. A tantalum depth dose calorimeter was used to measure the front surface dose (FSD) and the deposition versus depth profile. A cross sectional diagram of the calorimeter positioned above the Snark diode and showing the location of the thermoluminescent dosimeters (TLD) is given in Figure 7.2. The calorimeter consists of a series of thin tantalum foils, each monitored with a thermocouple and contained within a small evacuated chamber with a beryllium window. Each foil is surrounded by a guard ring of the same material so that edge losses are minimized and the back foils are shielded from radiation incident at large angles with respect to the beam axis. The foil composite behaves to the incident radiation as if it were a solid material so that the energy deposited in depth in the material can be accurately measured. The dose in calories per gram for the i^{th} foil is given by

$$\frac{Q}{m_i} = \left[1 + \frac{X_i}{X_o}\right]^n 0.647 \ \Delta V_i \left(\frac{\text{cal}}{\text{gram}}\right) \text{ in Ta}$$

where, X_i = distance from the center of the first foil to the center of the i^{th} foil (cm)

X_o = distance from the X-ray source to the center of the first foil (cm)

ΔV_i = thermocouple response of the i^{th} foil (millivolts)

n = exponent to convert for dose fall-off over the thickness of the foils.

The millivolt readings (ΔV_i) of the foils were read out with a VIDAR digital voltmeter and printed on a tape.

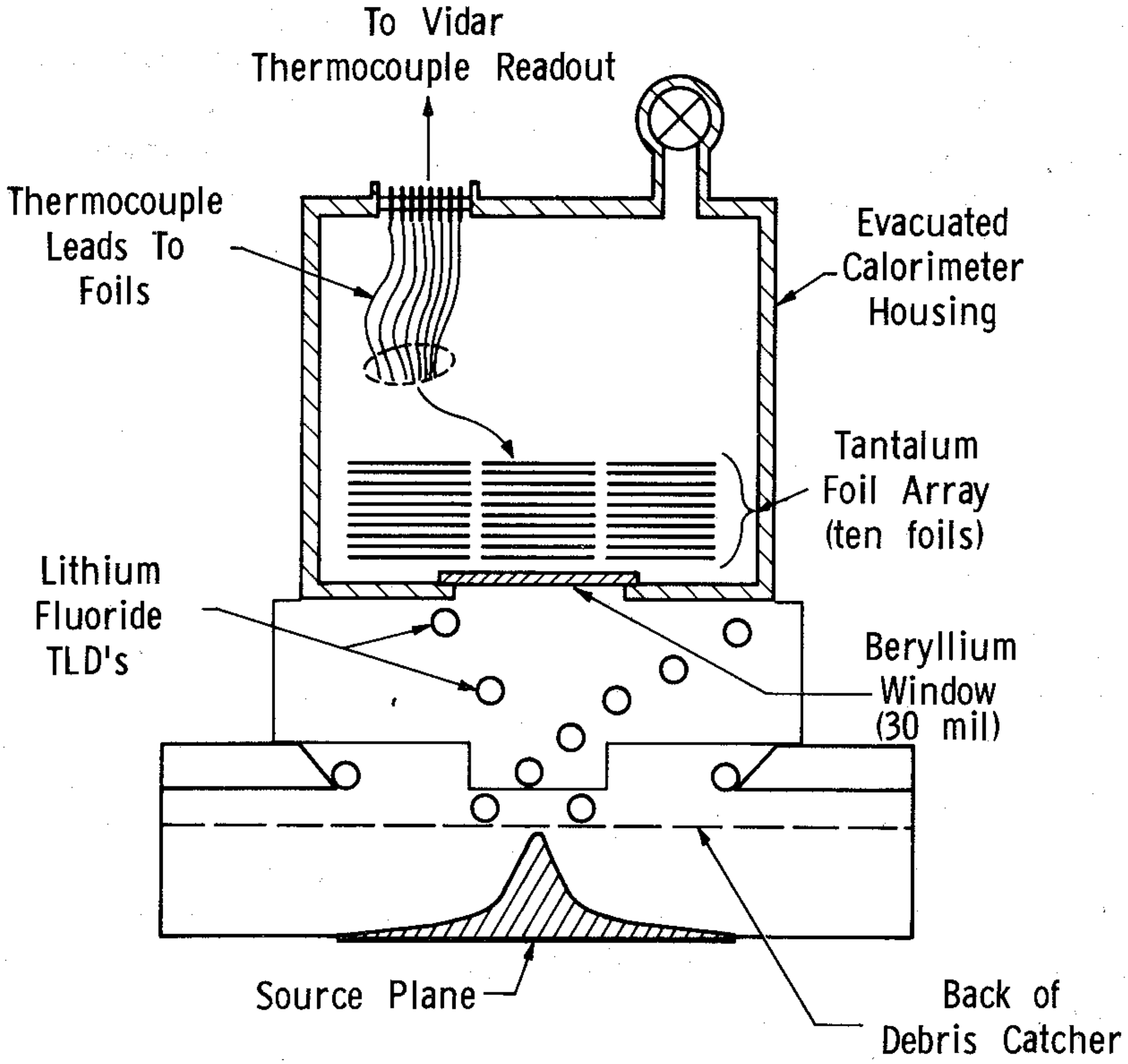

Figure 7.2 Schematic cross section of depth dose calorimeter and thermoluminescent dosimeter array showing relative position of X-ray source.

A328

The above relation accounts for the axial dose fall-off and extrapolates the dose in all foils back to the location of the first foil.

The FSD is calculated from the above equation where the value of ΔV_1 is determined by extrapolating the cooling curve for the first foil to the time the shot fired. The FSD represents the average deposition across a 0.0005-inch tantalum foil. The fluence (in calories per square centimeters) is determined by the area under the deposition profile. Since the tail of the profile is the most difficult to measure experimentally, some error is inherent in determining the fluence and it is highly desirable to have an independent measurement of X-ray fluence.

7.3.2 <u>Fluence Calorimeter</u>. The fluence calorimeter provides a direct measurement of X-ray fluence. A cross sectional schematic diagram is shown in Figure 7.3. The calorimeter housing is approximately 4 inches in diameter by 9 inches long and is easily portable. An ion pump and absorption pump provide the required vacuum. The aluminum heat shield attached to the end of reservoir forms an isothermal cavity at the reference temperature. The absorbing mass is a solid cylinder of tungsten and is suspended inside the isothermal cavity by silk threads. Intermittent manual contact of the absorber to the face of the reservoir provides accurate temperature reference (T_o). The area through the circular cross section of the absorber is 5.63 cm and its length is 1.5 cm, which gives only 10 percent transmission at 660 keV. Temperature changes induced by X-ray deposition are monitored with a thermistor. The fluence is calculated from the equation,

$$\frac{Q}{A} = \frac{m}{A} C_p \left(\frac{\Delta T}{\Delta R}\right)_o \Delta R \ (\mathrm{cal/cm^2})$$

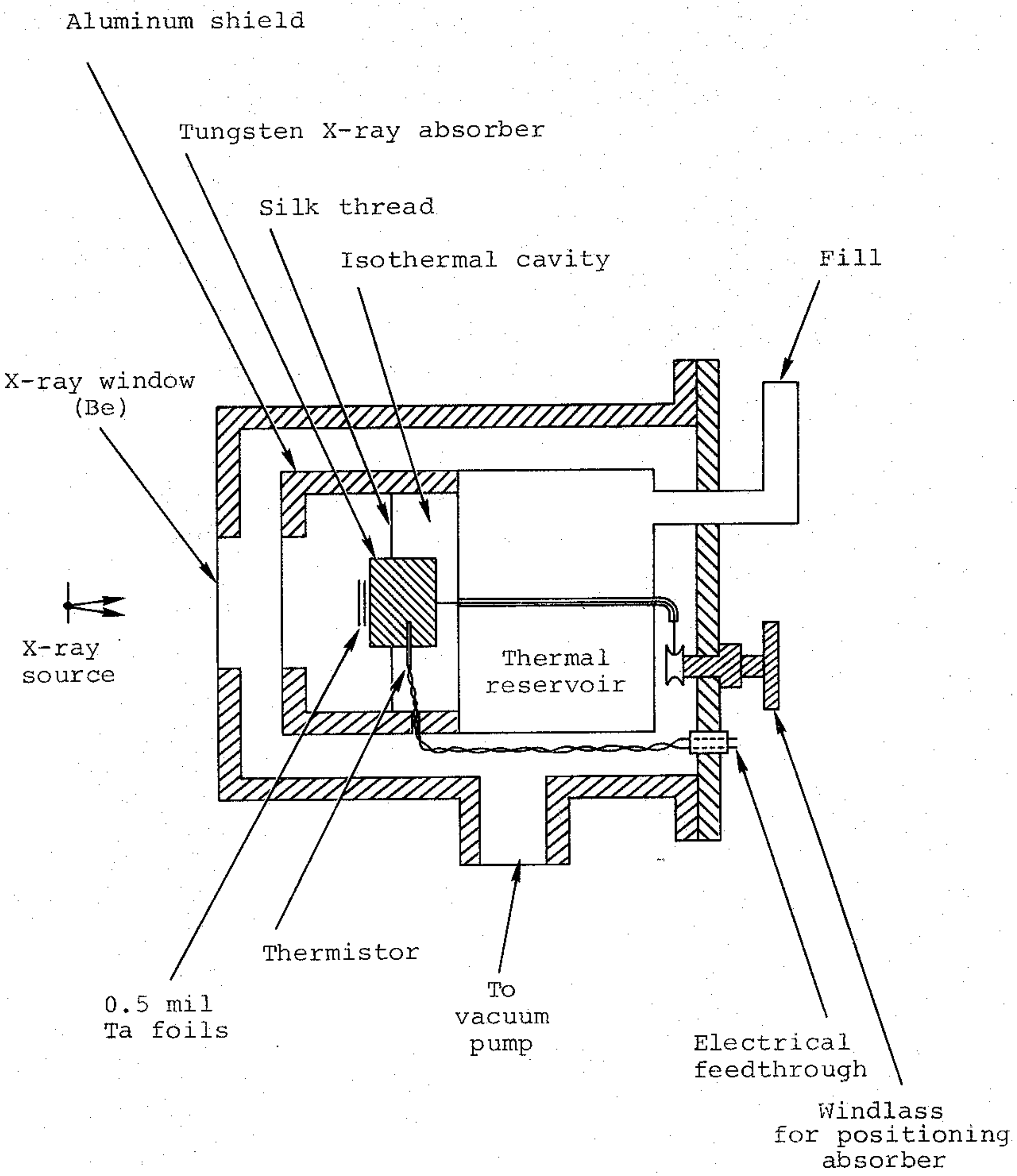

Figure 7.3 Schematic cross section of fluence calorimeter.

where

m = mass of tungsten absorber
C_p = specific heat of tungsten
A = area of front face
$(\Delta T/\Delta R)_o$ = temperature coefficient of thermistor at the reference temperature (T_o).
ΔR = resistance change

The temperature coefficient of the thermistor ($\Delta T/\Delta R$) was measured by simultaneously monitoring the thermistor and a thermocouple also attached to the absorber and varying the temperature about the reference temperature (T_o). However, a more direct and accurate technique was also employed. The calorimeter was exposed to a 400 curie Cs^{137} gamma source (0.66 MeV) at Physics International Company. At this energy there is 10 percent transmission through the absorber so that the calibration must be increased by 10 percent for radiation which is totally absorbed. The calibration is

$$\frac{m}{A} C_p \left(\frac{\Delta T}{\Delta R}\right) = 6.21 \times 10^{-5} \pm 3 \text{ percent } (\text{cal/cm}^2\text{-ohm})$$

This value agrees to within 10 percent of the value calculated using the temperature coefficient of the thermistor.

Two 0.5 mil tantalum foils were also positioned directly in front of the tungsten to measure the FSD, and TLD's were placed outside the calorimeter housing.

REFERENCE

7.1. G. Yonas, P. Spence, D. Pellinen, B. Ecker, and S. Heurlin, "Dynamic Effects of High ν/γ Beam Plasma Interactions," DASA-2296, PITR-106-1, Physics International Company, San Leandro, California, April 1969.

SECTION 8

SUMMARY AND CONCLUSIONS

The conclusions of this work relating to beam generation, transport, and diagnostics (both e-beam and X-ray) are summarized below.

8.1 DIODES

Diode impedance laws and the phenomena of impedance collapse have been studied. Diode impedance prior to beam pinch in the anode-cathode gap has been accurately modeled using a Langmuir-Child's impedance law with a time-dependent gap spacing to include the effect of hydrodynamic expansion of the anode. Impedance levels of cathodes when current values are greatly in excess of the critical pinch current have been described by a parapotential flow model. Hollow cathodes have proved useful in extending the impedance lifetime of high-current pinched diodes. Measurements of current density at the anode plane as a function of radius and time have shown the existence of current "wings" (i.e. current density at the cathode edge) even for the highly pinched beams which appear to set a fundamental percentage limit on the energy one can deliver to the pinched core. Self-magnetic decoupling of nearby diodes has been demonstrated using isolated cathode shanks and ground return cylinders.

8.2 NEUTRAL GAS TRANSPORT-NO EXTERNAL FIELDS

Our approach to a neutral gas transport system (generation of small-diameter, 50 to 80 kA beams and transport in small-diameter guide pipes) was found to be infeasible because of diode pinch in both the circular and annular cathodes used in the tests. Because of an apparent decrease in the Langmuir-Child's impedance constant (K = 40 to 50 instead of 136) for this geometry it appears that currents ~ 25 kA per beam would be required to prevent diode pinch.

Other neutral gas approaches that may yet be feasible involve generation and transport of much lower current density beams followed by a compression and mixing stage.

8.3 TRANSPORT IN EXTERNAL B_θ FIELDS (LINEAR PINCH)

Efficient transport and combination of beams using linear pinch discharges to provide external B_θ fields has been shown feasible as a multi-beam handling approach. Approaches to beam compression in a tapered pinch have shown unacceptably large losses: this appears to be the only weakness of a B_θ transport system. Fluence control has been demonstrated by variation of injection time of the beam into the collapsing pinch, and transport has been described by a single particle model. Time phasing and operational features of a B_θ system make it a complex one; however, these complications may be justifiable depending on the status of other transport techniques.

8.4 TRANSPORT IN EXTERNAL B_z FIELDS

High transport efficiencies at current densities up to 40 kA/cm^2 have been observed using longitudinal magnetic fields in the range of 7 to 8 kG. (An optimum field was found for transport--higher and lower fields produced lower efficiencies). Higher levels of gas preionization have been shown to improve transport efficiencies at higher magnetic fields. Beam compression to higher current density and the convergence of beams to nearby spatial locations remain the major areas of uncertainty in the feasibility of a complete B_z transport system. Another disadvantage to B_z systems is the presence of fringing magnetic fields in the irradiation volume. However, these fringing fields may possibly be reduced to acceptable levels by shielding the sample volume from pulsed external fields or by configuring the solenoid coils in a closed field configuration.

Beam convergence has been effectively demonstrated by use of a large annular cathode injecting into a conical transport region. In this case, the B_z field was held constant throughout the transport region so that the beam cross-sectional area remained constant; the shape at injection (a large-diameter thin annulus) was transformed into a smaller-diameter, thicker annulus without loss of transport efficiency.

8.5 DIAGNOSTICS

Electron beam and X-ray diagnostics have been developed and modified for use on high current accelerators. Voltage measurement continues to be an area of minimum accuracy because of the inductive component present on the monitor output $[V_{inductive} = d/dt\ (LI)]$. A capacitive monitor located inside the tube near the cathode has proved useful at lower operating voltages, but it exhibits erratic behavior at voltages of 500 kV, and we have had to rely on voltage monitored external to the tube for routine voltage diagnostics (including correction for the inductive component). Diode current diagnosis has been accomplished by use of a Rogowski coil surrounding the cathode. One advantage of this technique (as opposed to current shunts external to the tube) is that it provides an accurate measure of accelerated current, independent of current flow along other paths (e.g., flashing across the insulator, or background emission by the high-voltage feed structure). Faraday cups and graphite calorimetry have been adapted for monitoring parameters of transported electron beams. Calorimetric X-ray diagnostics have been demonstrated as usable on a routine basis. They are able to provide direct measurement of X-ray fluence and X-ray energy deposition versus depth profiles (as well as front surface dose) in moderate to high-Z materials. The major advantage of this calorimetry approach (over TLD dosimetry) is that it eliminates the need for spectrum assumptions or bremsstrahlung production calculations to unfold fluence and front surface dose from the TLD readings.

APPENDIX A

QUASI-PARAPOTENTIAL ELECTRON FLOW IN A HIGH ν/γ DIODE

by
J. Creedon

A.1 INTRODUCTION

In the past several years, the high current relativistic diode has been the subject of extensive investigation (References A.1 through A.6). These diodes have pulsed voltages of 10^5 to 10^7 volts applied for periods of $\sim 10^{-7}$ seconds giving peak currents in the range of 10^4 to 10^6 amperes.

For many cases, the pulse length is sufficiently long so that the anode current approaches a steady state value. For this reason, only steady state solutions will be considered in the following analysis.

A typical diode might have the configuration shown schematically in Figure A.1. The anode is a plane. The cathode shank is a cylinder of radius R_C, and the face of the cathode is spaced a distance d from the anode. Actual cathodes are usually composed of needles or of some other roughened surface so that the emission process is initiated by field emission.

There is evidence that a cathode plasma forms (References A.2, A.4, and A.5), due to the vaporization of metallic whiskers on the cathode surface (References A.10, A.11, and A.12). The existence of this plasma at the cathode is the basis for the treatment of these diodes as "space-charge-limited"; that is, the emitted current density is limited to that value for which the associated space charge cloud reduces the electric field to zero at the cathode.

For the space-charge-limited case, and with a sufficiently low potential difference between the cathode and anode, one could (neglecting fringing effects) apply a nonrelativistic Child's law

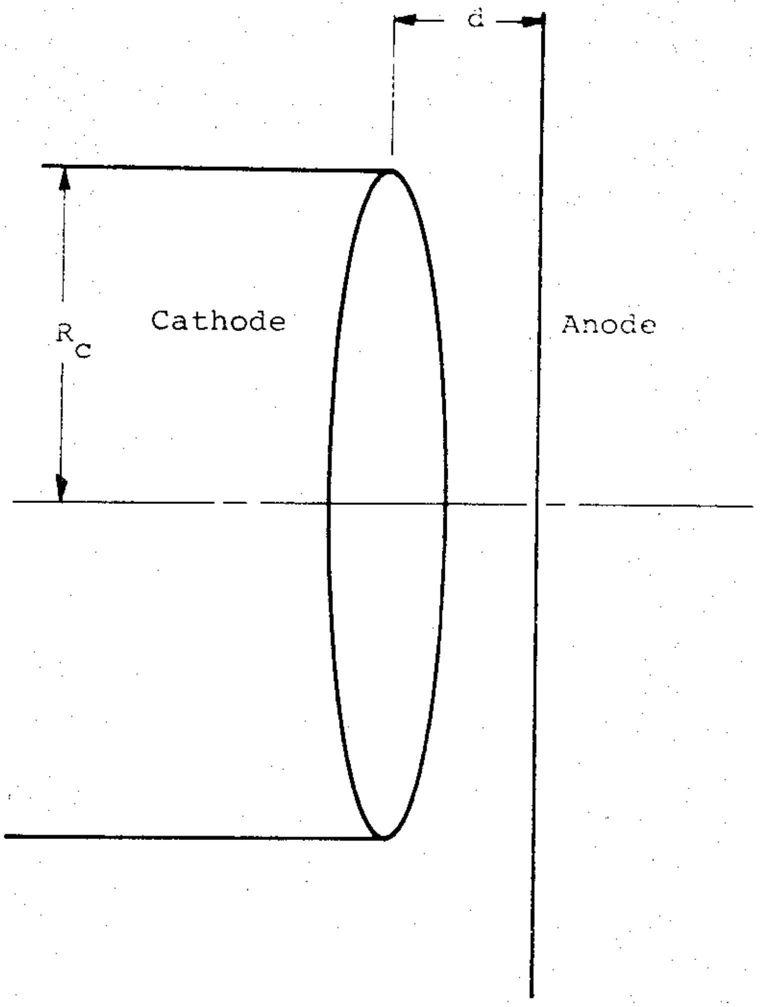

Figure A.1 Diode configuration.

theory for plane-parallel electron flow. (All symbols are defined at the end of this appendix and MKS units are used throughout.)

$$j_o = \frac{2.34 \times 10^{-6} V_o^{3/2}}{d^2} \qquad \text{(A-1)}$$

where j_o is the current density, V_o the anode-cathode potential difference, and d the anode cathode spacing.

For diode currents below the critical current (to be defined presently) the observed current densities tend to be considerably higher than values calculated from Equation A-1. One explanation for this discrepancy is the impedance collapse phenomena (References A.1 and A.4). It has been postulated that the large energy density of the electron beam at the anode creates a highly conducting plasma, and that the hydrodynamic motion of the anode plasma (as well as the cathode plasma) reduces the value of d during the pulse.

Another mechanism which must be considered is the emission of positive ions from the anode plasma. The problem of plane-parallel bipolar flow of electrons and positive ions has been considered by Langmuir (Reference A.7) and others (References A.8, A.9, and A.15). If j_o is the electron current density in the absence of positive ions (Equation A-1), j_e the electron current density with positive ions, and j_p the positive ion current density, then (nonrelativistically):

$$(j_e/j_o)^{\frac{1}{2}} = \frac{3}{4}\int_0^1 \frac{dU}{\left\{U^{\frac{1}{2}} + \alpha\left[(1-U)^{\frac{1}{2}}-1\right]\right\}^{\frac{1}{2}}} \qquad \text{(A-2)}$$

where

$$\alpha = \frac{j_p}{j_e}\left(\frac{\eta_e}{\eta_p}\right)^{\frac{1}{2}}$$

and η_e and η_p are the charge to mass ratio for the electron and the positive ion.

For the completely space-charge-limited case ($\alpha = 1.0$) the electric field is reduced to zero at the anode (as well as at the cathode). Numerical evaluation (Reference A.7) of the integral in Equation A-2 gives $j_e = 1.86\ j_o$ for $\alpha = 1.0$, and j_p is negligible because $\eta_e >> \eta_p$.

As the applied potential and the anode current of the diode increase, two new phenomena become important.

a. Equations A-1 and A-2 must be modified by using the correct relativistic relations between velocity and kinetic energy.

b. The self-magnetic field of the anode current causes the trajectories to be curved towards the axis.

The relativistic velocity correction has been worked out (References A.5, A.6 and A.9) for both unipolar and bipolar plane-parallel flow.

When considering the effect of the self-magnetic field, it is convenient to define a critical current I_c (References A.5, A.6, and A.14):

$$I_c = 8500\ \beta_o\ \gamma_o\ \frac{R_c}{d} \qquad \text{(A-3)}$$

where β_o is the ratio of the electron velocity to the speed of light at the anode and $\gamma_o = (1-\beta_o{}^2)^{-\frac{1}{2}}$.

Equation A-3 is an approximation derived by neglecting the radial electric field and the variation of the magnetic field along the path of the electron. The current I_c is the anode current which causes an electron emitted at the cathode edge to follow a path which is tangent to the anode surface.

Despite its approximate nature, Equation A-3 gives a good indication of the current level that will cause pinching. For currents higher than the critical current the anode current will be concentrated around the axis of the diode.

It is possible to minimize the effects of the anode plasma by constructing the cathode in the form of a hollow ring. For a pinched electron beam the anode plasma and positive ions will be concentrated around the axis and will have a minimum interaction with the emitting areas of the cathode.

There remains the problem of calculating the anode current in the presence of the large magnetic field. The problem of the very high current diode in many ways suggests the Brillouin type of electron flow that exists in crossed electric and magnetic fields (Reference A.13).

DePackh (Reference A.14) explored just such a possibility when he calculated the parapotential (i.e., along equipotentials) flow in a diode. Friedlander et al. (Reference A.6) have carried out a similar calculation.

In the following sections we will develop a parapotential model for the diode which predicts anode currents that are in good agreement with measured values.

A.2 PARAPOTENTIAL MODEL

The object of any model for electron flow in a diode is a consistent solution for the coupled equations that describe the interaction of the electromagnetic fields and the motion of the electrons. In other words, the motion of the electrons under the influence of the electromagnetic fields will give a certain space-charge distribution. This distribution, when combined with the equations of the electromagnetic fields and the boundary conditions, must give the original fields.

The model proposed here is not completely consistent in the above sense. The principal assumption of the model is that the electron flow is parapotential in most of the diode, but that there is a small region around the axis in which the electrons travel across the equipotentials to reach the anode. The total current carried by the electrons is calculated as a function of the anode potential by neglecting this small region around the axis.

Other features of the model may be seen by referring to Figure A.2. The emission is assumed to occur principally at the edges of the cathode and on the cathode shank. The emission for most of the central area of the cathode is suppressed because the electron sheath has depressed the potential to zero in this region. The details of how the electrons leave the cathode edge or shank and reach higher equipotentials are not considered.

It is at least plausible that the anode current is determined by the amount of current that can flow from the edge of the cathode to the axis, and that one can calculate the anode current without considering in detail the process that occurs at the axis.

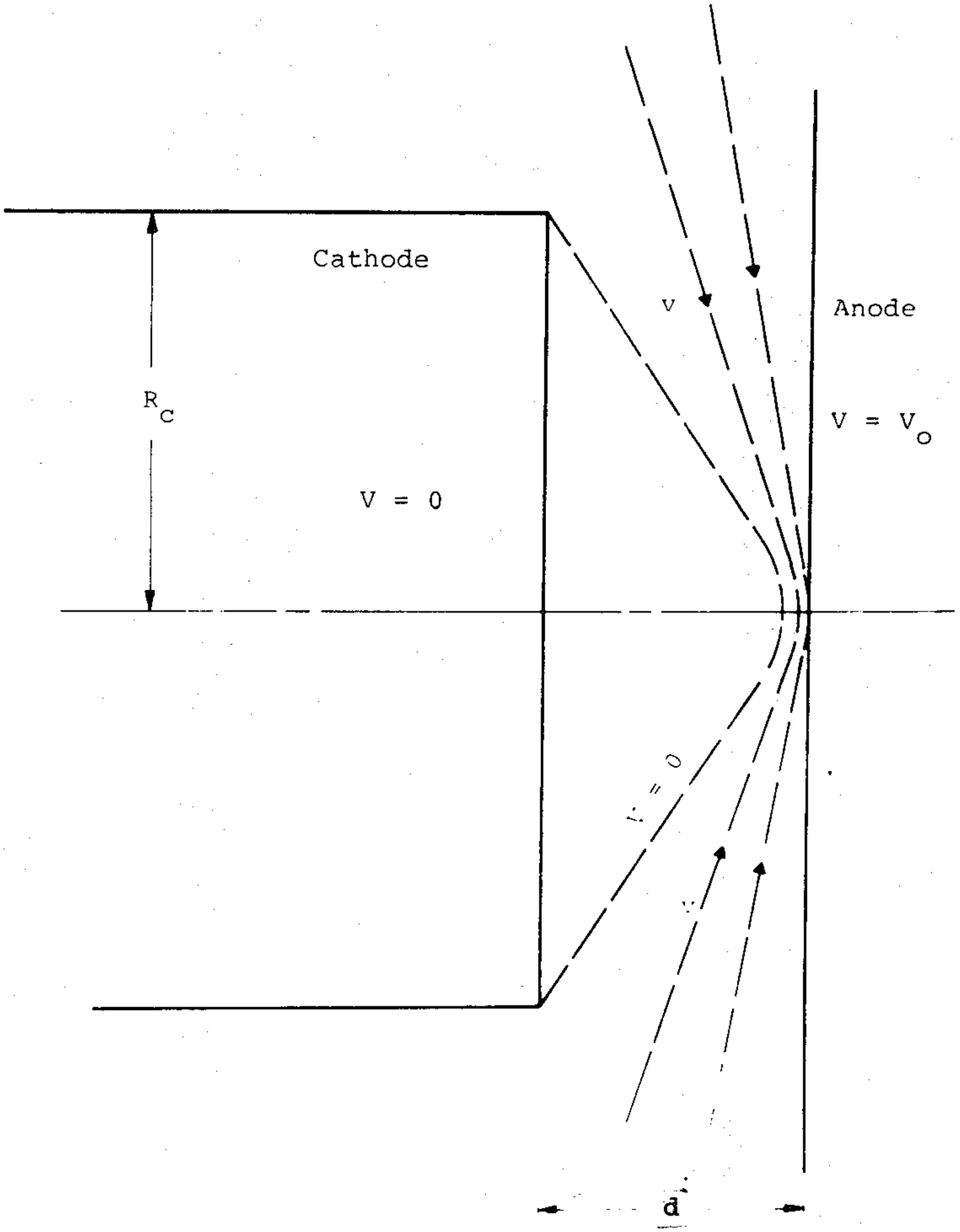

Figure A.2 Schematic of electron flow.

The current flowing in the diode is presumed to have only radial and axial components and it is assumed to be cylindrically symmetrical. Only the steady state case is considered. Because of the symmetry and the lack of an azimuthal component of current, the magnetic field in the diode has only an azimuthal component. The magnetic field is given by

$$B_\phi = (\mu_o/2\pi R)\int \vec{j} \cdot \vec{d\sigma}$$

where R is the radial distance from the axis and $\int \vec{j} \cdot \vec{d\sigma}$ is taken over an area whose boundary is the circle (centered on the axis) of radius R located in a plane parallel to the anode.

For the steady state, the equation of continuity gives

$$\nabla \cdot \vec{j} = 0$$

From the divergence theorem and the assumption of electron flow along equipotentials one can see that

$$\int \vec{j} \cdot \vec{d\sigma}$$

(taken over an area as specified above) is a constant for any point on a given equipotential. Therefore, along an equipotential

$$B_\phi \; \alpha \; \frac{1}{R}$$

The parapotential flow condition for a trajectory that is approximately straight is

$$\vec{E} = -\vec{u} \times \vec{B}$$

and since u is a constant

$$E = |\nabla V| \; \alpha \; \frac{1}{R} \qquad \text{(A-4)}$$

along any equipotential.

Now consider a polar coordinate system with its z axis along the axis of the diode and with its origin at the anode surface (see Figure A.3). The form for the gradient in spherical polar coordinates

$$\nabla V = \frac{\partial V}{\partial r} \vec{e}_r + \frac{1}{r} \frac{\partial V}{\partial \theta} \vec{e}_\theta + \frac{1}{r \sin\theta} \frac{\partial V}{\partial \phi} \vec{e}_\phi$$

suggests a very simple set of equipotentials. If V is only a function of the polar angle θ then

$$V = V(\theta)$$

and

$$E = \frac{-1}{r} \frac{\partial V}{\partial \theta}$$

The equipotentials are the cones

$$\theta = \text{constant}$$

and the condition in Equation A-4 is satisfied since

$$R = r \sin \theta$$

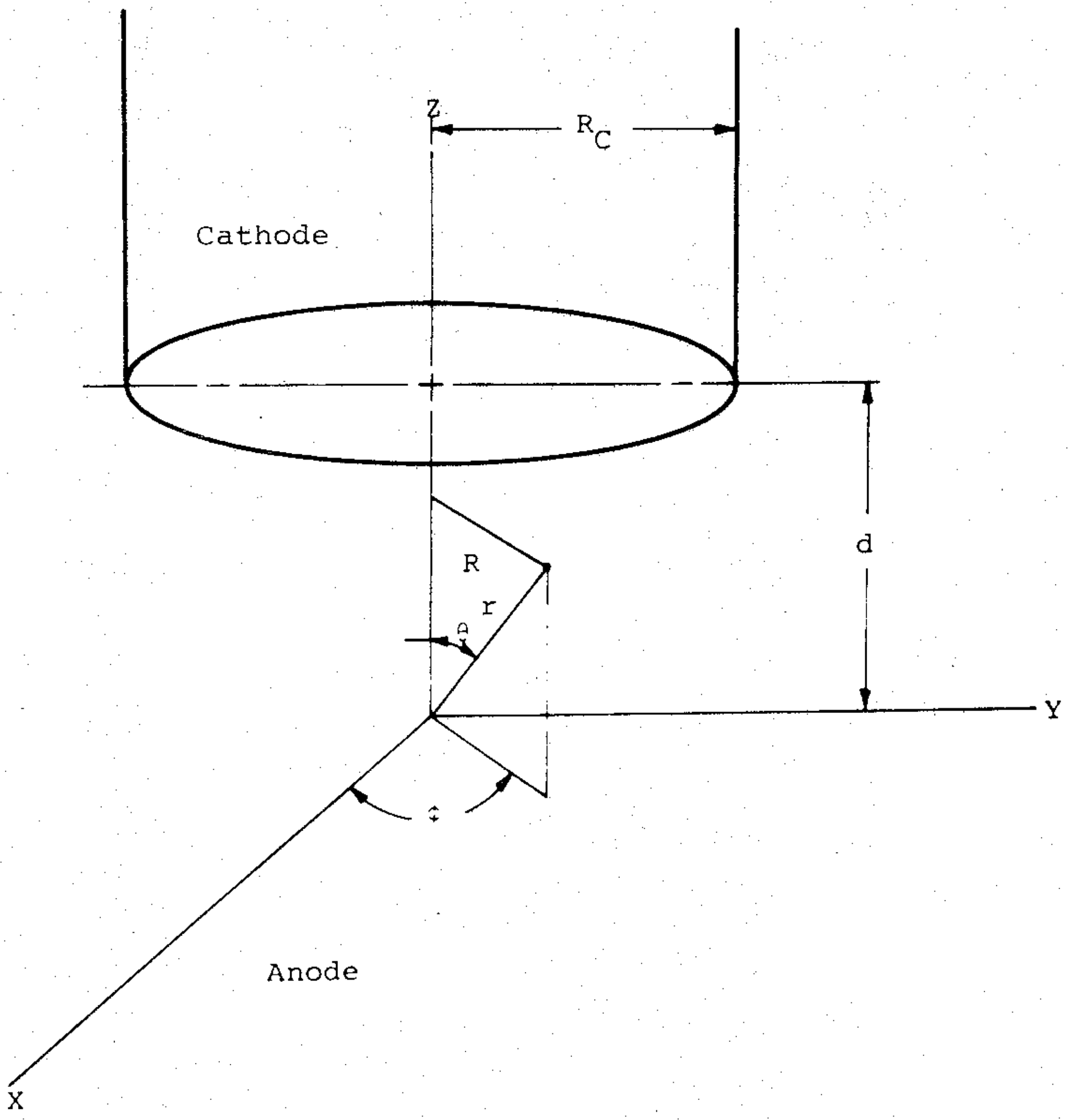

Figure A.3 Coordinate system for diode calculations.

These considerations result in what is perhaps the simplest possible set of equipotentials. Of course, there is no guarantee of uniqueness.

The derivation which follows is very similar to that presented by Friedlander et al. (Reference A.6) for conical equipotentials.

A.3 RELATIONSHIP BETWEEN CURRENT AND POTENTIAL FOR CONICAL EQUIPOTENTIALS

The system of equations that must be solved (see symbol list at the end of this appendix) is

Poisson's equation:

$$\nabla^2 V = -\frac{\rho}{\varepsilon_o} \tag{A-5}$$

Current inside a given equipotential:

$$I = \int \vec{j} \cdot \vec{d\sigma} \tag{A-6}$$

Parapotential flow condition:

$$\vec{E} = -\vec{u} \times \vec{B} \tag{A-7}$$

Magnetic field:

$$B_\phi = \frac{\mu_o I}{2\pi R} \tag{A-8}$$

Relationship between electron velocity and potential:

$$u = \beta C = C \left[1 - \frac{1}{\gamma 2}\right]^{\frac{1}{2}} \qquad \text{(A-9)}$$

$$\gamma = \frac{eV + m_o C^2}{m_o C^2}$$

From the divergence theorem and the conical flow lines for j one can see that

$$j \;\alpha\; \frac{1}{r^2}$$

on an equipotential, and since the velocity u is a constant on an equipotential, the charge density must have the form

$$\rho = g(\theta)/r^2 \qquad \text{(A-10)}$$

where $g(\theta)$ is some function to be determined.

The current flowing between polar angles θ and $\theta + \Delta\theta$ is given by

$$\Delta I = - \rho\beta C\Delta A \;=\; - \frac{g(\theta)}{r^2} \beta \; C \; 2\pi \; r^2 \sin\theta \; \Delta \; \theta$$

so that

$$\frac{dI}{d\theta} = - 2\pi \; g(\theta) \; \beta \; C \sin \theta \qquad \text{(A-11)}$$

Combining Equations A-5 and A-10 and expressing the result in spherical polar coordinates gives

$$\frac{d^2V}{d\theta^2} + \frac{\cos\theta}{\sin\theta}\frac{dV}{d\theta} = -\frac{g(\theta)}{\varepsilon_o} \qquad \text{(A-12)}$$

Writing E as $-\nabla V$ and combining Equations A-7 and A-8 gives

$$\frac{dV}{d\theta} = \frac{\beta C\, \mu_o\, I}{2\pi\, \sin\theta} \qquad \text{(A-13)}$$

If Equation A-13 is differentiated and combined with Equation A-11 to eliminate $dI/d\theta$, the resulting expression for $g(\theta)$ can be substituted into Equation A-12. If the result of this process is combined with Equation A-9 one gets, after some manipulation,

$$\frac{d^2\gamma}{d\theta^2} + \frac{\cos\theta}{\sin\theta}\frac{d\gamma}{d\theta} = \frac{\gamma}{\gamma^2-1}\left(\frac{d\gamma}{d\theta}\right)^2 \qquad \text{(A-14)}$$

which is the fundamental relation for the parapotential flow.

For a solution to Equation A-14 make the substitution:

$$y = \ln\left[\tan\frac{\theta}{2}\right] \qquad \text{(A-15)}$$

giving

$$\frac{d^2\gamma}{dy^2} = \frac{\gamma}{\gamma^2-1}\left(\frac{d\gamma}{dy}\right)^2$$

which has the solution

$$y = k_1 \ln \left[\gamma + (\gamma^2-1)^{\frac{1}{2}}\right] + k_2 \qquad \text{(A-16)}$$

If we designate by δ and θ_m the polar angles of the equipotentials that comprise the minimum and maximum extent of the electron flow, then the boundary conditions are

$$\theta = \delta \longrightarrow \gamma = 1$$

$$\theta = \theta_m \longrightarrow \gamma = \gamma_m$$

This gives

$$k_2 = \ln \left[\tan \frac{\delta}{2}\right]$$

$$k_1 = \frac{\ln \left[\tan \frac{\theta_m}{2}\right] - \ln \left[\tan \frac{\delta}{2}\right]}{\ln \left[\gamma_m + (\gamma_m{}^2-1)^{\frac{1}{2}}\right]} \qquad \text{(A-17)}$$

The current flowing with polar angle $\leqslant \theta$ can be evaluated from Equations A-13 and A-9:

$$I = \frac{2\pi}{\mu_o C} \frac{m_o C^2}{e} \frac{\sin \theta}{\beta} \frac{d\gamma}{d\theta} \tag{A-18}$$

$$= 8500 \frac{\sin \theta}{\beta} \frac{d\gamma}{d\theta}$$

from Equations A-9, A-15, A-16, and A-17

$$\frac{d\gamma}{d\theta} = \frac{d\gamma}{dy} \frac{dy}{d\theta} = \frac{(\gamma^2-1)^{\frac{1}{2}}}{k_1} \frac{1}{\sin \theta} \tag{A-19}$$

Combining Equation A-18 and A-19 and using the relation $\beta\gamma = (\gamma^2-1)^{\frac{1}{2}}$ gives

$$I = 8500 \ \gamma/k_1$$

or substituting for k_1 from Equation A-17

$$I = \frac{8500 \ \gamma \ \ln \left[\gamma_m + (\gamma_m{}^2-1)^{\frac{1}{2}}\right]}{\ln \left[\tan \frac{\theta m}{2}\right] - \ln \left[\tan \frac{\delta}{2}\right]} \tag{A-20}$$

and the anode current I_o is given by this expression for $\gamma = \gamma_m$ at $\theta = \theta_m$:

$$I_o = \frac{8500\ \gamma_m \ln\left[\gamma_m + (\gamma_m^2 - 1)^{\frac{1}{2}}\right]}{\ln\left[\tan\frac{\theta m}{2}\right] - \ln\left[\tan\frac{\delta}{2}\right]} \qquad \text{(A-21)}$$

By setting $\gamma = 1$ in Equation A-20 it can be seen that, as an essential boundary condition for the differential equation describing current flow, there must be a boundary current I_b flowing for $\theta \leqslant \delta$

$$I_b = \frac{8500 \ln\left[\gamma_m + (\gamma_m^2 - 1)^{\frac{1}{2}}\right]}{\ln\left[\tan\frac{\theta m}{2}\right] - \ln\left[\tan\frac{\delta}{2}\right]} = \frac{I_o}{\gamma_m}$$

For the region between the equipotential at $\theta = \theta_m$ and the anode at $\theta = \pi/2$ the potential is given by a solution of Laplace's equation:

$$V = V_o + (V_m - V_o) \frac{\ln\left[\tan\frac{\theta}{2}\right]}{\ln\left[\tan\frac{\theta_m}{2}\right]} \qquad \text{(A-22)}$$

where V_o is the anode potential and V_m is the potential for $\theta = \theta_m$.

The electric field calculated from the parapotential solution and from the Laplace solution (Equation A-22) must give the same result for $\theta = \theta_m$. Differentiating Equation A-22, expressing the results in terms of γ and equating to $d\gamma/d\theta$ from Equation A-18 gives

$$I_o = \frac{8500\ \gamma_m\ (\gamma_m - \gamma_o)}{(\gamma_m^{\,2} - 1)^{\frac{1}{2}}\ \ln\left[\tan\frac{\theta_m}{2}\right]} \qquad \text{(A-23)}$$

Equations A-21 and A-23 can be combined to eliminate θ_m.

$$I_o = \frac{8500\ \gamma_m}{-\ln\left[\tan\frac{\delta}{2}\right]} \left\{ \ln\left[\gamma_m + (\gamma_m^{\,2} - 1)^{\frac{1}{2}}\right] + \frac{\gamma_o - \gamma_m}{(\gamma_m^{\,2} - 1)^{\frac{1}{2}}} \right\} \qquad \text{(A-24)}$$

From Equation A-24 it can be shown that the minimum value of I_b (i.e, I_o/γ_m) occurs for

$$\gamma_m = \gamma_o$$

For a given diode geometry and anode voltage (i.e. γ_o) we wish to calculate the anode current I_o. The basic assumptions of the model are that the emission occurs principally on the cathode edge or shank, and that the equipotentials are cones, so that it seemed only natural to pick the angle δ such that (see Figure A.2):

$$\tan \delta = R_c/d$$

The quantities θ_m, γ_m, and I_o are all unknown; although the specification of any one of them determines the other two by a simultaneous solution of Equations A-21 and A-23. The simple parapotential theory is not sufficient to solve the problem completely since it excludes the region around the axis where the flow crosses the equipotentials and where the boundary current flows.

The total diode current (from Equation A-24) is plotted in Figure A.4 versus the potential V_m which occurs for $\theta = \theta_m$ at the edge of the parapotential flow. From Figure A.4 it can be seen that when $V_m = V_o$ (the anode potential) the total current I_o reaches a relative maximum value called the saturation current.

Parapotential flow with I_o greater than the saturation value can only occur for the portion of the curve to the left of the minimum. Since $I_o = \gamma_m I_b$ and $\gamma_m \longrightarrow 1$ for small V_m, values of I_o greater than the saturation current would imply that most of the current is boundary current.

Experimental evidence strongly suggests that the actual current which flows is the saturated parapotential current: that is (from Equation A-23 and A-24),

$$\gamma_m = \gamma_o, \ \theta_m = \pi/2$$

For these conditions the anode current is given by (see Equation A-21)

$$I_o = \frac{8500\ \gamma_o \ \ln \left[\gamma_o + (\gamma_o^2 - 1)^{\frac{1}{2}}\right]}{-\ \ln \left[\tan \delta/2\right]}$$

The relation can be expressed in a more useful form by expanding the denominator (for tan $\delta >> 1$):

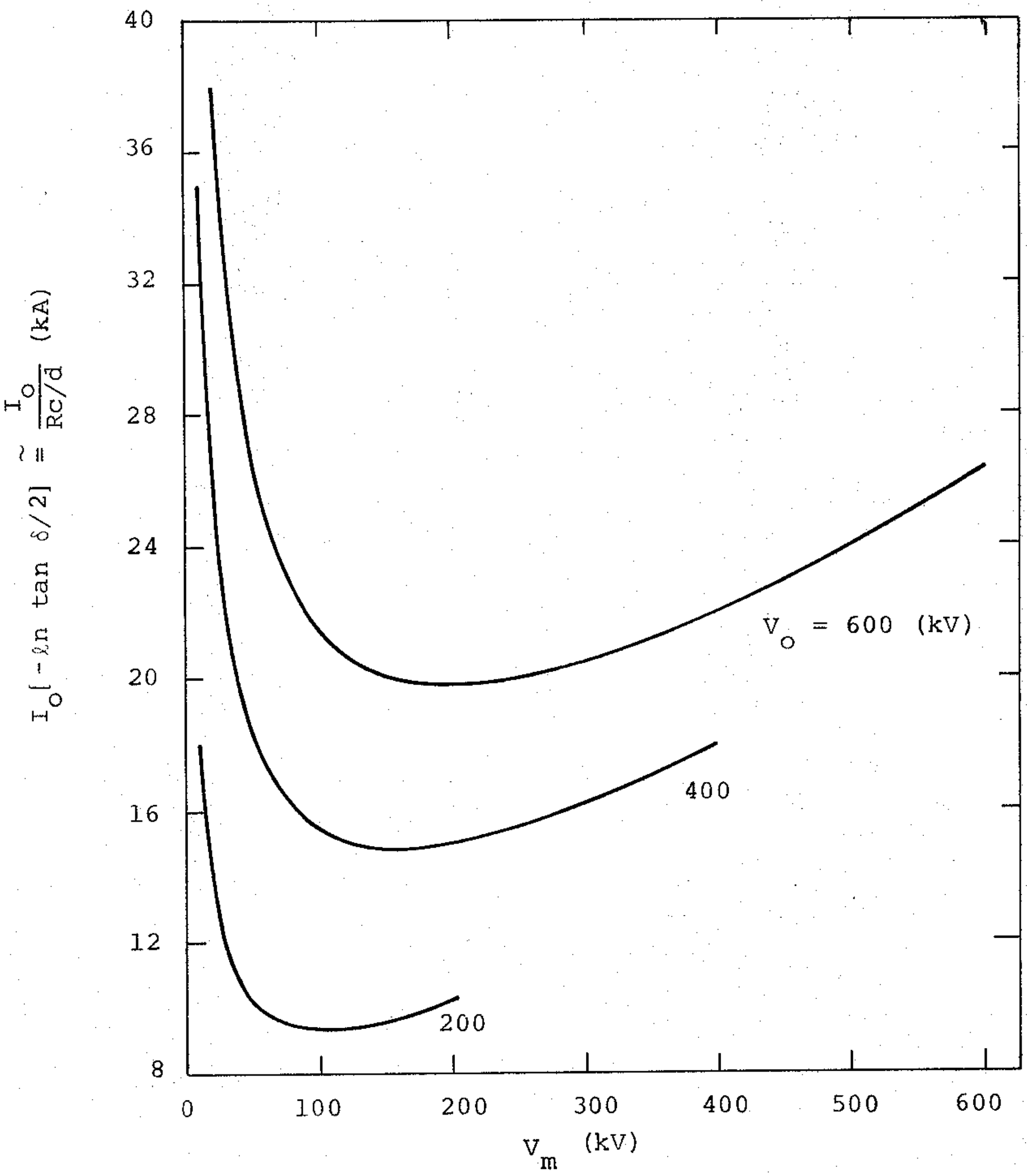

Figure A.4 Total diode current versus V_m.

$$\tan \frac{\delta}{2} = \frac{1 - \cos \delta}{\sin \delta} \cong 1 - \frac{1}{\tan \delta}$$

$$\ln x = (x-1) - \frac{1}{2} (x-1)^2 + \frac{1}{3} (x-1)^3 + \ldots \qquad \text{(A-25)}$$

so that

$$\ln \left[\tan \frac{\delta}{2}\right] \cong - \frac{1}{\tan \delta} = - \frac{d}{R_c}$$

The anode current is then given by

$$I_o \cong 8500 \frac{R_c}{d} \gamma_o \ln \left[\gamma_o + (\gamma_o{}^2 - 1)^{\frac{1}{2}}\right] \qquad \text{(A-26)}$$

SYMBOL LIST
(MKS Units)

j_o	anode current density
V_o	anode potential
d	anode-cathode spacing
R_c	cathode radius
j_e	electron current flowing in the presence of positive ion
j_p	positive ion current
$\eta_e = e/m_o$	charge to mass ratio for an electron
η_p	charge to mass ratio for a positive ion
α	$j_p/j_e \, (\eta_e/\eta_p)^{\frac{1}{2}}$
I_c	critical current
c	velocity of light
u_o	velocity of the electrons at the anode
β_o	u_o/c
γ_o	$(1 - \beta_o^2)^{-\frac{1}{2}}$
$\vec{B}, B_\phi$	magnetic field and its azimuthal component
j	current density in the diode
R	radial distance from the axis
u	electron velocity in the diode
$\vec{E}$	electric field in the diode
V	potential
r, θ, ϕ	spherical coordinates of a point in the diode
ρ	charge density

μ_o, ε_o	permeability and permitivity of free space
I	diode current flowing with polar angle $\leqslant \theta$
β	u/c
γ	$(1 - \beta^2)^{-\frac{1}{2}}$
δ	polar angle of electron flow for which $\gamma = 1$
θ_m	maximum polar angle of electron flow
γ_m	value of γ for $\theta = \theta_m$
I_b	boundary current

REFERENCES

A.1 G. Loda and P. Spence, PIIR-4-71, Physics International Company, San Leandro, California, 1970 (unpublished), and _Bull. Amer. Phys. Soc._, _15_, 1401 (1970).

A.2 J. Clark, S. Linke, Laboratory for Plasma Studies, Cornell University Report No. LPS 23, 1969, (unpublished).

A.3 G. Yonas, P. Spence, D. Pellinen, B. Ecker, S. Heurlin, PITR-106-1, Physics International Company, San Leandro, California, 1969 (unpublished).

A.4 H. Epstein, W. Gallagher, P. Mallozi, T. Stratton, _Phys_. _Rev_. _A2_, 146 (1970).

A.5 DASA 2167, Ion Physics Corporation Report, 1968, (unpublished).

A.6 F. Friedlander, R. Hechtel, H. Jory, and C. Mosher, DASA 2173, Varian Associates, 1968 (unpublished).

A.7 I. Langmuir, _Phys. Rev_., _33_, 954 (1929).

A.8 W. Howes, _J. Appl. Phys_. _36_, 2039 (1965).

A.9 W. Howes, _J. Appl. Phys_. _37_, 437 (1966).

A.10 F. Charbonnier, C. Bennett, L. Swanson, _J. Appl. Phys_. _38_, 627 (1967).

A.11 R. Little, W. Whitney, _J. Appl. Phys_. _34_, 2430 (1963).

A.12 W. Dyke, J. Trolan, E. Martin, and J. Barbour, _Phys. Rev_. _91_, 1043 (1953).

A.13 _Crossed-Field Microwave Devices_, E. Okress, ed., Academic Press, Inc. (New York, 1961).

A.14 D. de Packh, Radiation Project Progress Report No. 5, Naval Research Laboratory, Washington, D.C., 1968 (unpublished).

A.15 K. Muller-Lubeck, _Z. Agnew Phys_. _3_, 409 (1951).

APPENDIX B

A HIGH CURRENT, SUBNANOSECOND RESPONSE FARADAY CUP

A High Current, Subnanosecond Response Faraday Cup

D. Pellinen

Physics International Company, San Leandro, California 94577

(Received 1 December 1969; and in final form, 4 May 1970)

A subnanosecond risetime, milliohm resistance Faraday cup was designed and tested for measuring fractional megampere electron beams from pulsed electron accelerators. The device has been typically operated at electron beam currents of 60 kA with an average electron kinetic energy of 4 MeV. Under short circuit conditions the device has measured currents exceeding 0.25 MA.

A SERIES of pulsed electron accelerators having power outputs exceeding 10^{11} W and pulse durations of approximately 50 nsec has been developed for beam-plasma interaction studies and material response applications.[1,2] A subnanosecond risetime, high current charge collector, and low inductance shunt resistor combination was designed and built to measure intercepted beam currents and to act as a shunt to measure short circuit currents on the accelerators.

The device is illustrated by a schematic in Fig. 1 and by a photograph in Fig. 2. The charge collector is an 8.7 cm diam 8.7 cm long cylinder of graphite which acts as the center conductor. The resistor is a 0.0025 cm thick coaxial tube formed of 302 alloy stainless steel, separated from the center conductor by 0.0075 cm of Mylar dielectric. Connection is made by four straps soldered to the stainless steel resistor. The ground connection is made by a cylindrical shell connected to the outer conductor of a coaxial cable. The shell also forms a vacuum seal for the shunt. Computed inductance of the coaxial resistor is less than 3×10^{-11} H. The resistance of the cup is typically 7 mΩ.

The device is calibrated by two independent methods. First, a known dc current is passed into the cup, and the resistive voltage drop is measured with a millivoltmeter. Second, a pulse generator is connected to the device as shown schematically in Fig. 3, and the output waveform and input current are monitored consecutively with a sampling oscilloscope. A typical calibration trace is shown in Fig. 4 which is a double exposure where the upper trace is the output of the cup, and the lower trace is the input pulse; both are at 2 nsec/div. The risetime of the device is shown to be less than 1 nsec.

Typical current waveforms on two high current pulsers are shown in Figs. 5 and 6. The first is a short circuit shot into the cup with the Physics International model 730 Pulserad. Peak current is 2.8×10^5 A. The second shows a record for a 4 MeV mean energy electron beam on the model 1140 Pulserad accelerated into the cup. Both waveforms are consistent with calculated peak currents and magnetic probe waveforms.

Basically the device is a short circuited, lossy, coaxial transmission line. The current is monitored by measuring the resistive voltage drop along the stainless steel outer conductor. A current injected into the collector will propagate toward the rear, simultaneously inducing an image current in the outer conductor. When the wave reaches the shorted back end in approximately 0.47 nsec, the voltage wave will reverse polarity and reflect backward, largely canceling the inductive voltage. This wave will be damped in several transits by the resistive losses in the stainless steel and graphite. Because the outer conductor is electrically sealed, the current must penetrate the outer conductor to generate a difference in potential between the readout terminals. The ratio of current density at the outer surface of the conductor of thickness X_0 to the current at the inner surface is given by

$$I/I_0=\exp[-X_0((\omega/2)\mu\sigma)^{\frac{1}{2}}],$$

where ω is the angular frequency, μ the magnetic permeability of the conductor, and σ the conductivity of the conductor. For the 1.0 GHz transient wave

$$I/I_0=e^{-1.6}\approx\tfrac{1}{6}.$$

Thus the outer conductor will tend to filter out high frequency transients generated in the cup. The risetime predicted solely from current penetration time in the foil resistor is about 1.1 nsec. The observed risetime is slightly less.

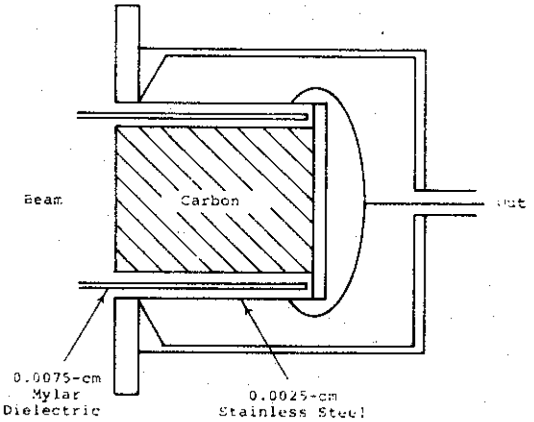

FIG. 1. Schematic of Faraday cup.

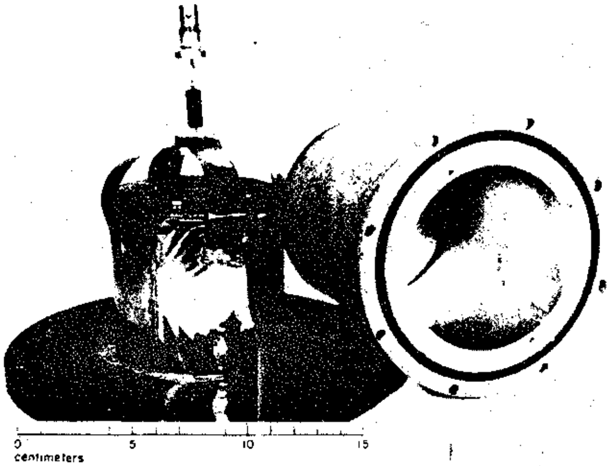

FIG. 2. Faraday cup.

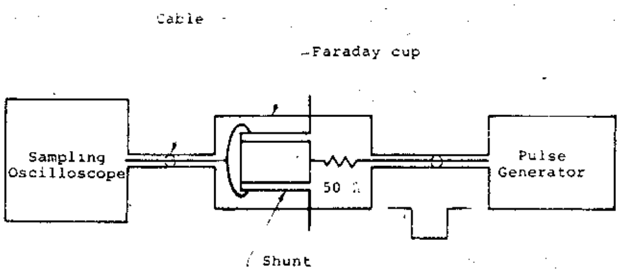

FIG. 3. Faraday cup connected to oscilloscope and pulse generator.

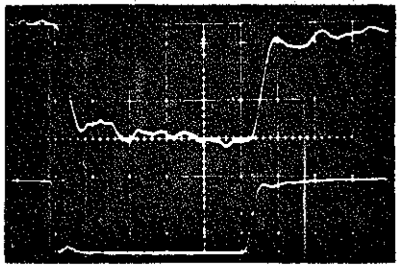

FIG. 4. Faraday cup calibration trace, 6.5 mΩ shunt. Horizontal, τ(2 nsec/div); cup output, 20 mV/div; input waveform, 5 A/div.

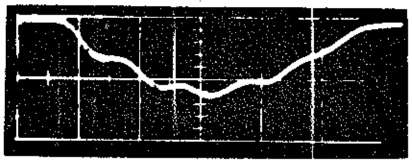

FIG. 5. Short circuit current pulse on model 730 Pulserad, 4.0 mΩ cup. Horizontal, τ(20 nsec/div); output, 960 V/div (2.4×10^5 A/div).

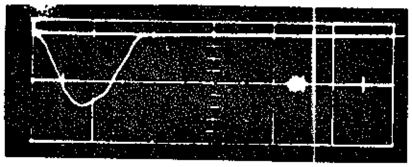

FIG. 6. Accelerated current on model 1140 Pulserad beam of 4 MeV electrons, 4 mΩ cup. Horizontal, 50 nsec/div; vertical, 190 V/div = 47.5 kA/div.

---

[1] H. F. Rugge *et al.*, Bull. Amer. Phys. Soc. **12**, 5 (1967).

[2] W. T. Link, IEEE Trans. Nucl. Sci. **NS-14**, No. 3, 777 (1967).

APPENDIX C

A NANOSECOND RISETIME MEGAMP CURRENT MONITOR

by

D. G. Pellinen and P. W. Spence

(Accepted for publication in RSI)

Several self-integrating Rogowski coils (Reference C.1) with a risetime of approximately 2 nsec and a typical sensitivity of 250 V/MA were developed for measuring megamp currents on pulsed electron accelerators. The coils operate in electric fields of 0.5 MV/cm and in the vicinity of large gamma radiation sources without objectionable noise pickup or signal degradation. The coil is located directly beneath the accelerator anode and encircles the field emission cathode to ensure that only current emitted by the cathode is measured. The coil itself is enclosed in a polyethylene envelope to shield it from charge pickup and physical damage if the electron beam strikes it.

Two sizes of coils were made to accommodate various anode-cathode configurations similar to that shown in Figure C.1 and all were built to essentially the same design as shown in Figure C.2. Integration of the coil output voltage was performed on a low inductance 0.1 Ω resistor similar to that previously described by the author (Reference C.2) differing only in that the resistor was fabricated of 0.0125-mm-thick stainless steel. The coil was a helix of copper wire with a mean diameter of 3.3 mm and a pitch of 7 mm and it was inserted into a 6.4 mm o.d. by 3.7 mm i.d. commercial polyflow tube (Reference C.3). The coil is connected to the integrator terminals and the assembly plotted in epoxy in a form. Coil characteristics for the two sized coils used to date are tabulated in Table C.1.

Table C.1

CHARACTERISTICS OF SELF-INTEGRATING ROGOWSKI COILS

Inside Diameter (cm)	Absolute Sensitivity (V/MA)	Absolute Sensitivity ($V/W/m^2$)	Decay Time (μsec)
10.2	360	92.5	1.2
15.3	260	100	1.4

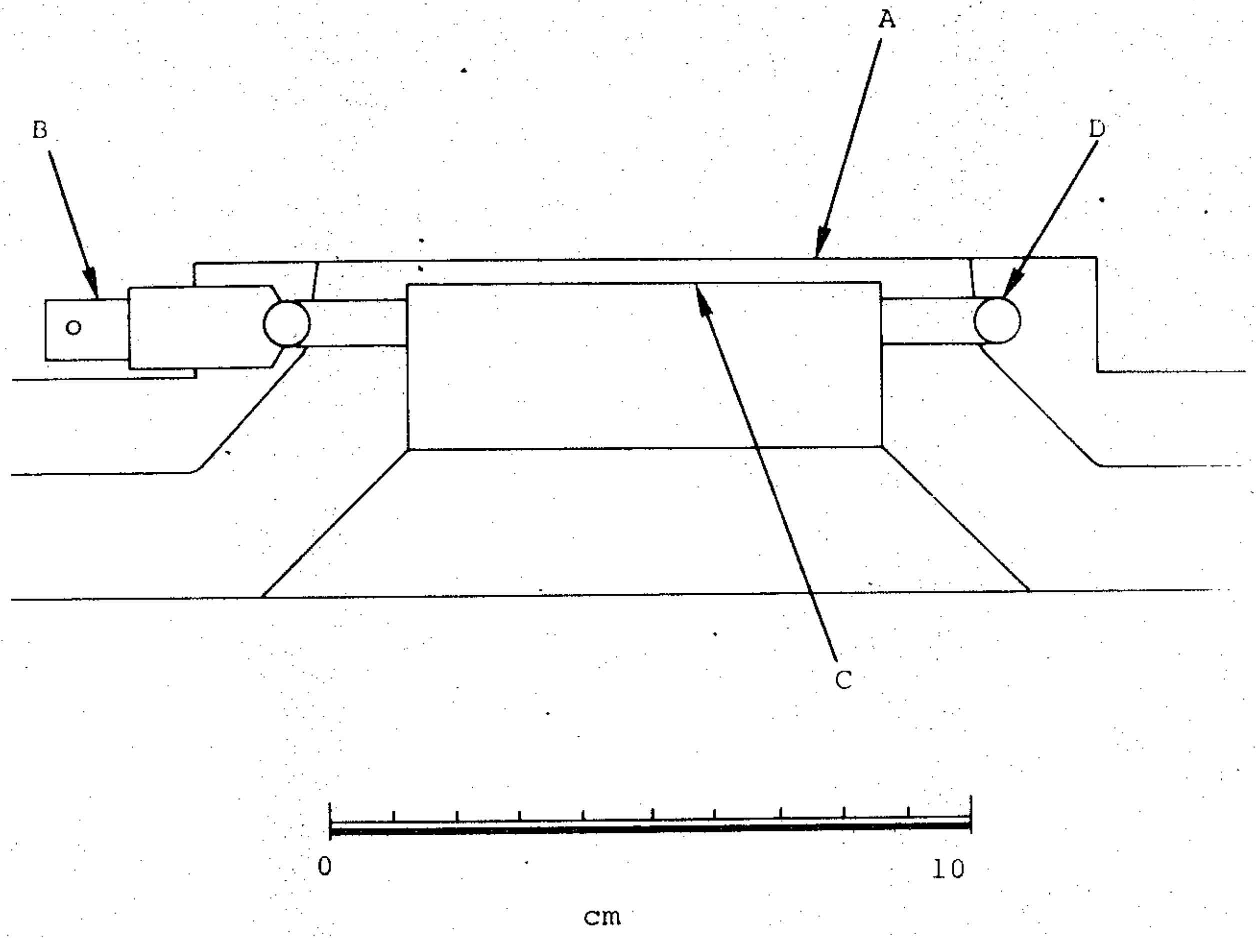

A is the accelerator anode

B is the integrator built on UG 491 BNC connector

C is the field emission cathode

D is the Rogowski coil

Figure C.1 Field emission diode with a 10 cm i.d. current monitor in place.

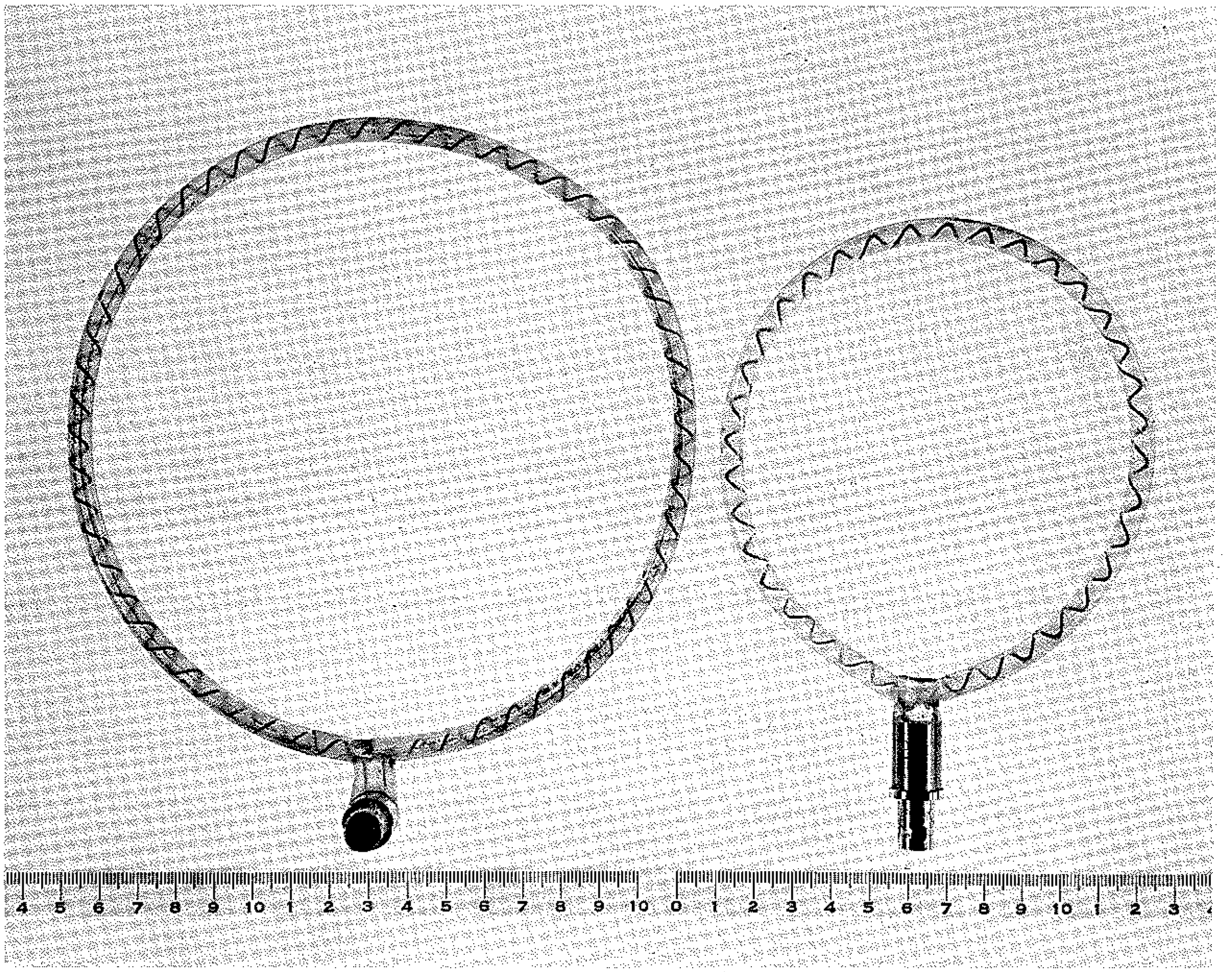

Figure C.2 Integrating Rogowski coils, 10 and 15 cm i.d.

Calibration was made by threading the center conductor of a coaxial cable through the loop and shorting it to a ground plane connected to the outer conductor, and driving it with a current pulse from a 50 Ω pulse generator.

The absolute sensitivity in $V/(W/m^2)$, V/A, the decay constant L/R, and coil transient response are measured by this method. Figure C.3a shows the 15 cm coil being driven by a 325-nsec, 20-ampere pulse and the coil output recorded by a Tektronix 454 oscilloscope at 1 mV/cm. Figure C.3b shows the leading edge waveform from the same coil on a 1.9 nsec risetime Tektronix 7704 oscilloscope at 2 nsec/cm. The line from the coil was not terminated at the oscilloscope in order to double the voltage amplitude. The risetime of the trace from 10 to 90 percent of maximum amplitude is approximately 2 nsec, which is very nearly the risetime of the oscilloscope. Generally one expects the risetime of such a coil to be comparable to the transit time around the coil (Reference C.4). This is about 1.5 nsec for the 10 cm coil and 2.4 nsec for the 15 cm coil. The measured risetime of the 15 cm coil is somewhat faster than 2.4 nsec. Part of this may be a bit of voltage peaking by the self-inductance of the integrating resistor. Also on loosely wound coils, such as these driving a small resistance, the turns adjacent to the resistor provide the majority of the very fast rising current.

The Rogowski coils were also cross calibrated against a high current Faraday cup (Reference C.5) with an accelerator pulse at about 500 kA peak current.

Output waveforms from several accelerator pulses are shown in Figures C.4 and C.5. Figure C.4 shows the current on a shot where the accelerator was accidentally shorted and the current

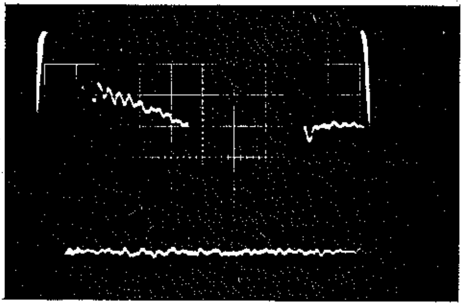

Vertical - 1 mV/div
Horizontal - 100 nsec/div

a. Output waveform of 15 cm i.d. Rogowski coil driven by a 20 ampere current pulse

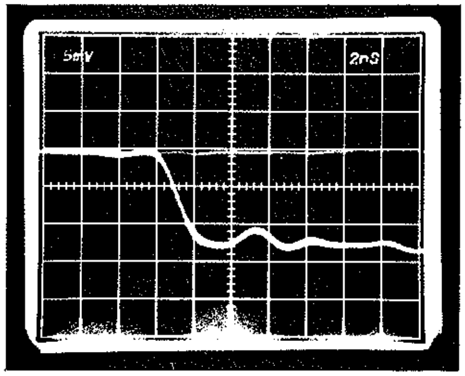

Vertical - 5 mV/div
Horizontal - 2 nsec/div

b. Oscilloscope input unterminated

Figure C.3 Calibration traces.

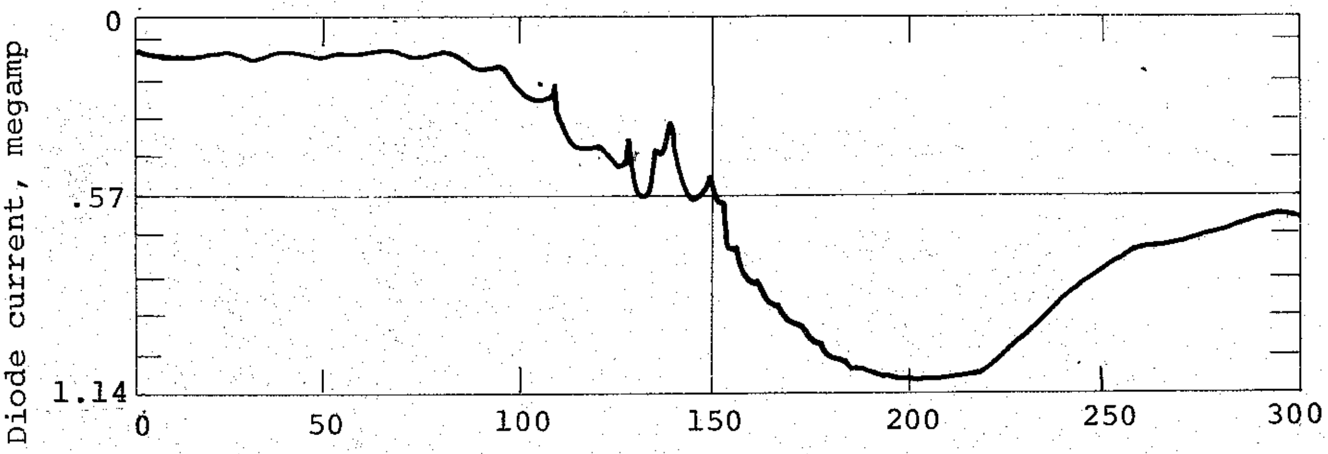

Figure C.4 Current waveform on accidental accelerator short, 0.57 MA/div, 50 nsec/div.

rose to 1.0 MA. Peak magnetic field at the 10.2 cm fluxmeter was 39 kG. Figure C.5 shows instrument traces from an accelerator pulse with a 1.0 Ω field emission diode. The voltage waveform was obtained from a capacitive voltage divider in the pulse-forming network and correction was made for the inductive voltage drop by the method similar to that previously described by the author (Reference C.6). The current monitor was the 15.3 cm i.d. Rogowski coil.

The coils have proved to be rugged both mechanically and electrically. Both coils described went through an accelerator test series without being destroyed or showing any calibration drift.

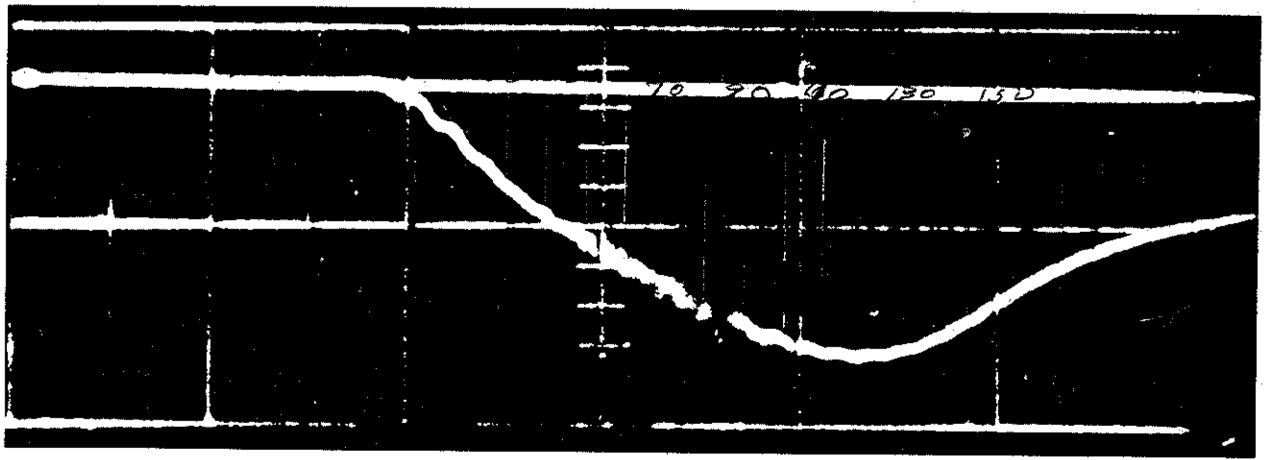

a. Diode current from Rogowski coil, 0.730 MA/cm (190 V/cm)

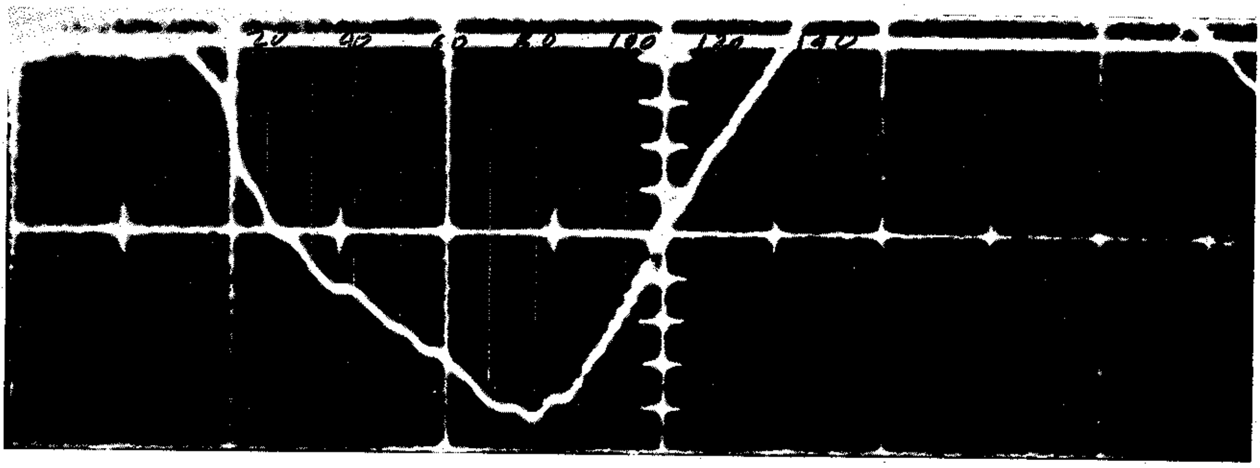

b. Pulse forming network voltage, 0.58 MV/cm

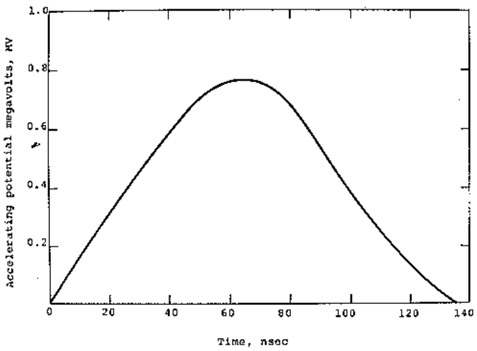

c. Accelerating potential

Figure C.5 Instrument traces from accelerator pulse, 50 nsec/cm.

REFERENCES

C.1 W. Rogowski and W. Steinhaus, Arch. Electrotech., 1, 141 (1912).

C.2 D. Pellinen, "A Subnanosecond Response Fluxmeter," Review of Scientific Instruments, to be published.

C.3 Eastman Polyflow, #44-P-1/4.

C.4 J. Cooper, Plasma Phys., 5, 285 (1963).

C.5 D. Pellinen, Rev. Sci. Instrum., 41, 9 (1970).

C.6 D. Pellinen and S. Heurlin, "A Nanosecond Risetime Megavolt Voltage Divider," Review of Scientific Instruments, 42, 6, 824 (1971).